Synthesis and Characterization of Intergrowth Bismuth Layered Structure Ferroelectrics in the System $SrO-Bi_2O_3-TiO_2$

A Thesis Submitted in Partial Fulfillment of the
Requirements for the Degree of

DOCTOR OF PHILOSOPHY

By

GEETANJALI PARIDA

(Roll No: 510CR102)

Supervisor:
Dr. Japes Bera

Department of Ceramic Engineering
National Institute of Technology
Rourkela–769008, Odisha, India
January, 2015

Dedicated

To

My Beloved Parents

DECLARATION

Date: 18th January 2015

I hereby declare that the work presented in the thesis entitled "**Synthesis and Characterization of Intergrowth Bismuth Layered Structure Ferroelectrics in the System SrO-Bi_2O_3-TiO_2",** submitted for Ph.D. Degree in the National Institute of Technology, Rourkela, has been carried out by me at the Department of Ceramic Engineering, National Institute of Technology, Rourkela and under the supervision of Dr. **Japes Bera**. The work is original and has not been submitted in part or full by me for any degree or diploma at this or any other University/Institute.

GEETANJALI PARIDA
Department of Ceramic Engineering
National Institute of Technology, Rourkela
Rourkela – 769008
Odisha, India

DEPARTMENT OF CERAMIC ENGINEERING

NATIONAL INSTITUTE OF TECHNOLOGY

ROURKELA-769008

CERTIFICATE

This is to certify that the thesis entitled **"Synthesis and Characterization of Intergrowth Bismuth Layered Structure Ferroelectrics in the System SrO-Bi_2O_3-TiO_2"** submitted by **Geetanjali Parida**, for the degree of **Doctor of Philosophy in Ceramic Engineering,** to the National Institute of Technology, Rourkela, is a record of bona fide research work carried out by her under my supervision and guidance. Her thesis, in my opinion, is worthy of consideration for the award of the degree of Doctor of Philosophy in Ceramic Engineering in accordance with the regulations of the Institute.

The results embodied in this thesis have not been submitted to any other university or institution for the award of any degree.

Dr. Japes Bera
Professor
Department of Ceramic Engineering
National Institute of Technology
Rourkela-769008
Email id: jbera@nitrkl.ac.in, jbera@rediffmail.com

ACKNOWLEDGMENTS

First, I would like to express my thanks and gratitude to my supervisor Prof. Japes Bera for his unlimited guidance, insight and suggestions throughout the research. I thank him from the bottom of my heart for introducing me to the area of electroceramic. I thank him for his great patience, constructive criticism and myriad useful suggestions apart from invaluable guidance to me.

I am grateful to Prof. S.K. Pratihar, Head of the department of Ceramic Engineering, for his encouragement and help to carry out the thesis work.

I would also take this opportunity to express my gratitude and sincere thanks to Prof. S. Bhattacharyya and all faculty members of the ceramic department, for their invaluable advice, encouragement, inspiration and blessings.

I would also like to acknowledge the other members of my DSC committee, Dr. Dillip Kumar Pradhan and Dr. Rupam Dinda for their patience reading my manuscript and adding some useful comments.

I wish my sincere thanks to Dr. Ganesh Sahoo, Dr. Arundhati Chakrabarty, Dr. Subrat Mohanty, Mr. Sarat Rout, Ms. Smruti Dash, Mr. Nadiya Nayak, Mr. Jayrao, Mr. Abhisek, Ms. Swarnima, Mr. Akhilesh, Mr. Kanchan, Mr. Snehesh & Family, Ms. Debasmita, Mr. Sonaipandian, Mr. Durga Prasad and all research scholars in our lab for their cooperation.

I would take this opportunity to thank all technical, non-technical staff of ceramic engineering specially Dhala Sir, Mr. Bapi Mohanty, Mr. Susil Sahoo, Mr. Subhobrata Chakrobarty and Mr. Aurbind. Also I would like to thanks Mr. Udya Sahoo, Mr. Subrat Pradhan, Mr. Rajesh Patnaik and Mr. Radhamohan, technical assistant of metallurgical and materials Engineering Department and Physics department, who helped me for the Characterization of my materials.

I would express my sincere thanks to Dr. Anindya Basu and Dr. P.K. Roy for their valuable suggestions in my research Carrier. I would also thank to my friends Priya, Pankajini, Arpna, Bhabani, Arpita, Swagatika, Millan and Jashashree, for their support on my research carriers.

Finally, I owe my deepest gratefulness to my loving family for their patience, understanding, and unconditional love to strengthen me and to make this accomplishment possible.

DATE: 18th January 2015

GEETANJALI PARIDA

ABSTRACT

Intergrowth bismuth layered structure ferroelectrics (BLSFs) in the system SrO-Bi_2O_3-TiO_2 have been investigated with an objective to improve the dielectric and ferroelectric properties of them. There are three BLSFs in this system namely $Bi_4Ti_3O_{12}$ (BIT), $SrBi_4Ti_4O_{15}$ (SBTi4) and $Sr_2Bi_4Ti_5O_{18}$ (SBTi5) and one stable intergrowth BLSF compound between BIT-SBTi4. All these BLSFs compounds have been synthesized through a modified oxalate route. Their phase formation behavior during synthesis has been investigated in details using TG/DSC and XRD analysis. The crystal structures of all the compounds were refined through Rietveld analysis to find accurate lattice parameters. Densification characteristics, microstructure development, dielectric and ferroelectric properties of all compounds were analysed and correlated with each other. The major findings were:

i. BIT-SBTi4 intergrowth compound showed an enhanced $2P_r$ than their individual constituent BIT and SBTi4.

ii. Only a short range intergrowth structure between SBTi4-SBTi5 could be possible, which showed a broaden permittivity temperature characteristics.

iii. The remnant polarization of BIT-SBTi4 intergrowth has been enhanced with Nb doping and doping helps in reducing oxygen vacancy in the ceramics.

iv. The ferroelectric properties of Nb modified BIT-SBTi4 intergrowth can be further enhanced by the La substitution for Bi in the structure, however with a disadvantage of decreased T_c.

v. Keeping the T_c unchanged, the ferroelectric property of the intergrowth can be improved by CuO addition, which helps in better densification of the ceramics.

Key Words: Lead-free Ferroelectric; Intergrowth Bismuth Layered Structure; X-ray diffraction; Dielectric properties; Ferroelectric properties.

LIST OF FIGURES

Page no.

LIST OF TABLES

Nomenclature

θ : Bragg’s angle

JCPDS : Joint committee on powder diffraction standards

XRD : X-ray diffraction

a, b, c : Lattice parameter

(hkl) : Miller index

R_b : Bragg factor

R_{wp} : Weighted residual error

R_{exp} : Expected error

G : Goodness of Fit

t : Tolerance factor

ρ : Density

I : Intensity

N : Avogadro’s number

K : Boltzmann constant

T_c : Curie temperature

λ : X-ray wavelength

°C : Degree in Celsius

^{o}K : Degree in Kelvin

C : Capacitance

R_g : Grain Resistance

C_g : Grain Capacitance

ε' : Relative Permittivity

ε_m''	: Maximum Permittivity
ε_{rm}	: Room temperature Permittivity
$\tan\delta$	: Dissipation factor
A	: Area
d	: Thickness
T_m	: Maximum permittivity temperature
P_r	: Remnant polarization
E_c	: Coercive field
γ	: Diffuseness constant
DSC	: Differential Scanning Calorimetry
TG	: Thermo-Gravimetric Analysis
F	: Frequency
s	: Second
MAUD	: Materials Analysis Using Diffraction
SEM	: Scanning Electron Microscope
FESEM	: Field emission Scanning Electron Microscope
BLSF	: Bismuth layer structured ferroelectrics
BIT	: $Bi_4Ti_3O_{12}$
SBTi4	: $SrBi_4Ti_4O_{15}$
SBTi5	: $Sr_2Bi_4Ti_5O_{18}$
BIT-SBTi4	: $Bi_4Ti_3O_{12}$- $SrBi_4Ti_4O_{15}$ or $SrBi_8Ti_7O_{27}$
Z'	: Real part of Impedance
Z''	: Imaginary part of impedance

CONTENTS

Chapter 1

Introduction

1.1 Introduction

Aurivillius phase bismuth layer structured ferroelectric (BLSF) materials have generated increased attention due to their potential use in non-volatile ferroelectric random-access memory, high temperature piezoelectric applications and electro-optic devices. BLSFs have many advantages over other conventional ferroelectric ceramics like; low operating voltage, fast switching speed, negligible fatigue, excellent retention characteristics and low leakage current density, large remnant polarization, low coercive field, high curie temperature (T_c), low temperature coefficient of dielectrics, low ageing rate, strong anisotropic character and electro-optic switching behavior [1].

The general structural formula for BLSF is $(Bi_2O_2)^{2+}(A_{m-1}B_mO_{3m+1})^{2-}$. The Aurivillius phase is symbolized by fluorite-like $(Bi_2O_2)^{2+}$ layer, interspersed between perovskite-like $(A_{m-1}B_mO_{3m+1})^{2-}$ slabs, where *A* is a 12-coordination site and *B* is an octahedral coordination site, with *m* indicating the number of octahedral stacked along the *c*-axis between two neighboring $(Bi_2O_2)^{2+}$ layers. *A*-site cations can be monovalent, divalent or trivalent or mixture of these; such as Na^+, K^+, Ca^{2+}, Sr^{2+}, Ba^{2+}, Pb^{2+}, Y^{3+}, Ln^{3+}, Bi^{3+}, etc and *B*-site cations can be trivalent, tetravalent, pentavalent or hexavalent or a mixture of these four; such as Fe^{3+}, Cr^{3+}, Ti^{4+}, Zr^{4+}, Nb^{5+}, Ta^{5+}, Mo^{6+}, W^{6+}, etc. The value of *m* may be 1, 2, 3, 4 or 5. Presently there are more than 70 compounds reported in this Aurivillius family and more than 50% of them are ferroelectric. The schematic structures of *m*=1, 2, and 3 members of Aurivillius family are shown in Fig. 1.1.

The (Bi_2O_2) sheet is made up of square pyramidal BiO_4 groups sharing their basal edges [2]. Bismuth ions of the (Bi_2O_2) sheet occupy positions closer to the *A*-sites. The bypyramidal Bi_2O_2 group shares the edges with perovskite block. The compounds with *m* equal to 6, 7 or 8 are difficult to synthesize and their existence is, therefore, doubtful. The BLSF compounds with *m* equal to an odd number of perovskite layers have the crystal symmetry of *B2cb* space group, whereas even layer compounds preferred to crystallize in $A2_1am$ space group. These structures have distortions from a high symmetry tetragonal parent structure (*I4/mmm*) due to the anisotropy behavior of the lone pair of Bi^{3+} cation. In case of even layered structure compound, the center of pseudo-perovskite block is laying in the *A*-position, which is the mirror plane normal to *c*-axis. However, if *m* is odd, then the center is in the *B*-position. In that case mirror plane divides the octahedrons. For these structures, the *ab* plane (basal plane) of the unit cell is the plane parallel to the (Bi_2O_2) layer.

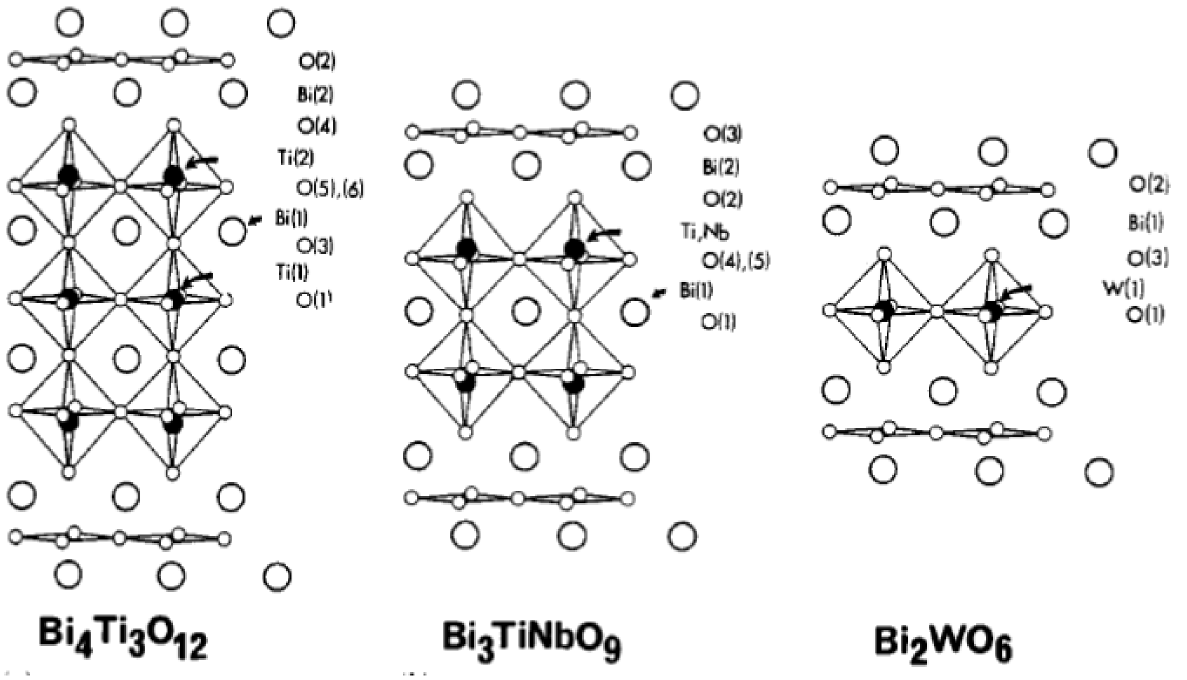

Fig.1.1 The schematic structure of m=1(Bi_2WO_6), 2 (Bi_3TiNbO_9), 3 ($Bi_4Ti_3O_{12}$) member of Aurivillius family [2].

Due to the distortion created by the presence of lone pair Bi^{3+} cations, two types of atomic movement are observed in the system:

i. The movement of atoms parallel to (*00l*) plane: *A*-type cation Bi^{3+} shifts along the polar *a*-axis and octahedron rotate along *c*-axis, this leads to the decrease of *a* and *b*-parameters and orthorhombic distortion (i.e. $b<a$).
ii. Atomic movement parallel to (100) plane: There is also the rotation of octahedra around *a*-axis. All these movement result in a strong elongation of octahedra along *c*, despite its tilting around *a*.

The presence of asymmetric Bi^{3+} cation causes the orthorhombic distortion of the structure where *c*-parameters increases and both *a* and *b* parameters decrease. Hence the replacement of the asymmetric Bi^{3+} cations by any symmetric cation will decrease the orthorhombic distortion. This is actually observed while La^{3+} is substituted for Bi^{3+}[2].

The stability of BLSF structure depends on 2 parameters:

i. The stability of perovskite block and
ii. The level of mismatch between Bi_2O_2 and perovskite layer.

The stability of perovskite depends on the classical tolerance factor represented as:

$$t = \frac{(r_A + 0.140)}{\sqrt{2}(r_B + 0.140)} \tag{1.1}$$

where, r_A, r_B are the ionic radius of *A* and *B* respectively. The stability depends on the relative size of *A* and *B* cations.

In general the tolerance factor for perovskite varies between 0.77 to 1.01. However, in case of the BLSF structure that limit is within 0.86 to 0.97. This narrow range is due to the limitation of the lateral dimension mismatch between Bi_2O_2 and perovskite layer. The bismuth atom in the perovskite can be replaced by other atoms with radii between 0.134 nm (Ca^{+2} in 12-coordination) and 0.161 nm (Ba^{2+}). The B-type cation has the radii in the range 0.059 nm (W^{6+}) to 0.065 nm (Fe^{3+}) [2]. However, the pure oxide perovskite can accept cations in the range from 0.0535 nm (Al^{3+}) to 0.087 nm (Ce^{4+}).

The ferroelectric properties for even ($m=2n$) and odd-layer ($m=2n+1$) BLSFs are different. The spontaneous polarization (P_s) of even-layer compounds is only along the *a*-axis. Based on their orthorhombic space group $A2_1am$, the polarization along *c*-axis is cancelled because of mirror symmetry. However, in odd-layer compounds; like in 3-layered $Bi_4Ti_3O_{12}$, a small degree of spontaneous polarization along *c*-axis can be observed besides the major polarization along *a*-axis as the structure has the space group *B2cb*, in which the center of the pseudo-perovskite set of layers is in the *B* position and a mirror plane divides the octahedrons.

Some useful approaches by which the polarization properties of BLSFs can be improved are; (i) formation of intergrowth between two BLSFs, (ii) high valent cation doping at *B*-site, and (iii) substitution of cations at *A*-site. Many research efforts have been focused on the formation of intergrowth between even and odd layer BLSF compounds. Intergrowths are also called mixed layer Aurivillius compound. Mixed layer Aurivillius phase compounds were first discovered by Kikuchi *et al.* [3, 4]. They consist of the regular intergrowth of one half of the unit cell of a *m*-member structure and one half the unit cell of a ($m+1$)-member structure BLSF. The schematic intergrowth structure between m= 2 and 3 is shown in Fig. 1.2. Some examples of intergrowths are; $Bi_7Ti_4NbO_{21}$ (intergrowth between Bi_3TiNbO_9 and $Bi_4Ti_3O_{12}$), and $SrBi_8Ti_7O_{27}$ (between $Bi_4Ti_3O_{12}$ and $SrBi_4Ti_4O_{15}$). Recently, they have generated a renewed interest because of their superior and interesting ferroelectric properties. For example; the polarization in the intergrowth of $Bi_4Ti_3O_{12}$-$PbBi_4Ti_4O_{15}$ single crystals, was observed not only along *a*-axis but also along the *c*-axis, and the *c*-axis component is suggested to originate from the $Bi_4Ti_3O_{12}$ unit in the intergrowth structure. Enhanced remnant polarization (P_r) was also found in the intergrowth between $Bi_4Ti_3O_{12}$-$SrBi_4Ti_4O_{15}$ and $Bi_4Ti_3O_{12}$-$BaBi_4Ti_4O_{15}$ ceramics.

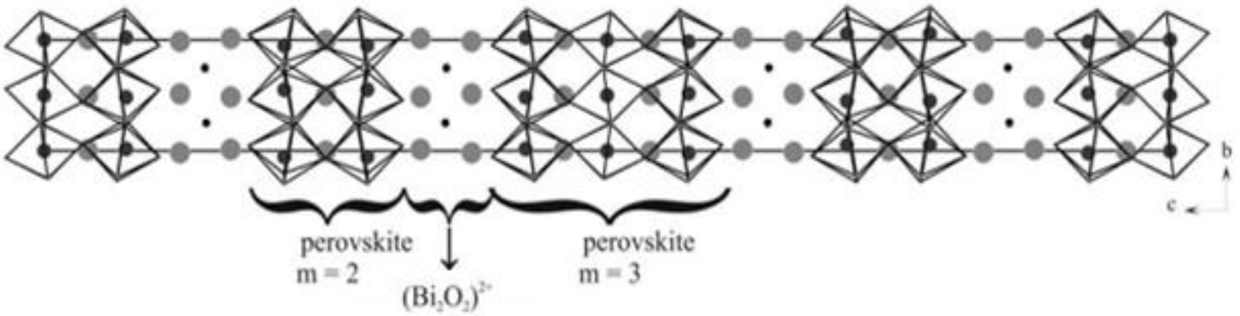

Fig.1.2 Example of intergrowth m = 2 and m = 3 [5].

In BLSFs materials, the electrical conductivity has two components, the conductivity along the *c*-axis which is electronic *p*-type and in the *ab*-plane which is ionic by oxygen vacancies. At low temperatures the conduction is dominant by the hole whereas at high temperatures by oxygen vacancies. As BLSFs ceramics has relatively high electrical conductivity in the *ab*-plane that makes it difficult to pole. Doping with donor cations, like Nb^{5+} to the Ti^{4+} site, can reduce the conductivity. Also, the incorporation of trivalent La^{3+}ions in the Bi^{3+} site could effectively stabilize the oxygen ions in the lattice and lead to the reduction in the conductivity and dielectric loss.

The intergrowth BLSF compound of interest in the system SrO-Bi_2O_3-TiO_2 is $Bi_4Ti_3O_{12}$–$SrBi_4Ti_4O_{15}$ (BIT-SBTi4) intergrowth, which is composed of half the unit cell of $Bi_4Ti_3O_{12}$ and $SrBi_4Ti_4O_{15}$ respectively, as shown in Fig. 1.3. The value of the *c* parameter of the intergrowth, 36.9 Å is almost the same as the value obtained by adding 16.42 Å, one-half of the *c* parameter of BIT to 20.48 Å, one-half of the *c* parameter of SBTi4. This thesis mainly focuses on the synthesis and characterization of BIT-SBTi4 intergrowth ferroelectrics with donor doping at *B*-site and substitution at the *A*-site of the structure.

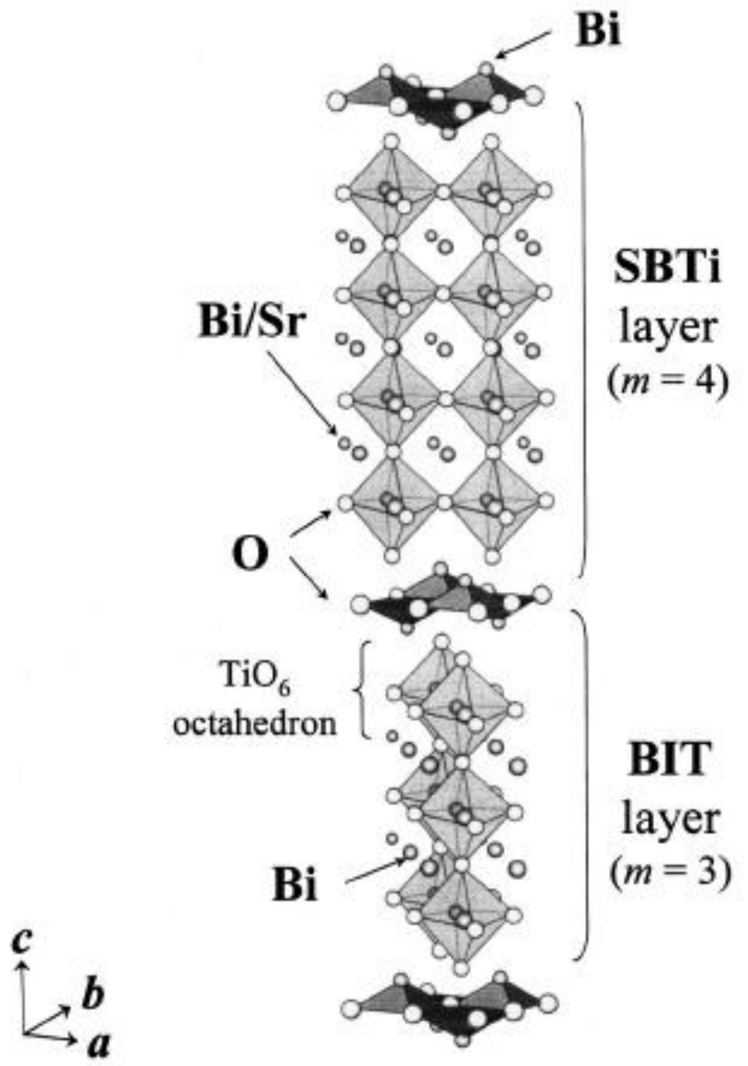

Fig. 1.3 Structure of $Bi_4Ti_3O_{12}$– $SrBi_4Ti_4O_{15}$ ($SrBi_8Ti_7O_{27}$) intergrowth [6].

1.2 Organization of the Thesis

The thesis has been divided into five chapters:

Chapter–I presents a brief introduction on BLSF, $Bi_4Ti_3O_{12}$-$SrBi_4Ti_4O_{15}$ intergrowth and organization of the thesis.

Chapter–II deals with a detailed literature review of some BLSFs. Attempts have been made to systematically classify the available information under different sections. This chapter incorporates background information to assist in understanding the aims and objectives of this investigation, and also reviews recent reports by other investigators with which these results can be compared.

Chapter–III enunciates with the detail experimental process related to this research work.

Chapter–IV describes the results and discussion, which has been divided into 5 sections, where, **Section 1** describes the Preparation of **$Bi_4Ti_3O_{12}$, $SrBi_4Ti_4O_{15}$ and $Sr_2Bi_4Ti_5O_{18}$** powder through a modified oxalate route, sintering behavior, microstructure, dielectric and ferroelectric properties. **Section 2** describes the preparation of $Bi_4Ti_3O_{12}$-$SrBi_4Ti_4O_{15}$ (BIT-SBTi4) and $SrBi_4Ti_4O_{15}$-$Sr_2Bi_4Ti_5O_{18}$ (SBTi4-SBTi5) intergrowth compounds through a modified oxalate route and structural, dielectric characterization. **Section 3** narrates the study of the structure, dielectric properties of niobium doped BIT-SBTi4 ceramics, **Section 4** deals with the effect of La-substitution on the Nb modified BIT-SBTi4 intergrowth and dielectric and ferroelectric properties of all the ceramics. **Section5** describes the effect of CuO additive on the ferroelectric properties of Nb modified BIT-SBTi4 intergrowth.

Chapter–V contains the concluding remarks and the scope of future work.

A complete list of references has been provided at the end of each chapter of the thesis. Finally, a concise list of publications in-peer reviewed international journals related to present research work has been presented in the end.

1.3 References

[1] B H Park, B S Kang, S D Bu, T W Noh, L Lee and W Joe, *Nature (London)* 401 (1999) 682-684.

[2] B. Frit and J. P. Mercurio, *Journal of Alloys and Compounds*, 188 (1992) 27-35.

[3] T. Kikuchi, A. Watanabe, and K. Uchida, *Mater. Res. Bull.* 12 (1977) 299-304.

[4] T. Kikuchi, *J. Less-Common Met.* 48 (1976) 319-323.

[5] J Tellier, *Ph. D. Thesis, University Of Limoges,* (2006).

[6] Y. Noguchi, M. Miyayama, and T. Kudo, *Appl. Phys. Lett.* 77 (2000) 3639-3641.

Chapter II

Literature Review

Literature Review

2.1 Introduction

In this chapter, a comprehensive literature review on Bismuth layer structured ferroelectrics (BLSFs), more precisely; in the SrO-Bi_2O_3-TiO_2 based BLSFs system has been made with respect to synthesis methods, dielectric and ferroelectric properties. The effect of various ionic substitutions on the structure, dielectric, ferroelectric properties of different BLSF compounds and their intergrowth has been reviewed. A review has been made of the intergrowth $Bi_4Ti_3O_{12}$-$SrBi_4Ti_4O_{15}$ (BIT-SBTi4) compound to the scope of further research conducted on the system.

2.2 Synthesis of BLSF Compounds

SrO-Bi_2O_3-TiO_2 based BLSFs system, namely $Bi_4Ti_3O_{12}$ (BIT), $SrBi_4Ti_4O_{15}$ (SBTi4), $Sr_2Bi_4Ti_5O_{18}$ (SBTi5) and their intergrowth compounds have been synthesized by different methods such as conventional solid-state reaction route, mechanochemical activation route, co-precipitation, sol gel, molten salt and hydrothermal methods, self-propagating high temperature synthesis, etc. However, properties of the final ceramics are greatly dependent on the characteristics of the powder, such as particle size, morphology, purity and chemical composition. Depending on the synthesis method and raw materials used, the nature of powder, as well as the microstructure of the final material, can be completely different.

2.2.1 Synthesis of BLSF Compounds by Solid Oxide Route

The BLSF compounds have been synthesized conventionally through solid oxide reaction. M. Alguero *et al.* [1] prepared BIT by the solid oxide route, taking stoichiometric mixture of Bi_2O_3 and TiO_2. They got the pure phase after calcination at 800^oC/20h and 900^oC/10h. T. Kikuchi synthesized the BIT-SBTi4 intergrowth compound by the solid oxide route by mixing raw materials; $SrCO_3$, Bi_2O_3 and TiO_2 and calcining twice at 1100^oC for 24 h in an electric furnace. Also, Yuji Noguchi *et al.* [2] synthesized BIT-SBTi4 by solid oxide route. To get a dense sample and to compensate for Bi vaporization during the sintering process, 3 atom % excess of Bi_2O_3 for BIT and 2 atom % for SBTi4, was added to the starting batch composition. The final sintering of the pellets was performed at 1200 °C for 1 h. The density of the samples obtained was over 90% of theoretical density.

The conventional solid-state route involves the mixing of oxides and/or carbonates raw materials and then repeated calcinations with intermediate grinding. The high calcination temperature, stoichiometry losses, uncontrolled particle size and high sintering temperature with long soaking periods required in the solid-state route are some of the disadvantages of the method. To avoid these problems, mechanochemical activation has been tried. Mechanochemically assisted preparation is a technique in which mechanical energy is supplied to the starting products by means of vigorous ball milling.

BIT, SBTi4 and SBTi5 compounds were synthesized by using mechanochemical activation method [3] where Bi_2O_3, TiO_2 and $SrCO_3$/SrO were mechanochemically activated in a vibrating milling/attrition milling with stainless steel media/ zirconia media for some hours to some days of milling. Yu Zhao *et al.* [4] synthesized $Bi_4Ti_3O_{12}$-$CaBi_4Ti_4O_{15}$ **(**BIT-CBTi4) using Bi_2O_3, TiO_2, $CaCO_3$ as initial powders. The mixed powders were milled and treated in the temperature range 550°C to 1000°C at 100°C intervals. The intergrowth phase BIT-CBTi4 formed above a calcination temperature of 900°C.

However, this method has several disadvantages like; inhomogeneity, non-uniformity of particle size and shape, high impurity content, lack of reproducibility and the necessity of repeated processing etc. Furthermore, the conventional method of synthesis by, solid-state reaction at high temperatures is not suitable for ferroelectric applications since the high-temperature synthesis can lead to the formation of an unwanted non-ferroelectric bismuth-deficient pyrochlore phase [5]. Ultra-fine powder with high purity is needed in order to fabricate well-sinterable and phase-pure ferro-electric ceramics. Compared to solid-state reaction method, the chemical route of synthesis has several advantages like better control of composition and homogeneity, low processing temperature, etc. So the chemical method is preferable for the synthesis of BLSF ceramics.

2.2.2 Synthesis of BLSF Compounds by Chemical method

There are different techniques for the chemical solution synthesis like co-precipitation, hydrothermal, sol-gel, molten salt, citrate combustion method, etc. used for the synthesis of BLSF. For example; M. Villegas *et al.* [6] synthesized BIT by a co-precipitation method using titanium tetra butoxide ($Ti(OC_4H_9)_4$) and bismuth nitrate ($Bi(NO_3)_3.5H_2O$) raw materials.

Jefferey A Horn *et al.* [7] also synthesized BIT by the same method where Bi_2O_3 and TiO(OH)Cl were taken as raw materials for bismuth and titanium ions respectively. These raw materials were dissolved in HNO_3 solution at a pH less than 3 to produce a clear solution. The solution was slowly added to concentrated NH_4OH solution at pH greater 10 to produce a gel-like precipitate. The precipitate was washed using dilute NH_4OH solution. Also, Szu Hwee Ng *et al.* [8] synthesized the same ceramics using $TiCl_4$ and $Bi(NO_3)_3.5H_2O$ raw materials where NH_4OH solution was used to precipitate the BIT precursor powder.

BLSFs can be synthesized under hydrothermal conditions where all the raw materials can be dissolved in water under high temperature and pressure [9-13]. In these methods, titanium tetra butoxide ($Ti(OC_4H_9)_4$), titanium chloride ($TiCl_4$) or anatase titania (TiO_2) powders were used; bismuth nitrate ($Bi(NO_3)_3.5H_2O$) and bismuth hydroxide ($Bi(OH)_3$) were used as bismuth salts; potassium hydroxide (KOH) and sodium hydroxide NaOH were used as mineralizers. The hydrothermal process was carried out in the teflon-lined stainless steel autoclave with a filling capacity of nearly 80%. The Bi:Ti metal ratio was maintained at 4:3. The digestion temperature was in between 140^{o}C to 250^{o}C with time periods varying from 5 hr to 3 days at a preferred pH of 7. The powders synthesized by this method were having spherical plate like morphology with the low agglomeration and narrow particle size distribution.

Sridhara Komarneni *et al.* [14] prepared BIT using a sol gel method. They prepared it by taking $Bi(C_2H_3O_2)_3$ and $Ti(OC_3H_7)_4$ as the starting precursors where the bismuth acetate was dissolved in 2:1 2-methoxyethanol and acetic acid mixture and titanium isopropoxide was dissolved in 2-methoxyethanol. Bi and Ti solutions were mixed together and then refluxed in an argon atmosphere; subsequently extra water was distilled off and finally hydrolyzed to get the gel. Calcined gel powders yielded a crystalline powder of BIT at 700^{o}C for 2 h with a fine and small particle having surface area of 0.7 m^2/g. Xianfeng Du *et al.* [15] prepared the same BIT by taking the raw materials; tetra-n-butyl titanate and bismuth nitrate, where they were simultaneously dissolved in lactic acid. The pH of the sol was mentained at 1.4. Fine and nano plate like powders were obtained by calcining the precursor at 500^{o}C. SBTi4 was synthesized by sol-gel method by Dan Xie *et al.* [16] using the chemical reagents; strontium acetate, bismuth nitrate, and the titanium butoxide. Both strontium acetate, bismuth nitrate were dissolved in acetic acid separately and the titanium butoxide in ethanol. The transparent and stable mixtures solution was refluxed and dried on a hot plate with constant stirring. The crystallization temperature of the powder was about 700°C and the particle size was about 100 nm [16].

BIT and SBTi4 can also be synthesized by molten salt synthesis (MSS) techniques [17-18]. For molten salt synthesis, KCl and NaCl are usually taken as salts and conventional electric furnace is used for the processing. SBTi4 was synthesized by taking the stoichiometric mixtures of Bi_2O_3, TiO_2, and $SrCO_3$. The reaction temperature was varied from 600°C to 800°C and soaking time 10 to 30 min. After heating, the solidified mass was ground in an agate mortar and washed using 80°C distilled water until the Cl^- ions were not detected in the $AgNO_3$ solution. It produced more distinct plate like grains and the material was proposed for the high temperature piezoelectric transducer application.

R Q. Chu *et al.* [19] synthesized SBTi4 through the auto-combustion of citrate-nitrate gel. $Sr(NO_3)_2$, $Bi(NO_3)_3$ $5H_2O$, $(C_4H_9O)_4Ti$ and citric acid were used as starting materials. The $(C_4H_9O)_4Ti$ and nitrates were weighted according to the nominal composition of SBTi4; then nitrates were dissolved in deionized water and the $(C_4H_9O)_4Ti$ in ethanol. Citric acid (fuel) was added for complete reaction with nitrates. pH of the solution was maintained such that it wasn't precipitated. The sol was dried at nearly 110°C with stirring on the hot plate. The powder produced by this method has greater compositional uniformity finer particle size. SBTi4 ceramic, was sintered at 1060°C for 1hr, exhibited a relative density of more than 90%. For the preparation of BIT, S R Dhage *et al.* [20] have used $TiCl_4$, Bi_2O_3. The molar ratio used for Bi:Ti:citric acid was 4:3:7. The average particle size of the powder prepared by this method was 20nm.

However, raw materials used for chemical synthesis routes are very costly compared to the solid oxide route raw materials. For example, $Ti(OC_4O_9)_4$ and $TiCl_4$ raw materials are used as a precursor for TiO_2, which are very costly as compared to TiO_2 used in solid oxide route. So a combined method consisting of solid oxide and chemical route will be more effective for a commercial process.

2.3 Intergrowth BLSF

T. Kikuchi *et al.* [21, 22] discovered the mixed layer compound BLSFs including $Bi_7Ti_4NbO_{21}$, $Bi_7Ti_4TaO_{21}$, $SrBi_6Ti_3Nb_2O_{21}$ and $BaBi_6Ti_3Nb_2O_{21}$. The $Bi_7Ti_4NbO_{21}$ compound structure is built up by an intergrowth of a half unit cell of Bi_3TiNbO_9 and a half unit cell of the $Bi_4T_3O_{12}$ in the direction of their common *c*-axis. The $SrBi_8Ti_7O_{27}$ BLSF structure is built up by the half of the unit cell of $Bi_4Ti_3O_{12}$ and $SrBi_4Ti_4O_{15}$ structures [21]. Presently, mixed-layer BLSFs have generated renewed interest due to their improved and interesting ferroelectric properties. Bi_3TiNbO_9-$Bi_4Ti_3O_{12}$ [23], $Bi_4Ti_3O_{12}$-$BaBi_4Ti_4O_{15}$ (BIT-BBTi4) [24] and $Bi_4Ti_3O_{12}$-$SrBi_4Ti_4O_{15}$ (BIT-SBTi4) [25, 26] are some intergrowth BLSFs having improved electrical and piezoelectric properties than individual. Yuji Noguchi *et al.* [25] reported that intergrowth BIT-SBTi4 have a large remnant polarization ($2P_r$) of 30 mC/cm^2 and a high Curie temperature of 610°C. The Rietveld analysis of the powder x-ray diffraction patterns showed that there are two kinds of Bi ions in Bi_2O_2 layers. One Bi ion in the Bi_2O_2 layers was displaced relative to the other Bi ion along the polarization direction by about 2% of the parameter a, which would contribute to the large $2P_r$. The spontaneous polarization of BIT-BBTi4 single crystal was 52 $\mu C/cm^2$ and that was larger than either BIT or BBTi4 crystals [24].

2.4 Substitutions at the B-site

In spite of several advantages of BLSFs, they are still not commercially applicable as they have high leakage current due to the presence of defects like oxygen and bismuth ion vacancies. Volatilization of bismuth during high temperature sintering of BLSFs is an inherent problem which generates oxygen vacancies to compensate the charge. Many efforts have been done to solve this through donor-doping of cations like Nb^{5+}, V^{5+}, W^{6+} at the *B*-site of BLSFs [27-35]. Nb^{5+} doping in BLSFs is very effective for compensating oxygen vacancies, which reduce dielectric losses [27-29]. It has been reported that the ferroelectric properties of BIT were enhanced by Nb doping [30].

Noguchi *et al.* reported that the incorporation of vanadium and tungsten into the Ti site of BIT resulted in a very large $2P_r$ of about 40 $\mu C/cm^2$ which was due to the reduced effect of domain pinning [25]. J. Hou *et al.* [31] reported that Nb/Ta doping at *B*-site of BIT caused a remarkably suppressed grain growth, increased permittivity and piezoelectric activity.

J.D. Bobic *et al.* [32] reported an increased degree of diffuseness of the dielectric peak in $BaBi_4Ti_4O_{15}$ (BBTi4) with Nb-doping. Nb doping also influences in a way that T_c decreased as well as the dielectric permittivity at T_c decreased. Enhanced remnant polarization and excellent fatigue-endurance properties were reported in V-doped SBTi4 thin film [33].

J K Kim *et al.* [28] reported that the remnant polarization and coercive field of $Bi_{4-x/3}Ti_{3-x}Nb_xO_{12}$ (x=0.03) film annealed at 700°C were 28 $\mu C/cm^2$ and 110 kV/cm respectively.

Substitution of Nb in BIT thin films acts as a grain-growth inhibitor in bismuth titanate and gave rise to a random orientation of grains. The film showed good switching endurance under bipolar pulse at least up to 4.5×10^{10} cycles.

Wei Wang *et al.* [26] reported that the remnant polarization of tungsten-doped BIT-SBTi4 intergrowth ceramics was twice as large as that of non-doped ones. The coercive field shows a weak dependence on tungsten content. The enlarged $2P_r$ could be mainly considered due to the restraint of oxygen vacancies as well as the weakening of their mobility. The activation energy of BTW-SBTW was increased to 1.22 eV, from that of undoped value 1.09 eV. The Curie temperature decreased about 15°C with the increasing doping content to 0.12.

Wei Wang *et al.* [36] reported on the electrical properties of Nb-, V-, and W-doped BIT–$MBi_4Ti_4O_{15}$ (BIT-MBTi4) (M=Ca, Sr) compounds. W-doped and Nb-doped BIT-SBTi4 exhibited an enhancement in $2P_r$ and d_{33} respectively. Nb doping also increases $2P_r$ and d_{33} of BIT-CBTi4 though not that much as in the BIT-SBTi4 case. BIT-CBTi4 thin film shows a high $2P_r$ value of 39μC/cm^2. The enhanced properties are thought to stem from the reduced concentration and weakened mobility of the oxygen vacancies.

Holly S. Shulman *et al.* [37] studied the complex permittivity of bismuth titanate (BIT). An anomaly in the real part of the permittivity below the Curie temperature was observed and found to be frequency dependent as a consequence of the combination of two relaxation phenomena that appeared in the imaginary part of the permittivity. One of the relaxation showed the classic characteristics of an ion-jump process. Niobium doping suppressed this relaxation and eliminated the non-ferroelectric anomalies of permittivity. Niobium is taken to affect the ion-jump relaxation through a decrease in the concentration and possibly the mobility of oxygen vacancies.

2.5 Substitutions at the A-site

Oxygen ions near the Bi ions are likely to be less stable than those near the Sr ions due to the volatility of the Bi ions in SBTi4. B. H. Park *et al.* [38] tried to stabilize oxygen ion in the structure through the substitution of the Bi^{3+} cation by tri-valent lanthanoid ions, which substantially improve the fatigue endurance and ferroelectric properties. Among the lanthanoid dopants, La^{3+} is the most favorable element used in BLSFs as well as in their intergrowth compounds. Some of the Bi ions located in the pseudo perovskite layers,

containing TiO_6 octahedra, are preferentially substituted by La ions. $Bi_{3.25}La_{0.75}Ti_3O_{12}$ shows the largest remnant polarization among various La-modified BIT materials and also high fatigue endurance. For instance, Z.G. Yi *et al.* [39] reported an enhancement of remnant polarization in $Bi_7Ti_4NbO_{21}$ intergrowth ceramics upon La-substitution. Similarly, the enhancement of $2P_r$ has been reported in BIT-SBTi4 intergrowth when Bi is substituted by La^{+3} [40-43], Nd^{+3} [44] or Eu^{3+} [45]. Bi in BIT has been substituted by the lanthanoid elements such as Nd, Sm, and Pr. These elements are of carrying interest because the extent of enhancement of the spontaneous polarization in BIT and other BLSFs. For these materials, the rotation of TiO_6 octahedra in the *ab* plane, accompanied by a tilt of the octahedra around the *c* axis is largely enhanced by the lanthanoid substitution in the perovskite layer [28, 37].
C. Y. Yau *et al.* [46] reported the mechanism of polarization enhancement in La -substituted BIT thin films. Independently, controlling the processing temperature or La substitution could adjust the orientation and enhance the P_r. With increasing La substitution, c orientation decreased but P_r increased. The lattice parameters *a, b* and *c* of $Bi_{4-x}La_xTi_3O_{12}$ thin films increase monotonously with La content *x* from *x*=0-0.6, which also lowered the orthorhombic distortion. This strongly suggested that the relaxation of structural distortion and strain arise from the La substitution.

J. K. Lee *et al.* [47] reported a correlation between internal stress and ferroelectric fatigue in La-substituted BIT films. The chemical stability, as well as internal strain of the ions, plays a significant role in the fatigue behavior of BLT films. Chemical stability of oxygen ions could not fully explain the effect of La substitution on fatigue. When the La content exceeded x=0.25, there was a little change in the chemical stability of elements. At x=0.75, the decrease of the strain was saturated and the film showed fatigue-free characteristics.

Feng Qiang *et al.* [48] worked on the system $Sr_2Bi_{4-x}Ln_xTi_5O_{18}$ (Ln=La, Nd, Sm and Dy) ceramics and reported that the remnant polarization increases at first and then decreases with the doping contents. At doping content 0.01, Sm and Dy-doped SBTi5 samples exhibited the maximum $2P_r$ of 18.2 and 20.1µC/cm2 respectively. The ferroelectric properties are increased by the decrease of oxygen vacancy concentration and the relief of the structural distortion.

Jun Zhu *et al.* [49] reported that, the structure of Bi_2O_2 layers and TiO_6 octahedra in the intergrowth was found to be different from those of BIT and SBTi4. La-doping gives rise to the enlargement of remnant polarization of BIT-SBTi4. The La^{3+} ions exhibit pronounced occupancies of the A site, when the La content is lower than 0.50 and tends to occupy the

Bi_2O_2 layers when the La content is higher than 0.50. Lanthanum substitution brings about a structural phase transition in BIT-SBTi4. Variation of ferroelectric properties may be due to the combined contributions from the decreased oxygen vacancies, the relaxation of the lattice distortion, the destroying of the insulation and the space charge compensation effects of the Bi_2O_2 slabs.

Jun Zhu *et al*. [43] also reported that the remnant polarization of La=0.5 BIT-SBTi4 is measured to a maximum value of 25.6 m C/cm^2 .The Curie temperature of BLT±SBLT(x) is the average value of the two constituents. The result shows that when *x* is not larger than 1.25, the La content in BIT is higher than that in SBTi4, but when *x* is 1.50, La content in SBTi4 is higher. It coincides with the variation of lattice space $d_{(118)}$ and the relaxation characteristics of BLT±SBLT~1.50, and might be associated with the higher La content in SBTi4 constituent.

Wei Wang *et al.* [44] reported that the activation energy of conductivity increased with increasing Nd content. This can be considered as direct proof of the restraint of oxygen vacancies. Thermal variations of dielectric permittivity and loss $\tan \delta$ with Nd content were characteristics of a diffuse phase transition while the defect-related relaxation phenomenon was not found. In contrast to La modification, Nd modification does not induce the relaxor behavior even at very high doping concentration.

X. M. Chen *et al.* [41] reported that the mixed layer BIT-SBTi4 Aurivillius structure was modified by La-substitution for Bi and the dielectric properties were investigated together with the microstructure characterization. Solid solutions of $Sr(Bi_{1-x}La_x)_8Ti_7O_{27}$ formed in the present ceramics for $x \leq 0.1$ whereas at x=0.15, $(Bi,La)_4Ti_3O_{12}$ appeared as a secondary phase and for $x \geq 0.25$, $Sr(Bi,La)_4Ti_4O_{15}$ appeared as a secondary phase. $(Bi,La)_4Ti_3O_{12}$ disappeared gradually with increasing x and vanished entirely at x = 0.35. With increasing x, both the dielectric constant and dielectric loss of the present ceramics increased initially and reached their maxima with values 291 and 0.023 at 1 MHz, then decreased after x>0.25. A temperature stable high dielectric constant ceramic was formed at the composition x=0.5 with ε=122, $\tan \delta$=0.0003 at 1 MHz.

2.6 Substitutions at both the A and B-sites

C.H. Song *et al.* [50] reported that in $Bi_{4-x/3}Ti_{3-x}Nb_xO_{12}$ (BTN) and $Bi_{3.25-x/3}La_{0.75}Ti_{3-x}Nb_xO_{12}$ (BLTN) films exhibit a maximum remnant polarization at a Nb content of x=0.018. At this Nb content, the BLTN film has a P_r value 25 mC/cm^2, which is much higher than that of BIT and a coercive field E_c=120 kV similar to that of BIT. The polarization of this BLTN film is fatigue-free up to 10^9 switching cycles. High fatigue resistance is mainly due to the substitution of Bi^{3+} ions by La^{3+} ions at the *A* site and the enhanced P_r arises mostly from the replacement of Ti^{4+} ions by Nb^{5+} ions at the *B* site.

S. K. Singh *et al.* [30] reported that the substitution of Nb^{5+} for Ti^{4+} in $Bi_{3.25}La_{0.75}Ti_{3-x}Nb_xO_{12}$ was limited to $x = 0.04$ due to the large difference in the ionic radius between Nb^{5+} and Ti^{4+}cations and the pyrochlore phase $Bi_2Ti_2O_7$ appeared afterwards. The Nb-doping improved the fatigue endurance by 27%, and the remnant polarization increased.

J.S. Kim *et al.* [29] observed that with an increase in Nb content in Nb-doped $Bi_{3.25}La_{0.75}(Ti_{1-x}Nb_x)_3O_{12}$ ceramics, the T_c decreased and the dielectric peak broadens. Below T_c, the conductivity of BLT-$Nb_{0.05}$ ceramics steadily increased while that of the BLT ceramic remarkably increased at temperature above 100^{o}C. High-valence Nb doping suppresses the formation of oxygen vacancies and then decreases bismuth defects accompanied by oxygen vacancies.

H. Nagata *et al.* [51] investigated environmentally friendly lead-free piezoelectric ceramic resonators. The Nd and V co-doped BIT ceramics seems to be a superior candidate for lead-free piezoelectric application such as in ceramic resonators.

M Roy *et al.* [52] reported that the lanthanum and niobium substitution do not cause any secondary phase formation. La^{3+} ion doping reduces the grain size and the morphology changes from the plate-like form to a spherical staking like form. Substitution of Nb^{5+} for Ti^{4+} ions affected the degree of disorder and modified the dielectric properties leading to more resistive ceramic compounds. The shape and size of the grains are strongly influenced by the addition of niobium to the system. The activation energies of all the compounds were calculated by measuring their *dc* electrical conductivities. The frequency and temperature dependent dielectric behavior of all the compounds has also been studied. The substitution of La and Nb on the Bi and Ti sites respectively, decreased the T_c and improved the dielectric and ferroelectric behavior of the materials.

Watanabe *et al.* [53] reported the effect of co-substitution of La and V in BIT thin film fabricated by metal-organic chemical vapor deposition at 600°C, where they got $(Bi_{3.2}La_{0.8})_3(Ti_{2.97}V_{0.03})O_{12}$ films with P_r ~58.5 µC/cm^2 and good fatigue endurance up to 10^9 switching cycles.

2.7 Sintering Additives

One of the major problems of BLSF ceramics is the oxygen ion vacancies created during the high temperature sintering process. During sintering, bismuth ion volatilizes and oxygen ion vacancies are created to compensate this bismuth loss. These defects are responsible for the high conductivity and increased dielectric losses in BLSF ceramics. One effective way to alleviate this problem is decreasing the processing temperature i.e. sintering temperature. There are very few reports available in the literature related to low temperature sintering of BLSFs. Recently A. R. James [54] reported that the densification of SBTi4 ceramics improved under oxygen atmosphere sintering and that more than 96% of the theoretical density can be achieved after sintering at 1200°C in an oxygen atmosphere. However, 1200°C is still comparatively higher temperature. The next effective approach could be the addition of sintering additives. Different sintering additives, like B_2O_3, CuV_2O_6, ZnBO, CuO etc., have been employed to decrease the sintering temperature of many ferroelectric materials. Among these CuO is most promising sintering additive and was widely use in different ferroelectrics; including $(Bi_{0.5}Na_{0.5})TiO_3$-$BaTiO_3$-$(K_{0.5}Na_{0.5})NbO_3$ [55], $(Na_{0.5}Bi_{0.5})_{0.94}Ba_{0.06}TiO_3$ [56], $Bi_{0.98}Ca_{0.02}Zr_{0.02}Ti_{0.98}O_3$ [57]. The introduction of CuO has been found to improve the densification by lowering the sintering temperature due to formation of a liquid phase during the sintering process. The higher density thus achieved improved the ferroelectric and dielectric properties of different ceramics. There appears to be no report available regarding the effect of CuO additives on the properties of BLSF ceramics.

2.8 Summary and Scope of Work

From the above literature review, it can be concluded that the properties of BLSFs are dependent on the characteristics of the starting raw materials, processing route for powder synthesis, fabrication, densification process and its parameters, etc. There is scope to enhance the synthesis of the material through hybrid processing such as combined solid-state and chemical solution route. BLSFs have a relatively high electrical conductivity in the *ab*-plane due to Bi volatilisation during high temperature densification process which makes it difficult to pole. To improve the ferroelectric properties of BLSFs, some potentially useful approaches are; formation of intergrowth between two compounds, high valent cation doping at *B*-site (for Ti^{4+}) of perovskite like block to suppress conductivity, isovalent lanthanoid cation substitution on *A*-site Bi cation to stabilize oxygen in the lattice and uses of sintering additives to decrease the sintering temperature so that Bi volatilisation can be suppressed.

2.9 Objectives of the Work

The purpose of this work is to synthesize the different BLSFs compounds in the system SrO-Bi_2O_3-TiO_2 through combined solid-state and oxalate chemical route. The intergrowth compound of the system; BIT-$SrBi_4Ti_4O_{15}$ and the composite; $SrBi_4Ti_4O_{15}$-$Sr_2Bi_4Ti_5O_{18}$ will be synthesized and modified to enhance dielectric and ferroelectric properties through Nb^{5+} doping, La^{3+} substitution and CuO addition with the following details:

1) Preparation and characterization of $Bi_4Ti_3O_{12}$, $SrBi_4Ti_4O_{15}$, $Sr_2Bi_4Ti_5O_{18}$ through modified oxalate route.
2) Synthesis and characterization of $Bi_4Ti_3O_{12}$-$SrBi_4Ti_4O_{15}$ and $SrBi_4Ti_4O_{15}$-$Sr_2Bi_4Ti_5O_{18}$ intergrowth ceramics.
3) The third objective of the work is to improve dielectric and ferroelectric properties in BIT-SBTi4 intergrowth. To achieve this, following approaches have been investigated:

(a) Nb^{5+}doping in BIT-SBTi4 intergrowth ferroelectrics.

(b) La-substitution for Bi^{3+} in Nb modified BIT-SBTi4 intergrowth.

(c) Effect of CuO additive on the ferroelectric properties of Nb modified BIT-SBTi4 intergrowth.

2.10 References

[1] M. Alguero, P. Ferrer, E. Vila, J. E. Iglesias and A. Castro, *J. Am. Ceram. Soc.* 89 [11] (2006) 3340–3347.

[2] Y. Noguchi, M. Miyayama, T. Kudo, *Appl. Phys. Lett.* 77 (2000) 3639-3641.

[3] P. Ferrer *et al.*, *J. Euro. Ceram. Soc.* 27 (2007) 3641–3645.

[4] Y. Zhao, Y. Li, Y. Lu, Y. Wang, *Ferroelectrics* 404 (2010) 45–49.

[5] C. H. Lu, C. H. Wu, *J. Euro. Ceram. Soc.* 22 (2002) 707–714.

[6] M. Villegas, C. Moure, J. F. Fernandez, P. Duran, *J. Mat. Sci.* 31(1996) 949-955.

[7] J. A. Horn, S. C. Zhang, U. Selvaraj, G. L. Messing, S. Trolier-Mckinstry, *J. Am. Ceram. Soc.* 82[4] (1999) 921-926.

[8] S. H. Ng, J. Xue, and J. Wang, *J. Am. Ceram. Soc.* 85 [11] (2002) 2660–65.

[9] H. Xu, K. J. Bowman and E. B. Slamovich, *J. Am. Ceram. Soc.* 86 [10] (2003) 1815–17.

[10] P. Pookmanee, P. Uriwilast, S. Phanichpant, *Ceram. Intern.* 30 (2004) 1913–1915.

[11] Y. Shi, C. Cao, S. Feng, Mater. Lett. 46(2000)270–273.

[12] D. Chen, X. Jiao, *Mater. Res. Bull.* 36 (2001) 355–363.

[13] Q. Yang, Y. X. Li, Q. Yin, P. Wang, Y. B. Cheng, *J. Euro. Ceram. Soc.* 23 (2003) 161–166.

[14] S. Komarneni, I. R. Abothu and A. V. P. Rao, *J.Sol-Gel Sci. and Techn.* 15 (1999) 263–270.

[15] X. Du, Y. Xu, H. Ma, J. Wang and X. Li, *J. Am. Cerm. Soc.*, 91[7] (2008) 2079-2082.

[16] D. Xie, W. Pan, H. Shi, *Mater. Sci. and Engg.* B99 (2003) 352-355.

[17] V. K. Seth and W. A. Schulze, *IEEE Transactions on Ultrasonics, ferroelectrics and Frequency Control*, 36 (1989) 41-49.

[18] H. Hao, H. X. Liu, Y. Liu, M. H. Cao, and S. X. Ouyang, *J. Am. Cerm. Soc.*, 90[5] (2007)1659-1662.

[19] R.Q. Chu, Z.J. Xu, Z.G. Zhu, G.R. Li, Q.R. Yin, *Mater. Sci. and Eng. B* 122 (2005) 106–109.

[20] S.R. Dhage, Y.B. Khollam, S.B. Dhespande, H.S. Potdar, V. Ravi, *Mater. Res. Bull.* 39 (2004) 1993–1998.

[21] T. Kikuchi, A. Watanabe, and K. Uchida, *Mater. Res. Bull.* 12 (1977) 299-304.

[22] T. Kikuchi, *J. Less-Common Met.* 48 (1976) 319-323.

[23] K. Kawada, A. Kan, Y. Ueda, T. Moriyama, and H. Ogawa, *Ferroelectrics* 427 (2012)105-113

[24] T. Kobayashi, Y. Noguchi, and M. Miyayama, *Appl. Phys. Lett.* 86 (2005) 012907:1-3.

[25] Y. Noguchi, M. Miyayama, and T. Kudo, *Appl. Phys. Lett.* 77 (2000) 3639-3641.

[26] W. Wang, J. Zhu, X. Y. Mao, and X. B. Chen, *Mater. Res. Bull.* 42 (2007) 274-280.

[27] S. Hong, S. Trolier-mckinstry, G.L. Messing, *J. Am. Ceram. Soc.* 83(2000) 113–118.

[28] J.K. Kim, J. Kim, T.K. Song, S.S. Kim, *Thin Solid Films* 419 (2002) 225–229.

[29] J.S. Kim, C.W. Ahn, H.J. Lee, I.W. Kim, B.M. Jin, *Ceram. Intern.* 30(2004)1459–1462.

[30] S.K. Singh, H. Ishiwara, *Thin Solid Films* 497 (2006) 90–95.

[31] J. Hou, R.V. Kumar, Y. Qu, D. Krsmanovic, *Scripta Materialia* 61 (2009) 664–667.

[32] J.D. Bobić, M.M. Vijatović Petrović, J. Banys, B.D. Stojanović, *Mater. Res. Bull.* 47 (2012) 1874–1880.

[33] D. Do, S. S. Kim, J. W. Kim, *Appl.Surf. Sc.* 255 (2009) 4531-4535.

[34] H. Sun, J. Zhu, H. Fang, X.B. Chen, *J. Appl. Phys.* 100 (2006) 074102.

[35] M. Adamczyk, L. Kozielski, M. Pilch, M. Pawełczyk, A. Soszyński, *Ceram. Intern.* 39 (2013) 4589–4595.

[36] W. Wang, D. Shan, J. Sun, X. Mao, X. Chen, *J. Appl. Phys.* 103 (2008) 044102.

[37] H.S. Shulman, M. Testorf, D. Damjanovia, N. Setter, *J. Am. Ceram.Soc.* 79 (1996) 3124-3128.

[38] B H Park, B S Kang, S D Bu, T W Noh, L Lee and W Joe, *Nature (London)* 401 (1999) 682.

[39] Z.G. Yi, Y.X. Li, Y. Wang, Q.R. Yin, *Appl. Phys. Lett.* 88 (2006) 2909.

[40] J.S. Zhu, D. Su, X.M. Lu, H.X. Qin, Y.N. Wang, D.Y. Wang, H.L. W. Chan, K.H. Wong, C.L. Choy, *J. Appl. Phys.* 92 (2002) 5420-5424.

[41] X. M. Chen, R. Z. Hou, and N. P. Jiang, *J. Electroceramics* 8 (2002) 229-232.

[42] J. Zhu, R. Hui, X.Y. Mao, W.P. Lu, X. B. Chen, Z-P. Zhang, *J. Appl. Phys.* 94 (2003) 5143-5146.

[43] J. Zhu, X.B. Chen, W.P. Lu, X.Y. Mao, R. Hui, *Appl. Phys. Lett.* 83 (2003) 1818-1820.

[44] W. Wang, S.P. Gu, X.Y. Mao, X.B. Chen, *J. Appl. Phys.* 102 (2007) 024102.

[45] T. Wei, C.Z. Zhao, C.P. Li, Y.B. Lin, X. Yang, H.G. Tan, *J. Alloys Comp.* 577 (2013) 728-733.

[46] C. Y. Yau, R. Palan, K Tran, R. C. Buchanan, *Appl. Phys. Lett.* 86 (2005) 032907.

[47] J. K. Lee, C. H. Kim, H. S. Suh, K.S. Hong, *Appl. Phys. Lett.* 80 (2002) 3593-3595.

[48] Feng Qiang, Jun-Hui He, Jun Zhu, Xiao-Bing Chen, *Journal of Solid State Chemistry* 179 (2006)1768-1774.

[49] J. Zhu, X. B. Chen, J. H. He, and J. C. Shen, *J. Sol. Stat. Chem.* 178 (2005) 2832-2837.

[50] C.H. Song, W. Li, J. Ma, J. Gu, Y.Y. Yao, Y. Feng, X.M. Lu, J.S. Zhu, Y.N. Wang, W.L.H. Chan, C.L. Choy, S*olid State Communications* 129 (2004) 775-780.

[51] H. Nagata, S. Matsuzawa, T. Tokutsu, S. Inai, M. Suzuki, Y. Hiruma, T. Takenaka, *Ceramics International* 35 (2009) 163-167.

[52] M. Roy, Indu Bala, S.K. Barbar, S. Jangid, P. Dave, *Journal of Physics and Chemistry of Solids* 72 (2011)1347-1353.

[53] T Watanabe, K Saito, H Funakubo, *Journal of Crystal Growth* 235(2002) 389–393.

[54] A. R. James, *Ceramics International* 41 (2015) 5100-5106.

[55] W. Jo, J-B. Ollagnier, J-L Park, E-M Anton, O-J Kwon, C Park, H-H Seo, J-S Lee, E Erdem, R-A. Eichel, J. Rodel, *J. Euro. Ceram. Soc.* 31 (2011) 2107–2117.

[56] N. Zidi, A. Chaouchi, S. d’Astorg, M. Rguiti, C. Courtois, *J. Alloys Compd.* 590 (2014) 557–564.

[57] H. Sun, Y. Zhang, X. Liu, Y. Liu, W. Chen, *Ceramics International* 41(2015) 555–565.

Chapter III

Experimental work

Experimental

3.1 Powder Synthesis

BLSF compounds synthesized in the present investigation are shown in the Table 3.1. All these ceramics were synthesized through modified oxalate route. In this method, oxalate salts of some metal components were co-precipitated from nitrate solution in a suspension of some other solid oxide raw materials. In the conventional oxalate co-precipitation route, all the metals are co-precipitated from a solution. Since, some of the metal components will be used as solid oxide; the present synthesis is termed as a modified oxalate route. The solid-state powder synthesis route uses simple processing steps and relatively less costly raw materials. However, a high calcination temperature is required for the final phase formation in the case of the solid-state route. Also, powders synthesized by the solid-state route require high temperature for their densification. On the other hand, chemical routes have advantages like more homogeneous mixing of raw materials, easy phase formation at relatively low calcination temperature and the synthesized powders can be sintered at relatively low temperature. Usually, Ti-alkoxides or Ti-chlorides are used as the Ti-metal source in a chemical route. Since Ti-alkoxides/chlorides are relatively costlier than TiO_2, the use of the oxide powder can reduce the powder synthesis cost. Also, Ti-alkoxides/chlorides are unstable/volatile relative to the oxide raw material. Looking at these factors, TiO_2 raw material was used in the present synthesis. Sr- and Bi-oxalates were precipitated from their nitrate solution inside the TiO_2 suspension. The detailed procedure is outlined below.

Table 3.1 List of compositions synthesized through modified oxalate route.

1.	BLSF compounds in the system SrO-Bi_2O_3-TiO_2.	$Bi_4Ti_3O_{12}$, $SrBi_4Ti_4O_{15}$, $Sr_2Bi_4Ti_5O_{18}$
2.	Intergrowth of BLSF compounds in the system SrO-Bi_2O_3-TiO_2.	$Bi_4Ti_3O_{12}$-$SrBi_4Ti_4O_{15}$ (or $SrBi_8Ti_7O_{27}$) and $SrBi_4Ti_4O_{15}$-$Sr_2Bi_4Ti_5O_{18}$
3.	Nb doped $Bi_4Ti_3O_{12}$-$SrBi_4Ti_4O_{15}$ intergrowth.	$Bi_4Ti_{3-x}Nb_xO_{12}$-$SrBi_4Ti_{4-x}Nb_xO_{18}$ with x=0.04, 0.06 and 0.08
4.	La substitution in (optimized) Nb doped $SrBi_8Ti_7O_{27}$ intergrowth.	$SrLa_xBi_{8-x}Ti_{6.88}Nb_{0.12}O_{27}$ with x=0.2, 0.4, 0.6, 0.8 and 1
5.	CuO addition in (optimized) Nb doped $SrBi_8Ti_7O_{27}$ intergrowth.	CuO addition (0.2, 0.4 and 0.6 wt %) in $SrBi_8Ti_{6.88}Nb_{0.12}O_{27}$

3.1.1 Synthesis of $Bi_4Ti_3O_{12}$ (BIT)

BIT powder was synthesized using bismuth nitrate $Bi(NO_3)_3.5H_2O$ (Merck India Ltd., Assay >99%), titanium dioxide TiO_2 (Merck India Ltd., Assay >99%, particle size: d_{10} = 0.27 µm, d_{50} = 0.35 µm, d_{90} = 0.48 µm), oxalic acid $(COOH)_2.2H_2O$ (Merck India Ltd., Assay >99%) and concentrated nitric acid HNO_3 (Merck India Ltd., GR Grade) as raw materials. Excess 2 wt% $Bi(NO_3)_3.5H_2O$ was taken to avoid Bi loss at high temperature.

BIT has been synthesized through the modified oxalate route. The flow chart of the route is shown in Fig. 3.1 for the synthesis of $SrBi_4Ti_4O_{15}$. For 10gm BIT powder preparation, we have taken 16.893gm $Bi(NO_3)_3.5H_2O$, 2.046gm TiO_2 and 7.244gm oxalic acid. For BIT synthesis, the strontium nitrate solution (shown in the Fig. 3.1) was not used. Briefly, the required amount of $Bi(NO_3)_3.5H_2O$ was dissolved in minimum quantity of concentrated nitric acid. The required amount of TiO_2 was dispersed in 0.4 M oxalic acid solution. Bismuth nitrate solution was then added into the oxalic acid-TiO_2 particle suspension under vigorous stirring. Bismuth oxalate hydrate was precipitated in the suspension through heterogeneous nucleation. Finally, the pH of the suspension was set to 7 using ammonium hydroxide solution. The mixture of precipitate and TiO_2 was separated from the solution by filtration and was washed thoroughly using water, followed by drying at 50^oC for 24 h. The powder was calcined at various temperatures in the range $200\text{-}800^oC$ in air atmosphere to study the phase formation behaviour. Pure phase of the BIT was found after calcination of the precursor powder at 800^oC for 4h.

3.1.2 Synthesis of $SrBi_4Ti_4O_{15}$ (SBTi4)

Fig. 3.1 indicates the flow chart for SBTi4 synthesis. For 10gm SBTi4 powder preparation, we have taken 1.562gm $Sr(NO_3)_2$, 15.035gm $Bi(NO_3)_3.5H_2O$, 2.359gm TiO_2 and 7.471gm oxalic acid. 5% excess $Bi(NO_3)_3.5H_2O$ have taken here for avoiding Bi ion evaporation. In addition to the raw materials used for the BIT synthesis as stated above, strontium nitrate ($Sr(NO_3)_2$) (Merck India Ltd., Assay >99%) was also used for the SBTi4 synthesis. $Sr(NO_3)_2$ was dissolved in minimum quantity of water. Bismuth nitrate solution was subsequently added drop wise to strontium nitrate solution under stirring condition. Bismuth and strontium nitrate mixed solution was then added drop by drop into the oxalic acid-TiO_2 suspension under vigorous stirring. The remaining steps were the same as described for BIT synthesis in section 3.1.1. The precursor powder was calcined at different temperature in the range 600 to

1050°C for 4 h with intermediate grinding after each firing to get pure phase SBTi4 powder. SBTi4 pellets were sintered at 1150°C for 7 h.

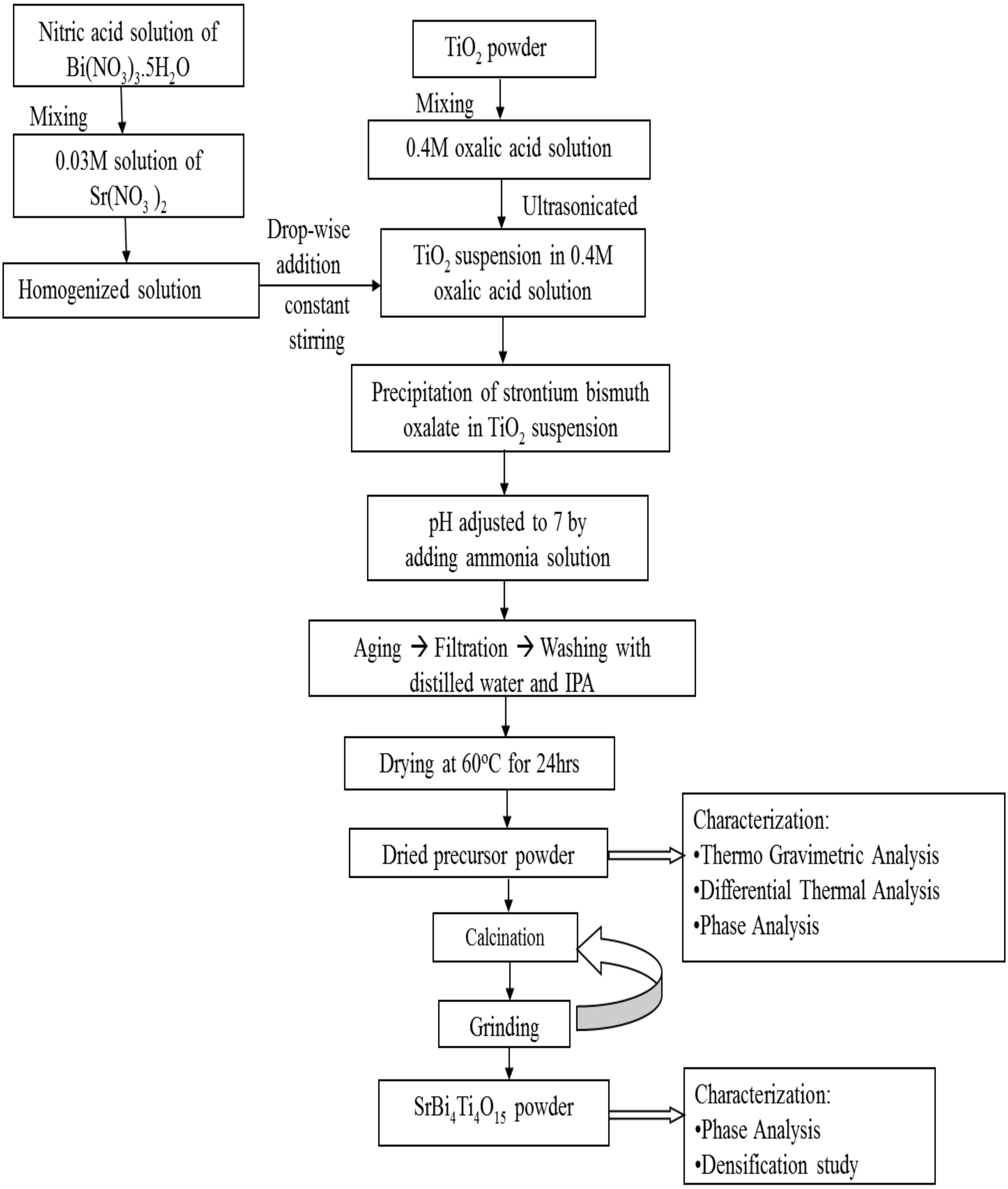

Fig. 3.1 Flow chart for $SrBi_4Ti_4O_{15}$ synthesis through modified oxalate route.

3.1.3 Synthesis of $Sr_2Bi_4Ti_5O_{18}$ (SBTi5)

SBTi5 was also synthesized following the process shown in Fig.3.1. For 10gm SBTi5 powder preparation, we have taken 2.751gm $Sr(NO_3)_2$, 13.242gm $Bi(NO_3)_3.5H_2O$, 2.597gm TiO_2 and

7.481gm oxalic acid. Here also 5wt % excess $Bi(NO_3)_3.5H_2O$ have taken here for avoiding Bi ion evaporation at high calcination temperature. The final precursor powder was calcined in the temperature range 800 to 1100^oC for 4 h with intermediate grinding. SBTi5 pellets were sintered at 1230^oC for 4 h.

3.1.4 Synthesis of $Bi_4Ti_3O_{12}$ - $SrBi_4Ti_4O_{15}$ intergrowth

The BIT-SBTi4 intergrowth, in 1:1 molar ratio was synthesized by the modified oxalate route (Fig. 3.1). The final precursor powder was calcined in the temperature range 800 to 1000^oC for 4 h with intermediate grinding after each firing. BIT-SBTi4 pellets were sintered at 1150^oC for 2 h.

3.1.5 Synthesis of $SrBi_4Ti_4O_5$ – $Sr_2Bi_4Ti_5O_{18}$ intergrowth

The SBTi4-SBTi5 composite in 1:1 molar ratio was synthesized by the modified oxalate route. The final precursor powder was calcined in the temperature range 800 to 1100^oC for 4h with intermediate grinding. SBTi4-SBTi5 composite pellets were sintered at 1150^oC for 7 h.

3.1.6 Synthesis of $Bi_4Ti_{3-x}Nb_xO_{12}$ - $SrBi_4Ti_{4-x}Nb_xO_{15}$ (x=0.04, 0.06, and 0.08)

In addition to the raw materials used for the synthesis of BIT-SBTi4 intergrowth, Nb_2O_5 (Alfa Aesar, Assay >99%) was used for this synthesis. The required amount of TiO_2 and Nb_2O_5 was dispersed in 0.4 M oxalic acid solution. Other steps were the same as shown in Fig. 3.1. The final precursor powder was calcined in the temperature range 800 to 1050^oC for 4 h and pellets were sintered at 1150^oC for 2 h.

3.1.7 Synthesis of $SrLa_xBi_{8-x}Ti_{6.88}Nb_{0.12}O_{27}$ (x=0.2, 0.4, 0.6, 0.8, and 1.0)

Lanthanum oxide La_2O_3 (Merck, India Ltd., Assay >99%) was also used for the synthesis, in addition to the other raw materials stated above. After dissolving bismuth nitrate in nitric acid, required amount of lanthanum oxide was added to this solution. The solution was stirred vigorously. The lanthanum oxide dissolved and a clear transparent solution formed. After that, the usual procedure was followed. The calcination and sintering temperatures were the same as stated in section 3.1.6 above.

3.1.8 Synthesis of CuO added (0.2, 0.4 and 0.6 wt %) $SrBi_8Ti_{6.88}Nb0._{12}O_{27}$ intergrowth

Required amounts of $Sr(NO_3)_2$ and $Cu(NO_3)_2$ were dissolved in water. Bismuth nitrate solution was then added drop wise to the mixed strontium and copper nitrate solution. Other steps were the same as those shown in Fig. 3.1. The calcination and sintering temperatures were the same as those stated in section 3.1.6 above.

3.2 Characterization of powder

3.2.1 Differential Scanning Calorimetry (DSC) and Thermo-gravimetric Analysis (TGA)

The precursor powder was characterized by DSC and TGA using NETZSCH STA (Model No 409C) instrument with the heating rate of 10^oC/min, using α-Al_2O_3 as reference material. The phase transition behavior can be understood by considering the heat absorbed and released. TGA is a simple analytical technique that measures the weight loss (or weight gain) of a material as a function of temperature. As materials are heated, they can lose weight due to drying or evolution of gases from chemical reactions taking place in the specimen. Some materials can gain weight by reacting with the atmospheric gases in the testing environment.

3.2.2 Phase analysis

Phase formation behavior was studied by powder X-ray diffraction (XRD) using a RIGAKU JAPAN/ULTIMA-IV instrument. The source radiation used is Cu K_α with a wavelength of 1.541874 Å and equipped with Ni β-filter. Bragg-Brentano focusing geometry was used for the measurement of the intensity of diffraction [1]. The current and voltage used during the experiment are of 40 kV and 40 mA, with a step size of 0.05^o. The identification of different phases was carried out by Hanawalt method using X-pert Highscore software.

3.2.3 Densification Study

Densification behaviour of the powder was investigated using a NETZSCH dilatometer model DIL 402 C, Germany, where the linear dimensional change i.e. shrinkage or expansion of the specimen is transmitted through the push rod (pressed against the sample inside the furnace) to the measuring head. For dilatometer experiment samples were made in the form of rods having diameter 5 mm and length 15 mm. The heating rate was maintained at 10^oC/min. The measurements were carried out from room temperature to 1200^oC in air.

3.3 Fabrication of Pellet and Sintering

The pure phase powders were mixed with 3 weight% polyvinyl alcohol (PVA) as granulating additive. The granulated powder was pressed into circular disks using stearic acid as a lubricant. Pellets were compacted at a pressure of 220 Mpa with a holding time of two minutes and were sintered at different temperatures depending on the composition. During sintering, the specimens were placed in a sealed alumina crucible to minimize bismuth volatilization. Sintering temperature/time for different compositions is shown in Table 3.2.

Table 3.2 Sintering temperature/time for different compositions.

	Composition	**Sintering temperatures**
1.	$Bi_4Ti_3O_{12}$, $SrBi_4Ti_4O_{15}$, $Sr_2Bi_4Ti_5O_{18}$	850°C/4h, 1150°C/4h and 1230°C/4h, respectively.
2.	$Bi_4Ti_3O_{12}$-$SrBi_4Ti_4O_{15}$, $SrBi_4Ti_4O_{15}$-$Sr_2Bi_4Ti_5O_{18}$	1150°C/2h and 1200°C/2h, respectively.
3.	$Bi_4Ti_{3-x}Nb_xO_{12}$ - $SrBi_4Ti_{4-x}Nb_xO_{15}$ with x=0.04, 0.06 and 0.08	1150°C/2h
4.	$SrLa_xBi_{8-x}Ti_{6.88}Nb_{0.12}O_{27}$ with x=0.2, 0.4, 0.6, 0.8 and 1	1150°C/2h
5.	CuO_2 addition (0.02, 0.04 and 0.06 wt %) in $SrBi_8Ti_{6.88}Nb_{0.12}O_{27}$	1150°C/2h

3.3.1 Density measurements

The density of the sintered samples was measured by the Archimedes principle. The sintered samples were immersed in water and kept under a vacuum until the water filled the open pores completely. The suspended weight of the pellet was measured by hanging the pellet on the hanger inside the water. The soaked weight was then measured by removing excess water from the pellet with a wet paper. The bulk density and apparent porosity was calculated from the formula:

$$\mathrm{D_{bulk}} = \frac{W_{dry}}{W_{soak} - W_{sus}} \tag{3.1}$$

where, W_{dry} = Dry weight of the sample, W_{soak} = Soaked weight of the sample,
W_{sus} = Suspended weight of the sample.

Theoretical density was calculated from the unit cell volume determined by X-ray method using the formula:

$$\rho = \frac{\Sigma A_w}{NV} \tag{3.2}$$

where, ρ is the theoretical (X-Ray) density (gm/cc), ΣA_w is the sum of the atomic weights of all the atoms in the unit cell, N is the Avogadro's number and V is the volume of unit cell (cc).

3.3.2 Microstructural study

The surface morphology of the sintered specimen was studied using field emission scanning electron microscope (FE-SEM) NANO-NOVA, FEI. In FE-SEM, a field emission cathode in the electron gun under vacuum emits an electron beam which passes through a series of electromagnetic lenses. The sample is then bombarded with the fine beam of electrons having acceleration potentials ranging from 0.5 to 30 kV. Images were taken in low vacuum secondary electron beam. The as-sintered samples were used for studying microstructure. The grain size was determined using **'ImageJ'** software. Individual length, breadth and thickness of the plate like grain were determined and their mean values calculated.

3.3.3 Lattice parameter determination and Quantitative phase estimation through Rietveld refinement

Lattice parameters can be determined more accurately through Rietveld refinement of full XRD pattern. In the Rietveld method [2,3], the least square refinements are carried out until the best fit is obtained between the observed pattern and the calculated pattern based on the simultaneous refinement of the models for the crystal structures, diffraction optics effects, instrumental factors and other specimen characteristics like lattice parameters. As it is known that the lab XRD is generally inadequate for these types of materials analysis, the atomic coordinates and displacement parameters were not refined and fixed at literature values during the refinement.

The Rietveld refinement was carried out using MAUDWEB (version 2.031) software [4]. This software is especially designed to refine both the structural and microstructural parameters simultaneously. The peak shape was fitted using pseudo-Voigt function. The background factor of each pattern was fitted to a polynomial of degree 5.

The residual quantity S_y was minimized in the least-squares refinement:

$$S_y = \sum_i w_i \left(y_i - y_{ci}\right)^2 \tag{3.3}$$

Where,

$$w_i = \frac{1}{y_i}$$

y_i = observed (gross) intensity at the *i*th step,

y_{ci} = calculated intensity at the *i*th step.

It is possible that multiple Bragg reflections contribute to the intensity y_i, observed at an arbitrarily chosen point *I* in the pattern. The calculated intensity $\mathrm{y_{ci}}$ is determined from the $|F_k|^2$ values calculated from the structural model by summing of the calculated contributions from the neighboring (i.e. within a specified range) Bragg reflections plus the background:

$$\mathrm{y_{ci}} = s\sum_k L_k |F_k|^2 \varphi(2\theta_i - 2\theta_k) P_k A + y_{bi} \tag{3.4}$$

Where, s is the scale factor, *k* represents the Miller indices, h, k, l for the Bragg reflection, L_k contains the Lorentz polarization and multiplicity factors, ϕ is the reflection profile function, P_k is the preferred orientation function, A is the absorption factor, F_k is the structural factor for the k_{th} Bragg reflection, and y_{bi} is the background intensity at the i_{th} step.

The R-factor are weighted profile (R_{wp}), Bragg factor (R_B) and expected R factor (R_{exp}):

$$R_{wp} = \left\{ \frac{\sum w_i (y_i(obs) - y_i(calc))^2}{\sum w_i (y_i(obs))^2} \right\}^{1/2} \tag{3.5}$$

$$R_B = \frac{\sum I_K(obs) - I_K(calc)}{\sum I_K(obs)} \tag{3.6}$$

$$R_{exp} = \left[\frac{(N-P)}{\sum W_i y_{obs}^2} \right]^{\frac{1}{2}} \tag{3.7}$$

Where, *obs* and *calc* are observed and calculated value. I_K is the intensity assigned to the K_{th} Bragg reflection at the end of the refined cycle. *N* is the number of experimental observations and *P* is the number of fitting parameters. Among all these *R*-factors, R_{wp} is the most meaningful as its numerator is the residual being minimized.

Another useful numerical criterion is the “goodness of fit” S, which is expressed as

$$\mathrm{S} = \left(\frac{R_{wp}}{R_{exp}} \right) \tag{3.8}$$

Refinement continues till the convergence is reached with the minimum value of S that can be achieved.

3.4 Electrical Property Measurements

3.4.1 Dielectric Measurements

For electrical measurements, both surfaces of a pellet were painted with silver conductive paste (Alfa Aesar) and then cured at 700^{o}C for 15min. Thus, a pellet with two parallel electrodes acts as a single layer capacitor. The capacitance (*C*), dielectric constant (ε') and dielectric loss (*tan* δ) of this disc capacitor was measured using a Solatron 1260 Impedance/Gain-Phase Analyzer, in the temperature range 25 to 800^{o}C, frequency range 1Hz – 1MHz.

The capacitance (*C*) of a capacitor is given by [5]

$$C = \frac{\varepsilon\,\varepsilon_o A}{d} \tag{3.9}$$

Where, ε_o is the permittivity of free space (8.854 x 10^{-12} F/m), *A* is the area of the electrodes and *d* is the thickness of the dielectrics. ε is the relative permittivity which is dimensionless; ε can be explained by:

$$\varepsilon = \varepsilon' + i\varepsilon'' \tag{3.10}$$

ε' and ε'' are the real and imaginary part of relative permittivity.

The dielectric loss (*tan* δ) is the measure of energy dissipated in a dielectric on application of an electric field, which is expressed as:

$$\tan\delta = \frac{\varepsilon''}{\varepsilon'} \tag{3.11}$$

3.4.2 Impedance Spectroscopy

Impedance spectroscopy is a powerful tool for investigation of complex electrical properties. The technique is advantageous in separating and determining the values of grain and grain boundary effects and is also helpful in correlation with the properties such as composition, microstructure, defects, dielectric properties, etc.

$$Z = Z' - j\,Z'' \tag{3.12}$$

In impedance spectroscopy analysis, the impedance $|Z|$ and the phase difference (θ) between voltage and current are measured as a function of frequency. Analysis of the data and separation of the various phenomena are carried out by plotting the real part of impedance $Z' = |Z| \sin\theta$ versus $Z'' = |Z| \cos\theta$, called Cole-Cole plot. This impedance plot is used to examine the equivalent circuit representing it. The impedance plot of an ideal capacitor is represented by a straight line coinciding with the imaginary axis while that of an ideal resistor is a point on the real axis. An equivalent circuit model consisting of the parallel resistor (*R*) and capacitor (*C*) is shown in Fig.3.3. The following relation is used to represent a parallel *RC* equivalent circuit

Simplifying the above relation,

$$\left(Z' - \frac{R}{2}\right)^2 + Z''^2 = \left(\frac{R}{2}\right)^2$$

(3.13)

The resulting Equation 3.19 represents the equation of a circle with a radius of *R*/2 and Centre at (*R*/2, 0). Thus, it can be said that the plot of -Z″ versus Z′ will be semicircular in shape with a radius of *R*/2. The time constant (τ) of the parallel *RC* is expressed as:

$$\tau = RC = \frac{1}{\omega} = \frac{1}{2\pi f} \qquad (3.14)$$

where, *f* is the characteristic frequency lying at the peak of the semicircle. A typical Cole-Cole plot is shown in Fig.3.2. The high frequency arc corresponds to the bulk property or grain behaviour of the polycrystalline material while the low frequency arcs represent the grain boundary effect and electrode effect. A Solatron 1260 was used for impedance measurements.

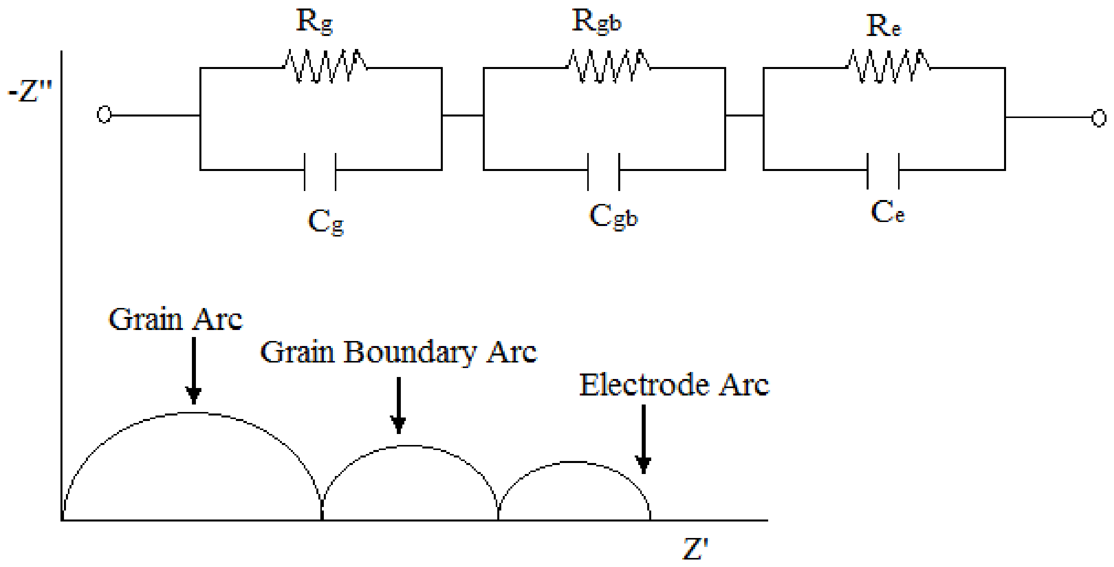

Fig. 3.2 Cole-Cole plot showing grain, grain boundary and electrode effects and its equivalent circuit model consisting of parallel resistor and capacitor.

3.4.3 Polarization versus Electric field study

The hysteresis loop measurement was carried out by a Radiant *P*-*E* loop tracer instrument, applying 10 Hz frequency. The pellets were electroded with silver paint on a minimum surface area on one side and the whole surface of the other and cured at 650°C for 30min. All the measurements were carried out at room temperature.

The instrument is based on the Sawyer-Tower method [6, 7], as shown in Fig. 3.3. *C* is the sample capacitor and C_o is the standard reference capacitor as shown in the figure. An *ac* signal voltage *V* is applied across the capacitor *C*. However, the voltage applied should be adequate to bring the saturation in polarization. So that V_o should be proportional to the polarization charge $V_o = AP/C_o$, where *A* is the area of the sample. C_o is usually much larger than the sample capacitor and is connected in series with it, such that it can store the polarization charges generated during the polarization switching without affecting the process.

Ferroelectric materials possess spontaneous polarization in the absence of an electric field. The spontaneous polarization can be reversed on the application of an external electric field. Hysteresis is one of the prominent features of ferroelectricity exhibiting a non-linear relationship between the polarization *P* and applied field *E*. Fig. 3.4 shows a typical hysteresis plot.

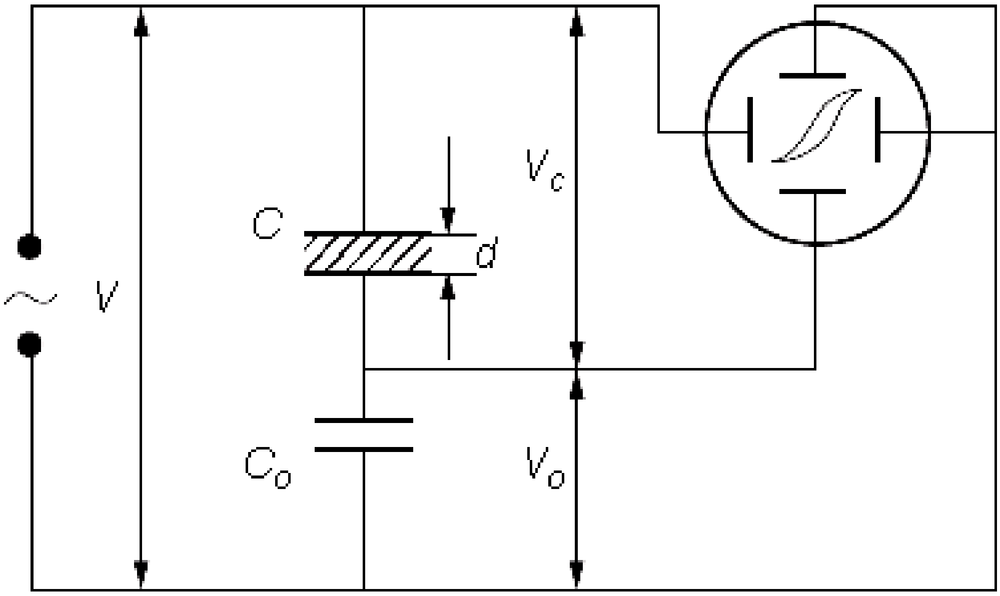

Fig. 3.3 Sawyer-Tower method for polarization versus electric field measurement [6].

In portion *OA* of the graph, field induced polarization occurs on the application of a low field. On increasing the field strength, polarization increases non-linearly with the field as the domains start to align in the direction of applied field (portion *AB*). On further increase in the field strength, the polarization attains a saturation value (*BC*), where maximum domains are aligned in the field direction. On gradually decreasing the field strength, the polarization decreases following the path *CBD*. The extrapolation of the *CB* region to zero-field axis at *E*, gives the region *OE*, *i.e.*, spontaneous polarization P_s and the region *OD* represents the remnant polarization P_r. The electric field required to bring the polarization to zero is called the coercive field (E_c), shown in region *OR*. E_c depends on the frequency, temperature and waveform applied.

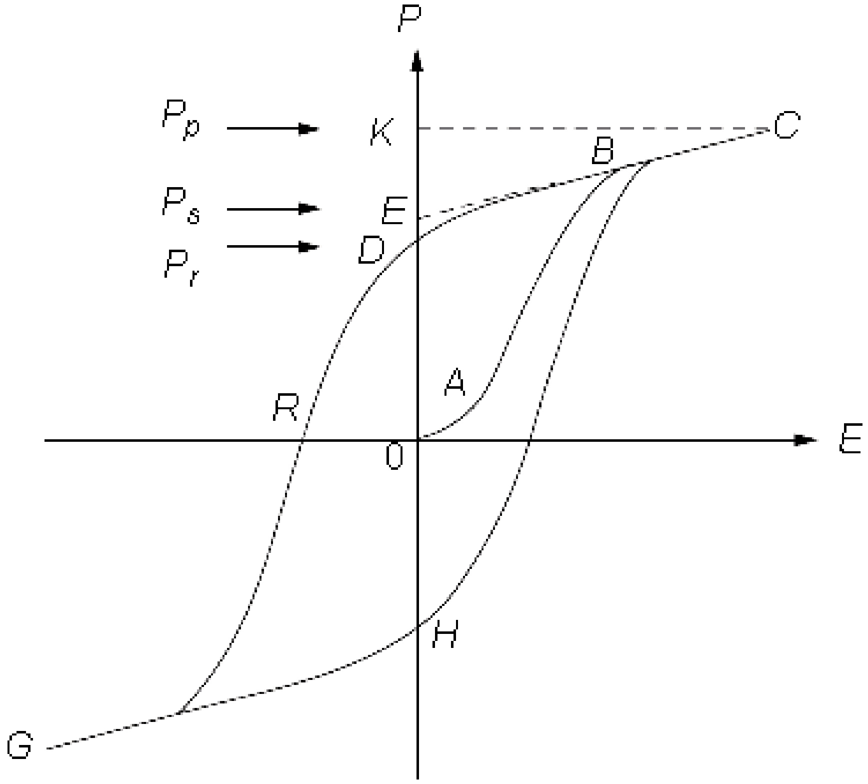

Fig. 3.4 Schematic figure of a typical *P*-*E* hysteresis loop [7].

3.5 References

1. B. D. Cullity, *Elements of. X-Ray diffraction* (1978).
2. H. M. Rietveld, *J. Appl. Cryst.* **2** (1969) 65,
3. R.A. Young, Rietveld Method, *International Union of Crystallography, Oxford University Press*, (1996).
4. http://www.ing.unitn.it/~maud/] [Maud software 2.23 version]
5. B. Jaffe, W. R. Cook, H. Jaffe, *Piezoelectric Ceramics, London and New York* (1971).
6. Y. Xu, Ferroelectric Materials and Their Applications, *North-Holland Elsevier Sci. Publ., Amsterdam* (1991).
7. A. J. Mouson, J. M. Herbert. *Electroceramics- Materials properties, applications. Chapman and Hall*, (1990).

Chapter IV

Results and Discussions

4.1 Synthesis and Characterization of $Bi_4Ti_3O_{12}$, $SrBi_4Ti_4O_{15}$ and $Sr_2Bi_4Ti_5O_{18}$ Ceramics

4.1.1 Introduction

Conventionally, $Bi_4Ti_3O_{12}$ (BIT), $SrBi_4Ti_4O_{15}$ (SBTi4) and $Sr_2Bi_4Ti_5O_{18}$ (SBTi5) are synthesized by solid-state reaction route. The solid-state route requires repeated grinding of raw materials, high calcination temperature for phase formation and high sintering temperature/time to achieve high density. Compared to solid-state reaction method, the chemical route of synthesis has several advantages like better control of composition and homogeneity, low processing temperature, etc. However, the major disadvantage of chemical route is the high cost of raw materials required for the process. Usually, titanium alkoxide raw material is used in chemical route, which is very costly compared to TiO_2 used in the solid-state route. In the present investigation, a modified chemical route has been used to obtain advantages of both the chemical and solid-state route. Bismuth and strontium nitrate solutions are used to get the advantage of solution processing route and TiO_2 powder is used to reduce the cost of the material. Bi-, Sr-oxalates were precipitated from their nitrate solution inside the TiO_2 powder suspension. This route will be termed as the modified oxalate route. BIT, SBTi4 and SBTi5 compounds have been synthesized through this route and their formation mechanisms have been investigated. These information will be helpful for the successful synthesis of BIT-SBTi4 intergrowth and SBTi4-SBTi5 composite ceramics. In addition, the dielectric and ferroelectric properties of three compounds are investigated to correlate their properties with those of intergrowth ceramics.

4.1.2 Results and Discussions

(A) Synthesis and characterization of $Bi_4Ti_3O_{12}$

4.1.2.1 Thermal decomposition and Phase formation behavior

Fig. 4.1.1 shows the thermal decomposition behavior of the precursor powder for BIT synthesized through modified oxalate route. The figure shows weight losses in three different stages. First weight loss (about 1 wt%) up to 150°C is due to the dehydration of adsorbed water and is endothermic in nature as shown in the DSC curve. Second weight loss (about 8 wt%) up to about 300°C is due to the decomposition of oxalates salts which corresponds to the exothermic peak at 294°C. The third stage weight loss of about 4.5% in the range 300°C to 400°C is associated with one exothermic DSC peak at 340°C and one endothermic decomposition peak at 376°C respectively. The exothermic peak may be due to the decomposition of nitrates and the endothermic peak is due to the decomposition of carbonates.

The broad exothermic peak in the range 400 to 800°C corresponds to the crystallization of different phases. The final exothermic peak at 830°C may be due to the crystallization of $Bi_4Ti_3O_{12}$.

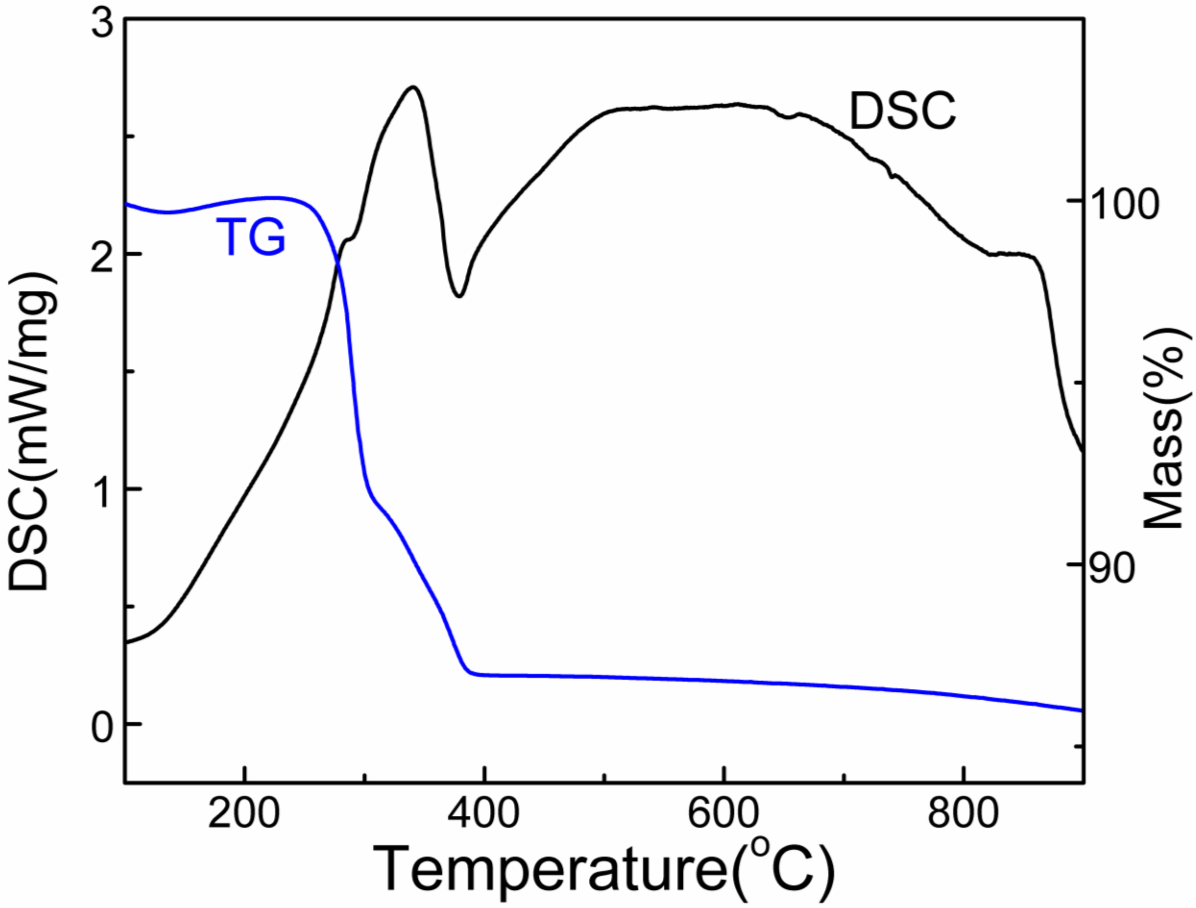

Fig. 4.1.1 DSC/TG plot of the precursor powder for BIT ceramics.

To investigate the phase formation behavior, the precursor powder is calcined at different temperatures in the range 200°C to 800°C. Fig. 4.1.2 shows the room temperature XRD pattern of BIT precursor powder after calcination at different temperatures. The XRD pattern (Fig. 4.1.2 (a)) of 200°C calcined powder shows the presence of anatase (TiO_2; JCPDS No: 71-1167), bismuth oxalate hydrate ($Bi_2(C_2O_4)_3 .7H_2O$; JCPDS No:-38-0548), bismuth hydroxide ($Bi(OH)_3$; JCPDS No: 01-0898) and bismuth oxide nitrate hydroxide hydrate ($Bi_6(NO_3)_4(OH)_2O_6 .2H_2O$; JCPDS No:28-0654). Fig. 4.1.2 (b) (350°C calcined powder) shows peaks due to Bi_2O_3 and $Bi_2O_2CO_3$ suggesting that most of the bismuth-compound decomposed through decarburization and dehydration reactions. Bi_2O_3 is formed due to the decomposition of bismuth hydroxide and bismuth oxide nitrate hydroxide hydrate. Bismuth carbonate formed from bismuth oxalate hydrate. The bismuth carbonate decomposition is completed by 400 ^{o}C as there is no weight loss above that temperature.

These decomposition reactions may be expressed as:

$$Bi_6(NO_3)_4(OH)_2O_6.2H_2O \xrightarrow{<400^o C} 3Bi_2O_3 + 4NO_2(\uparrow) + 3H_2O(\uparrow) + O_2(\uparrow). \quad (4.1.1)$$

$$Bi_2(C_2O_4)_3.7H_2O \xrightarrow{<400^o C} Bi_2(C_2O_4)_3 + 7H_2O. \quad (4.1.2)$$

$$2\,Bi_2(C_2O_4)_3 + 3O_2 \xrightarrow{<400^o C} 2Bi_2O_2CO_3 + 10CO_2(\uparrow). \quad (4.1.3)$$

$$Bi_2O_2CO_3 \xrightarrow{<400^o C} Bi_2O_3 + CO_2(\uparrow). \quad (4.1.4)$$

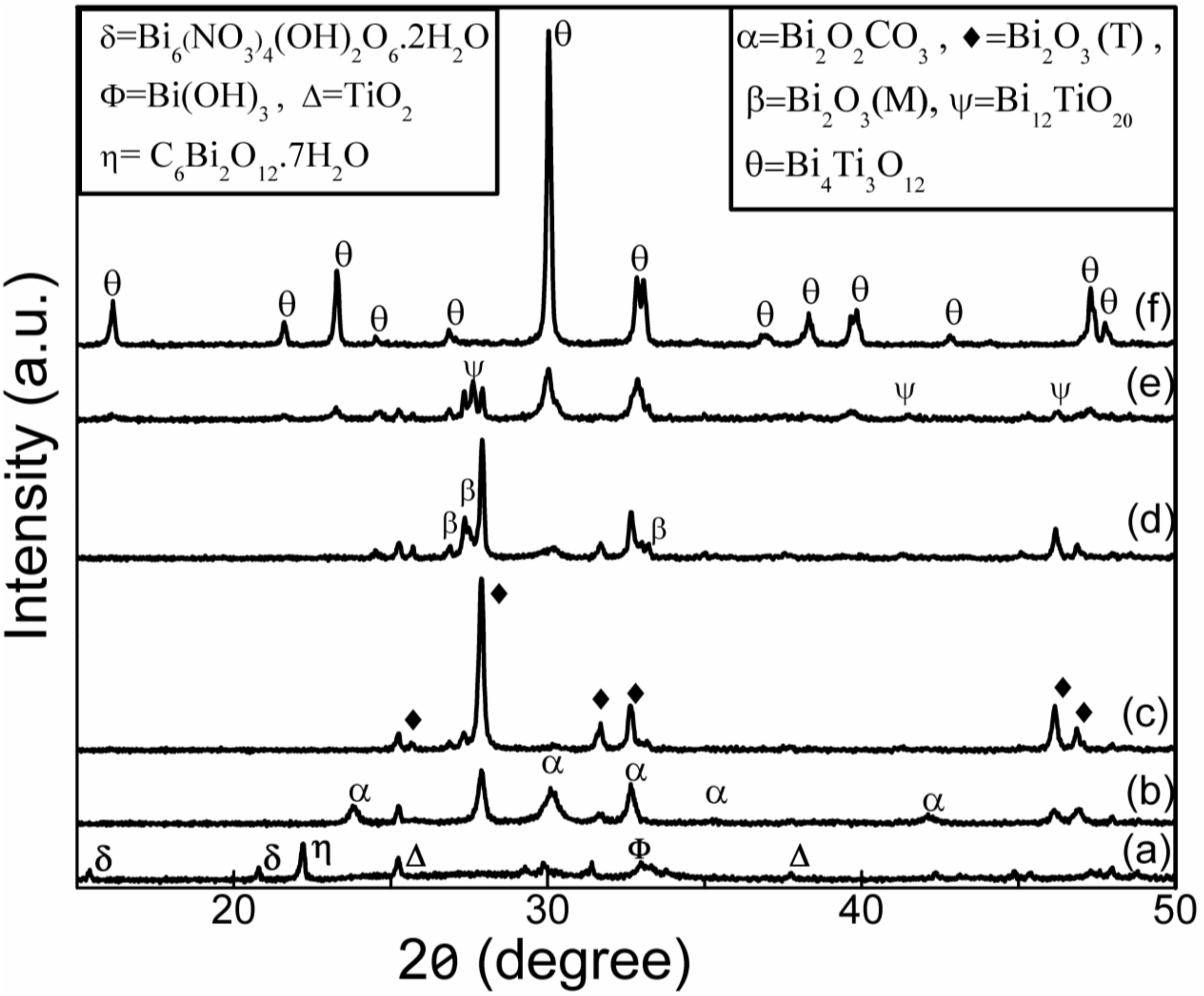

Fig. 4.1.2 Room temperature XRD pattern of BIT precursor powder calcined at (a) 200, (b) 350, (c) 500, (d) 600, (e) 700 and (f) 800°C. Major phases identified are also shown in the figure.

The pattern of the 500°C calcined powder shows anatase and bismuth oxide peaks. The pattern of the 700°C calcined powder shows the formation of intermediate phase

$Bi_{12}TiO_{20}$ along with desired phase $Bi_4Ti_3O_{12}$. Bi_2O_3 reacts with TiO_2 to form the intermediate phase $Bi_{12}TiO_{20}$ as per equation 4.1.5.

$$6Bi_2O_3 + TiO_2 \xrightarrow{700^o C} Bi_{12}TiO_{20} \text{ .} \qquad (4.1.5)$$

The formation of this phase is also reported by M. I. Morozov *et al.* [1] during the synthesis of BIT. These authors explained that $Bi_{12}TiO_{20}$ has cubic structure and identical cell parameters similar to that of γ-Bi_2O_3. So the intermediate phase $Bi_{12}TiO_{20}$ will form. The pattern of the 800°C calcined product shows peaks due to pure BIT, as a result of the conversion of intermediate $Bi_{12}TiO_{20}$ phase as per the reaction:

$$Bi_{12}TiO_{20} + 8TiO_2 \xrightarrow{800^o C} 3Bi_4Ti_3O_{12} \text{ .} \qquad (4.1.6)$$

4.1.2.2 Structural Analysis

Lattice parameters of BIT are refined by Rietveld refinements using the MAUD [2], considering orthorhombic space group *B2cb* for the structure [3, 4]. Initial cell parameters, atomic coordinates and atomic displacements parameters used in the refinement are taken from the reference [4]. The refinement consisted of the parameters set including the modeling of background scale factor, detector zero point and profile parameters, lattice parameters etc. Fig. 4.1.3 shows the Rietveld refinement plot for BIT ceramics. Final lattice parameters and R-factors after refinement are a=5.4442(2) Å, b= 5.4089(3) Å and c= 32.824(5) Å and R_w=4.03 %, R_b=3.21 % and Sigma=1.25. All these values are also summarized in the Table 4.1.1.

The lattice parameters demonstrate the structure to be orthorhombic. The orthorhombicity of the structure is determined by the equation:

$$\text{Orthorhombicity} = \frac{2(a-b)}{(a+b)} \qquad (4.1.7)$$

Orthorhombicity of the BIT structure was 0.0065.

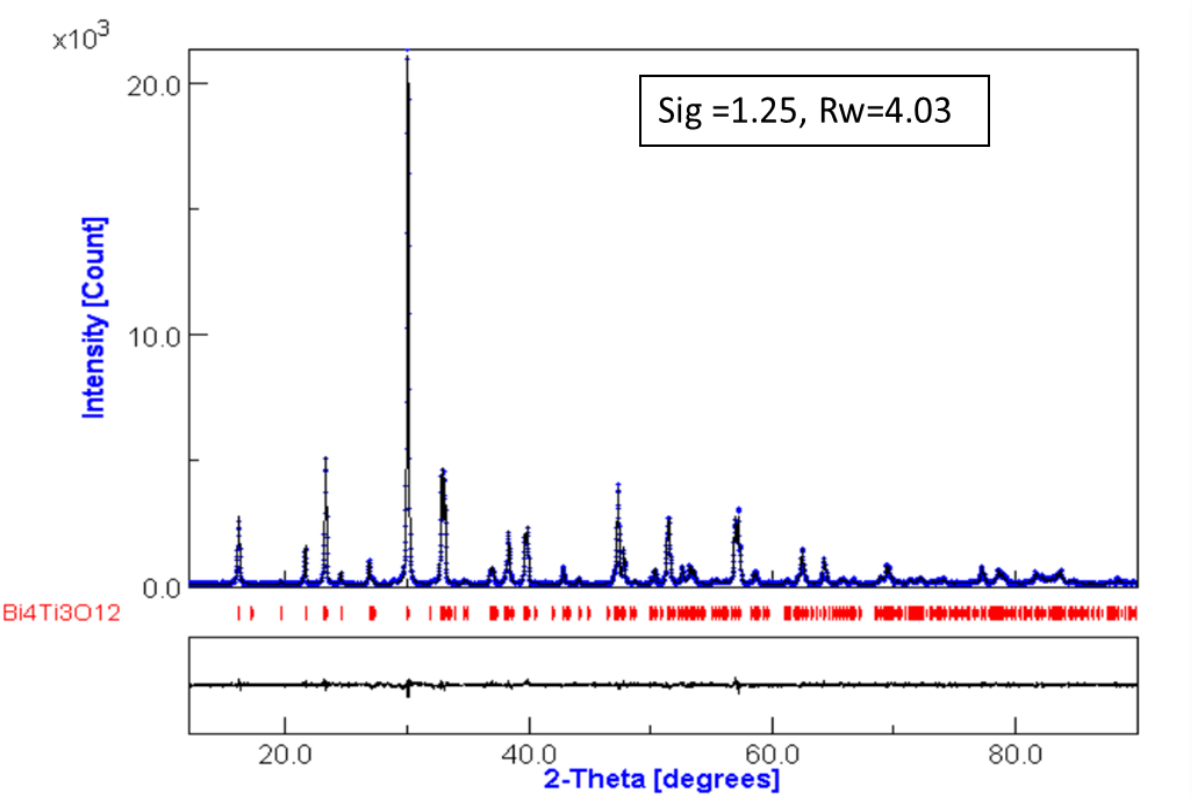

Fig. 4.1.3 Rietveld refinement plot for the sintered BIT ceramics showing observed (+), calculated (solid line) XRD profile, their differences in the bottom and position of allowed Bragg reflections (tick marks).

Table 4.1.1 Symmetry, Space group, refined lattice parameters ‘*a*’, ‘*b*’ and ‘*c*’, *R*-factors, sigma, orthorhombicity of BIT ceramics.

Parameters	**Values**
Symmetry	Orthorhombic
Space group	*B2cb*
a (Å)	5.4442(2)
b (Å)	5.4089(3)
c (Å)	32.824(5)
R_w (%)	4.03
R_b (%)	3.21
Sigma	1.25
Orthorhombicity	0.0065

4.1.2.3 Densification behavior and microstructure.

Fig. 4.1.4 shows the non-isothermal shrinkage behavior of the pure BIT ceramics. It shows that the shrinkage of the specimen starts at about 610°C and continues up to 900°C. The onset temperature of the sintering is about 765°C and the maximum shrinkage rate is at 870°C. The sintering temperature selected for BIT is at 850°C. More than 94% dense ceramics are obtained by sintering pellets at 850°C for 4h. The micrograph of the sintered pellet surface is shown in the inset of Fig. 4.1.4. The micrograph shows plate like grains with random orientation. The plate like grain formation is a typical characteristic of bismuth layered structure ferroelectrics as they have highly anisotropic crystal structure with a lower surface energy of {001} planes. The grain growth is easy in the *ab* plane with the formation of plate-like morphology. The grains have the mean diameter of 2.2 μm, thickness of about 0.4 μm with an aspect ratio of ~5.5.

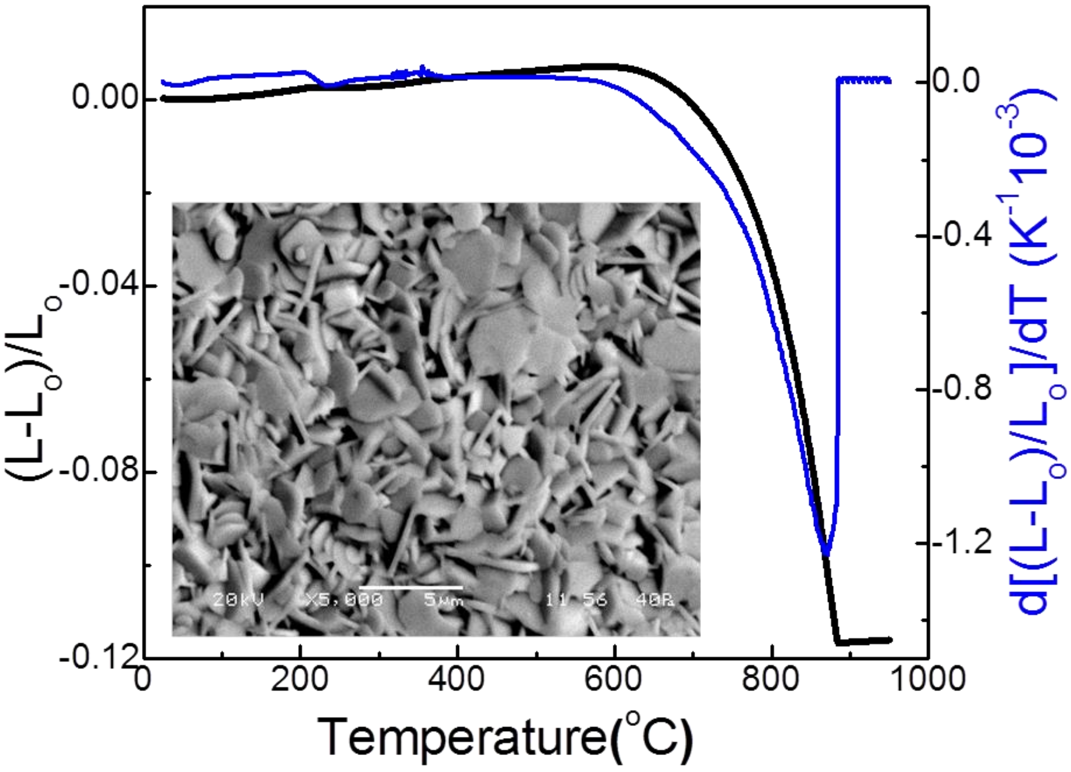

Fig. 4.1.4 Non-isothermal sintering behavior of BIT powder compacts. The inset figure shows the SEM micrograph of sintered sample surface.

4.1.2.4 Dielectric and Diffuse Phase Transition Behavior

Fig. 4.1.5 shows the temperature dependence of the dielectric constant (ε') and dielectric loss (tan δ) at various frequencies of BIT. The temperature T_c is called the Curie temperature and it corresponds to the maximum value of ε' i.e. ε_m'. Table 4.1.2 summarizes the values of room temperature dielectric constant (ε_{rm}), ε_m', *tan* δ and *tan* δ_m and T_c for BIT ceramics. The Curie temperature of BIT is at 660°C which is nearly same as papers [5] and is frequency independent as shown in the Fig. 4.1.5. This indicates that BIT is a normal ferroelectric.

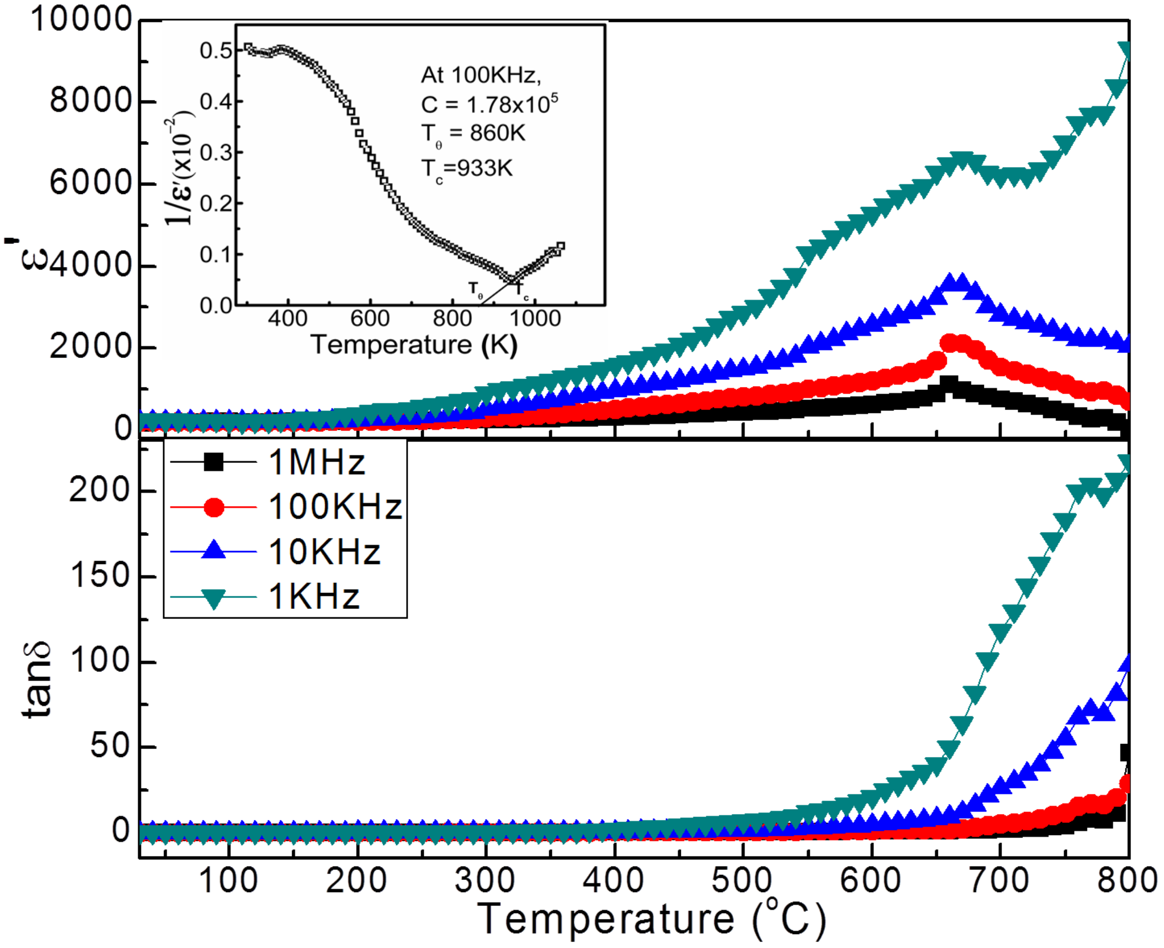

Fig. 4.1.5 Temperature dependence of (a) dielectric constant (ε') and (b) loss (*tan* δ) at different frequencies. Inset shows the inverse dielectric constant (1/ ε') as a function of temperature at 100 kHz.

Above the Curie temperature, the dielectric constant decreases at a rate that can be approximately described by the Curie-Weiss law;

$$\frac{1}{\varepsilon'} = \frac{T - T_\theta}{c} \tag{4.1.8}$$

where, T_θ is a temperature near to, but not identical with, the Curie point T_c and C is the Curie constant. The Curie–Weiss plot for BIT ceramics at 100 kHz is shown in the inset of Fig. 4.1.5. The solid line is the fit to the Curie–Weiss law. The parameters obtained from the linear fit are $C = 1.78 \times 10^5$ °K and $T_\theta = 860$ K. The magnitude of the Curie–Weiss constant is of the same order as that of the well-known displacive-type ferroelectrics such as $BaTiO_3$ (1.7×10^5) [6].

Table 4.1.2 Dielectric, ferroelectric and activation energy (from impedance) of BIT ceramics.

Dielectric properties at 100 kHz		**Polarization hysteresis** (electric field 20kV/cm)	
Room temperature permittivity (ε_{rm})	197	Remnant polarization ($2P_r$)	0.34μC/cm^2
Room temperature dielectric loss (tan δ)	0.05	Coercive field (E_c)	10.08 kV/cm
Maximum permittivity (ε_m')	2130	C (°K)	1.78×10^5
Dielectric loss at peak (tan δ_m)	1.837	**Impedance spectroscopy**	
Maximum permittivity temperature (T_c)	660°C	Activation energy E_a from relaxation time	1.06 eV
dc conductivity (σ_{dc}) at 500°C	9.11×10^{-6} Ω^{-1}	Activation energy E_{dc} from Cole-Cole plot	1.08 eV

4.1.2.5 Impedance Spectroscopy

Fig. 4.1.6 shows the variation of Z″ with frequency at different temperatures. This type of behavior suggests the relaxation process is thermally activated in terms of hopping of charge carriers and the relaxation time decreases with temperature. The relaxation time (τ) is calculated using the formula:

$$\tau = \frac{1}{\omega} = \frac{1}{2\pi f_{\max}} \tag{4.1.9}$$

Where $f_{\max}$ is the maximum frequency calculated from the Z″ vs frequency curve (Fig. 4.1.6). Ln τ has been plotted against the inverse of temperature (as shown in the inset of Fig. 4.1.6) using Arrhenius relationship;

$$\tau = \tau_0 \exp(-\frac{E_a}{k_B T}) \tag{4.1.10}$$

Where E_a is the activation energy, k is the Boltzmann's constant, T the temperature at which the relaxation peak has a maximum, and τ_0 is the time constant at 0K. This activation energy, called the AC activation energy (E_{ac}), has been found to be 1.06 eV, which is in good agreement with that of ion-jump mechanism proposed earlier [7, 8].

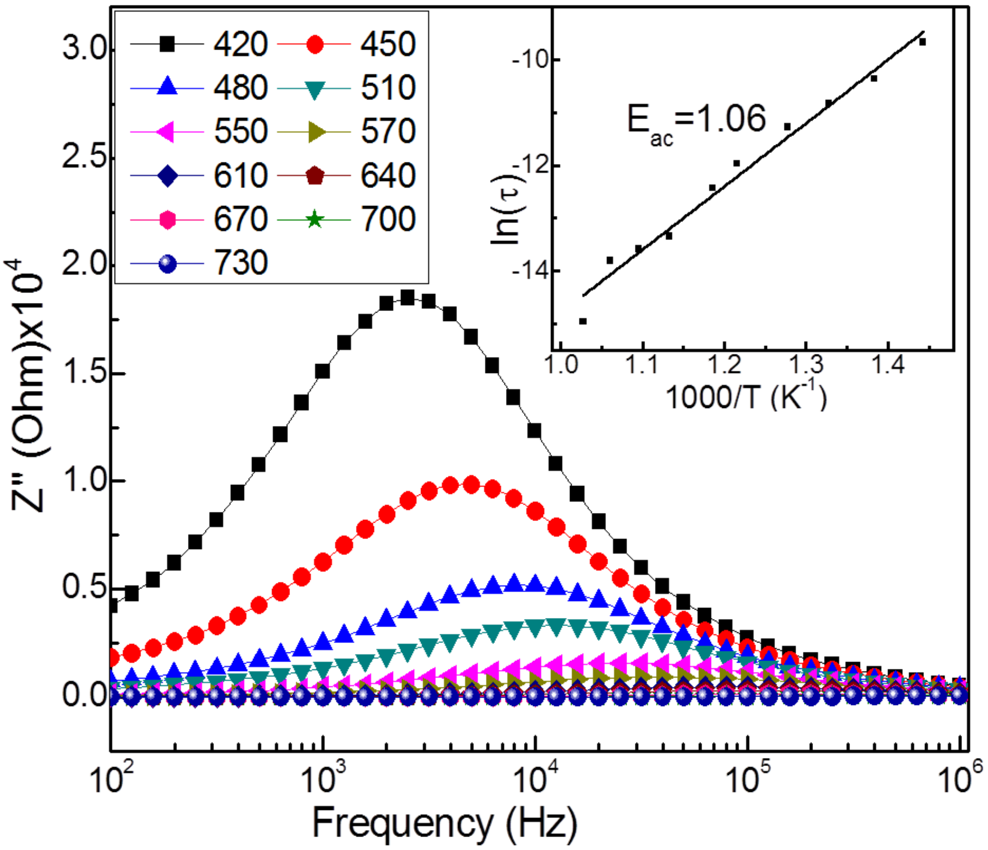

Fig. 4.1.6 Variation of Z'' with frequency. Inset figure shows Arrhenius plot of ac conductivity.

Fig.4.1.7 shows the temperature dependence of complex impedance plot. It is observed that with increase in temperature, the curve is suppressed and the intercept decreased with increase in temperature. A single semicircular arc is observed indicating transport through the grains. The Z' intercept of the semicircular arcs at different temperatures gives the grain resistance (R_g). It is clearly observed that R_g decreases with increase in temperature. Further, these R_g values are used to determine the *dc* conductivity of the sample based on the relation:

$$\sigma_{dc} = \frac{t}{R_g A} \tag{4.1.11}$$

where, t is the thickness of the pellet and A is the overlapping electrode area. The activation energy (E_{dc}) for the process, that is for the formation and hopping of defects can be calculated from the slope of the plot of ln σ versus inverse of temperature as shown in the inset of Fig 4.1.7 as per the Arrhenius equation:

$$\sigma = \sigma_0 \exp(\frac{-E_a}{k_B T}) \tag{4.1.12}$$

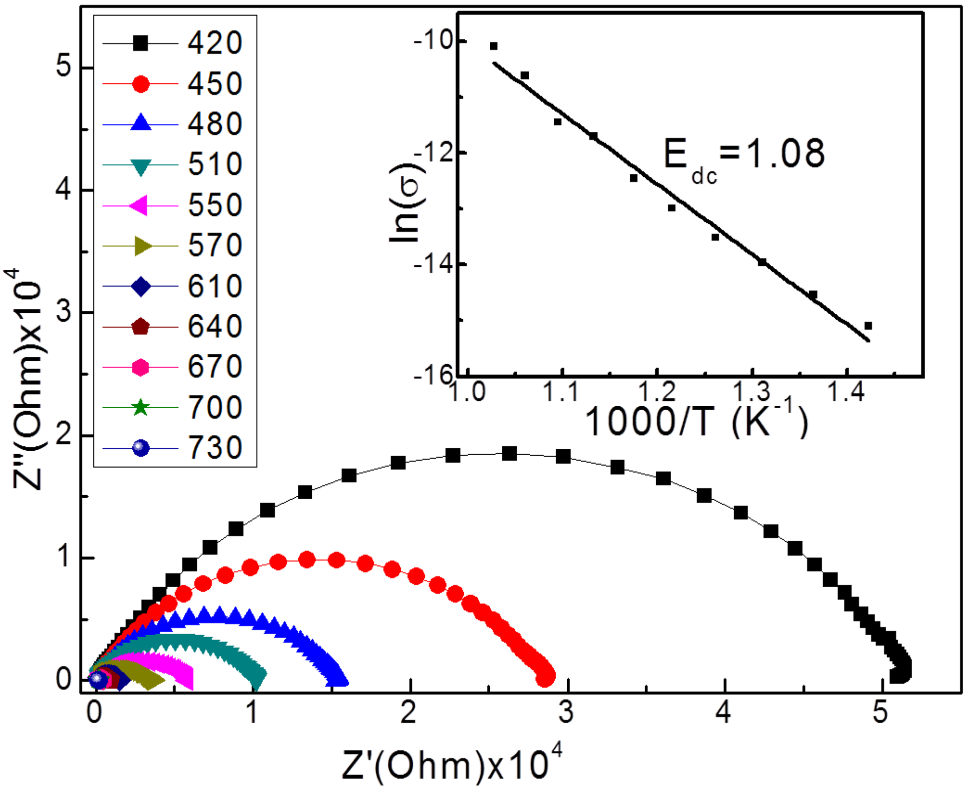

Fig. 4.1.7 Complex impedance plots of BIT at different temperature. Inset figure shows Arrhenius plot of dc conductivity.

The E_{dc} value calculated for the process was 1.08 eV, which is due to the hopping of thermally activated oxygen vacancies. In most of BLSF, the electrical conduction may be due to the movement of defects existing in the lattices. During sintering, volatilization of Bi_2O_3 generates the bismuth vacancy defects (V_{Bi}'') along with oxygen vacancies ($V_O^{\cdot\cdot}$) (Eq. 4.1.13). During cooling of the sintered ceramics, the oxygen enters into the lattice from the atmosphere and generates the holes ($h^{\cdot}$) as per the Eq. 4.1.14.

$$Bi_2O_3 \Leftrightarrow 2Bi(gas) + \frac{3}{2}O_2(gas)\uparrow + 2V_{Bi}''' + 3V_O^{\cdot\cdot} \qquad (4.1.13)$$

$$\frac{1}{2}O_2(g) + V_o^{\bullet\bullet} = O_o + 2h^{\cdot} \qquad (4.1.14)$$

At high temperature, ionic type oxygen vacancies would become predominant charge carriers in the *a-b* plane of BLSF structure, which makes a major contribution to the electrical conduction process in BIT. The ionization of oxygen vacancies can give electrons. These oxygen vacancies act as trapping sites for charge carriers and the free electrons generated may bond with Ti^{4+} and convert them to Ti^{3+} by:

$$Ti^{4+} + e' = Ti^{3+} \qquad (4.1.15)$$

And also some holes are neutralized by electrons as:

$$h^{\cdot} + e' \rightarrow null \qquad (4.1.16)$$

Thus the generation of oxygen vacancies lead to a rise in the conductivity of BLSF by the hopping mechanism. Shulman *et al.* [7, 9, 10] and Villegas *et al.* [11, 12] proposed that the conductivity may be generate due to the combined effect of hole and ionic mobility.

4.1.2.6 Polarization Hysteresis Characteristics

Fig. 4.1.8 shows the P-E hysteresis loops of two BIT specimens viz sintered at 850^{o}C and 950^{o}C. The ceramics are sintered at different temperatures 850^{o}C, 900^{o}C and 950^{o}C to compare their properties. The hysteresis loop of 850°C sintered specimen is narrow with small remnant polarization compared to 950^{o}C specimen; however the hysteresis loop of 950^{o}C sintered sample is very lossy. The bulk density of BIT ceramic sintered at 850^{o}C for 4h is of 94% and the average grain size is of 2.2 µm. The small hysteresis loop may be due to low grain size of the ceramics [13].

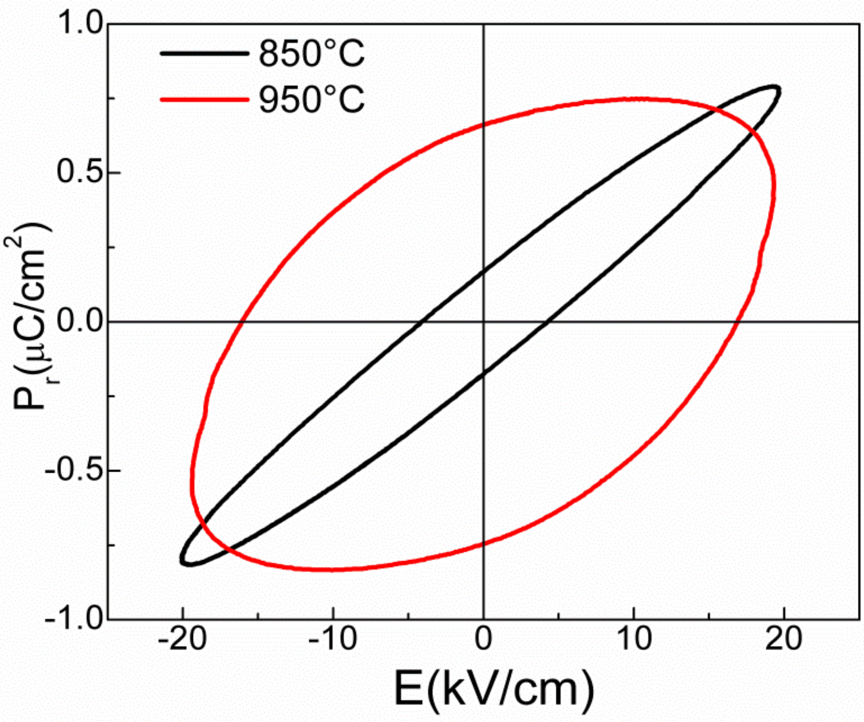

Fig. 4.1.8 Polarization-electric field hysteresis loops of BIT under an applied field at different temperature.

Fig. 4.1.9 shows the XRD patterns of these three ceramics with SEM microstructure shown on the right hand side of the figure. It shows abnormal increase of (00*l*) intensities with the increase in sintering temperature. For pellet sintered at 900^{o}C for 4h, there is much more increase in the length than the thickness. The pellet sintered at 950^{o}C for 4h shows two different types of grain size of the sample (Fig. 4.1.9(c)). The average grain size of large grains is 36 µm and thickness 2 µm whereas the average grain size of the smaller grains are 3.91 µm and thickness 2 µm. Abnormal grain growth is occurring in the ceramics at high temperature, where liquid phase is supposed to appear in large quantity. Few grains grow preferentially along (00*l*) plane with the expense of smaller grains [14]. However in case of 850°C and 900°C specimens, the abnormal grain growth was not so prominent.

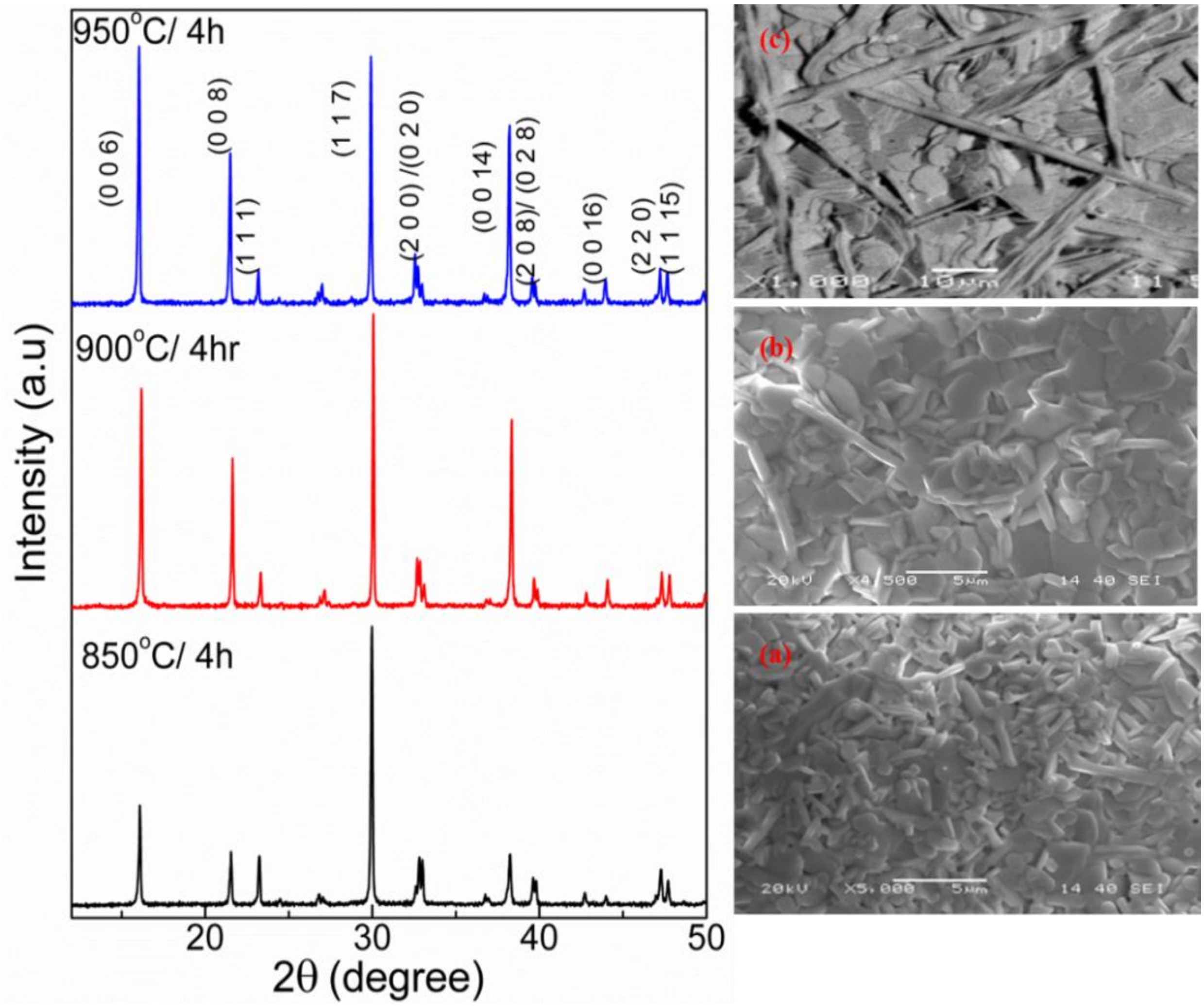

Fig. 4.1.9 XRD pattern of BIT sintered at different temperature and corresponding SEM micrograph of the sintered sample surface (a) 850°C (b) 900°C (c) 950°C.

Fig. 4.1.10 shows the temperature dependence of dielectric constant (ε′) and loss (tan δ). For the specimen sintered at different temperatures, the dielectric loss increases with increasing sintering temperature. The loss increases with the increase in sintering temperature due to Bi volatilization. The dielectric constant at room temperature as well as at Curie peak is decreased in case of 950^{o}C/4h sintered specimen, which may be due to the preferred orientation of grains [15]. In case of specimens sintered at 900^{o}C/4h and 950^{o}C/4h, the permittivity-temperature behavior becomes more broad. A secondary broad peak before Curie peak was observed at around 550^{o}C. Many authors reported these secondary peaks [16, 17] and this behavior is due to the space charge accumulation in the specimen those sintered at higher temperature. In case of 900^{o}C/4h and 950^{o}C/4h specimens, space charges are higher compared to 850^{o}C/4h because of the generation of more defects in specimen sintered at high temperature.

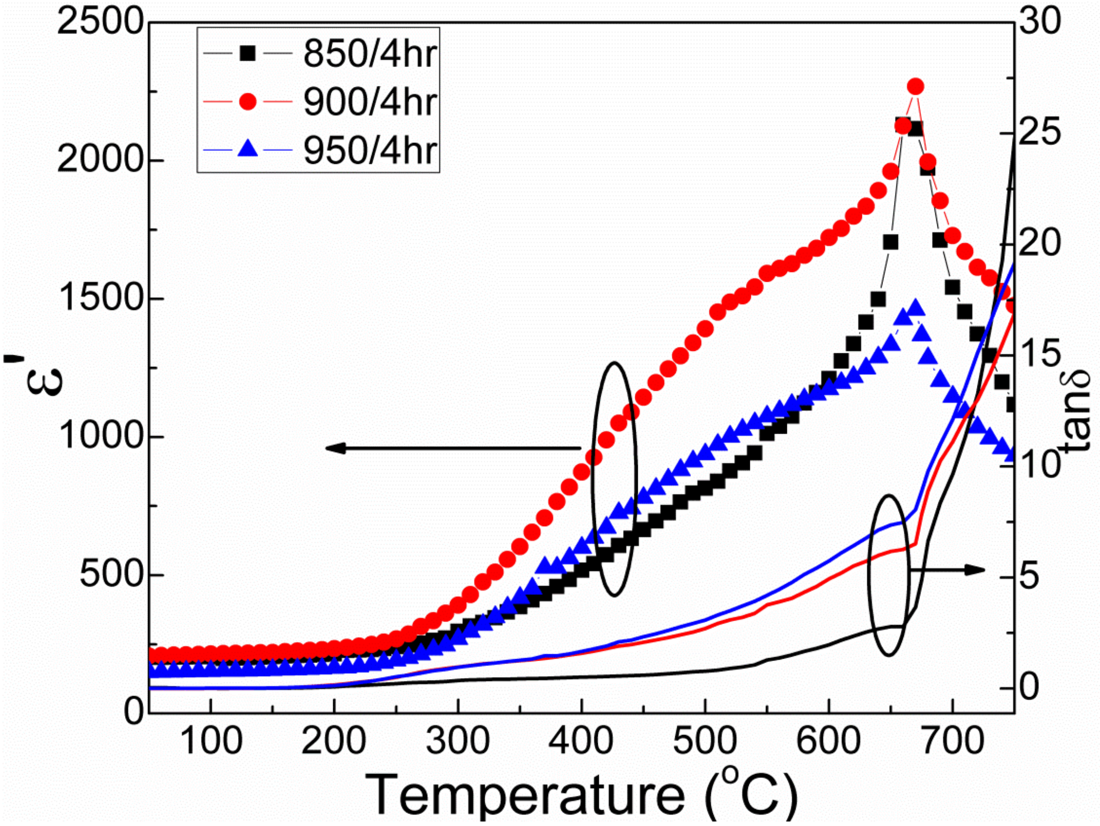

Fig. 4.1.10 Temperature dependence of dielectric constant (ε´) and loss (tan δ) for BIT samples sintered at different temperatures.

Fig. 4.1.11 shows the complex impedance graph at 440^{o}C for specimens sintered at different temperatures. Data are fitted by ZSimWin software. Here “z msd” indicates the experimental value and “z cal” is the fitted value. The figure shows that with the increase in sintering temperature, the grain resistance decreases due to the accumulation of spatial charges [16, 17]. For the samples sintered at 900 and 950^{o}C, ZSimWin software used three semicircular arcs to fit the observed data, indicating the conduction occurs through grains, grain boundary and electrode effect.

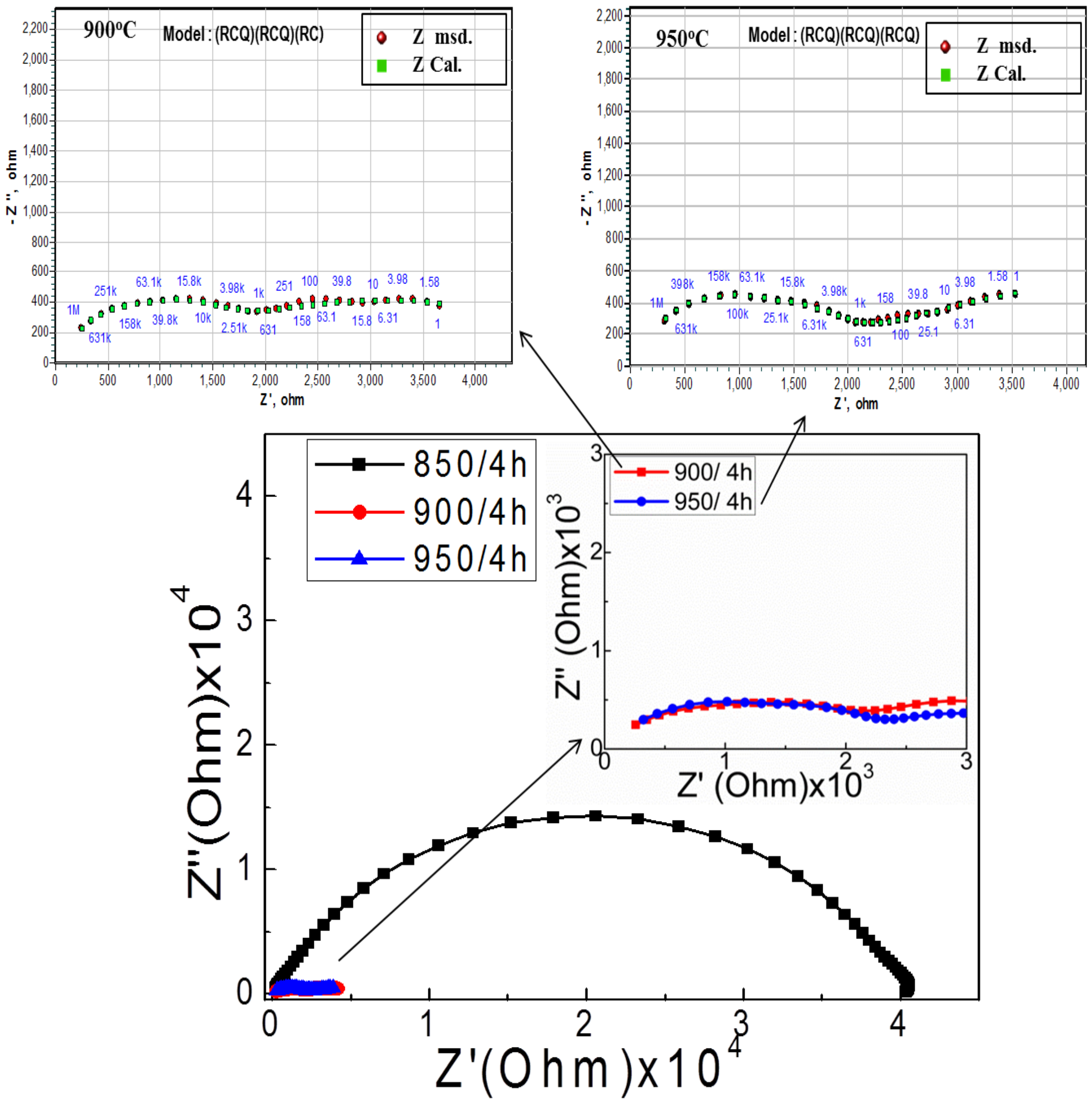

Fig. 4.1.11 Complex impedance graph of BIT at 440°C for samples sintered at different temperature.

4.1.2.7 Conclusions for BIT

BIT powder is synthesized by a modified oxalate route, where a mixture of Bi-oxalates and TiO_2 is calcined at 800°C to produce a pure phase BIT. The phase formation started at 700°C due to better homogeneity of the precursor. More than 94% dense ceramics can be formed by sintering at 850°C for 4h. The microstructure of this sintered specimen show randomly oriented plate like grains. The temperature dependence of dielectric constant at various frequencies explained the normal ferroelectric behavior of the ceramics with Curie temperature T_c = 660°C. The Curie–Weiss law is obeyed for the ferroelectrics; with Curie constant $C = 1.78 \times 10^5$ °K and Curie temperature T_θ = 587°C. The impedance spectroscopic analysis shows that the ferroelectric relaxation is thermally activated with activation energy for E_{ac} and E_{dc} of 1.06 eV and 1.08 eV respectively and suggesting an ion-jump mechanism.

(B) Synthesis and characterization of $SrBi_4Ti_4O_{15}$

4.1.3.1 Thermal decomposition and Phase formation behavior

The raw precursor powder is used to study the thermal decomposition behaviour using differential scanning calorimetry (DSC) and thermo-gravimetric (TG) analysis. Fig. 4.1.12 shows the thermal decomposition behavior of oxalate precursor powder for $SrBi_4Ti_4O_{15}$. The figure shows the weight losses in four different stages. First weight loss (about 3%) up to 120°C is due to dehydration of adsorbed water and is associated with endothermic peak shown in the figure. Second weight loss in the range 220 to 430°C is associated with the exothermic peak T_3 and is due to decomposition of oxalates in the precursor. Third weight loss between 430°C to 500°C (about 2%) corresponds to the decomposition of nitrates. The broad exothermic peak T_5 corresponds to the crystallization of different phases. The endothermic peak T_6 at about 800°C is due to the evaporation of excess Bi_2O_3. The exothermic peak T_7 at 820°C is due to the formation of $SrBi_4Ti_4O_{15}$ [18].

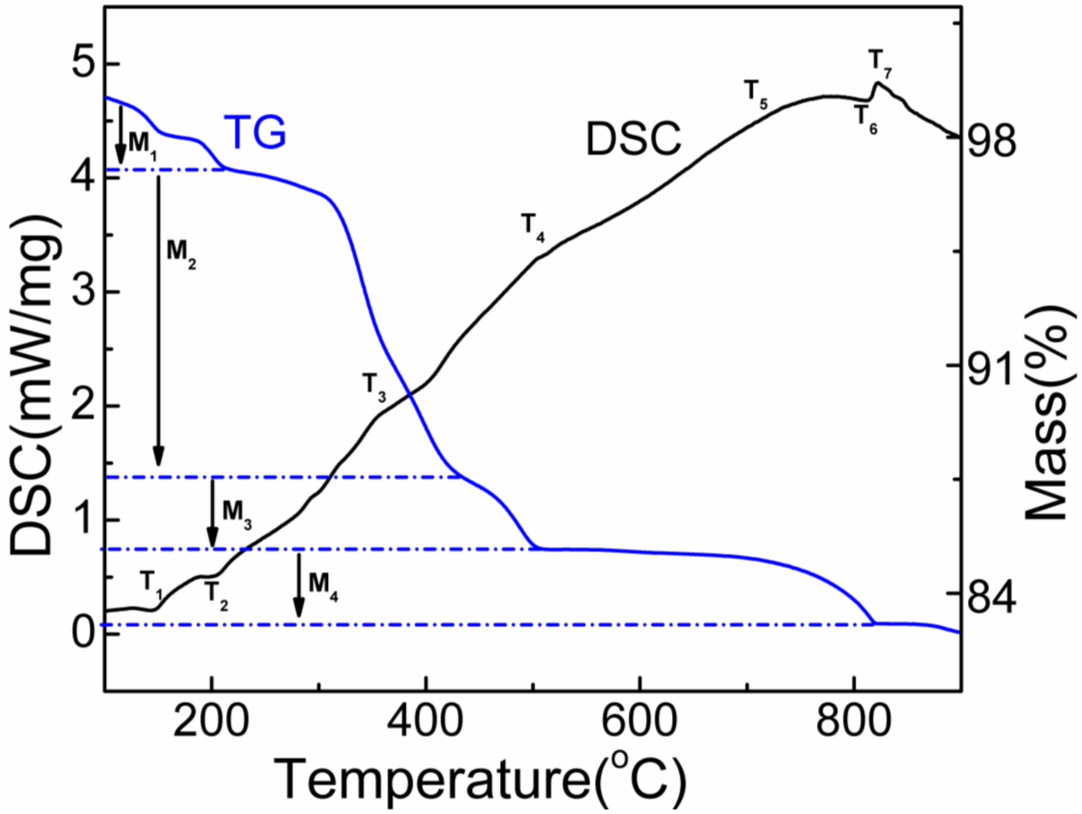

Fig. 4.1.12 DSC/TG plot of precursor powder of $SrBi_4Ti_4O_{15}$ ceramics at a heating rate of 10°C/min in air atmosphere.

To investigate the phase formation behavior in the precursor, the powder is calcined at different temperatures. The XRD pattern of raw powder (as synthesised) shows (Fig. 4.1.13 (a)) the presence of anatase along with the amorphous phase. The precursor powder is calcined at different temperature starting from 600°C, as it has been shown in the case of BIT in Fig. 4.1.2(d) that the BLSF phase starts forming at about 600°C [Fig. 4.1.13(b)]. At 600°C bismuth titanate ($Bi_4Ti_3O_{12}$) start to form where bismuth oxide (Bi_2O_3) is the main phase. At 700°C the bismuth oxide and titania reacts to form $Bi_4Ti_3O_{12}$ as shown in the Eq. 4.1.17. At 800°C, strontium bismuth titanate ($SrBi_4Ti_4O_{15}$) starts to form where $Bi_4Ti_3O_{12}$ is the main compound along with anatase and strontium bismuth oxide ($Sr_2Bi_2O_5$). At 900°C Strontium bismuth oxide ($Sr_2Bi_2O_5$) and anatase reacts to form a new phase strontium titanate ($SrTiO_3$) in Eq. 4.1.18. At 1050°C, the final product strontium bismuth titanate ($SrBi_4Ti_4O_{15}$) form by the reaction of strontium titanate ($SrTiO_3$) and bismuth titanate ($Bi_4Ti_3O_{12}$) shown in the Eq. 4.1.19. The results indicate that in spite of the presence of SrO in powder mixer of Bi_2O_3-TiO_2-SrO, the initial phase produces during the heat treatment is $Bi_4Ti_3O_{12}$ (BIT).

$$2Bi_2O_3 + 3TiO_2 \xrightarrow{700^{o}C} Bi_4Ti_3O_{12}. \qquad (4.1.17)$$

$$Sr_2Bi_2O_5 + 3Bi_2O_3 + 8TiO_2 \xrightarrow{900^{o}C} Bi_4Ti_3O_{12} + SrBi_4Ti_4O_{15} + SrTiO_3. \qquad (4.1.18)$$

$$Bi_4Ti_3O_{12} + SrTiO_3 \xrightarrow{105\,0^{o}C} SrBi_4Ti_4O_{15}. \qquad (4.1.19)$$

4.1.3.2 Structural Analysis

The parameters for Rietveld refinement are taken from SBTi4 as presented by B.J. Kennedy *et al.* [19], with orthorhombic space group $A2_1am$ and initial cell parameters of a = 5.4509Å, b = 5.4373Å and c = 41.005Å. Starting atomic coordinates and atomic displacements are also taken from the same reference. The lattice parameters of SBTi4 obtained after Rietveld refinements are shown in Fig. 4.1.14. The lattice parameters are: a=5.4504(3), b=5.4393(1), c=41.006(3) Å and R_w= 4.03 %, R_p=2.81 % and Sigma=1.43. These are shown in the table 4.1.3 with the orthorhombicity.

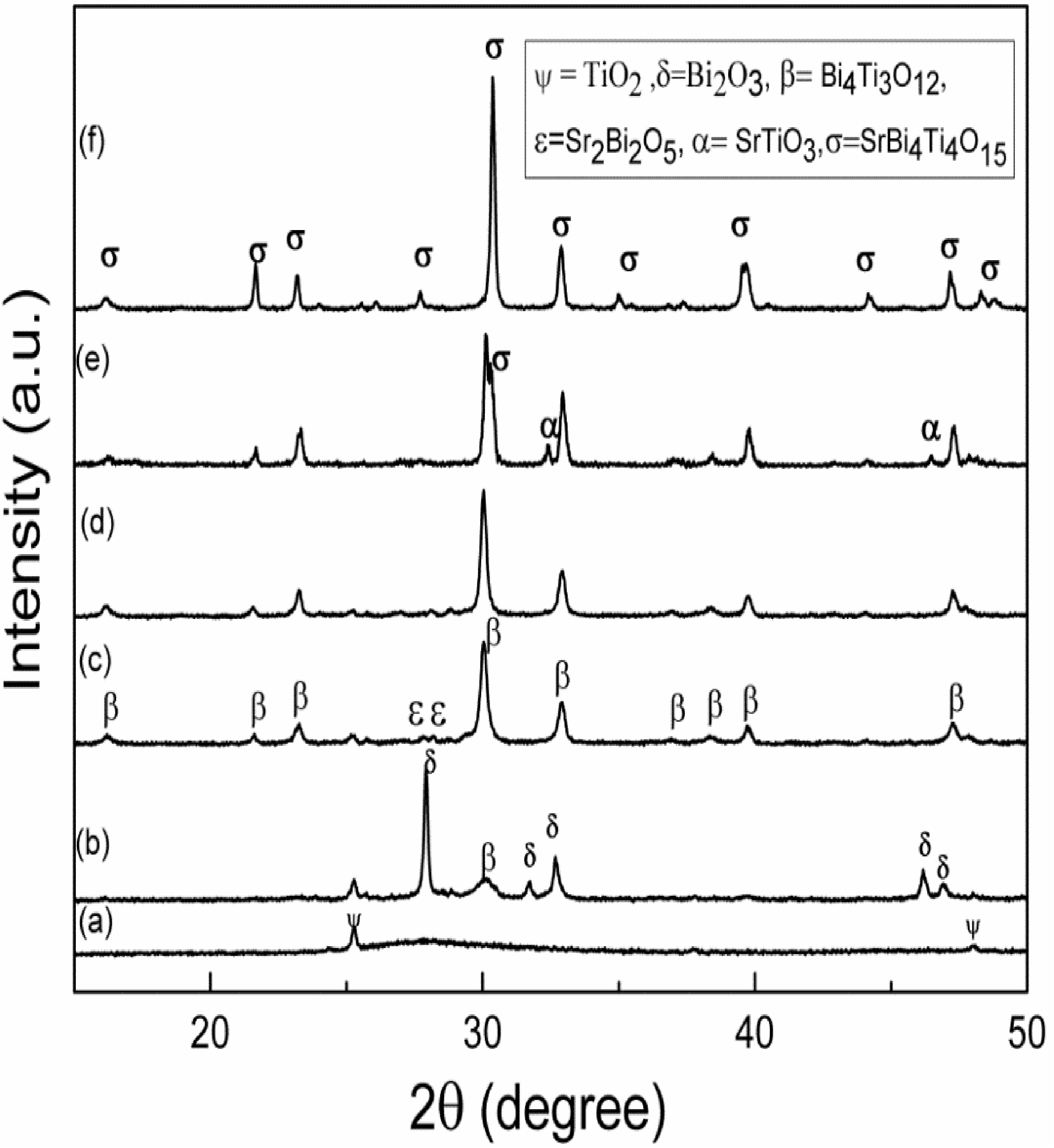

Fig. 4.1.13 Room temperature XRD patterns of the precursor (a) raw powder and calcined powders at (b) 600, (c) 700, (d) 800, (e) 900 and (f) 1050°C. Major phases identified are also shown in the Figure.

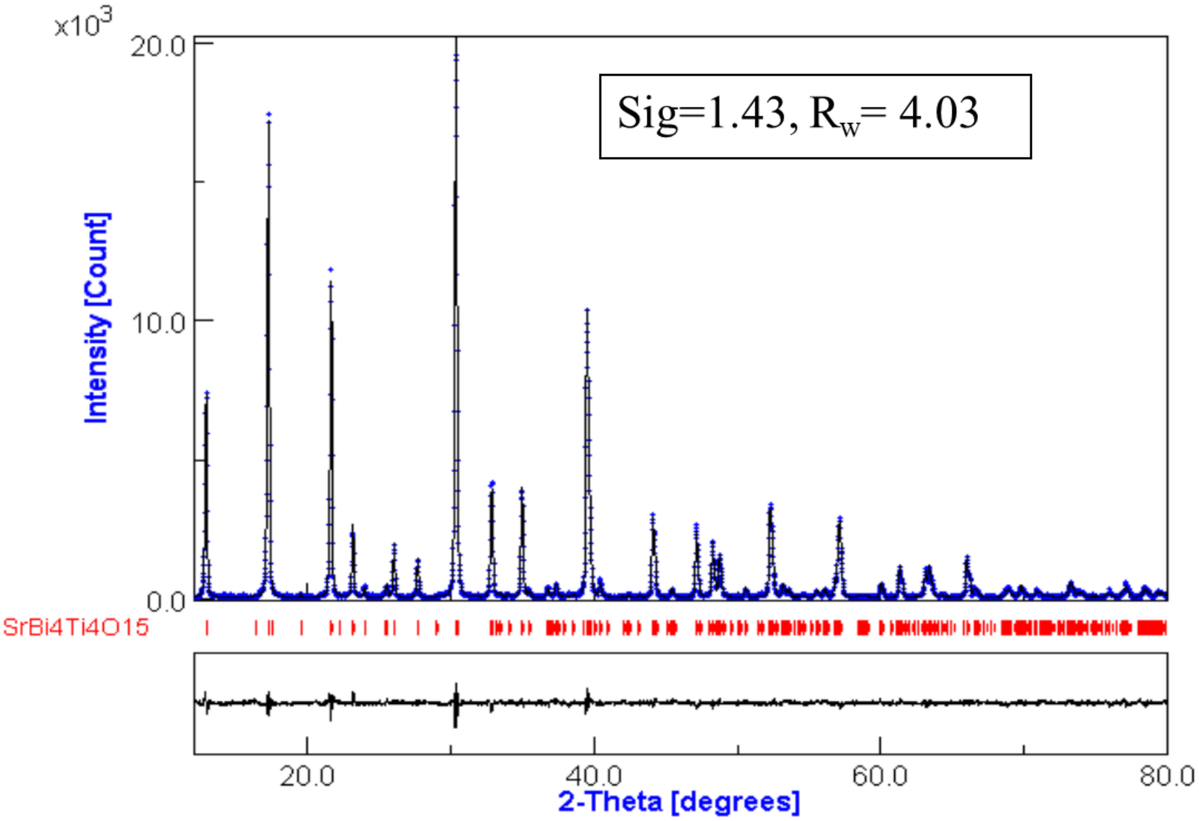

Fig. 4.1.14 Rietveld refinement plot for sintered SBTi4 composite ceramics showing observed (+), calculated (solid line) XRD profile, their differences in the bottom and position of allowed Bragg reflections (tick marks).

Table 4.1.3 Symmetry, Space group, refined lattice parameters '*a*', '*b*' and '*c*', *R*-factors, Sigma, Orthorhombicity of SBTi4 ceramics.

Parameters	**Values**
Symmetry	Orthorhombic
Space group	$A2_1am$
a (Å)	5.4504(3)
b (Å)	5.4393(1)
c (Å)	41.006(3)
R_w (%)	4.03
R_b (%)	2.81
Sigma	1.43
Orthorhombicity	0.0020

4.1.3.3 Densification Behavior and Microstructural Characteristics

Fig. 4.1.15 shows the non-isothermal shrinkage behavior of the SBTi4 ceramics. The powder of SBTi4 starts to shrink at 1020°C. In the case of the BIT powder, the onset temperature is 765°C. Linear shrinkage during heating is directly related with the densification of a material. The greater the shrinkage, the higher density will be achieved. Fig. 4.1.16 shows plate like grains with preferred orientation. As described in the section 4.2.2.3, the plate like grain growth is a typical characteristic of bismuth layered structure ferroelectrics. However in the case of SBTi4 sintered at 1100^{o}C/ 4h, the average grain size and aspect ratio of the grains is higher than BIT. The grains have the mean diameter of 4.1 μm and a thickness of about 0.6 μm. The aspect ratio of the grains is ~6.8, whereas for BIT it is ~5.5 as shown in Table 4.1.4.

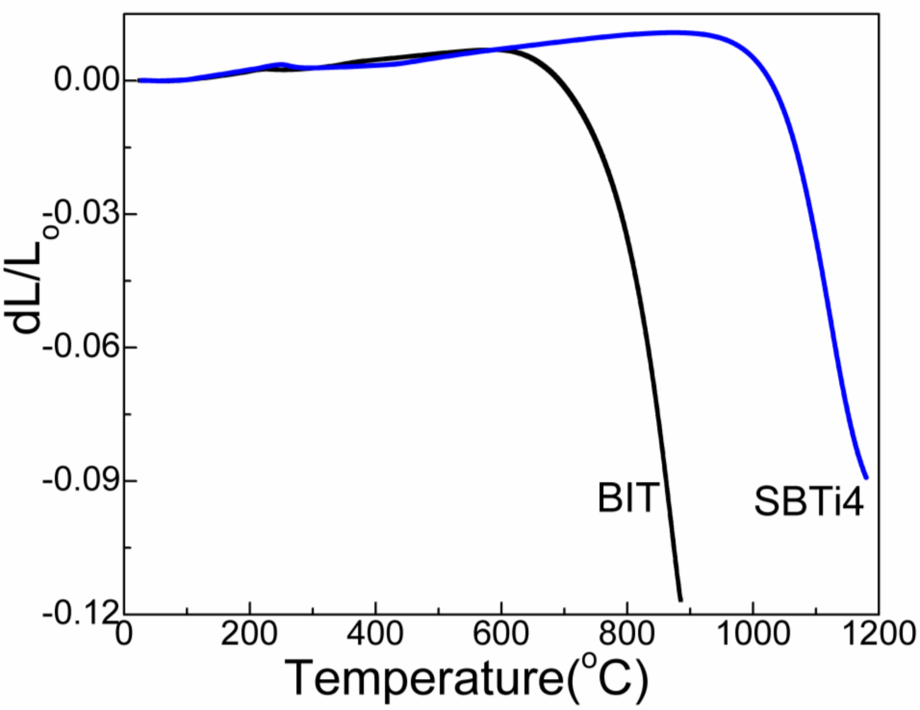

Fig. 4.1.15 Non-isothermal sintering behavior of SBTi4 powder compacts.

Table 4.1.4 Length, breadth, thickness and aspect ratio of BIT and SBTi4 ceramics

Sample ID	Length (μm)	Breadth (μm)	Thickness (μm)	Aspect Ratio
BIT (850^{o}C/4h)	2.2	1.2	0.4	5.5
SBTi4 (1100^{o}C/4h)	4.1	2.2	0.6	6.8

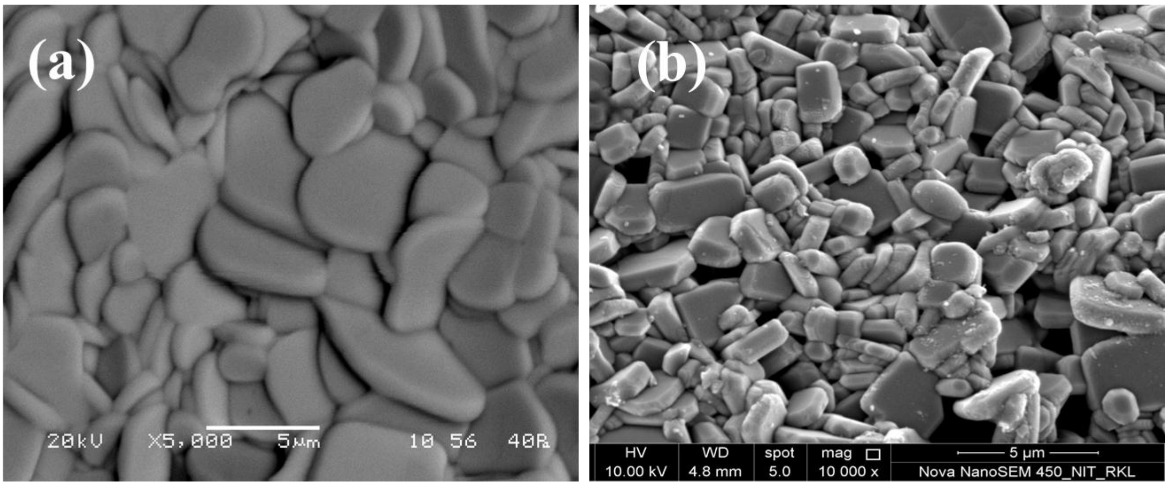

Fig. 4.1.16 SEM micrograph of SBTi4 sintered sample surface (a) and freshly broken bulk surface (b).

4.1.3.4 Dielectric and Diffuse Phase Transition Behavior

Fig. 4.1.17 shows the temperature dependence of the dielectric constant (ε') and dielectric loss (tan δ) at various frequencies. The temperature of maxima in ε' at 530^{o}C [5] is frequency independent which indicates that SBT is a normal ferroelectric and follows the Curie–Weiss law. The Curie–Weiss plot for SBT ceramics at 100 kHz is shown in the inset of Fig. 4.1.17. The solid line from 600 to 520^{o}C is the temperature range of fit to the Curie–Weiss law. The parameters obtained from the linear fit are $C = 1.78 \times 10^{5}$ ^{o}K and $T_{\theta} = 785$ ^{o}K. The magnitude of the Curie–Weiss constant is of the same order as that of the well-known displacive-type ferroelectrics such as $BaTiO_3$ (1.7×10^{5} ^{o}K) and BIT (1.78×10^{5} ^{o}K). Table 4.1.5 shows the dielectric constant and dielectric loss at room temperature and at Curie temperature.

Table 4.1.5 Dielectric, ferroelectric parameters and activation energy (from impedance) of SBTi4 ceramics.

Dielectric properties at 100 kHz		**Polarization hysteresis** (electric field 20kV/cm)	
Room temperature permittivity (ε_{rm})	208	Remnant polarization ($2P_r$)	0.53μC/cm^{2}
Room temperature dielectric loss (tan δ)	0.02	Coercive field (E_c)	14.78 kV/cm
Maximum permittivity (ε_m')	2467	C (°K)	1.78×10^{5}
Dielectric loss at peak (tan δ_m)	0.061	**Impedance spectroscopy**	
Maximum permittivity temperature (T_c)	530°C	Activation energy E_{ac} (relax time)	1.62 eV
dc conductivity (σ_{dc}) at 500^{o}C	1.38×10^{-7} $(\Omega cm)^{-1}$	Activation energy E_{dc} from Cole-Cole plot	1.51 eV

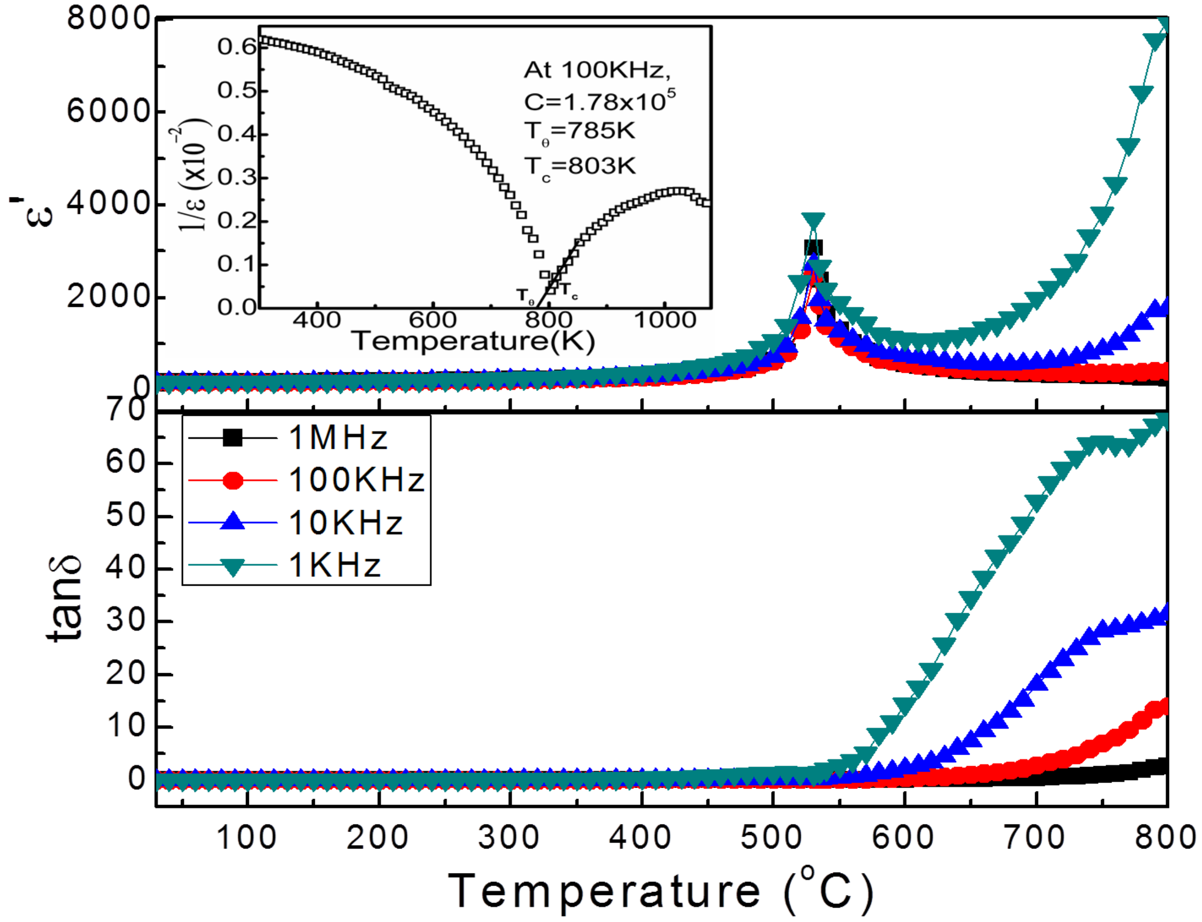

Fig. 4.1.17 Temperature dependence of (a) dielectric constant (ε') and (b) tan δ at different frequencies of SBTi4. Inset shows the inverse dielectric constant ($1/\varepsilon'$) as a function of temperature at 100 kHz.

4.1.3.5 Impedance analysis

Fig. 4.1.18 shows Z'' vs frequency plot, clearly indicating the maxima of Z'' is shifting towards higher frequency domain with increasing temperature. This type of behavior suggests that the relaxation process is thermally activated in terms of hopping of charge carriers and the relaxation time decreases with temperature. Ln of relaxation time (Ln τ) has been plotted against the inverse of temperature (as shown in the inset of Fig. 4.1.18). The value of the activation energy obtained 1.62 eV is in good agreement with the value proposed for ion-jump mechanism. SBTi4 has decreased oxygen ion vacancy due to the presence of Sr in the structure [20, 21]. Sr-O bonding is stronger than Bi-O bonding. Both Sr and Bi are present in the A-site of SBTi4 whereas only Bi is present in the A-site of BIT. As SBTi4 has lesser amount of Bi ion in the A-site, there will be less amount of Bi-volatilization and hence decreased oxygen ion vacancy in SBTi4.

Fig. 4.1.19 shows the complex impedance curve (Cole-Cole plot) It is clearly observed that R_g decreases with increase in temperature. The activation energy (E_a) for the *dc* conductivity can be calculated from the Arrhenius equation (Eq. 4.1.12). E_{dc} is 1.51eV and the energy may be associated for the hopping of defects. The defect is oxygen-ion vacancy defect produced by Bi-volatilization [22]. E_{dc} can be calculated from the plot of ln σ_{dc} versus inverse of temperature as is shown in inset Fig. 4.1.19.

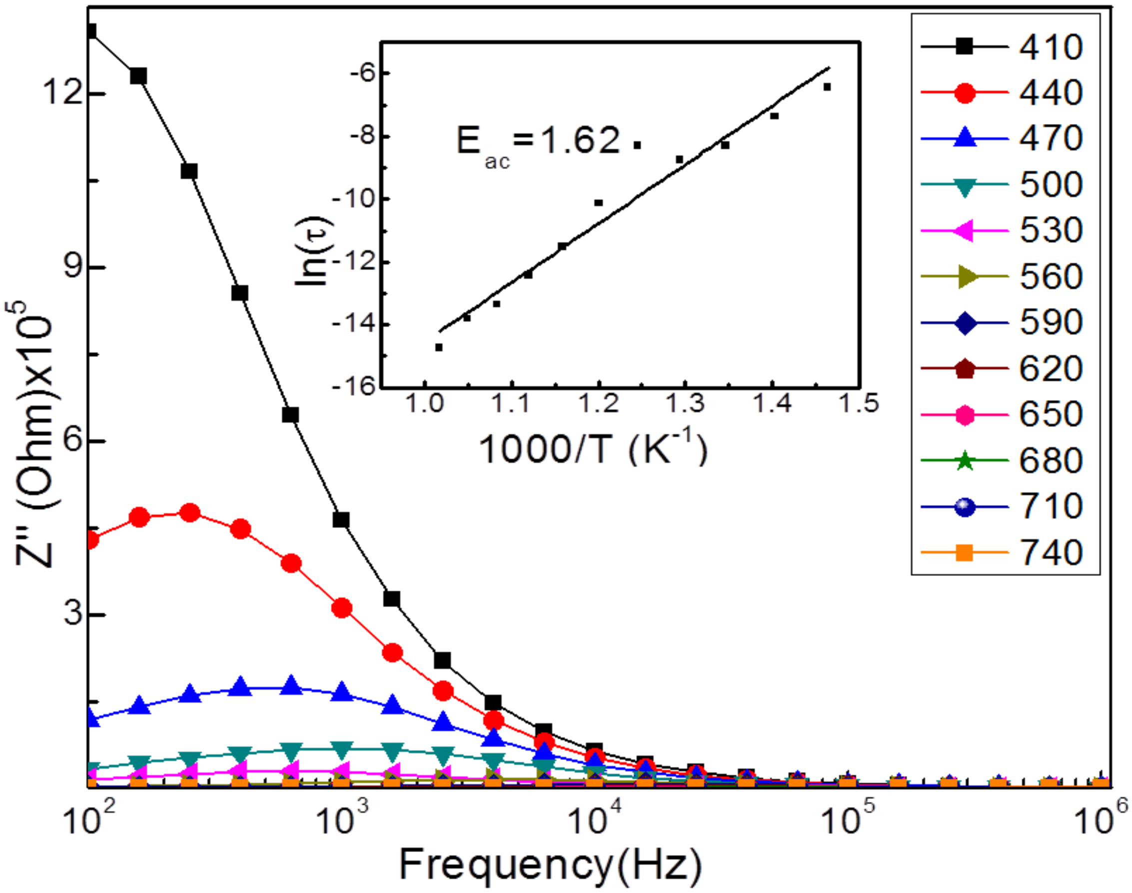

Fig. 4.1.18 Variation of Z″ with frequency of SBTi4. Inset figure shows Arrhenius plot of ac conductivity.

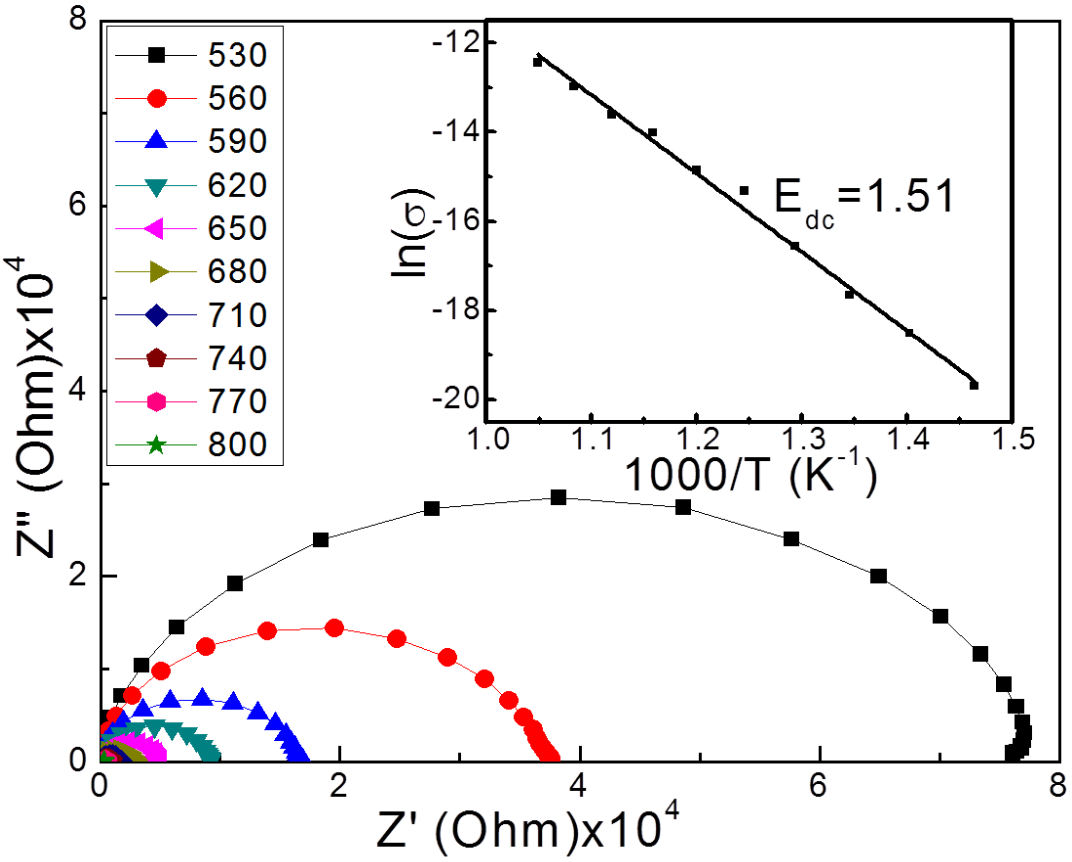

Fig. 4.1.19 Complex impedance curve for SBTi4 at varying temperature. Inset figure shows Arrhenius plot of dc conductivity.

4.1.3.6 Polarization Hysteresis Characteristics

Fig. 4.1.20 shows the P-E hysteresis loops of BIT and SBTi4. The P-E hysteresis loop for SBTi4 has higher remnant polarization than BIT under an applied field of 20KV/cm. The increased remnant polarization in SBTi4 may be due to the large grain size and lower dielectric loss/oxygen vacancy in SBTi4 ceramics.

4.1.3.7 Conclusion for SBTi4

Like BIT, SBTi4 powder is successfully synthesized by modified oxalate route. However the pure phase formed at 900°C; 200^o higher than BIT formation temperature. SBTi4 also showed normal ferroelectric behavior with a Curie temperature 530°C, same as literature value. The room temperature dielectric constant is about 200 similar to that of BIT. However, its dielectric loss is only 0.02 as compared to 0.05 found for BIT. The activation energy E_{ac} of SBTi4 is also higher (1.62 eV) than that (1.06 eV) of BIT, indicating SBTi4 has decreased oxygen ion vacancy due to the presence of Sr in the structure. SBTi4 also showed higher remnant polarization than BIT. This may be due to the large grain size and lower dielectric loss/oxygen vacancy in SBTi4 ceramics.

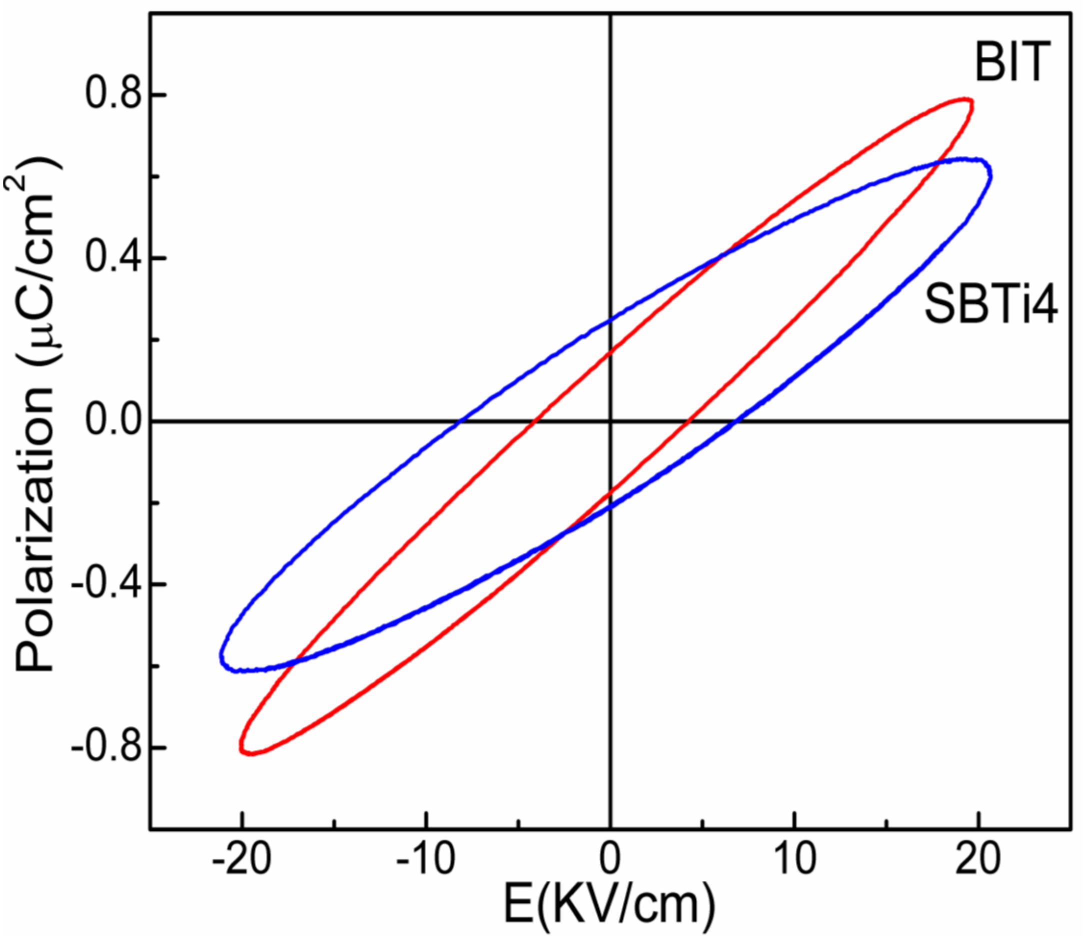

Fig. 4.1.20 Polarization-electric field hysteresis loops of BIT and SBTi4 under an applied field of 20 KV/cm.

(C) Synthesis and characterization of $Sr_2Bi_4Ti_5O_{18}$

4.1.4.1 Thermal decomposition and phase formation behavior

Fig. 4.1.21 shows the thermal decomposition behavior of oxalate precursor powder of SBTi5. The figure shows the weight loss in four different stages. First weight loss is about 3% up to 220°C is due to dehydration of adsorbed water and associated with endothermic peak T_1. Second weight loss (about 6%) in the range 270 to about 350°C is due to the exothermic decomposition of oxalates. Third weight loss (about 5%) in the range 350°C to 510°C is due to the decomposition of nitrates. The broad exothermic peak T_5 in the range of 600 to 800°C corresponds to the crystallization of different phases like Bi_2O_3, $Bi_4Ti_3O_{12}$, $Sr_2Bi_2O_5$ and $SrTiO_3$. There is one endothermic peak T_6 at about 840°C is due to the evaporation of excess Bi_2O_3. Another exothermic peak T_7 at 850°C is due to the phase formation of SBTi4 as explained by Gelfuso *et al.* [18].

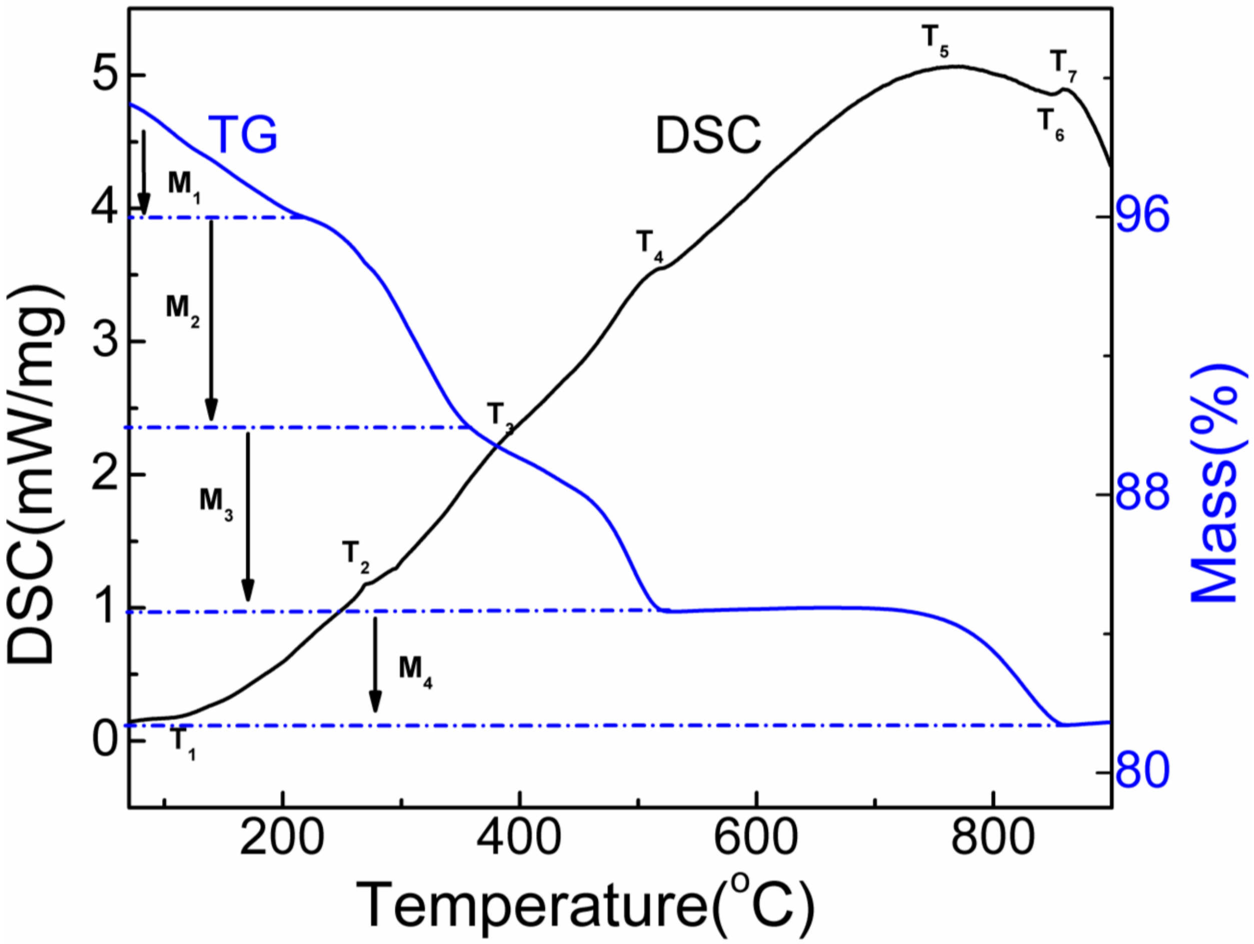

Fig. 4.1.21 DSC/TG plot of precursor powder of SBTi5 ceramics at a heating rate of 10°C/min in air atmosphere.

Precursor powder synthesized by this method is calcined at different temperatures to investigate the BLSF phase formation behavior, starting from 800^{o}C as it has been shown in the case of 4-layer SBTi4 that the 4-layered BLSF formation starts at 800^{o}C (Fig. 4.1.12). Fig. 4.1.22 shows XRD patterns of powders after calcination at different temperatures along with that the raw precursor powder. Raw powder shows anatase TiO_2 phase and other amorphous phases. The amorphous phases may contain Sr and Bi containing phases. Accordingly when the powder is calcined at 800^{o}C, the BLSF phase $Bi_4Ti_3O_{12}$ formed (Fig. 4.1.22(b)) along with $SrTiO_3$. So, further calcination at higher temperature must be needed to get the final 5-layer BLSF phase. The powders are than calcined at 900 ^{o}C, 1000 ^{o}C and 1100^{o}C. The 900^{o}C calcined powders showed again that the presence of $Bi_4Ti_3O_{12}$ (not shown in the figure) and $SrBi_4Ti_4O_{15}$ phase. $SrBi_4Ti_4O_{15}$ phase starts forming as per the Eq. 4.1.20 at 900^{o}C. The 1000^{o}C calcined powder showed the presence of 4-layer BLSF $SrBi_4Ti_4O_{15}$ phase along with some un-reacted $SrTiO_3$ (Fig. 4.1.22(c)). The final phase $Sr_2Bi_4Ti_5O_{18}$ is found after calcination at 1100^{o}C (Fig. 4.1.22(d)) as per the Eq. 4.1.21.

$$Bi_4Ti_3O_{12} + SrTiO_3 \xrightarrow{900^{o}C} SrBi_4Ti_4O_{15}\,. \qquad (4.1.20)$$

$$SrBi_4Ti_4O_{15} + SrTiO_3 \xrightarrow{1100^{o}C} Sr_2Bi_4Ti_5O_{18}\,. \qquad (4.1.21)$$

3-layered structure compound is very easy to form as explained in the session 4.1.2.1 and higher layers BLSF compounds are difficult to form due to high temperature requirement for the formation of their long *c*-axis stacking [23].

The XRD data are obtained on the unpolished surface of a sintered pellet which is perpendicular to the uniaxial pressing direction of pellet fabrication. Usually the dielectric properties are measured after applying electrode on the pellet surfaces. For that reason, XRD is obtained of the pellet not of the powder. The figure shows major differences in integrated intensity when compare with powder pattern shown in the Fig. 4.1.22(d). The pellet showed that (00*l*) peaks more intense than its powder pattern. This indicates that the relative intensities of (00*l*) peaks are increased by sintering process, indicating high temperature processing has influenced on texturing of the BLSF ceramics. The texturing of the BLSF ceramics is caused by the grains alignment in a preferred orientation along certain lattice directions. In this case, the relative intensity of the (00*l*) peak is increased due to preferred orientation of larger number of the grains with their c-axis aligned perpendicular to pellet faces, as shown in Fig. 4.1.25 (a).

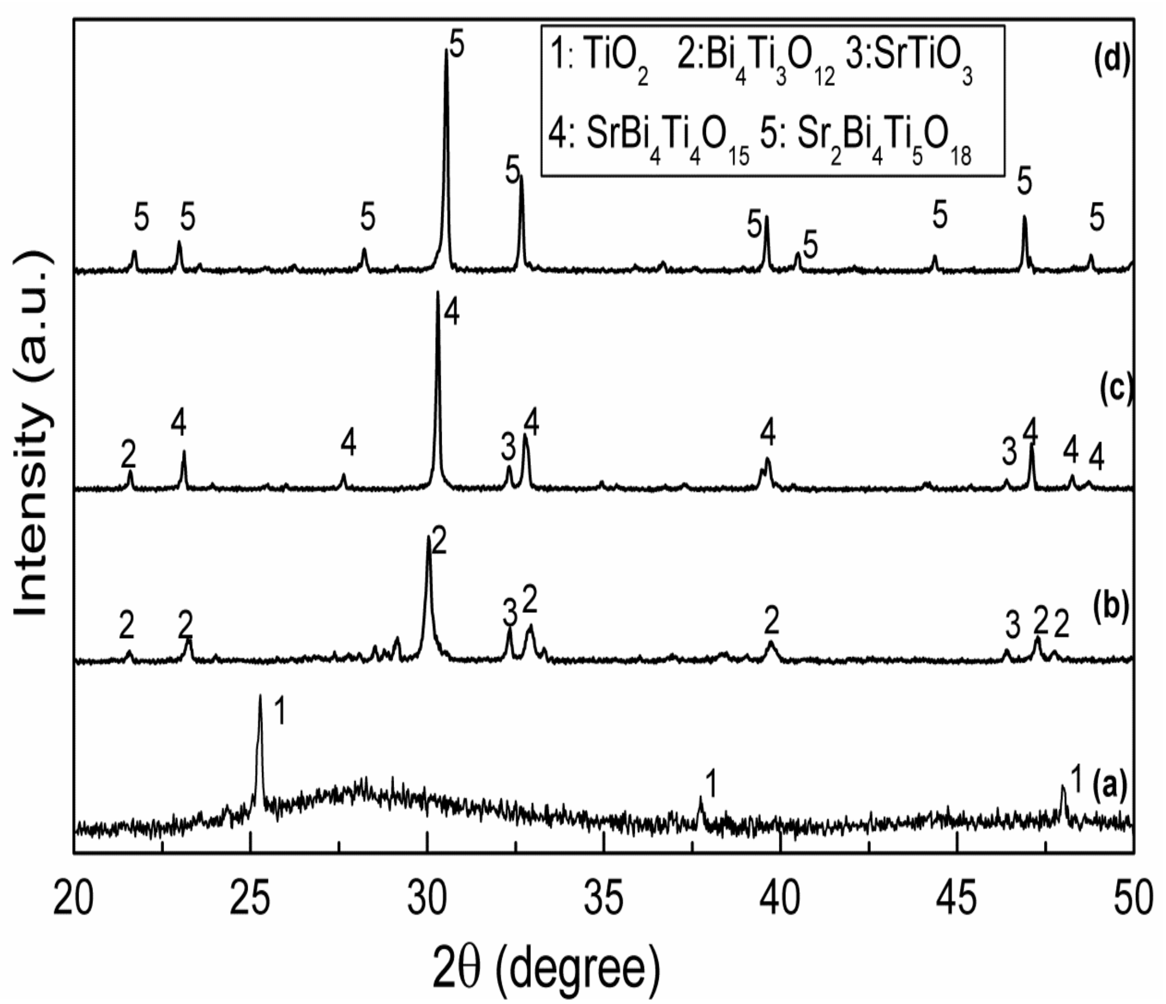

Fig. 4.1.22 Room temperature XRD pattern of precursor powders (a) raw and calcined powders at (b) 800, (c) 1000 (d) 1100. Major phases identified are also shown in the figure.

4.1.4.2 Structural Analysis

The structure of SBTi5 is refined considering orthorhombic space group B2cb as described by Ismunandar *et al*. [24]. Initial atomic co-ordinates, lattice parameters, isotropic atomic displacement parameters also have taken from the reference [24]. The initial lattice parameters taken for refinement are a=5.4647, b=5.4625 and c=48.8515. Final R-factors of the refinement are; Sigma= 2.101, R_{wp} (%) = 7.015, R_b (%) = 5.25 and R_{exp} (%) = 3.339087. Fig. 4.1.23 shows the Rietveld refinement output of sintered $Sr_2Bi_4Ti_5O_{18}$ pellet. The shell parameters are a= 5.4674(3), b= 5.4658(4), c=48.911(8) Å obtained after refinement. March Dollach texture model is used to find out the texture factor in the pellet. The factor for the sintered pellet pattern [Fig. 4.1.23] is 0.49. This indicates that the ceramic is highly textured i.e. there is the preferential growth of (00*l*) plane as shown in Fig. 4.1.23. Table 4.1.6 shows the symmetry, space group, refined lattice parameters and refined Rietveld factors and Orthorhombicity of SBTi5 ceramics.

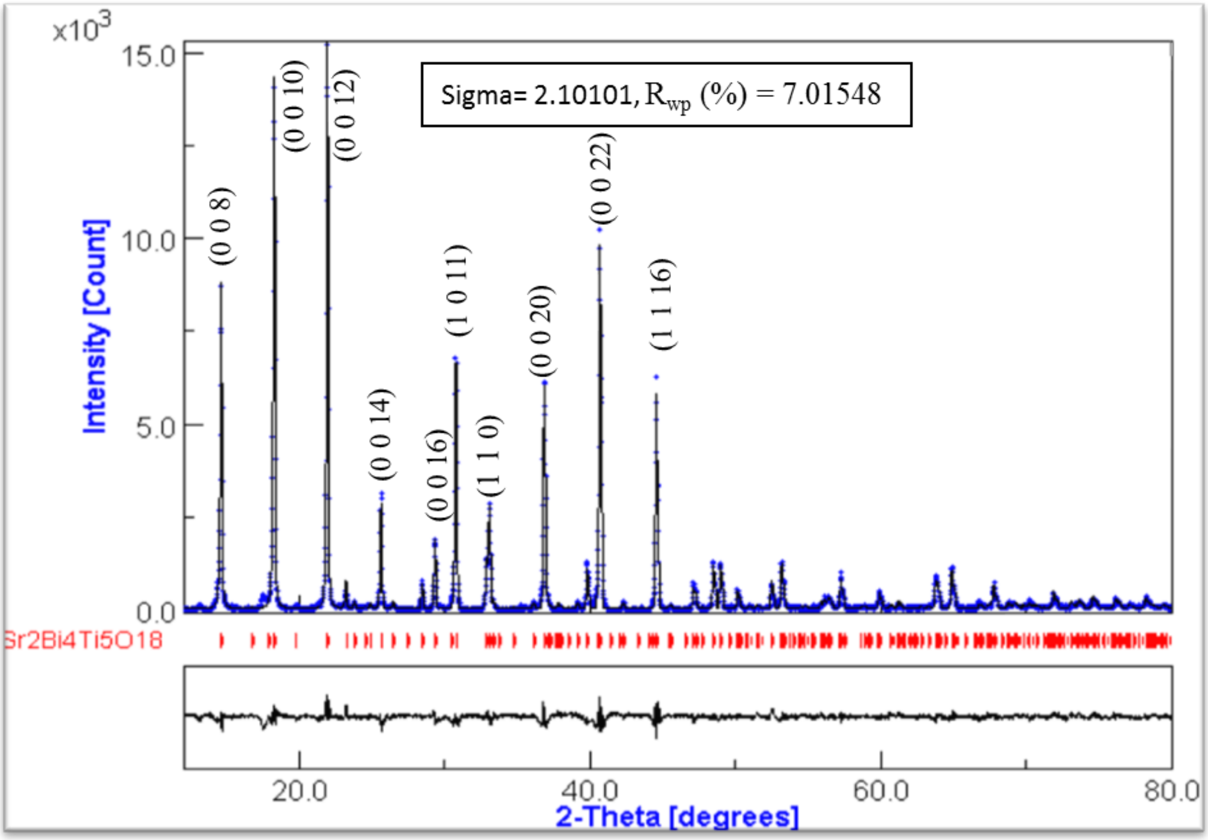

Fig. 4.1.23 Rietveld refinement plot for sintered SBTi5 composite ceramics, showing observed (+), calculated (solid line) XRD profile, their differences in the bottom and position of allowed Bragg reflections (tick marks).

4.1.4.3 Densification Behavior and Microstructural Characteristics

The densification behavior is studied on a pressed pellet. Fig. 4.1.24 compares the non-isothermal shrinkage behavior of the BIT, SBTi4 and SBTi5 powder compacts. The shrinkage of the specimen of BIT starts at about 610^{o}C. More than 94% dense ceramics of BIT is obtained by sintering pellet at 850^{o}C for 4h. For SBTi4 the shrinkage of the specimen starts at about 800^{o}C. Nearly 91% dense ceramics are obtained by sintering pellet at 1150^{o}C for 4h. For SBTi5 the shrinkage of the specimen starts at about 1100^{o}C. Nearly 89% dense ceramics is obtained by sintering pellet at 1230^{o}C for 4h. Fig. 4.1.25 shows plate like grains with preferred orientation, reflecting the highly anisotropic crystal. The grains have the mean diameter of 6 µm and a thickness of about 0.5 µm. The aspect ratio of the grains is in the range of ~12. The comparable data of different layer BLSFs and their surface morphology are listed in the table 4.1.7. These results indicate that the sintering temperature increases with the increase in large number in BLSFs.

Table 4.1.6 Symmetry, space group, refined lattice parameters '*a*', '*b*' and '*c*', *R*-factors, sigma, orthorhombicity of SBTi5 ceramics.

Parameters	**Values**
Symmetry	**Orthorhombic**
Space group	***B*2*cb***
***a* (Å)**	**5.4674(3)**
***b* (Å)**	**5.4658(4)**
***c* (Å)**	**48.911(8)**
R_w (%)	**7.015**
R_b (%)	**5.25**
Sigma	**2.101**
Orthorhombicity	**0.00029**

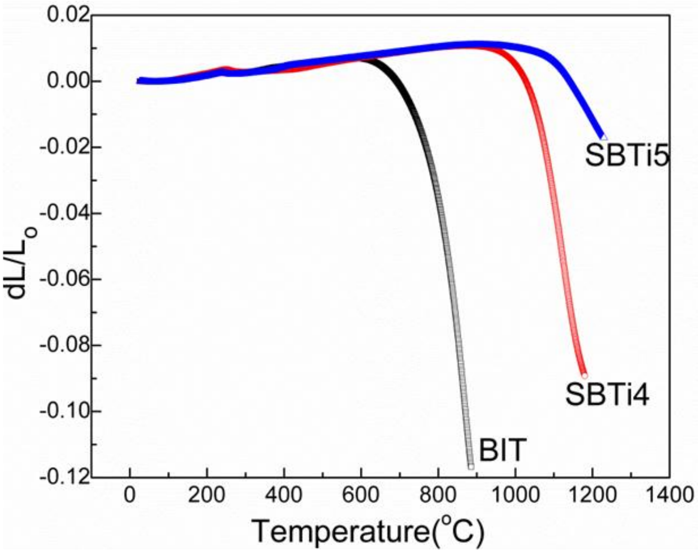

Fig. 4.1.24 Non-isothermal sintering behavior of BIT, SBTi4 and SBTi5 powder compacts.

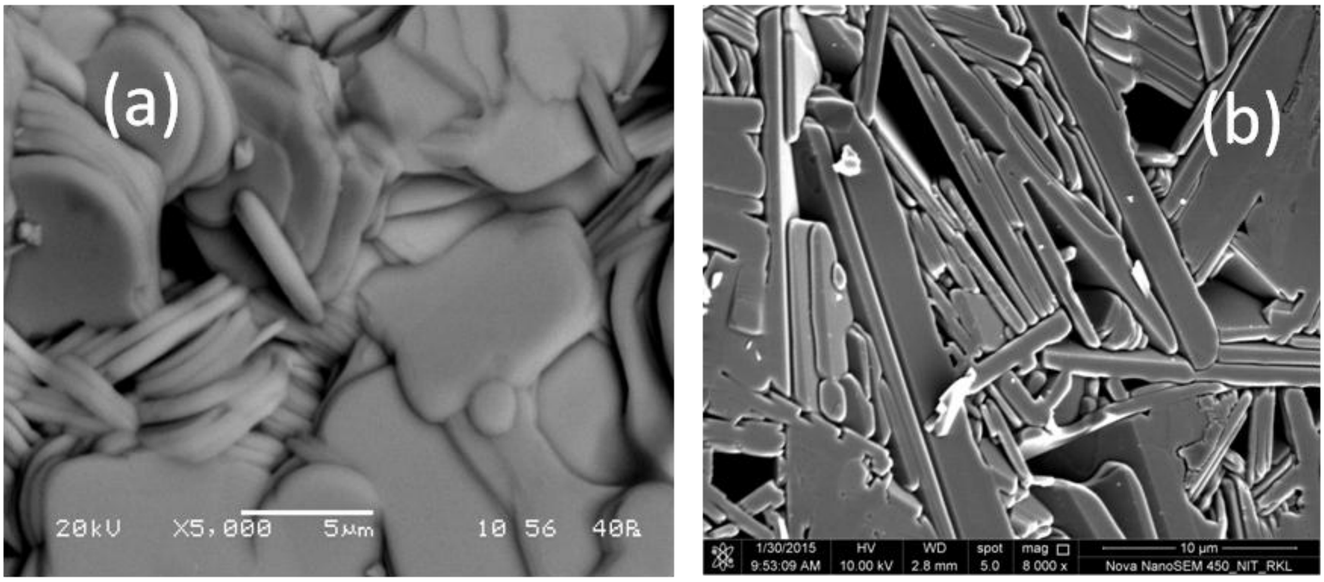

Fig. 4.1.25 SEM micrograph of the SBTi5 pellet surface (a) and freshly broken bulk surface (b).

Table 4.1.7 the length, breadth, thickness and aspect ratio of BIT, SBTi4 and SBTi5 ceramics.

Sample ID	Length (µm)	Breadth(µm)	Thickness(µm)	Aspect Ratio
BIT	2.2	1.2	0.4	5.5
SBTi4	4.1	2.2	0.6	6.7
SBTi5	6.2	4.4	0.5	14.4

4.1.4.4 Dielectric and Diffuse Phase Transition Behavior

Fig. 4.1.26 shows the temperature dependence of the dielectric permittivity (ε') and dielectric loss (tan δ) at various frequencies. Two anomalous peaks appear in this figure at 290^{o}C and 450^{o}C. The temperature of maximum dielectric permittivity is at 290^{o}C. The Curie–Weiss plot for SBTi5 ceramics at 100 kHz is shown in the inset of Fig. 4.1.26. The solid line is the fit to the Curie–Weiss law. The parameters obtained from the linear fit are C = 3.65 × 10^4 ^{o}K and T_θ=533 ^{o}K. The order of magnitude is lower than that of the displacive phase transitions but is of same order as for SrBi$_2$Ta$_2$O$_9$ and SrBi$_2$Nb$_2$O$_9$ reported by AmorIn *et al.* [25-27]. The second peak at 450^{o}C is due to the occurrence of second transition which has also been reported by Ferrer *et al.* [21]. Table 4.1.8 shows the dielectric data of SBTi5 ceramics.

Table 4.1.8 Dielectric, ferroelectric and activation energy (from impedance) of SBTi5 ceramics.

Dielectric properties at 100 kHz		**Polarization hysteresis** (electric field 20kV/cm)	
Room temperature permittivity (ε_{rm})	226	Remnant polarization (2P_r)	2.96µC/cm^2
Room temperature dielectric loss (tan δ)	0.016	Coercive field (2E_c)	17.76kV/cm
Maximum permittivity (ε_m')	1167	C (°K)	3.65x10^4
Dielectric loss at peak (tan δ_m)	0.2832	**Impedance spectroscopy**	
Maximum permittivity temperature (T_c)	290°C	Activation energy E_{ac} (relax time)	1.70 eV
dc conductivity (σ_{dc}) at 500^{o}C	4.35×10^{-9} (Ωcm)$^{-1}$	Activation energy E$_{dc}$ (Cole-Cole plot	1.74 eV

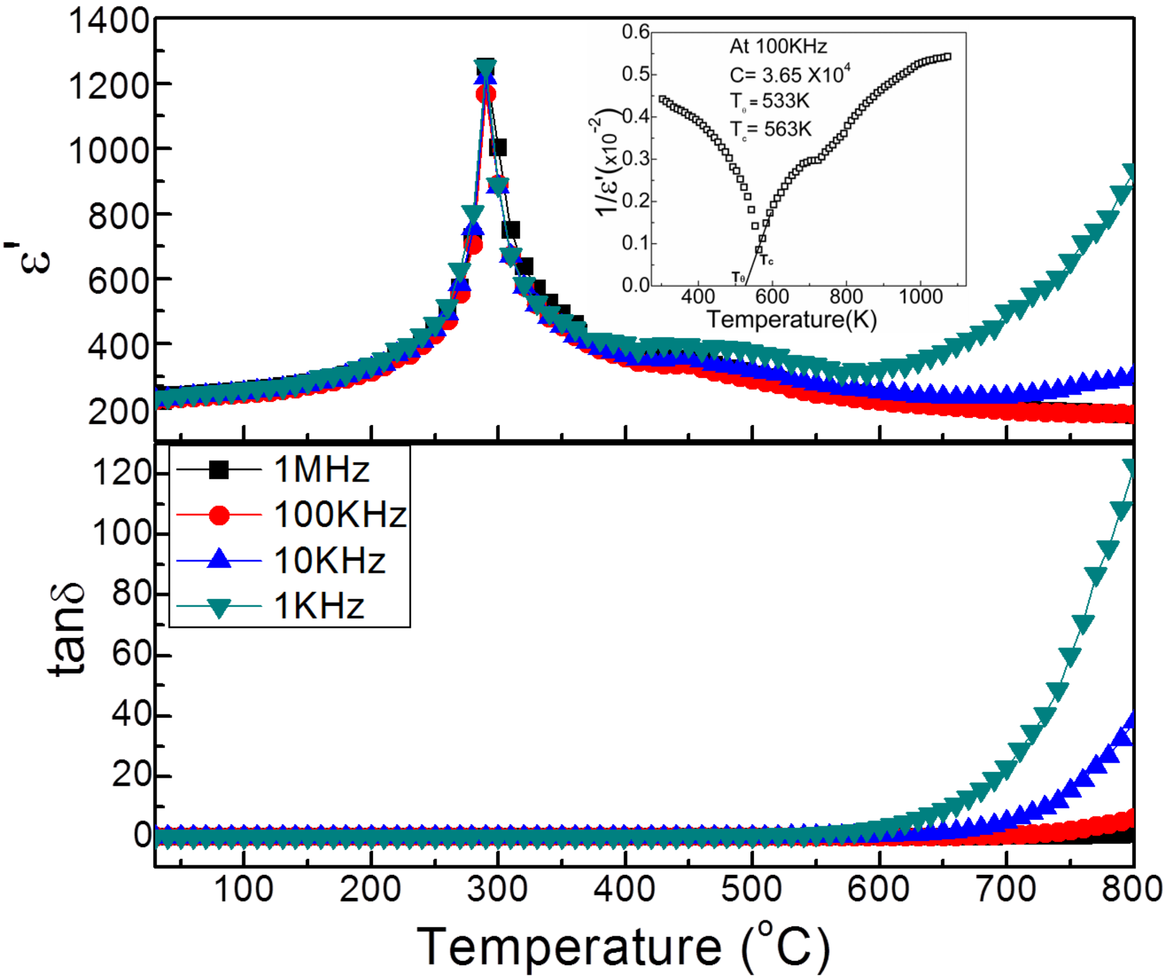

Fig. 4.1.26 Temperature dependence of (a) dielectric constant (ε') and (b) loss (tan δ) at different frequencies of SBTi5. Inset shows the inverse dielectric constant ($1/\varepsilon'$) as a function of temperature at 100 kHz.

4.1.4.5 Impedance Analysis

Fig. 4.1.27 shows the Impedance (Z) spectroscopic plots of Z'' vs frequency, clearly indicating the maxima of Z'' are shifting frequencies with increasing temperature. This type of behavior suggests the process is thermally activated due to of hopping of charge carriers and the relaxation time decreases with temperature. Logarithm of relaxation time (Ln τ) has been plotted against the inverse of temperature in Fig. 4.1.27.

Fig. 4.1.28 shows the complex impedance plots for SBTi5 at various temperatures. The E_a is 1.74eV similar value shown for the material $Sr_2Bi_2Nb_2O_9$-Bi_3TiNbO_9 [28], the activation energy for the formation and hopping of defects. E_a can be calculated from the plot of ln σ_{dc} versus inverse of temperature as is shown in Fig. 4.1.23. Such a high difference in activation energy is due to recrystallization of grains at high temperature (i.e. the large grain size shown in Fig. 4.1.25), hence reduce the concentration of defects [29] also explained by Alberto

Moure *et al.* [28]. E_a value is close to 1.5eV, which is explained by He *et al.* [30], as activation energy for conduction associated with relaxation of oxygen vacancy clusters near the 90° domains.

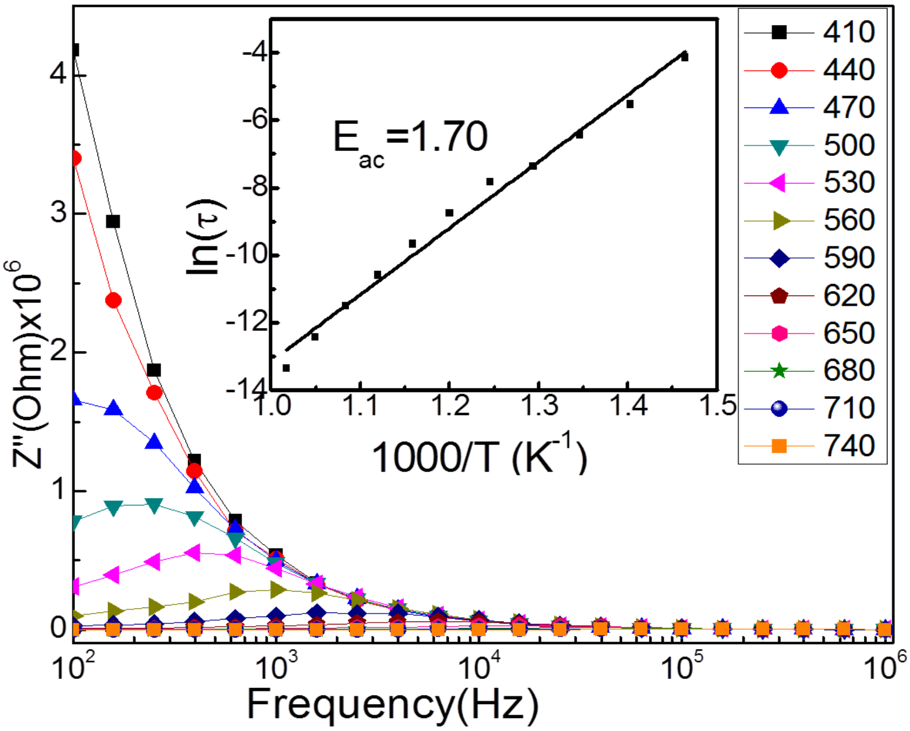

Fig. 4.1.27 Variation of Z″ with frequency. Inset figure shows Arrhenius plot of ac conductivity.

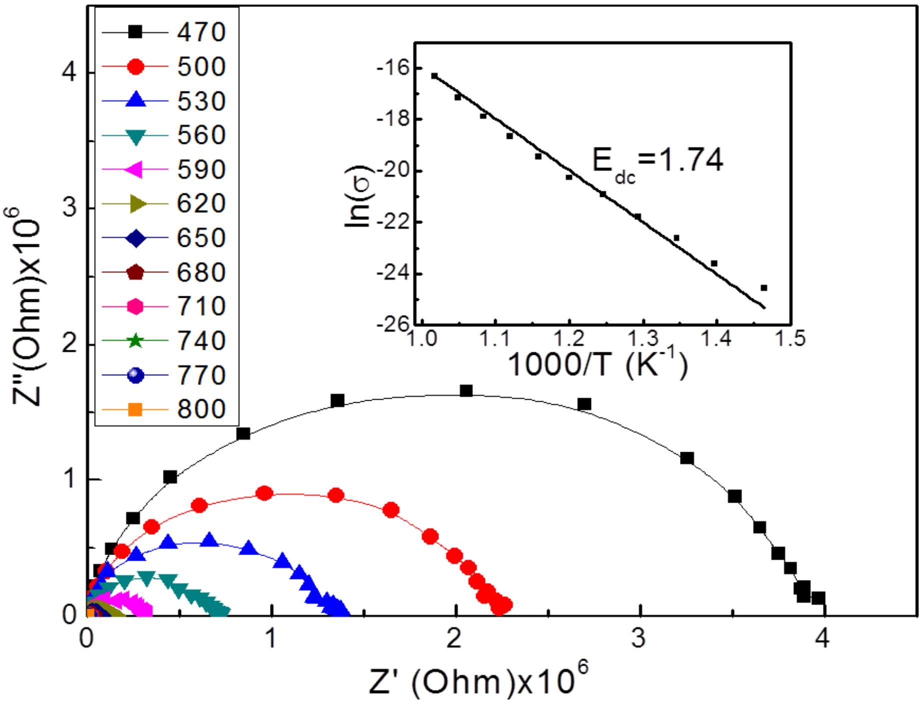

Fig. 4.1.28 Z″ vs Z′ curve for SBT5 at varying temperature. Inset figure shows Arrhenius plot of dc conductivity.

4.2.4.6 Polarization Hysteresis Characteristics

To estimate the ferroelectricity of SBTi5 ceramics, polarization versus electric field measurement on the ceramics is performed at room temperature. Fig. 4.2.29 shows the polarization versus electric field hysteresis loop for BIT, SBTi4 and SBTi5. Remnant polarization (P_r) of SBTi5 is 1.48μC/cm^2 with a coercive field (E_c) 8.9 kV/cm under an applied electric field of 20kV/cm. At the same electric field, the remnant polarization of SBTi5 is higher as compared with that of the BIT and SBTi4. This may be due to the large grain size of SBTi5 and also have low T_c (290°C), helps to saturate with low electric field and temperature. The saturation polarization curve is not achieved for all SrO-Bi_2O_3-TiO_2 based layered system at room temperature with the applied field stated. To saturate the polarization either higher field strength or measurement at elevated temperatures are usually applied. Table 4.1.9 shows the ferroelectric data (P_r and E_c) of BIT, SBTi4 and SBTi5 ceramics in applied electric field 22 KV/cm.

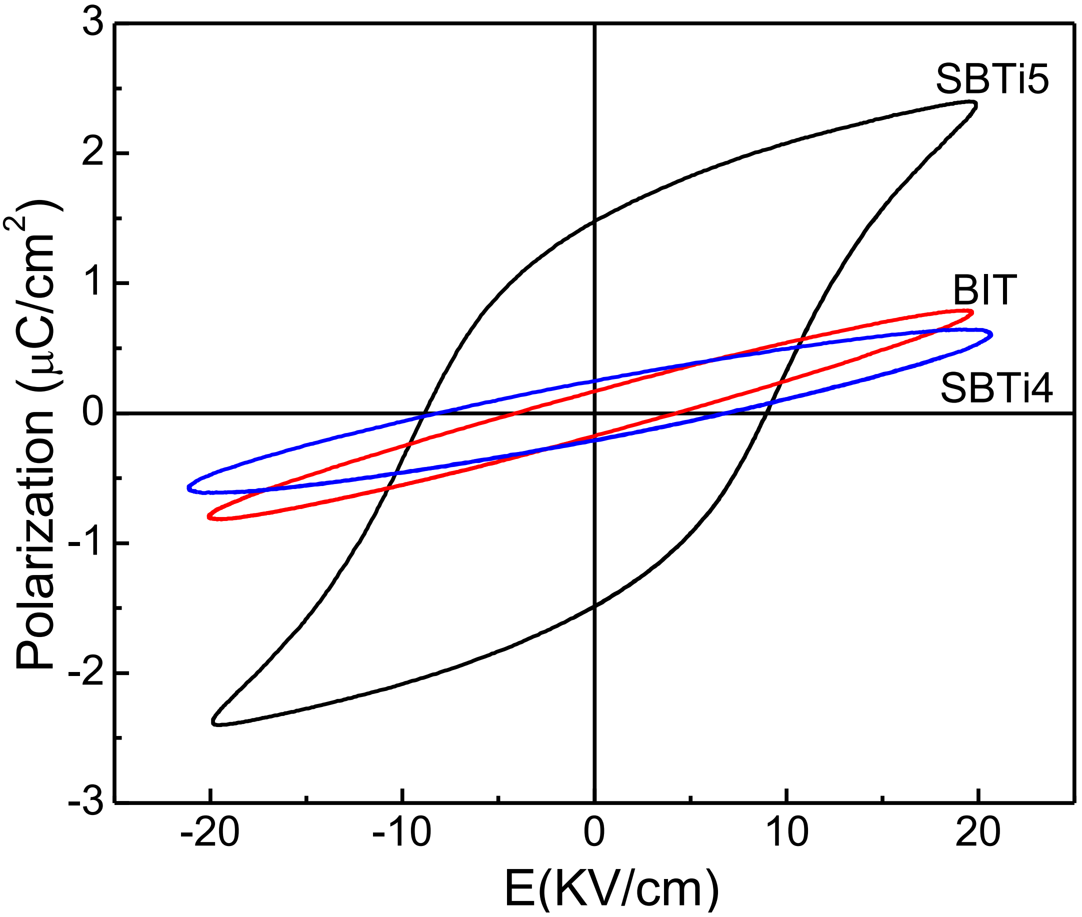

Fig. 4.2.29 Polarization-electric field hysteresis loops of SBTi5 under an applied field of 22KV/cm.

Table 4.1.9 Ferroelectric data ($2P_r$ and E_c) of BIT, SBTi4 and SBTi5 ceramics from hysteresis loop in applied electric field 20 KV/cm.

Sample ID	$2P_r$ (μC/cm^2)	E_c(kV/cm)
BIT	0.34	10.08
SBTi4	0.53	14.78
SBTi5	2.96	17.76

4.1.4.7 Conclusions for SBTi5

SBTi5 powder is successfully synthesized by this modified chemical route at a calcination temperature of 1100°C, highest among three samples studied due to its very long unit cell. SBTi5 powder has highest onset temperature of sintering ~1100^{o}C. All three samples have anisotropic plate like grain morphology and the grain size as well as aspect ratio increases in the order BIT to SBTi4 to SBTi5, as it is difficult to grow along c-direction with increasing unit cell length. However, the Curie temperature (T_c = 290°C), dielectric loss (0.016) are lowest in SBTi5, and E_{ac} (1.70 eV), $2P_r$ (2.96 μC/cm^2) are highest in SBTi5. All these results revealed that the presence of higher amount of Sr in SBTi5 stabilizes oxygen in the structure as SBTi4 and the amount of polarization is high due to higher number of perovskite layer in SBTi5.

4.1.5. References

[1] M.I. Morozov, L.P. Mezentseva, V.V. Gusarov, *Russian Journal of General Chemistry*, 72(2002)1038-1040.

[2] http://www.ing.unitn.it/~maud/

[3] F. Izumi, T. Ikeda, *Mater.Sci.Forum*, 321-324 (2000), 198-203.

[4] C. H. Hervoches and P. Lightfoot, *Chemistry of materials*, 11 (1999) 3359-3364.

[5] E. C. Subbarao, J. Phys. Chem. Solids, 23 (1962) 665-676.

[6] M.E. Lines, A.M. Glass, *Principles and Applications of Ferroelectrics and Related Materials, Claredon Press, Oxford*, 1977, p. 136.

[7] H.S. Shulman, D. Damjanovic, N. Setter, *J. Am. Ceram. Soc.,* 83 (3) (2000) 528-532.

[8] W. Li, D. Su, J. Zhu, Y. Wang, *Sol. Stat. Commun.*, 131 (2004) 189-193.

[9] H.S. Shulman, M. Testorf, D. Damjanovic, N. Setter, *J. Am. Ceram.Soc.*, 79 (1996) 3124-3128.

[10] B. Jimenez, A. Castro, L. Pardo, P. Millan, R. Jimenez, *J. Phys.Chem. Solids*, 62 (2001) 951-958.

[11] M. Villegas, A.C. Caballero, C. Moure, P. Duran, J.F. Fernandez, *J.Am. Ceram. Soc.*, 82 (1999) 2411-2416.

[12] M. Villegas, A.C. Caballero, C. Moure, P. Duran, J.F. Fernandez, *J.Eur. Ceram.Soc.*, 19 (1999) 1183-1186.

[13] J. Hao, W. Bai, W. Li, J. Zhai, *J. Am. Ceram. Soc.*, 95 (2012) 1998-2006.

[14] C. Jiang, K. Zhou, X. Zhou, Z. Li, D. Zhang, *Ceram. Int.*, 41 (2015) 6858-6862.

[15] S. K. Rout, P. K. Barhai, E. Sinha, A. Hussain, W. Kim, *Int. J. Appl. Ceram. Tech.*, 7 (2010) E114-E123.

[16] A. Fouskova, L. E. Cross, *J. Appl. Phys.*, 41 (1970) 2834-2838.

[17] M. Villegas, A. C. Caballero, J. F. Fernandez, *Ferroelectrics*, 267 (2002) 165-173.

[18] M. V. Gelfuso, T. Daniel, A. E. José, *J. Am. Ceram. Soc.*, 82 (1999) 2368-2372.

[19] B.J. Kennedy, Q. Zhou, Ismunandar, Y. Kubota, K. Kato, *J. Solid State Chem.*, 181 (2008) 1377–1386.

[20] S. T. Zhang, C. S. Xiao, A. A. Fang, B. Yang, B. Sun, Y. F. Chen, N. B. Ming, *Appl. Phys. Lett.*, 76 (2000) 3112-3114.

[21] P. Ferrer, M. Alguero, J.E. Iglesias, A. Castro, *J. Eur. Ceram. Soc.*, 27 (2007) 3641–3645.

[22] M. G. A. Ranieri, E. C. Aguiar, M. Cilense, B. D. Stojanovic, A. Z. Simões, J. A. Varela, *Mater. Res. Bull.*, 70 (2015) 20-25.

[23] C. H. Lu, C. H. Wu, *J. Euro. Ceram. Soc.* 22 (2002) 707–714.

[24] Ismunandar, T. Kamiyama, A. Hoshikawa, Q. Zhou, B.J. Kennedy, Y. Kubota, K. Kato, *J. Solid State Chem.*, 177 (2004) 4188–4196.

[25] H. Amorin, R. S. Martins, A. L. Kholkin and M. E. V. Costa, *Ferroelectrics* 320 (2005) 43–50.

[26] H. Amorin, I. K. Bdikin, V. V. Shvartsman, M. E. V. Costa and A. L. Kholkin, *Integrated Ferroelectrics* 68 (2004) 259–268.

[27] H. Amorin, V. V. Shvartsman, A. L. Kholkin, and M. E. V. Costa, *Appl. Phys. Lett.* 85 (2004) 5667-5669.

[28] A. Moure, A. Castro, L. Pardo, *Prog. Sol. State Chem.*, 37 (2009) 15-39.

[29] L. Sagalowicz, F. Chu, P. D. Martin, D. Damjanovic, *J. Appl. Phys.*, 88 (2000) 7258-7263.

[30] L.X. He, C. E. Li, T. G. Chen, Z.Y. Wang, H.X. Yan, *J. Funct. Mater. Devices*, 7 (2001)16.

4.2 Synthesis and Characterization of $Bi_4Ti_3O_{12}$-$SrBi_4Ti_4O_{15}$ Intergrowth and $SrBi_4Ti_4O_{15}$-$Sr_2Bi_4Ti_5O_{18}$ Composite Ceramics

4.2.1 Introduction

Numerous efforts have been made to improve the electrical properties of BLSFs. One useful approach is the formation of intergrowth between two BLSFs. The intergrowth compound is built up by regular stacking of one-half the unit cell of *m*-member structure and one-half the unit cell of (*m*+1)-member structure BLSF along their *c*-axis. For example, $SrBi_8Ti_7O_{27}$ BLSF structure is built up by an intergrowth of one half the unit cell of $Bi_4Ti_3O_{12}$ and one half the unit cell of $SrBi_4Ti_4O_{15}$ structure in the direction of their common *c*-axis. The spontaneous polarization (P_s) of BLSFs arises along ***a*** axis due to the displacement of Bi ion. In addition, the typical 3-layer (*m*=3) BLSF compound $Bi_4Ti_3O_{12}$ (BIT) shows a small P_s along the *c*-axis together with large P_s along *a*-axis. The BLSF with even number of *m* such as $SrBi_4Ti_4O_{15}$ (SBTi4) with *m*=4, shows no polarization along *c*-axis because of mirror symmetry of its orthorhombic crystal structure. Although the BIT has large P_s compared to SBTi4, it suffers from poor insulating properties. In contrast, SBTi4 has sufficiently high insulating properties and $Bi_4Ti_3O_{12}$-$SrBi_4Ti_4O_{15}$ (BIT-SBTi4) intergrowth compound has improved electrical and piezoelectric properties than either of the components.

The 5-layered candidate in this system $Sr_2Bi_4Ti_5O_{18}$ (SBTi5) has been reported as an attractive material for non-volatile ferroelectric memory and piezoelectric applications due to its excellent fatigue-free property. SBTi5 has higher P_r value than that of SBTi4. However, SBTi5 has lower T_c ~267 ^{o}C as compared to 503 ^{o}C of SBTi4. So, the intergrowth between SBTi4-SBTi5 could improve the overall temperature stability of the dielectric properties. Since, there is no report on their intergrowth; one objective is to investigate the possibility of their intergrowth or composite formation.

In the present investigation, the modified oxalate route has been used to synthesize the BIT-SBTi4 and SBTi4-SBTi5 intergrowth/composite, ceramics utilizing TiO_2, Bi-nitrate and Sr-nitrate as raw materials. Both the ceramics have been characterized for their phase formation behaviour, crystal structure, dielectric and ferroelectric behaviours. To the best of our literature review, there is no report yet about the dielectric properties of the composite system SBTi4-SBTi5.

4.2.2 Results and Discussion

(A) Synthesis and Characterization of $Bi_4Ti_3O_{12}$-$SrBi_4Ti_4O_{15}$ Intergrowth

4.2.2.1 Phase formation behavior

To investigate the phase formation behaviour, precursor powder is calcined at different temperatures. Fig. 4.2.1 shows XRD patterns of raw and calcined precursor powders. Raw powder pattern (Fig. 4.2.1 (a)) shows peaks for TiO_2 (PDF No. 78-2486) over amorphous phase background. The amorphous phase may contain Bi- and Sr-oxalate hydrate and/or hydroxide phases. When calcine at 300^oC, the amorphous phases decompose and convert into Sr-bismuth oxide phase $SrBi_2O_4$ (PDF No. 85-2493) and bismuth-oxy-carbonate phase $Bi_2(CO_3)O_2$ (PDF No.01-0884) as indicate in Fig. 4.2.1(b). There may also be formation of Ti-bismuth oxide phase $Bi_{12}TiO_{20}$ (PDF No. 42-0186) as reported earlier [1, 2]. $Bi_{12}TiO_{20}$ phase has not been identified in Fig. 4.2.1 as most of its strongest peaks overlap with those of $SrBi_2O_4$.

These Sr- and Ti-bismuth oxide phases are stable up to 500^oC as shown in Fig 4.2.1(c) and the amount of TiO_2 phase is small at that temperature. BIT phase formation started at 500^oC and it is well developed at 600^oC (Fig 4.2.1(d)). No separate pattern for SBTi4 phase is found. In addition, the amount of Sr-bismuth oxide phase is small at 600^oC. It may be concluded that SBTi4 phase forms solid solution in BIT. The separate pattern of SBTi4 is also absent at 800^oC. The strongest diffraction peak angle near 30^o is found to shift towards higher 2θ angle with increase in the calcinations temperature from 600 to 900^oC. This is due to increasing solid solution formation of SBTi4 with BIT, as the strongest peak of SBTi4 (PDF No. 43-0973) is at higher 2θ angle as compared to that of BIT (PDF No. 73-2181). A single phase BIT-SBTi4 intergrowth, that is $SrBi_8Ti_7O_{27}$ (PDF No. 31-1342), is detected in the powder calcined at 800^oC (Fig 4.2.1(e)). Hence, it may be concluded that the BIT-SBTi4 intergrowth formation started at temperatures as low as 600^oC in this modified oxalate powder synthesis route and a pure intergrowth phase could be obtained at 800^oC, a temperature 100^oC lower than usually needed in conventional solid-state route synthesis of similar intergrowth compound [3]. From this observation, it may be concluded that the BIT-SBTi4 intergrowth is occurring through the reaction:

$$3Bi_4Ti_3O_{12} + 2SrBi_2O_4 + 5TiO_2 \xrightarrow{800^oC} 2SrBi_8Ti_7O_{27} \qquad (4.2.1)$$

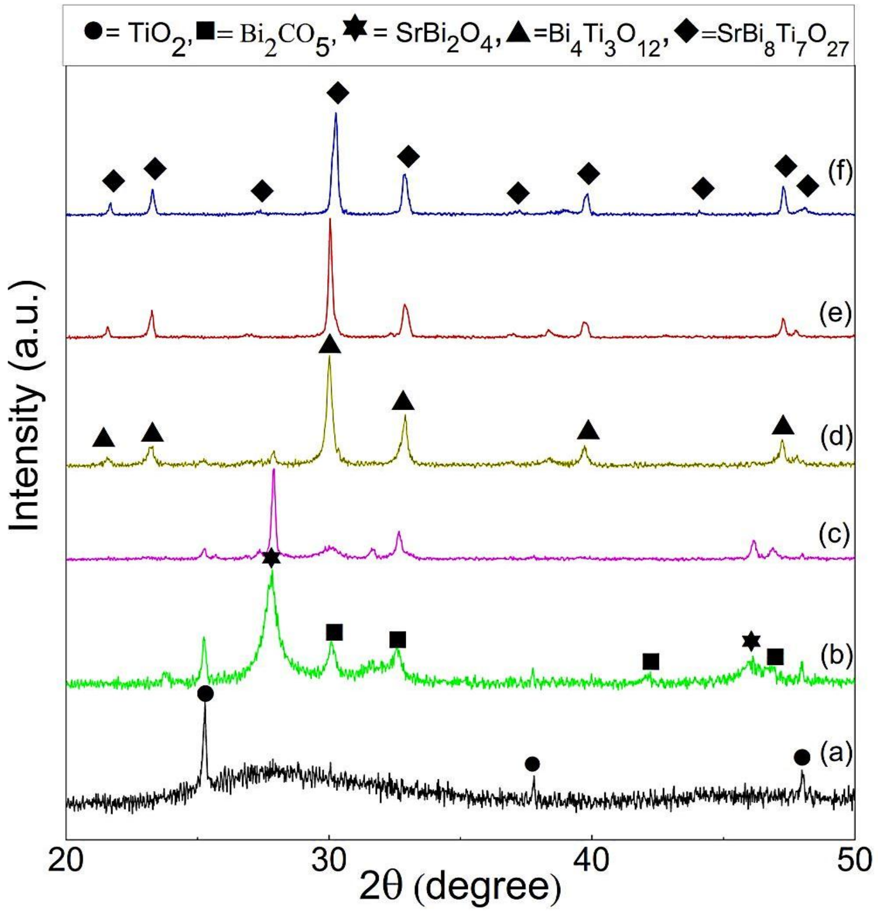

Fig. 4.2.1 Room temperature XRD pattern of (a) precursor raw powder and calcined powders at temperature (b) 300°C, (c) 500°C, (d) 600°C, (e) 700°C and (f) 800°C. Major phases identified are shown in the figure.

4.2.2.2 Structural Analysis

The lattice parameters of BIT-SBTi4 intergrowth compound are refined by Rietveld method using MAUD program [4], considering orthorhombic space group *I*2*cm* (SG N^o 46: -*cba*) as reported by Tellier *et al*. [5] for the similar intergrowth compound $PbBi_8Ti_7O_{27}$. However, the space group requires a doubling of the *c*-parameter ~ 37 Å. The initial atomic co-ordinates, lattice parameters, isotropic atomic displacement parameters for the refinement are taken from the same reference. The refinement rapidly converges due to the selection of the appropriate structural model. Fig 4.2.2 depicts the refinement results and Table 4.2.1 shows the refinement data. The calculated pattern fits fairly well with the observed data. Final R-factors and lattice parameters are, R_{wp} = 6.78, GOF = 2.1 and a = 5.4408(3) Å, b = 5.4505(1) Å, c = 74.085(4) Å. The cell parameters are similar with values reported previously for BIT-CaBTi4 intergrowth [6]. The *c*-parameter is close to the sum of *c*-parameters of BIT (32.84 Å) and SBTi4 (40.94 Å). The lattice parameters slightly increased as compared to BIT and SBTi4, which may be due to the crystal unit cell mismatch and stresses generated in intergrowth ceramics. Refined atomic coordinated are presented in Annexure-I.

Table 4.2.1 Symmetry, Space group, refined lattice parameters '*a*', '*b*' and '*c*', *R*-factors, Sigma, Orthorhombicity of BIT-SBTi4 ceramics.

Parameters	**Values**
Symmetry	Orthorhombic
Space group	*I2cm*
a (Å)	5.4408(3)
b (Å)	5.4505(1)
c (Å)	74.085(4)
R_w (%)	6.78
R_b (%)	3.21
Sigma	2.1
Orthorhombicity	0.0018

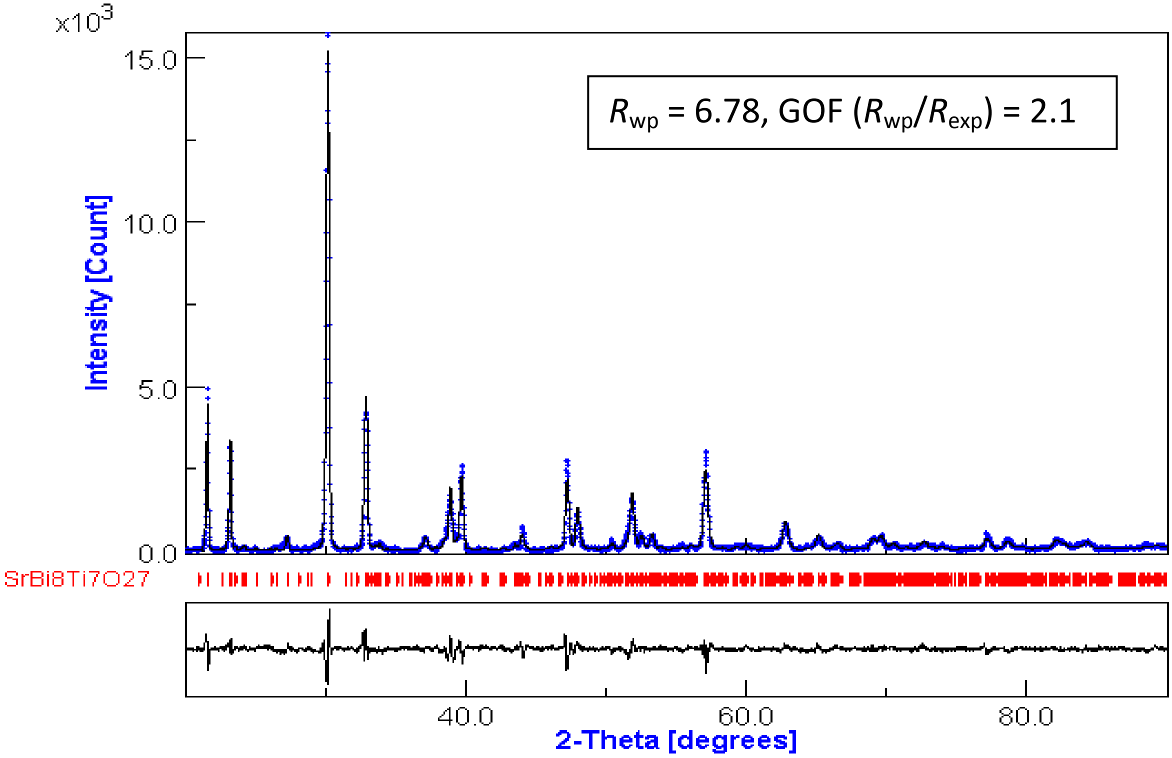

Fig. 4.2.2 Rietveld refinement plot for BIT-SBTi4 intergrowth, showing observed (+), calculated (solid line) XRD profile, their differences in the bottom and position of allowed Bragg reflections (tick marks).

4.2.2.3 Densification Behavior

The densification behavior of BIT-SBTi4 powder is studied on a pressed pellet. Fig. 4.2.3 depicts the shrinkage behavior with temperature of the intergrowth ceramics and of the individual BIT, SBTi4 ceramics. All ceramics show lower shrinkage during non-isothermal sintering in dilatometer. The lower shrinkage may be due to the flaky type grains of the ceramics. Another problem is the partial melting of samples at higher temperature during the test. This may be due to the presence of ~5% excess Bi_2O_3, used to compensate for Bi volatilization loss. The intergrowth ceramics shows an intermediate onset temperature and sintering behavior between two pure ceramics BIT and SBTi4. Also the intergrowth shows two different rates of shrinkages, first starting at 620 ^{o}C with a moderate rate and the second starts at 820 ^{o}C with an increased rate. The moderate rate between 620 to 820 ^{o}C may correspond to the rearrangement of grains [7] and fractional sintering of the composite. The increased rate above 820 ^{o}C may be owing to the formation of liquid phase at higher temperature. The BIT-SBTi4 ceramics are finally sintered at 1150^{o}C and the density obtained was about 93% of theoretical density.

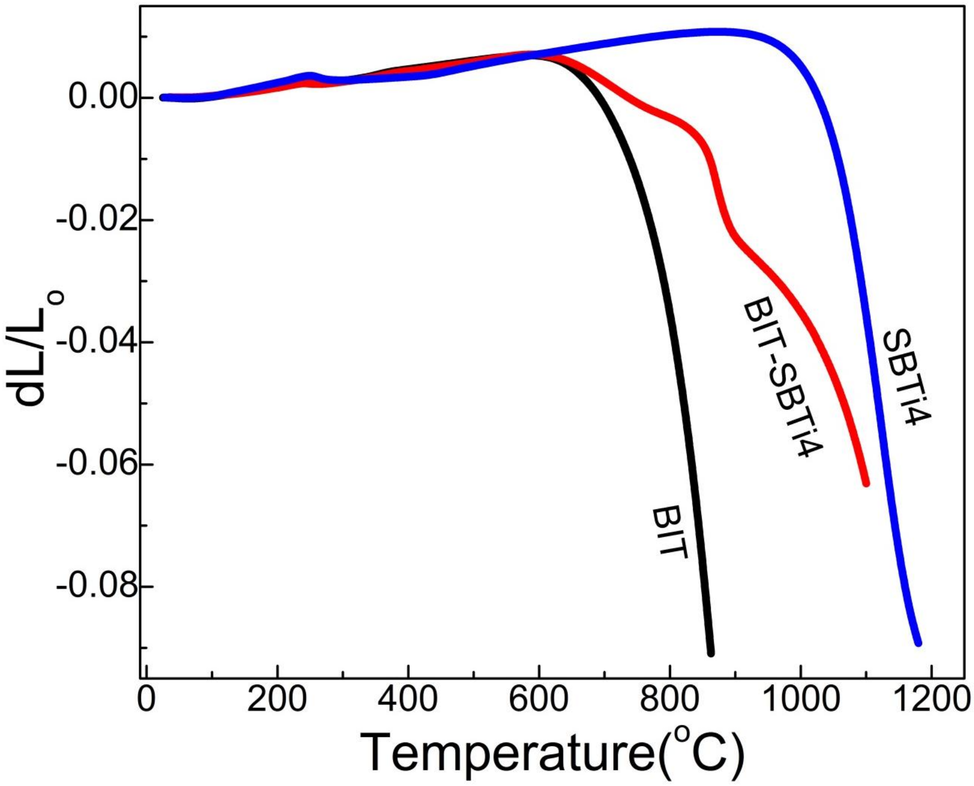

Fig. 4.2.3 Shrinkage behaviour with temperature for pure BIT, SBTi4 and BIT-SBTi4 intergrowth ceramics.

4.2.2.4 Microstructural Characteristics

Fig. 4.2.4 shows the microstructure of the as-sintered ceramics of BIT-SBTi4 pellets. Microstructure shows plate like grains with random orientation. The average edge length of the plate like grains is in between 1-3µm and a thickness of about 0.3 µm. The aspect ratio of the grains, which is the ratio between the largest to the smallest dimension, is in the range 4-10. The plate like grain formation is a typical characteristic of BLSFs. They have highly anisotropic crystal structure with a lower surface energy of {00*l*} planes which results an easy grain growth in the *a*–*b* plane and thus develop a plate-like morphology. (0 0 *l*) plane possess lower surface energy due to anisotropic crystal structure of BLSF where (0 0 *l*) planes lies in the *ab*-planes of the structure [12-13]. In BLSFs, *a* and *b* lattice parameters are only about 5Å and are shorter than the lattice parameter *c*, which is 7-9 times longer than *a* and *b* parameters. So arrangement of atoms to form the *ab*-plane requires less energy compares to other plane.

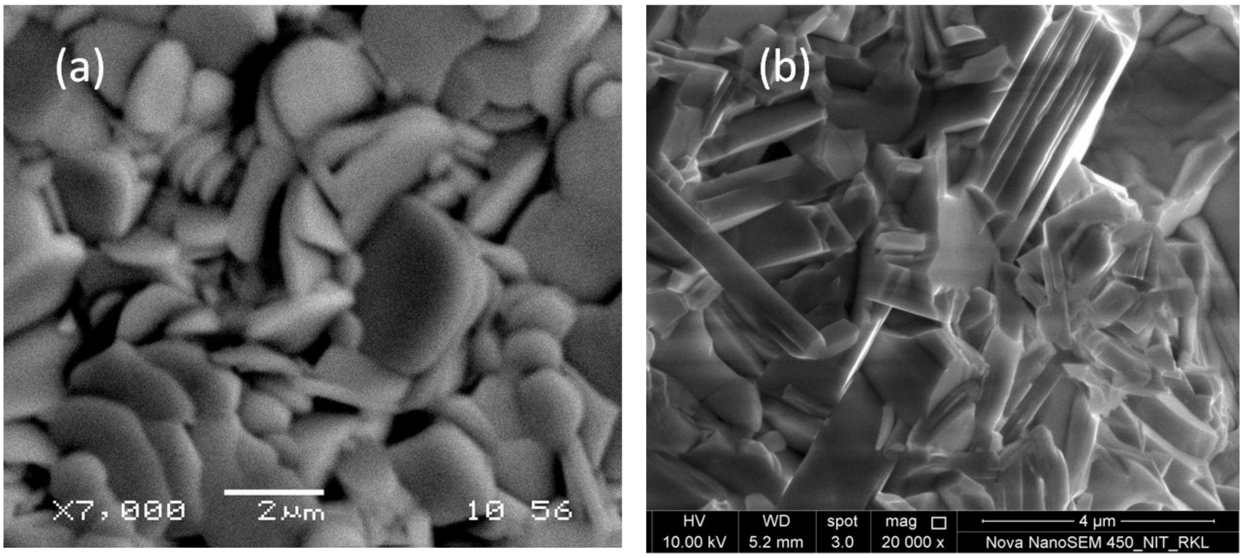

Fig. 4.2.4 SEM micrograph of the BIT-SBTi4 intergrowth pellet surface (a) and freshly broken bulk surface (b).

4.2.2.5 Dielectric and Phase Transition Behavior

Fig. 4.2.5 shows the temperature dependence of the dielectric constant (ε') and dielectric loss ($\tan\delta$) at various frequencies. T_c of BIT-SBTi4 is at 610^{o}C and is frequency independent. This indicates that BIT-SBTi4 is a normal ferroelectric. The dielectric-temperature anomaly is due to the transformation from ferroelectric to paraelectric phase of the intergrowth BLSF. The inset of Fig 4.2.5 shows comparison of T_c of BIT-SBTi4 with those of pure BIT and SBTi4 respectively. T_c of BIT and SBTi4 are 670 and 530^{o}C respectively and that (610^{o}C) for their intergrowth is about in the middle of BIT and SBTi4. This agrees well with the T_c reported previously [8]. This phenomena again indicates that BIT and SBTi4 are not present separately, rather they formed a homogeneous solid solution intergrowth. The dielectric losses increase with increase in temperature above 500^{o}C. This may be due to the increase in (thermally activated) electrical conductivity at high temperature.

Table 4.2.2 Dielectric, ferroelectric and activation energy (from impedance) of BIT-SBTi4 ceramics.

Dielectric properties at 100 kHz		**Polarization hysteresis** (electric field 20kV/cm)	
Room temperature permittivity (ε_{rm})	200	Remnant polarization ($2P_r$)	0.77μC/cm^2
Room temperature dielectric loss (tan δ)	0.014	Coercive field (E_c)	4.18 kV/cm
Maximum permittivity (ε_m')	1265		
Dielectric loss at peak (tan δ_m)	0.5775	**Impedance spectroscopy**	
Maximum permittivity temperature (T_m)	610°C	Activation energy E_{ac} (relax time)	1.6 eV
dc conductivity (σ_{dc}) at 500^{o}C	1.788×10^{-6} $(\Omega cm)^{-1}$	Activation energy E_{dc} (Cole-Cole plot	1.2 eV

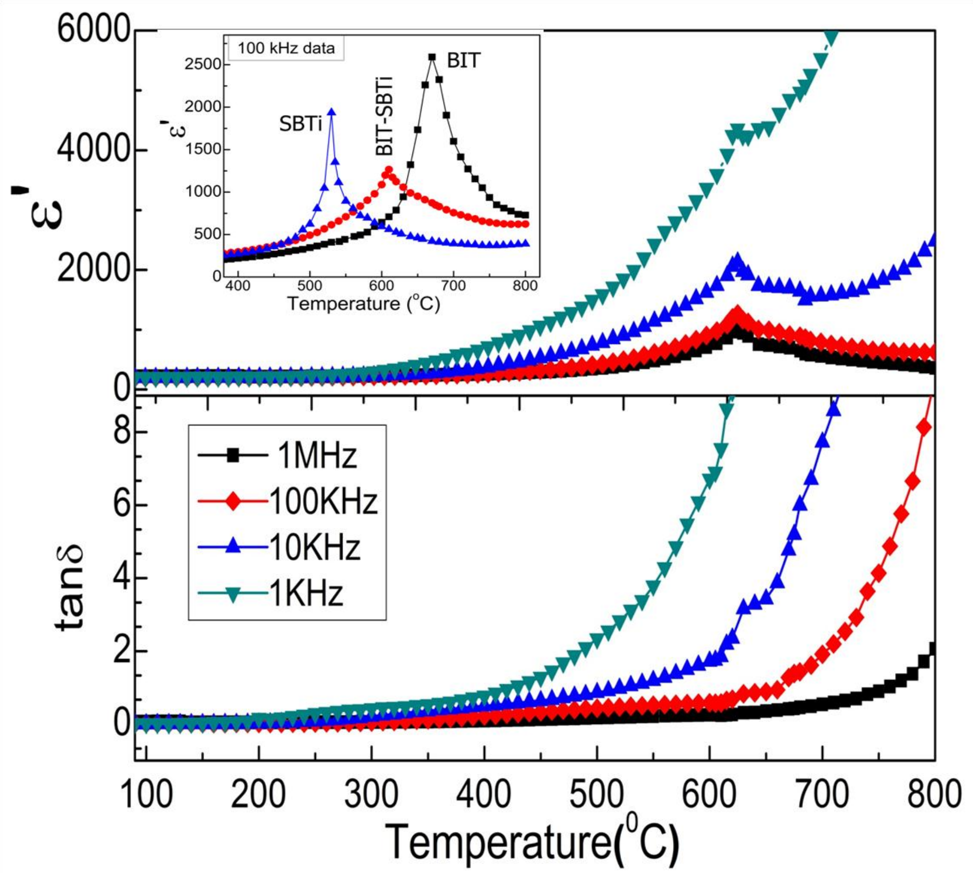

Fig. 4.2.5 Temperature dependence of dielectric constant (ε') and loss (*tan* δ) of BIT-SBTi4 at different frequencies. Inset shows the temperature dependence of dielectric constant of BIT, SBTi4 and their intergrowth BIT-SBTi4 at 100 kHz.

Fig. 4.2.6 shows the frequency dependence of permittivity of BIT, SBTi4 and BIT-SBTi4 intergrowth ceramics. BIT shows the highest frequency dependence of permittivity and loss. The SBTi4 and intergrowth ceramics have highly stable permittivity and losses with frequency. The BIT-SBTi4 intergrowth has $\varepsilon' \sim 200$ and tan $\delta \sim 0.002$ at room temperature and in the frequency range 1 kHz to 1 MHz. So, it is very promising for high frequency applications.

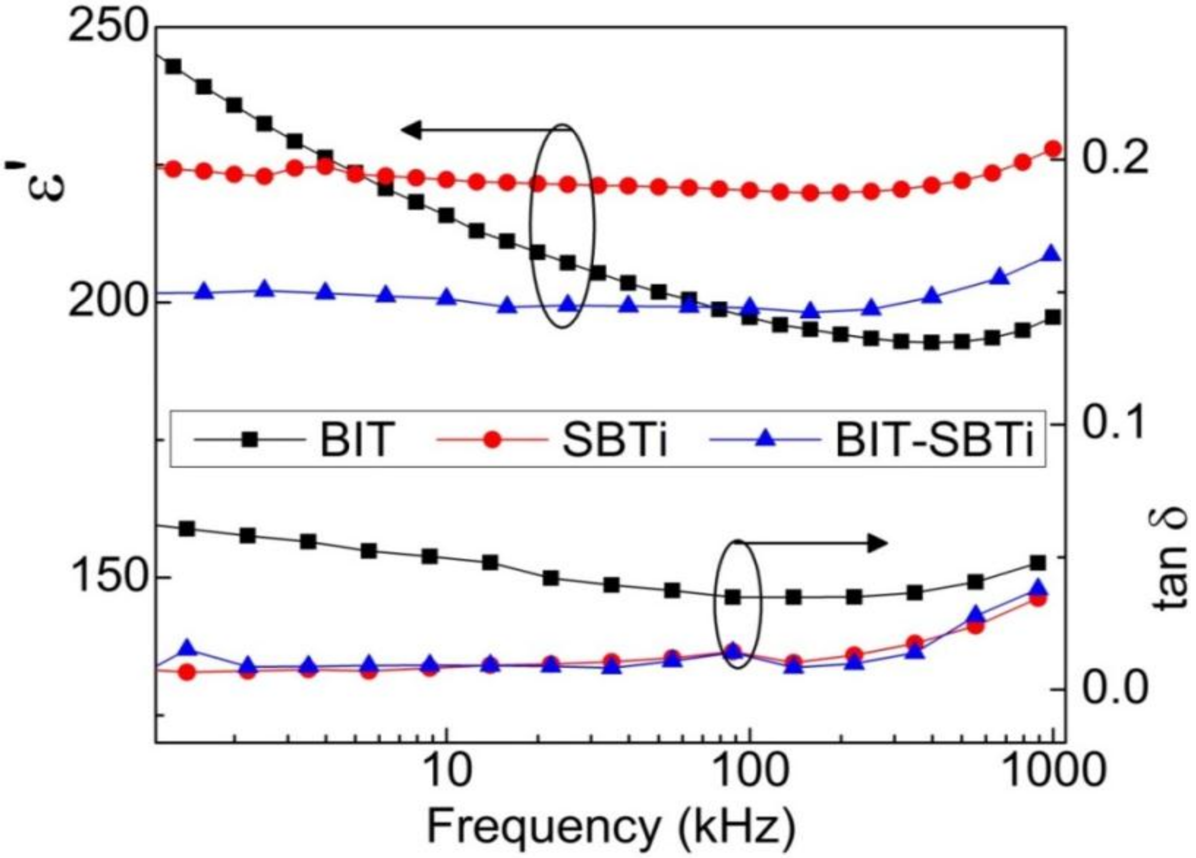

Fig. 4.2.6 Frequency dependence of dielectric constant and loss of BIT, SBTi4 and BIT-SBTi4 intergrowth ceramics at room temperature.

4.2.2.6 Impedance Spectroscopy

Fig. 4.2.7 shows the Z'' versus frequency plot. The value of τ is calculated for various temperatures using Eq. 4.1.9 and is found to decrease with increase in temperature. Inset figure shows the plot of ln (τ) versus 1000/T. The slope of the linear fit gives the E_{ac} values. E_a is 1.6 eV, which shows the high energy required for the hopping of charge carriers indicating that the conductivity of the system decreased or resistivity increased. These values are much high in comparison to that of BIT (~1.10 eV) but are approximately equal to that seen for SBTi4 (~1.62 eV).

Fig. 4.2.8 shows the complex plane impedance plot. The figure shows a single arc which is attributed to the contribution from the bulk of the ceramics. In order to determine the R_{tot} and C parameters, an equivalent circuit of parallel resistance and capacitance is found. In accordance with the previous chapters, the total resistance and capacitance are calculated. Using Eq. 4.1.5, the *dc* conductivity of the sample at various temperatures is determined based on the above calculated R_{tot}. The *dc* conductivity value increases with the increase in temperature. The *dc* conductivity is of the order $10^{-6}\ \Omega^{-1}cm^{-1}$ at 500°C which is the same as BIT and higher than the SBTi4 of $10^{-7}\ \Omega^{-1}cm^{-1}$. The inset figure in Fig. 4.2.8 shows the plot of ln (σ) versus 1000/T. The slope of the linear fit gives the E_{dc} values. E_{dc} was 1.20 eV, which is less compared to that of SBTi4 (~1.62 eV) and more than BIT (~1.06 eV).

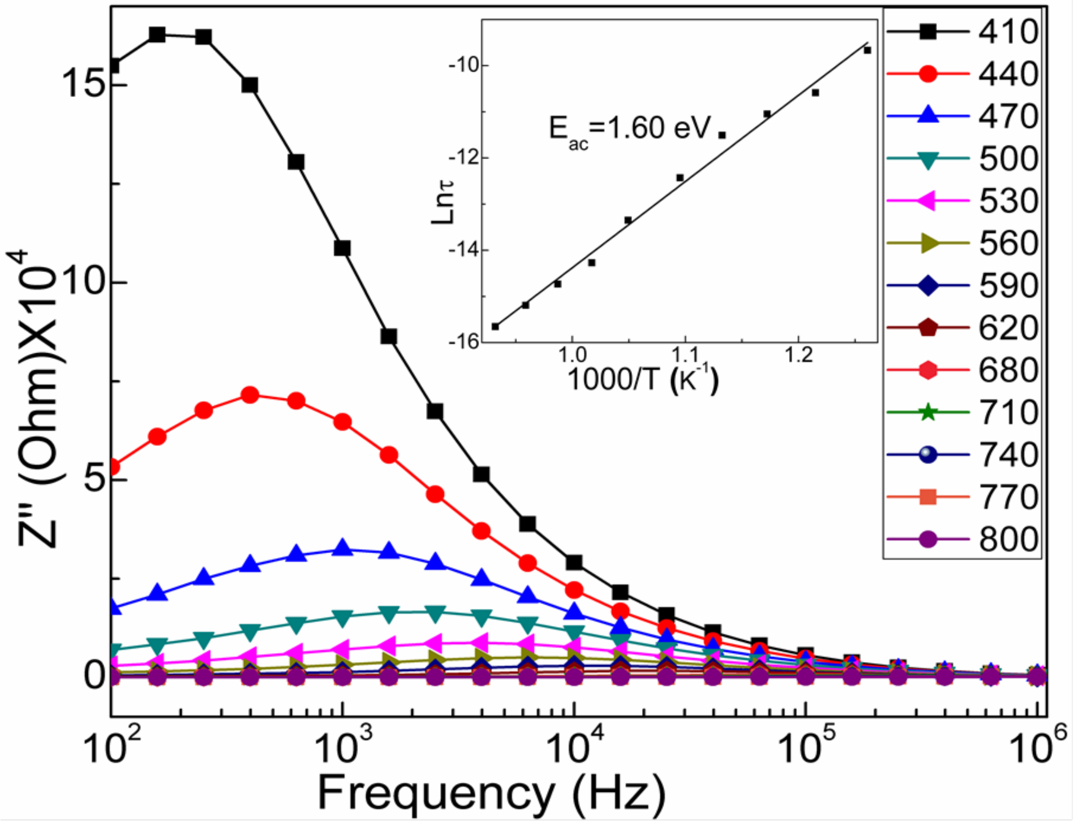

Fig. 4.2.7 Variation of Z″ with frequency of BIT-SBTi4. Inset figure shows Arrhenius plot of ac conductivity.

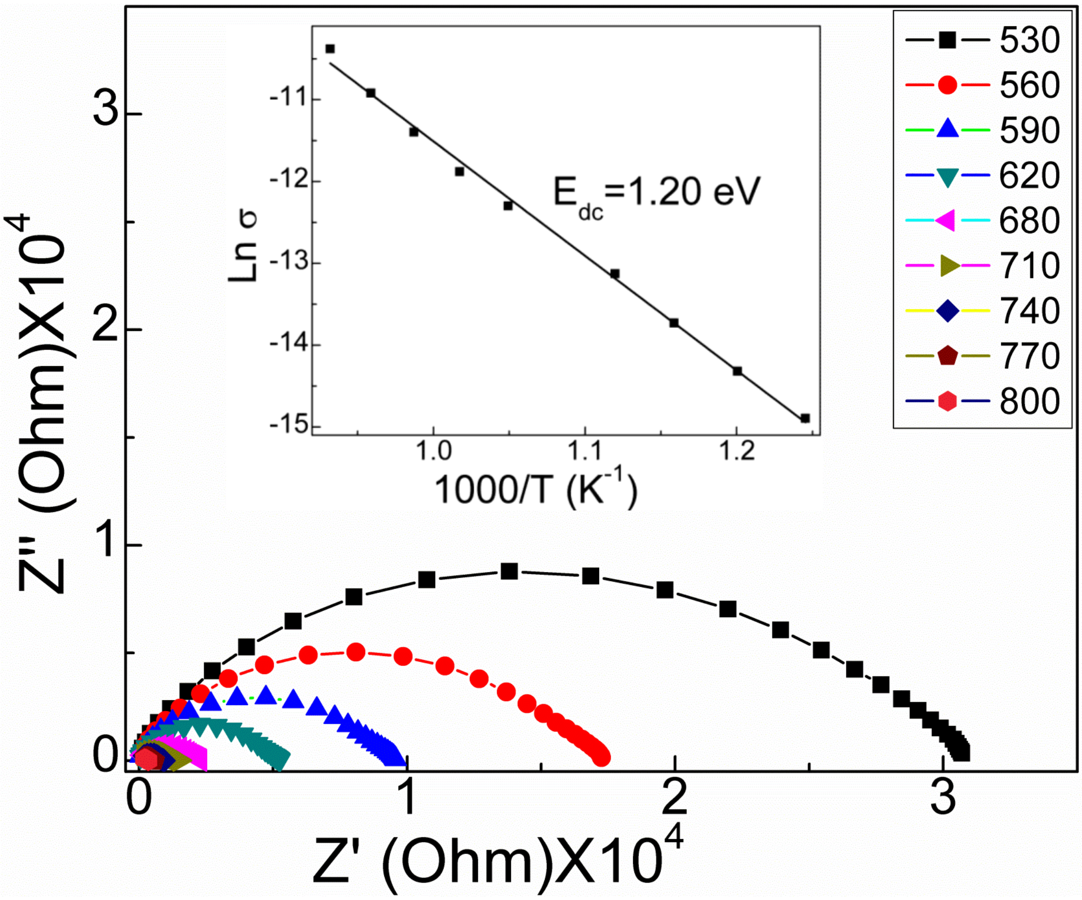

Fig. 4.2.8 Complex impedance plot of BIT-SBTi4. Inset figure shows Arrhenius plot of dc conductivity.

4.2.2.7 Polarization Hysteresis Characteristics

Fig. 4.2.9 presents the polarization-electric field (P-E) hysteresis loop measured at room temperature for BIT-SBTi4 intergrowth, pure BIT and pure SBTi4, respectively. The hysteresis loops are not saturated and minor loops are obtained due to the limitation of the applied electric field of the instrument. However, even in minor loop, the $2P_r$ of BIT-SBTi4 is larger than those of BIT or SBTi4. This indicates that the spontaneous polarization of BIT-SBTi4 intergrowth is larger than their individual components. As reported previously [8], the larger P_r in BIT-SBTi4 may be attributed to the displacement of Bi ion in the Bi_2O_2 layer caused by the lattice mismatch between BIT and SBTi4 blocks in the intergrowth ceramics.

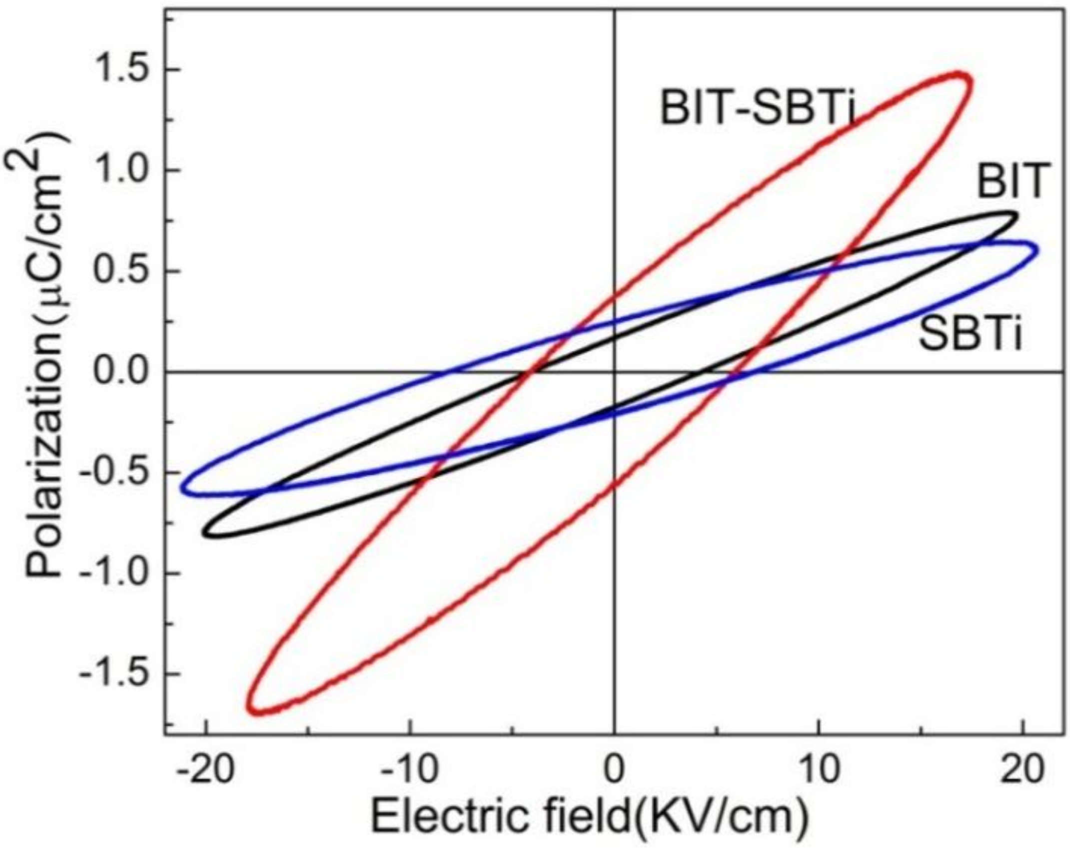

Fig. 4.2.9 P-E hysteresis loops for BIT, SBTi and BIT-SBTi4 intergrowth ceramics.

4.2.2.8 Conclusion

A pure phase BIT-SBTi4 intergrowth ferroelectric has been successfully synthesized through modified oxalate synthesis route at a temperature as low as 800^{o}C. The Rietveld analysis showed that there is increase in the lattice parameters due to the crystal structure mismatch and stresses generated in intergrowth ceramics. Dielectric measurement revealed that the T_c of BIT-SBTi4 is at 610^{o}C and the room temperature ε' ~ 200, tan δ ~ 0.002 in the frequency range 1 kHz to 1 MHz. The intergrowth ferroelectric showed a larger $2P_r$ than their constituents BIT and SBTi4. All these results suggest that this modified oxalate route may be a better process for commercial application.

(B) Synthesis and Characterization of $SrBi_4Ti_4O_{15}$-$Sr_2Bi_4Ti_5O_{18}$ Composite Ceramics

4.2.2.9 Phase formation behavior

SBTi4 and SBTi5 phases are synthesized simultaneously in a mixed precursor powder to investigate the possibility of their intergrowth formation in the composite. Phase formation sequence with calcination temperature is studied through XRD analysis (Fig. 4.2.10). The XRD pattern of raw precursor powder (Fig. 4.2.10 (a)) shows the presence of TiO_2 (PDF No. 78-2486), Sr-oxalate hydrate (PDF No. 20-1204) and some amorphous phases. The amorphous phase may contain Bi-oxalate and/or hydroxide phases. 800^{o}C calcined powder (Fig. 4.2.10(b)) shows BIT (PDF No. 73-2181) and other phases including $SrTiO_3$ (ST) (PDF No. 79-0174) and $SrBi_8Ti_7O_{27}$ (PDF No. 31-1342). As described earlier that BIT-SBTi4 intergrowth compound ($SrBi_8Ti_7O_{27}$) can be synthesized. The intermediate phase BIT first reacts with ST to form SBTi4 and then BIT reacts with SBTi4 to form $SrBi_8Ti_7O_{27}$ through the reactions:

$$Bi_4Ti_3O_{12} + SrTiO_3 \rightarrow SrBi_4Ti_4O_{15} \qquad (4.2.2)$$

$$Bi_4Ti_3O_{12} + SrBi_4Ti_4O_{15} \rightarrow SrBi_8Ti_7O_{27} \qquad (4.2.3)$$

The 900^{o}C calcined powder (Fig. 4.2.10 (c)) shows mainly SBTi4 phase. With the increase in calcination temperature from 800 to 900^{o}C, the strongest diffraction peak angle near 30^{o} has shifted towards higher 2θ angle and the amount of ST phase decreases. This is caused by the transformation of the major part of BIT to SBTi4 through the reaction (4.2.2). Finally, two separate phases SBTi4 and SBTi5 are identified in 1100^{o}C calcined powder (Fig. 4.2.10(d)). From this observation, it may be concluded that the SBTi5 phase is forming through the reaction:

$$SrBi_4Ti_4O_{15} + SrTiO_3 \rightarrow Sr_2Bi_4Ti_5O_{18} \qquad (4.2.4)$$

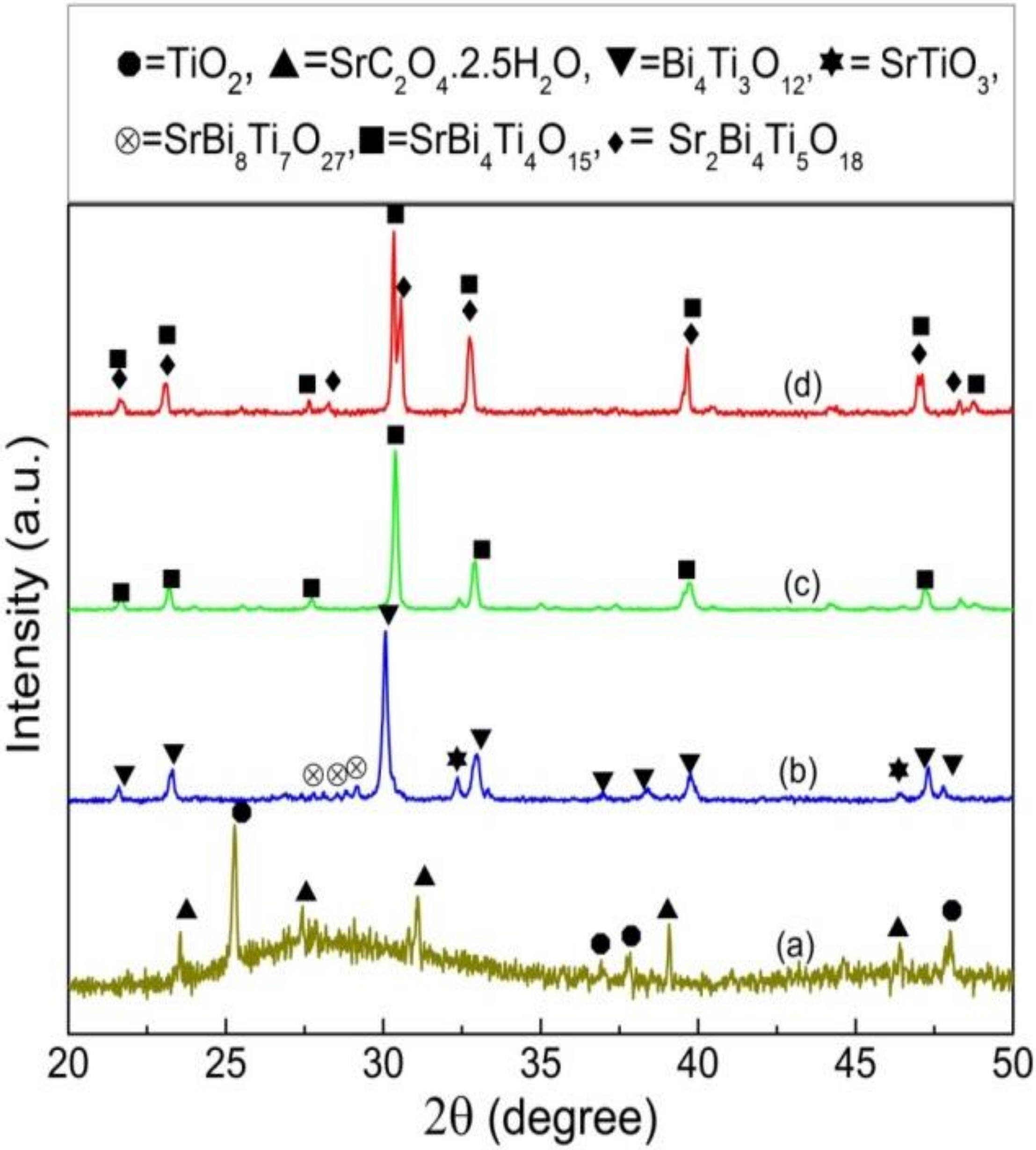

Fig. 4.2.10 Room temperature XRD pattern of SBTi4-SBTi5 composite ceramic (a) precursor raw powder and precursor powder calcined at (b) 800, (c) 900 and (d) 1100°C. Major phases identified are shown at the top of the figure.

The splitting of the strongest diffraction peak near 30° in Fig 4.2.10(d) indicates that SBTi4 and SBTi5 phases are not able to form a regular and long range intergrowth structure. The precursor powder is finally calcined at 1100°C for 4 h to obtain SBTi4-SBTi5 composite powder.

4.2.2.10 Structural Analysis

The lattice parameters of SBTi4 and SBTi5 in the composite ceramics are determined through Rietveld refinement of the XRD patterns. The refinement output is shown in Fig. 4.2.11. One prominent observation is the increase in lattice parameters of both the compounds. The final refined parameters are shown in Table 4.2.3. There is approximately 2 to 2.5% increases in the lattice parameter values compared to the values reported earlier [9, 10]. This may be resulting from the development of disordered crystal structure of both the compounds since they grow in presence of one another.

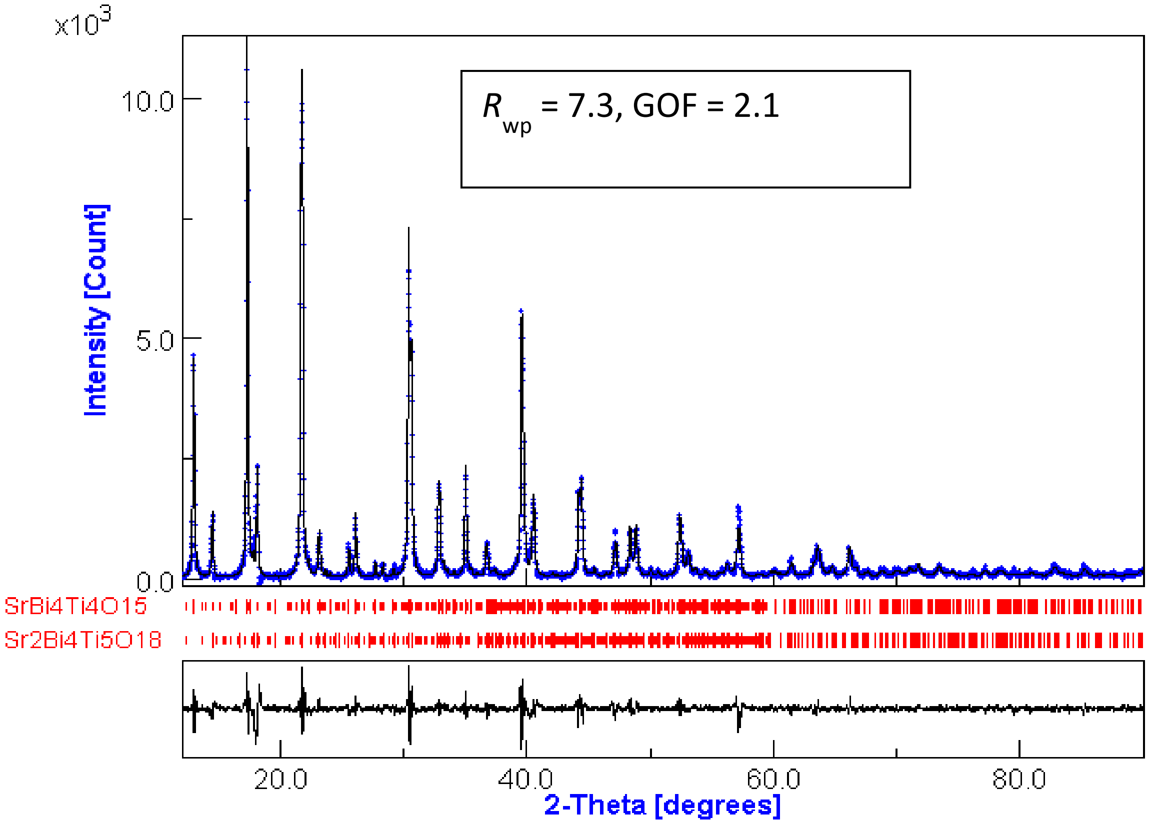

Fig 4.2.11 Rietveld refinement plot for sintered SBTi4-SBTi5 composite ceramic pellets, showing observed (+), calculated (solid line) XRD profile, their differences in the bottom and the position of allowed Bragg reflections (tick marks) for the two phases.

For structure refinement, SBTi4 and SBTi5 structures are considered orthorhombic with space group $A2_1am$ and $B2eb$, respectively [9, 10]. Initial lattice parameters and atomic coordinates of two structures are also taken from the literature. The final refinement parameters, lattice parameters, volume of unit cell, and March-Dollase texture factor are shown in Table 4.2.3.

The refinement parameters for sintered pellet are; R_{wp} = 7.3 and Goodness of Fit (GOF) = 2.1. The R_{wp}-factor is higher than that of the powder sample (Table 4.2.3). This is due to the problem of modeling the shape of some reflections (Fig 4.2.11). There is little anisotropic peak-base broadening in the sintered ceramics, which may be caused by a consequence of stacking faults along the *c*-axis of two structures. The refined lattice parameters of two structures (Table 4.2.3) are larger than the values obtained in their powder specimen and those reported previously by Kenedy *et al.* [9, 10]. The unit cell volume of two structures (Table 4.2.3) increased by about 4% upon sintering. This may be result from the increased deformation of their crystal structure with sintering. The March-Dollase texture factor evaluated through the Rietveld refinement also changes upon sintering. In the case of composite powder, the texture factor of the value is equal to 1 (one) due to the complete random distribution of the grains. The factor changes to about 0.5 in the sintered specimen due to the preferred orientation of the grains as revealed by SEM micrograph, where the *a*-*b* planes of the most of plate like grains are parallel to the pellet surface as in Fig 4.2.13.

Table 4.2.3 Rietveld refinement parameters R_{wp} , Goodness of Fit (GOF=R_{wp}/R_{exp}) and lattice parameters; *a*, *b*, *c* in Å, volume of the unit cell in (Å)^3, March-Dollase texture factor of SBTi4 and SBTi5 structures in powder and sintered pellet respectively.

SBTi4-SBTi5 Ceramics	*a*(Å)	*b*(Å)	*c*(Å)	Volume of unit cell(Å)^3	Texture factor	R_{wp}	GOF
Powder							
SBTi4	5.5719(1)	5.5636(3)	41.8534(6)	1297	1.0	6.9	1.9
SBTi5	5.5835(2)	5.5815(3)	50.1040(7)	1561	1.0		
Pellet							
SBTi4	5.6380(2)	5.6450(3)	42.4473(5)	1351	0.51	7.3	2.1
SBTi5	5.6604(3)	5.6609(1)	50.7105(6)	1625	0.54		

4.2.2.11 Densification Behavior

The composite powder densification behavior is studied on a pressed pellet. Fig. 4.2.12 depicts the shrinkage behavior with temperature for the composite and two individual ceramics. As stated earlier, all the ceramics show lower shrinkage. This may be due to the flaky type grains of the ceramics. Additional problem is the partial melting of the samples at higher temperature may be due to the presence of excess Bi_2O_3, used to compensate Bi volatilization loss. The composite shows a lower onset temperature of sintering than pure SBTi4 or SBTi5. Also the composite shows two different rates of shrinkage, first starting at 710°C with a moderate rate and the second starts at 1180°C with an increased rate. The moderate rate in between 710 °C to 1180 °C may correspond to the rearrangement of grains [11] and fractional sintering of the composite. The increased rate above 1180°C may be owing to the formation of liquid phase at higher temperature. The composite ceramics are finally sintered at 1230°C for 2 h. The sintered density is more than 92% of theoretical density.

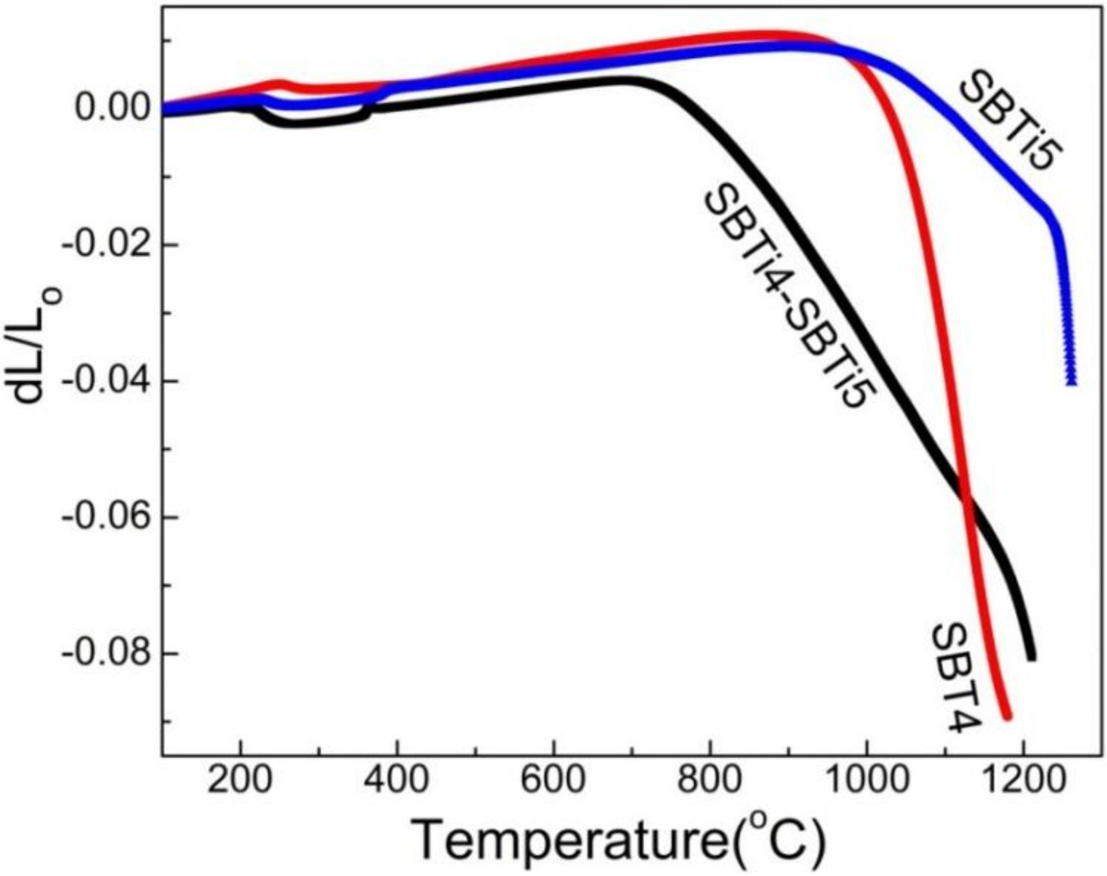

Fig. 4.2.12 Shrinkage behaviour with temperature for SBTi4-SBTi5 composite, pure SBTi4 and SBTi5 ceramics.

4.2.2.12 Microstructural Characteristics

Fig 4.2.13 shows the SEM micrograph of sintered sample surface. The most important difference between the XRD patterns of the powder (Fig. 4.2.10 (d)) and the pellet (Fig

4.2.11) is the increase in intensities of some peaks (in general {0 0 *l*} peaks) because of the preferred orientations in the sintered specimen. This is caused by the preferential growth of plate-like grains in BLSF ceramics. The SEM micrograph shows typical plate-like grains with their *a*-*b* plane parallel to the pellet surface. Since the BLSF has highly anisotropic crystal structure consisting of longer *c*-axis as compared to the *a* and *b*-axis, {0 0 *l*} planes possess lower surface energy [12, 13]. *a* and *b* lattice parameters are only about 5Å, and shorter than the lattice parameter *c*, which is 7-9 times longer than *a* and *b* parameters. So arrangement of atoms to structure the *ab*-plane requires less energy compares to other plane. This leads to a rapid grain growth in the *a*-*b* plane during sintering. The average length of the grains is in between 2-4 µm and a thickness of about 0.55 µm. The aspect ratio of the grains, which is the ratio between the largest to the smallest dimension, is in the range 4-8.

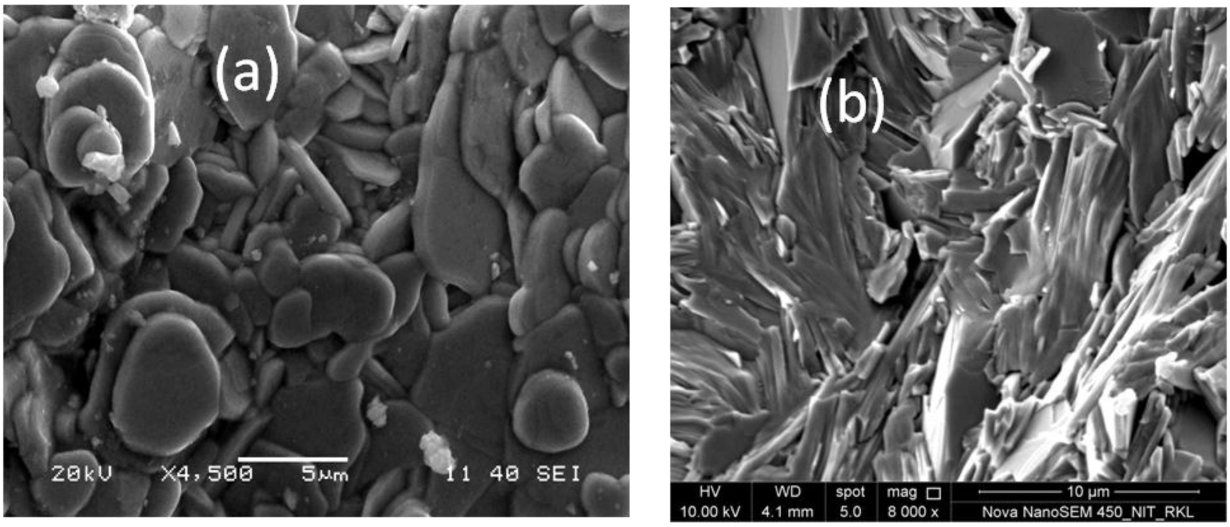

Fig 4.2.13 SEM micrograph of the SBTi4-SBTi5 composite pellet surface (a) and freshly broken bulk surface (b).

4.2.2.13 Dielectric and Diffuse Phase Transition Behavior

Fig 4.2.14 shows the temperature dependence of dielectric permittivity for SBTi4-SBTi5 composite, pure SBTi4 and SBTi5 ceramics. The composite shows two prominent and one diffuse dielectric anomaly peaks. The peaks are at 310, 470 and 530^{o}C, respectively. T_c of SBTi4 and SBTi5 have been reported to be 530 ^{o}C and 290 ^{o}C respectively by the previous investigators [11, 14]. The peak at 310^{o}C is attributed for the T_c of SBTi5 phase present in the composite. However, the peak is shifted to a high temperature by 20^{o} compared to the pure

SBTi5 (290 ^{o}C). The peak at 530^{o}C is assigned for the T_c of SBTi4, which is about the same as of pure SBTi4.

For the composite ceramics, the most striking observation is the occurrence of a diffuse dielectric anomaly peak at 470 ^{o}C. Similar additional anomaly peak was reported for Ca-substituted SBTi5 compounds above its T_c [15]. The peak may be due to short range intergrowth formation between SBTi4-SBTi5. Another possibility may be an intergrowth formation between SBTi5 and BIT, since the peak appears almost at the intermediate temperature of SBTi5 (290 ^{o}C) and BIT T_c (644 ^{o}C) [16]. However, it has been reported that intergrowth between 3 and 5 layered BLSF is improbable because the combined 8-layered BLSF structure can be replaced by a simpler 4-layered structure compound [17]. Consequently, the correct explanation is not known. The phenomenon is noteworthy for the making of a ferroelectric composition having a stable permittivity with temperature. The composite ferroelectric can be useful for practical application at elevated temperature.

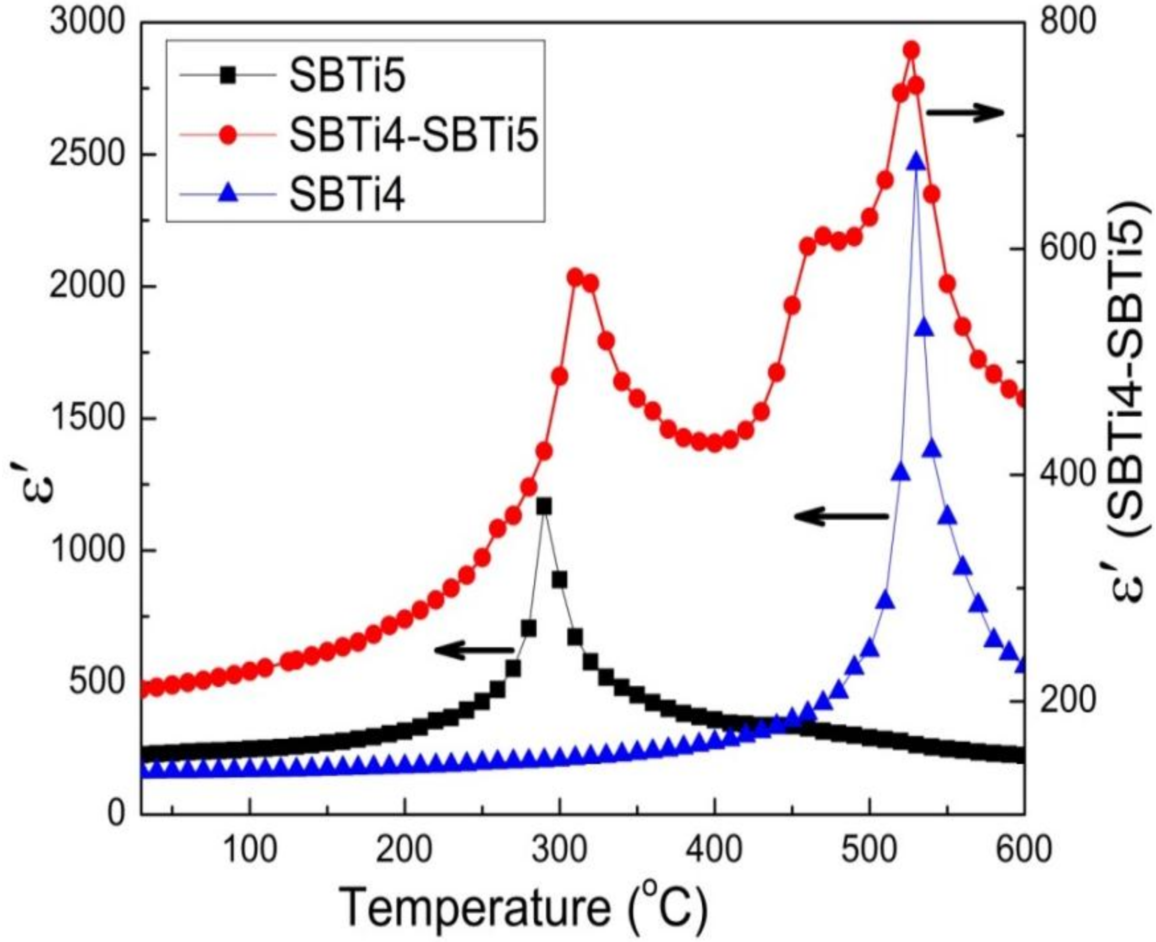

Fig 4.2.14 Temperature dependence of dielectric constant (ε') of SBTi4-SBTi5 composite, pure SBTi4 and SBTi5 ceramics respectively at 100 kHz frequency.

Table 4.2.4 Dielectric, ferroelectric and activation energy (from impedance) of SBTi4-SBTi5 ceramics.

<table>
<tr><th colspan="4">Dielectric properties at 100 kHz</th><th colspan="2">Polarization hysteresis (electric field 20kV/cm)</th></tr>
<tr><td>Room temperature permittivity (ε_{rm})</td><td colspan="3">211</td><td>Remnant polarization ($2P_r$)</td><td>1.71μC/cm^2</td></tr>
<tr><td>Room temperature dielectric loss (tan δ)</td><td colspan="3">0.009</td><td>Coercive field (E_c)</td><td>41 kV/cm</td></tr>
<tr><td>Maximum permittivity (ε_m')</td><td>575</td><td>611</td><td>776</td><td colspan="2"></td></tr>
<tr><td>Dielectric loss at peak (tan δ_m)</td><td>0.016</td><td>0.282</td><td>0.3</td><td colspan="2">Impedance spectroscopy</td></tr>
<tr><td>Maximum permittivity temperature (T_m) (°C)</td><td>310</td><td>470</td><td>525</td><td>Activation energy E_{ac} (relax time)</td><td>1.46 eV</td></tr>
<tr><td>dc conductivity (σ_{dc}) at 500^{o}C</td><td colspan="3">1.06×10^{-7} $(\Omega\mathrm{cm})^{-1}$</td><td>Activation energy E_{dc} from Cole-Cole plot</td><td>1.25 eV</td></tr>
</table>

4.2.2.14 Impedance Spectroscopy

Fig. 4.2.15 shows the Z'' versus frequency plots. The activation energy is calculated from Arrhenius relationship as in Eq. 4.1.10 shown in the inset figure of ln (τ) versus 1000/T. E_{ac} is 1.46 eV, which is less compared to 1.6 eV in BIT-SBTi4 intergrowth ceramic. This value is also less in comparison to that of SBTi5 (~1.70 eV) and SBTi4 ((~1.62 eV), which shows comparatively less energy required for the hopping of charge carriers than SBTi4 and SBTi5 layer.

Fig. 4.2.16 shows the complex impedance plot. This figure also shows a single arc which is attributed to the contribution from the bulk of the ceramics. Using Eq. 4.1.5, the *dc* conductivities of the sample at various temperatures are determined based on the above calculated R_{tot}. The *dc* conductivity value increases with the increase in temperature. The *dc* conductivity is of the order 10^{-7} $\Omega^{-1}\mathrm{cm}^{-1}$ at 500^{o}C, which is same as for SBTi4 and higher than that of the SBTi5 (10^{-9} $\Omega^{-1}\mathrm{cm}^{-1}$). From the inset of Fig. 4.2.16, the E_{dc} is 1.24 eV, which is nearly the same or little higher compared to the BIT-SBTi4 intergrowth ceramic.

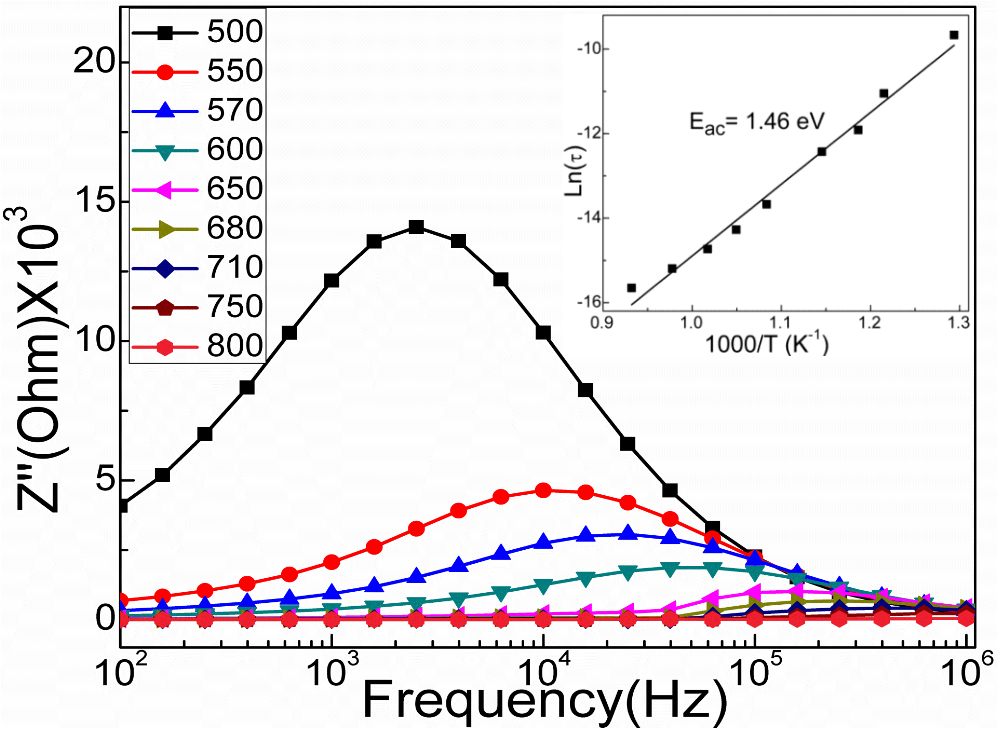

Fig 4.2.15 Variation of Z″ with frequency at various temperatures for the SBTi4-SBTi5 composite. Inset figure shows Arrhenius plot of ac conductivity.

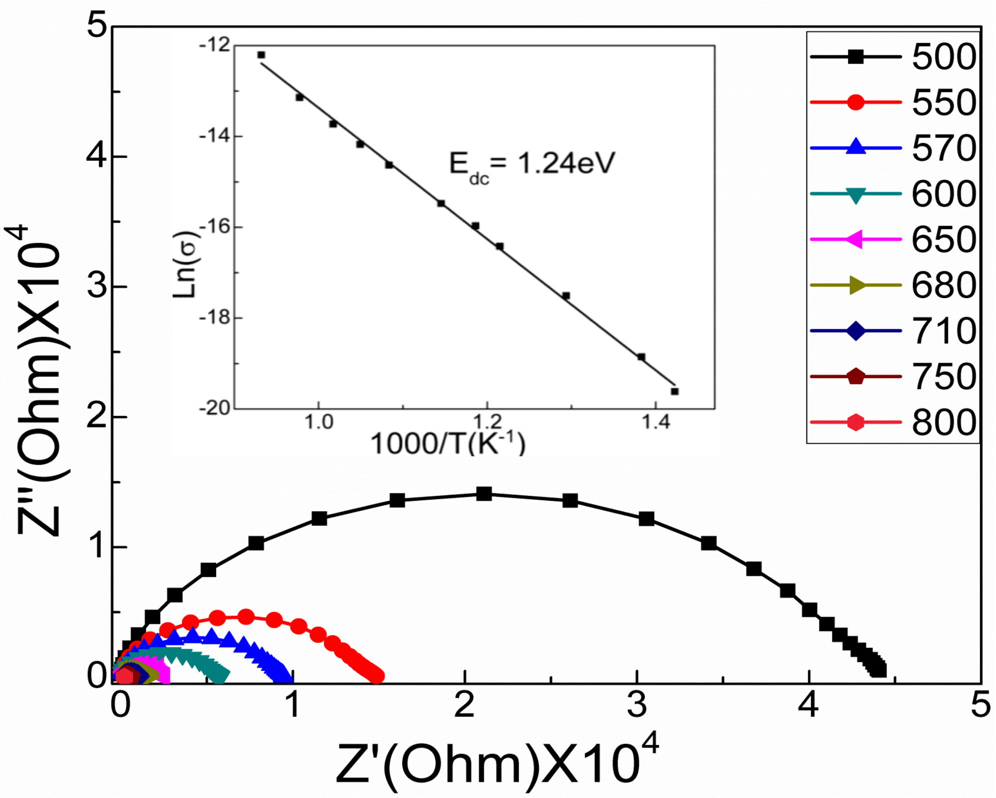

Fig 4.2.16 Complex impedance plots of SBTi4-SBTi5 composite. Inset figure shows Arrhenius plot of dc conductivity.

4.2.2.15 Polarization Hysteresis Characteristics

Fig. 4.2.17 shows the ferroelectric hysteresis behavior of SBTi4-SBTi5 composite ceramics in association with pure SBTi4 and SBTi5 compounds. The hysteresis behavior is not saturated due to the limitation of applicable field strength of the instrument. Pure SBTi5 has the highest ferroelectric properties owing to the presence of large grain size than SBTi4. Ferroelectric behavior of the composite is in-between the two pure compounds. So the ferroelectric properties can be customized by mixing of two phases as per requirement.

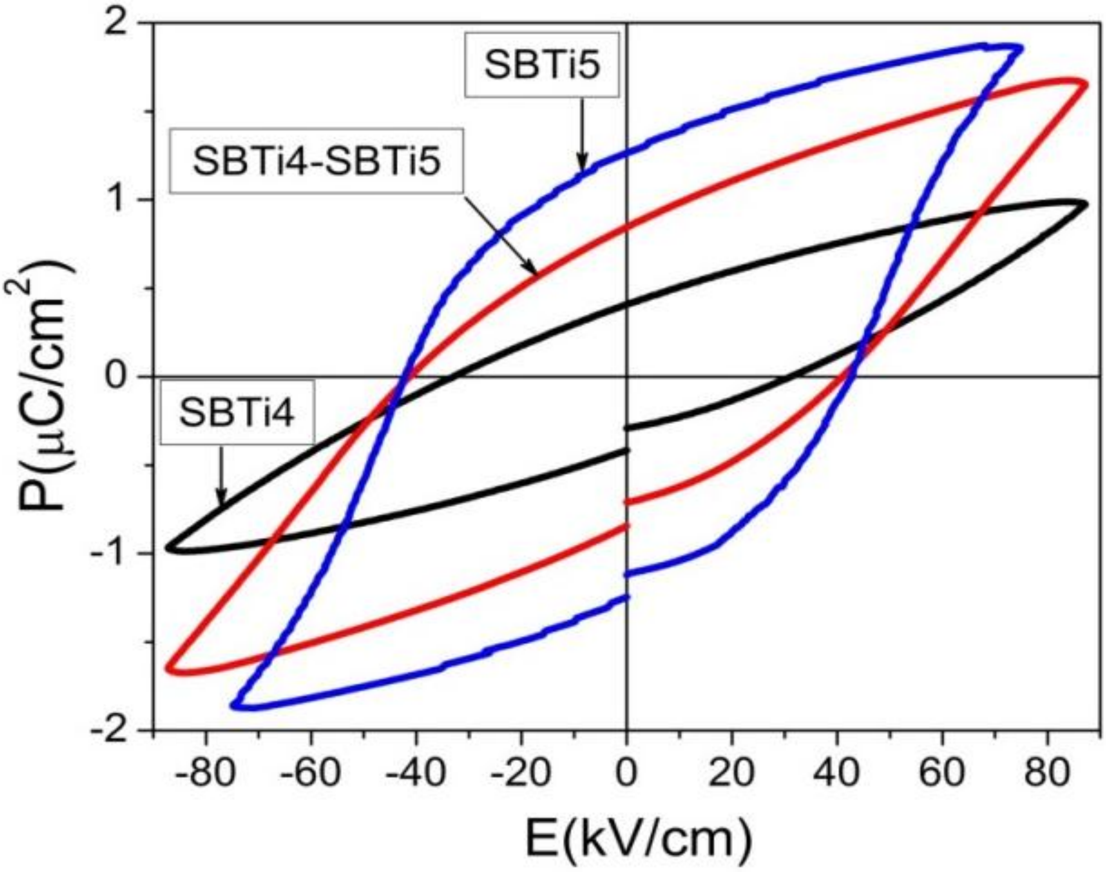

Fig.4.2.17 P-E hysteresis loops for pure SBTi4, SBTi5 and SBTi4-SBTi5 composite ceramics.

4.2.2.16 Conclusions

The SBTi4-SBTi5 composite ceramic is synthesized through the modified oxalate route. The XRD analysis confirmed that SBTi4 and SBTi5 are not able to form a long range periodic intergrowth structure. The Rietveld structure refinement revealed that the lattice parameters of both the structure increased upon composite formation. This may result from an increased deformation of the crystal structure owing to their crystallization from a single precursor powder. The composite ceramic showed a lower onset temperature (710^{o}C) of sintering with two stages of shrinkage kinetics. The composite exhibited two prominent dielectric anomaly peaks at 310 and 530°C corresponding to SBTi5 and SBTi4, respectively and one diffuse anomaly peak at 470°C. The diffuse peak may be owing to the short range intergrowth structure formation between SBTi4 and SBTi5. The broader permittivity with temperature shown by the composite can be useful for elevated temperature application. Ferroelectric behavior of the composite is in-between SBTi4 and SBTi5 compounds. Hence, the ferroelectric properties can be tailored through the composite formation.

4.2.3 References

[1] M.I. Morozov, L.P. Mezentseva, and V.V. Gusarov, *Russ. J. General Chemistry*, 72 (2002) 1038-1040.

[2] M.G. Navarro-Rojero, J.J. Romero, F. Rubio-Marcos, *Ceramics International*, 36 (2010) 1319–1325.

[3] Y. Zhao, Y. Li, Y. Lu, and Y. Wang, *Ferroelectrics* 404 (2010) 45-49.

[4] http://www.ing.unitn.it/~maud/

[5] J. Tellier, P. Boullay and D. Mercurio, *Z. Kristallogr.*, 222 (2007) 234-243.

[6] W. Wang, D. Shan, J. B. Sun, X. Y. Mao, and X. B. Chen, *J. Appl. Phys.*, 103 (2008) 044102:1 -7.

[7] M. Villegas, C. Moure, J. F. Fernandez, P. Duran, *Ceram. Int*, 22 (1996) 15-22.

[8] Y. Noguchi, M. Miyayama, and T. Kudo, *Appl. Phys. Lett.*, 77 (2000) 3639-3641.

[9] B.J. Kennedy, Q. Zhou, Ismunandar, Y. Kubota, K. Kato, *J. Solid State Chem.*, 181 (2008) 1377–1386.

[10] Ismunandar, T. Kamiyama, A. Hoshikawa, Q. Zhou, B.J. Kennedy, Y. Kubota, K. Kato, *J. Solid State Chem.* 177 (2004) 4188–4196.

[11] H. Hao, H. Liu, S. Ouyang, *J. Electroceramics*, 22 (2007) 357–362.

[12] J. A. Horn, S. C. Zhang, U. Selvaraj, G. L. Messing, S. Trolier-McKinstry, J. Am. Ceram. Soc., 82 (1999) 921-926.

[13] S. Kumar, S. Kundu, D. A. Ochoa, J. E. Garcia, K. B. R. Varma, Mat. Chem. Phys., 136 (2012) 680-687.

[14] S. Horiuchi, H. Nagata, T. Takenaka, *Ferroelectrics*, 324 (2005) 3-9.

[15] Z. Xu, R. Chu, J. Hao, Y. Zhang, Q. Chen, L. Zhao, G. Li, Q. Yin, *J. Alloys Compd.*, 487 (2009) 585–590.

[16] P. Ferrer, M. Algueró, J.E. Iglesias, A. Castro, *J. Eur. Ceram. Soc.*, 27 (2007) 3641–3645.

[17] T. Kikuchi, A. Watanabe, K. Uchida, *Mater. Res. Bull.*, 12 (1977) 299-304.

4.3 Synthesis and Characterization of niobium doped $Bi_4Ti_3O_{12}$-$SrBi_4Ti_4O_{15}$ intergrowth ferroelectrics

4.3.1 Introduction

Volatilization of bismuth during high temperature sintering of BLSFs is an inherent problem, which generates oxygen vacancies to compensate the charge due to Bi loss. The resistivity of BLSF decreases due to these vacancies [1]. Many efforts have been made to solve this problem through donor-doping of cations like Nb^{5+}, V^{5+}, W^{6+} at *B*-site of BLSFs [2-9]. Nb^{5+} doping in BLSFs is very effective for compensating oxygen vacancies, which reduce dielectric losses [2-4]. It has been reported that the ferroelectric properties of BIT were enhanced by Nb doping [5]. J. Hou *et al.* [6] reported that Nb/Ta doping at *B*-site of BIT caused a remarkably suppressed grain growth, increased permittivity and piezoelectric activity. J.D. Bobić *et al.* [7] reported an increase of the degree of diffuseness of the dielectric peak in $BaBi_4Ti_4O_{15}$ (BBTi4) with Nb doping. An increased remnant polarization and excellent fatigue-endurance properties were reported in V-doped SBTi4 thin films [8].

Currently there are very few reports [10, 11] related to such kind of *B*-site donor-doping in BIT-SBTi4 ceramics. W. Wang *et al.* [10] reported that the remnant polarization of tungsten-doped BIT-SBTi4 intergrowth ceramics was twice as large as that of non-doped one when W content was 0.03 atom percent. The same group [11] further reported that the remnant polarization and piezoelectric properties of BIT-SBTi4 were greatly improved by Nb and V doping. In the present investigation Nb^{5+} has been doped at *B*-site of BIT-SBTi4 intergrowth and the effect of the doping in the crystal structure, microstructure, dielectric and ferroelectric properties of the intergrowth ferroelectrics have been investigated.

4.3.2 Results and Discussion

4.3.2.1 Solid Solubility Limit and Structural Analysis

Fig. 4.3.1 shows the XRD patterns of Nb doped BIT-SBTi4 ceramics. All patterns shows single phase and these are matched with standard PDF File No. 31-1342 for the compound $SrBi_8Ti_7O_{27}$. The compound $SrBi_8Ti_7O_{27}$ has $Bi_4Ti_3O_{12}$ plus $SrBi_4Ti_4O_{15}$ mixed layered intergrowth structure. The diffraction peaks are indexed according to this standard powder diffraction data. A similar XRD pattern is reported earlier [10, 12] for BIT-SBTi4 intergrowth ceramics. XRD results indicate that Nb doping does not affect the basic crystal structure of the intergrowth ceramics, although, there is a small shift of the diffraction peaks towards lower 2-theta angle with Nb doping. Lattice parameters of intergrowth ceramics are refined by the

Rietveld method using MAUD program [13], considering orthorhombic space group *I*2*cm* (SG No 46: -*cba*). As mentioned in the previous chapter, this space group is reported by J. Tellier *et al.* [14] for similar intergrowth compound $PbBi_8Ti_7O_{27}$ and it requires only a doubling of the usual *c*-parameter ~ 37 Å. Refined lattice parameters and unit cell volume of different compositions are listed in Table 4.3.1. The variation of lattice parameters with the Nb concentration is shown in the Fig. 4.3.2. Since the ionic radii of Nb^{5+} (0.0640 nm) is closer to that of Ti^{4+} (0.0605 nm) [15], there is very little change in the unit cell volume at low concentration of Nb doping. However, a slight increase of cell volume in case of composition $BTN\text{-}SBTN_{0.08}$ may be due to increased concentration of doping. A similar increase in the lattice parameters of SBTi4 was reported by H. Hao *et al.* [16] at higher concentration of Nb doping.

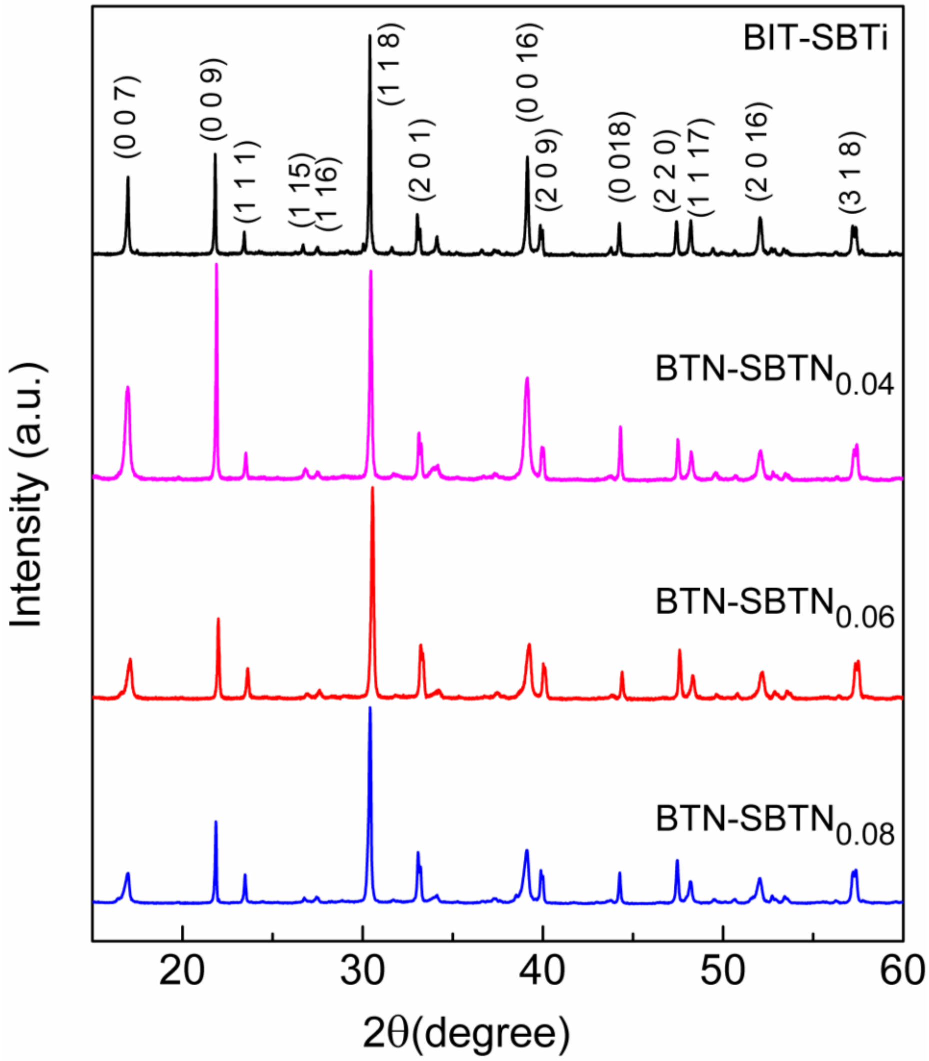

Fig. 4.3.1 X-ray diffraction patterns of BIT-SBTi4, $BTN\text{-}SBTN_{0.04}$, $BTN\text{-}SBTN_{0.06}$ and $BTN\text{-}SBTN_{0.08}$ ceramics.

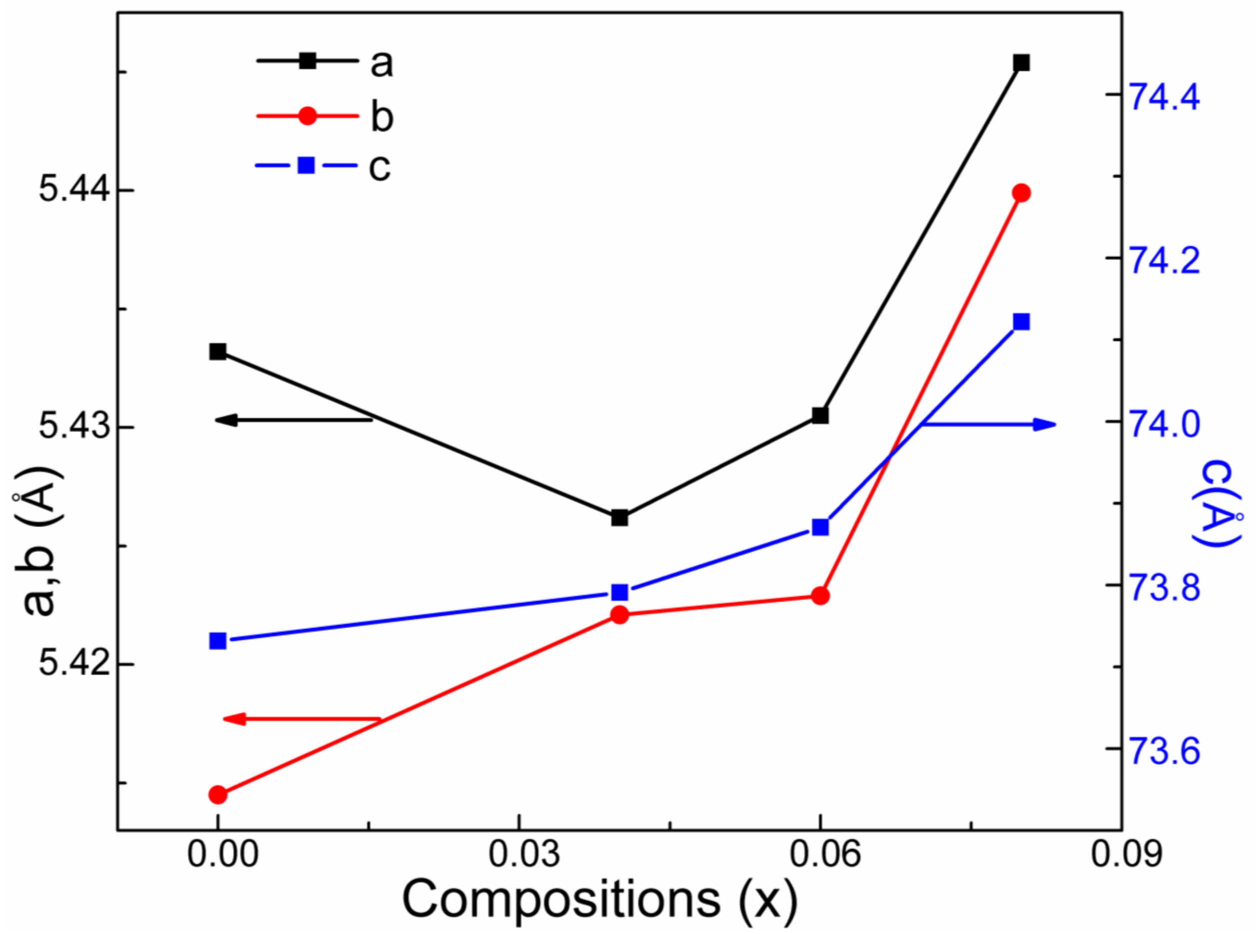

Fig. 4.3.2 Lattice parameters a, b, c of different compositions (x) in BTN-SBTN$_x$ intergrowth ceramics.

Table 4.3.1 Percent theoretical density, lattice parameters; a, b, c in Å, volume of unit cell in (Å)^3, and March-Dollase texture factor for different compositions (x) in BTN-SBTN$_x$ intergrowth ceramics.

x	% theoretical density	*a*(Å)	*b* (Å)	*c* (Å)	Volume of unit cell (Å)^3	Texture factor
0.00	92	5.4332(1)	5.4145(3)	73.7316(8)	2169	0.65
0.04	93	5.4262(3)	5.4221(1)	73.7911(6)	2171	0.58
0.06	95	5.4305(2)	5.4229(4)	73.8706(7)	2175	0.76
0.08	95	5.4454(2)	5.4399(3)	74.1221(9)	2196	0.77

Diffraction patterns show that there are preferred orientations of (0 0 ℓ) planes in pure and BTN-SBTN$_{0.04}$ ceramics, which is due to the preferential growth of plate like grain in BLSF ceramics. As these have a highly anisotropic crystal structure with longer *c*-axis compared to *a* and *b*, the $\{0\ 0\ \ell\}$ planes possess lower surface energy, resulting in a rapid grain growth in the *a-b* plane during sintering. The preferred orientation can be quantified by determining the texture factor in Rietveld analysis. March-Dollase texture factors refined for each composition are listed in Table 4.3.1. For completely random distribution of grains, the texture factor value equals to 1 (one) and the factor will be less than unity for plate like grains. The preferred orientation is highest in BTN-SBTN$_{0.04}$ ceramics as the factor is lowest ~0.58. However, the preferred orientation decreases with further increase in Nb. This is due to the fact that Nb acts as a grain growth inhibitor during sintering [16].

4.3.2.2 Microstructural Characteristics

All compositions are sintered to more than 90% of their theoretical density (Table 4.3.1). There is improvement in density with Nb doping. Similar improvement in the density of BBTi4 has also been reported [7] on Nb doping. Fig. 4.3.3 shows surface morphology of some selected composition, namely pure BIT-SBTi4 and BTN-SBTN$_{0.08}$ ceramics. It shows typical plate like grains in both. The average thickness and diameter of the plates were 0.6 and 3.5 µm respectively in pure BIT-SBTi4 and 0.36, 2.0 µm respectively in BTN-SBTN$_{0.08}$ ceramics. This indicates that the grain size and thickness decreases with Nb doping. It has been reported that Nb doping acts as a grain growth inhibitor in different BLSFs [3, 7]. The increase in density with Nb doping may be due to the decrease in grain size with doping [7].

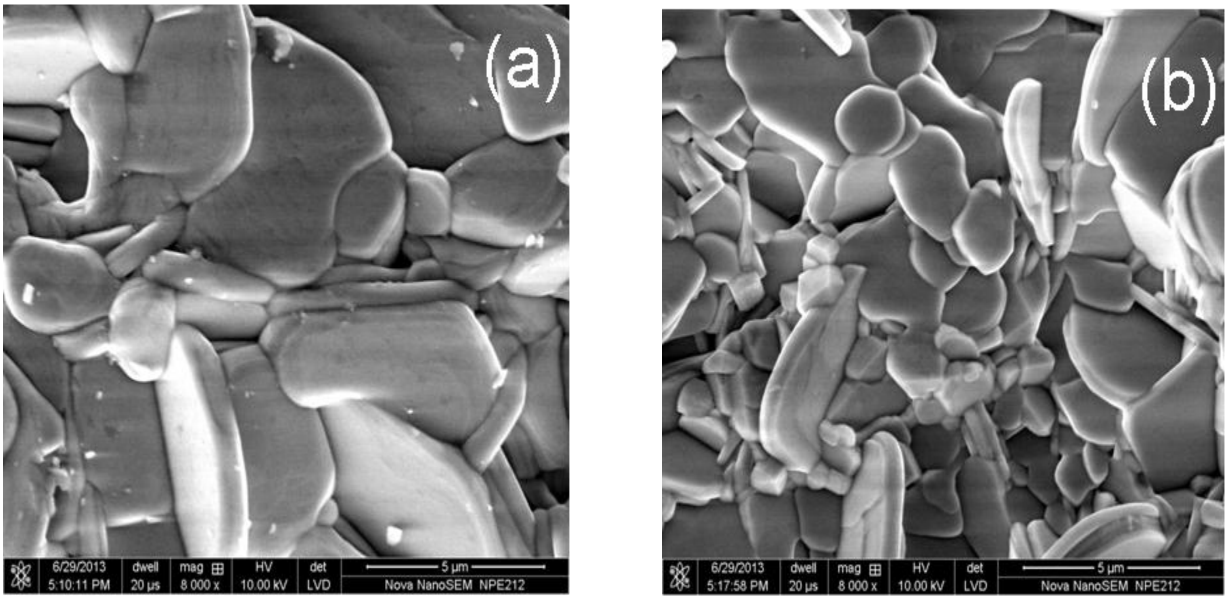

Fig. 4.3.3 Surface morphology of (a) BIT-SBTi4 and (b) BTN-SBTN$_{0.08}$ ceramics.

4.3.2.3 Dielectric and Phase Transition Behavior

Fig. 4.3.4 shows the temperature dependence of dielectric constant (ε) and dielectric loss (tan δ) measured at a frequency of 100 kHz for pure and Nb doped BIT-SBTi4. Curie temperatures (T_c) of different compositions are shown in Table 4.3.2. The T_c of pure BIT-SBTi4 is at 610°C and it decreases to 580°C when Nb doping was 0.08. This indicates that the Nb doping at *B*-site leads to very small shifting of T_c. In Aurivillius compounds, the shifting of T_c is related to the distortion of lattice [17] and T_c decreases with a decrease in distortion. There is a small decrease in orthorhombicity of the structure with Nb doping as shown in Table 4.3. 2. Decreased orthorhombicity is due to the decreased distortion of the structure. A small decrease in T_c with Nb doping may be due to this decreased distortion of the structure. So the Nb^{5+} doping for Ti^{4+} causes a negligible change in lattice distortion.

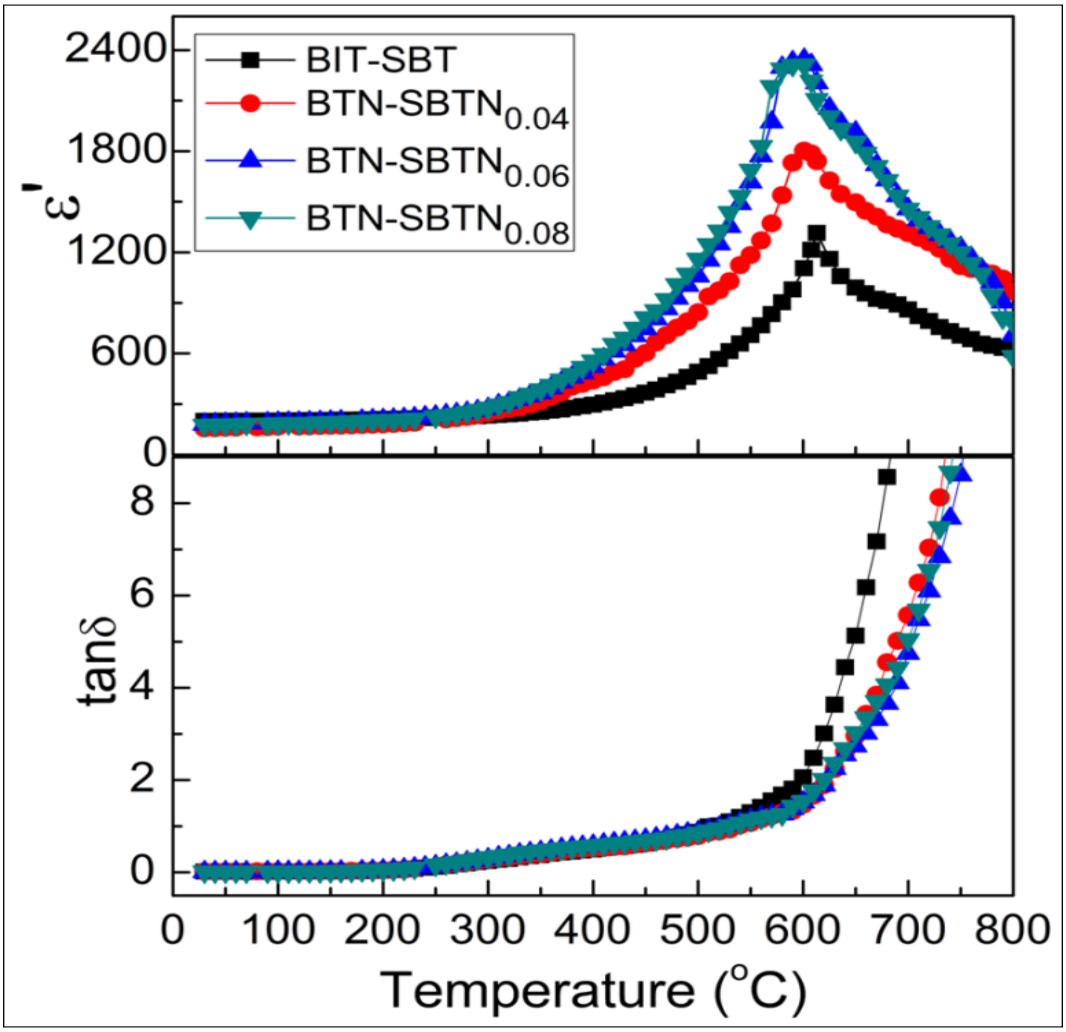

Fig. 4.3.4 Temperature dependence of dielectric permittivity (a) and loss (b) for BIT-SBTi4, $BTN\text{-}SBTN_{0.04}$, $BTN\text{-}SBTN_{0.06}$ and $BTN\text{-}SBTN_{0.08}$ ceramics.

Table 4.3.2 Temperature of dielectric maximum (T_c) measured at 100 kHz, orthorhombicity, the degree of diffuseness (γ) and activation energy for dc conductivity (E_{dc}) of different compositions (x) in BTN-SBTN$_x$ intergrowth ceramics.

x	T_c (^oC)	Orthorhombicity	γ	E_{dc} (eV)
0.00	610	0.0034	0.96	1.00
0.04	600	0.0010	0.98	1.02
0.06	590	0.0014	1.23	1.07
0.08	580	0.0010	1.27	1.12

Fig. 4.3.4 also shows that the peak permittivity increases and the peaks become broader with Nb doping. The Peak permittivity increases due to increased densification and decreased preferred orientation of ceramics with Nb doping. Also, Nb^{5+} ion act as active ferroelectric [18]. Similar peak broadening in Nb doped BIT has been reported earlier [4]. The broadness of permittivity peak originates from the compositional fluctuations in the crystallographic sites when more than one cation occupies the same site in the structure [19]. There is no dielectric loss relaxation peak in the tan δ vs temperature curve. At room temperature, the dielectric losses are comparable for all the compositions. Above about 600^{o}C, there is a sudden increase of tan δ in all the compositions due to increase in thermally assisted conductive current. Pure BIT-SBTi4 ceramics show higher dielectric losses as compared to Nb doped ceramics due to the presence of more oxygen vacancies in un-doped ceramics.

It has been stated above that the ferroelectric to paraelectric phase transition peak become broader and diffuse with Nb doping. The diffuseness of the phase transition can be described using a modified Curie-Weiss law:

$$\left(\frac{1}{\varepsilon'}-\frac{1}{\varepsilon'_m}\right)=\frac{\left[\left(T-T_m\right)^{\gamma}\right]}{C}\text{ for }(T>T_m) \qquad (4.3.1)$$

Where C is the modified Curie-Weiss constant and γ indicates the degree of diffuseness of the phase transition. The value of γ lies in the range $1 \le \gamma \le 2$; in the case of normal ferroelectric, γ=1 and for ideal relaxors, γ=2. The values of γ calculated for different compositions are shown in Table 4.3.2. The γ value increases gradually from 0.96 to 1.27 with Nb doping. This indicates that the doping changes the ferroelectric behavior from normal to a relaxor type in BIT-SBTi4 ceramics. D. Ben Jenneta *et al.* [20] reported a similar change of ferroelectric properties of BIT upon Nb doping. This phenomenon is correlated to the relaxation of polar clusters induced by hetero-valent Nb^{5+} at *B*-site.

4.3.2.4 Impedance Spectroscopy

One of the most important electrical properties of ferroelectrics is the dc conductivity due to vacancy conduction. The activation energy for that vacancy conduction can be evaluated from complex impedance (Cole-Cole) plot. Fig. 4.3.5(a), (b), (c) and (d) show the temperature dependence of the complex impedance spectra for pure BIT-SBTi4, BTN-SBTN$_{0.04}$, BTN-SBTN$_{0.06}$ and BTN-SBTN$_{0.08}$ ceramics, respectively. The plots for ln (σ) versus inverse of temperature (T) for all the ceramics are shown in the inset of Fig. 4.3.5(a), (b), (c) and (d), respectively.

The activation energy E_{dc}, calculated for all the compositions and listed in Table 4.3.2, increases with the increase in Nb doping. This implies that the amount of oxygen vacancies decreases with increasing in donor doping. The conductivity for all the samples is of the order of 10^{-5} $(\Omega cm^{)-1}$.

It is known that the point defects i.e. oxygen vacancies play an important role in electrical properties of ferroelectric ceramics [21]. The substitution of a higher valent cation at *B*-site decreases the concentration of oxygen vacancies as per the defect reaction;

$$Nb_2O_5 \leftrightarrow 2Nb_{Ti}^{\bullet} + 5O_O + 2e' \qquad (4.3.4)$$

$$\tfrac{1}{2} O_2(g) + V_O^{\bullet\bullet} + 2e' \leftrightarrow O_O \qquad (4.3.5)$$

Nb doping produces two Nb_{Ti} holes and two electrons. Theses two electrons combine with one oxygen atom, and can offset an oxygen vacancy, resulting in a decrease in oxygen vacancy concentration.

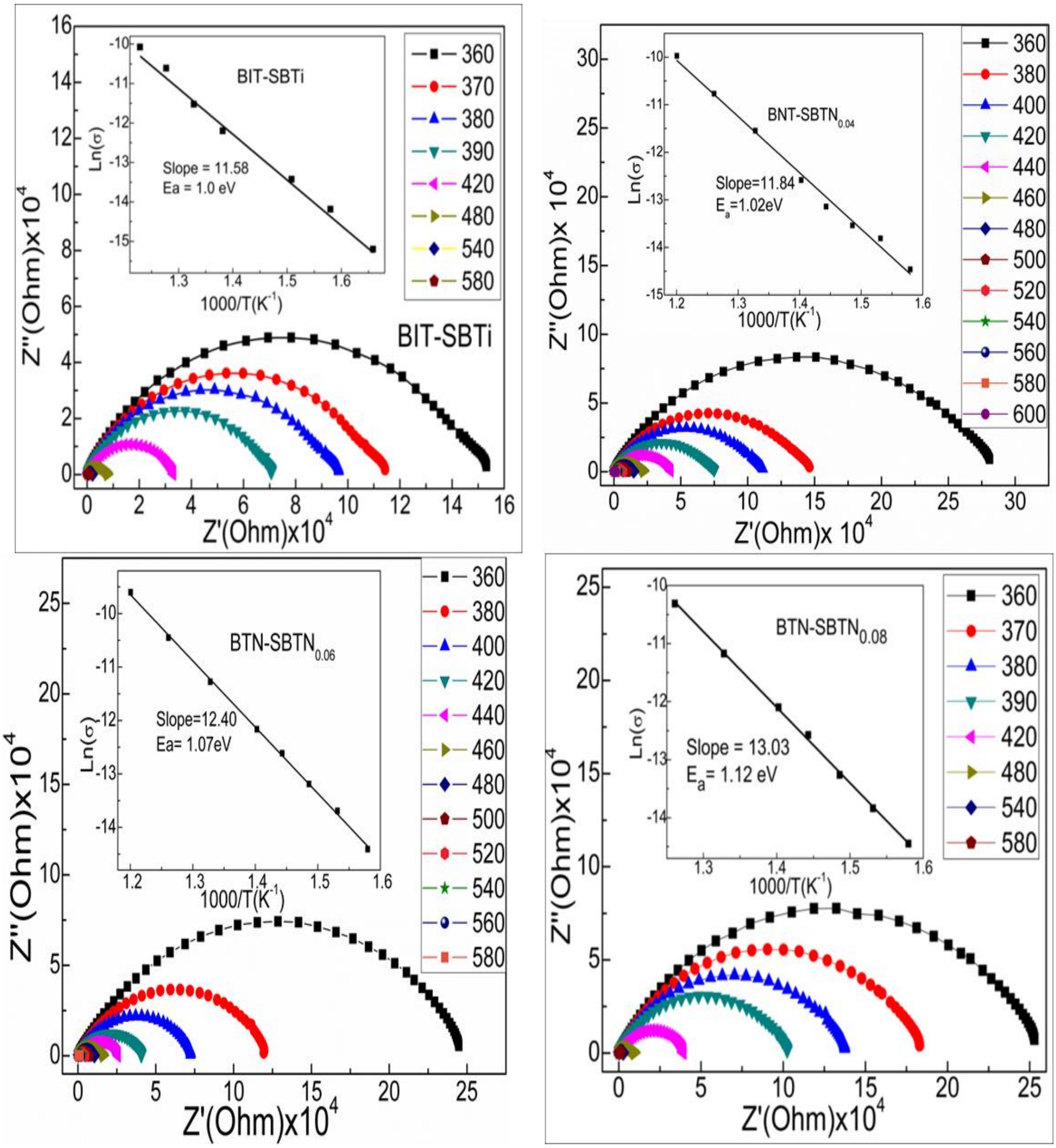

Fig. 4.3.5 Complex impedance plots of (a) BIT-SBTi4 (b) BTN-SBTN$_{0.04}$(c) BTN-SBTN$_{0.06}$ and (d) BTN-SBTN$_{0.08}$ ceramics at different temperatures. Insets are the Arrhenius plots of dc conductivity of respective ceramics.

4.3.2.5. Polarization Hysteresis Characteristics

Fig. 4.3.6 represents the polarization with the electric field (*P-E*) hysteresis loop of BTN-SBTN$_{0.06}$ and pure BIT-SBTi4 ceramic under an applied electric field of 32 KV/cm. Both the curves are minor loops and they aren't saturated due to the limitation of the applicable electric field of the equipment and room temperature measurement. However, they can be compared.

The $2P_r$ of BTN-SBTN$_{0.06}$ is higher than pure BIT-SBTi4 and was highest among all the compositions studied. It is known that oxygen vacancy space charge act as a domain pinning centers and reduces polarization [21,22]. The increased $2P_r$ of Nb doped ceramics may be due to the reduced number of oxygen vacancies in the doped ceramics.

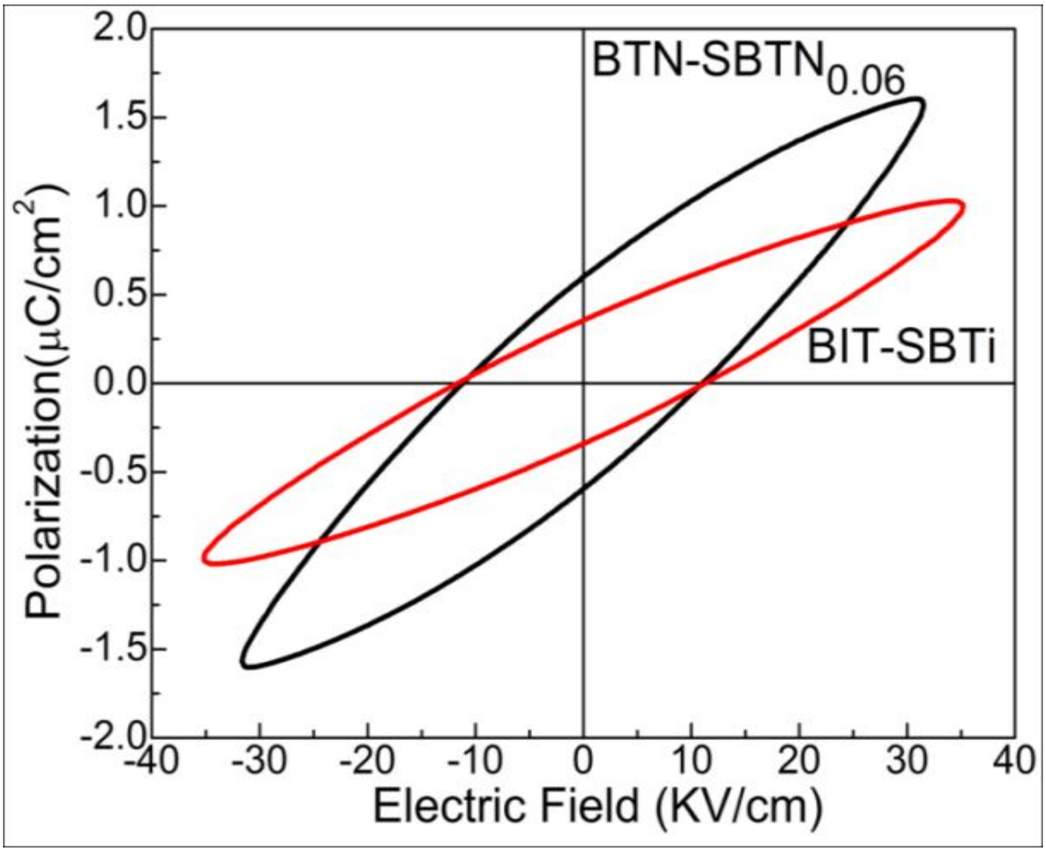

Fig. 4.3.6 P-E hysteresis loops for (a) BIT-SBTi4 and (b) BTN-SBTN$_{0.06}$ ceramics.

4.3.3 Conclusions

Nb doped $Bi_4Ti_3O_{12}$-$SrBi_4Ti_4O_{15}$ mixed layer intergrowth ceramics have been successfully synthesized through modified oxalate route at a temperature of 800°C. XRD analysis showed that the Nb doping does not affect the basic crystal structure, there being a small increase in the lattice parameters. The preferred orientation of plate-like grains and their size decreased with Nb doping. This indicates that Nb acts as a grain growth inhibitor. There is very nominal change in T_c as well as insignificance change of orthorhombicity with Nb doping. The peak permittivity of the intergrowth ferroelectrics increases due to the increase in the density and decrease in the preferred orientation of plate-like grains with Nb doping. Doping also introduces small relaxor behaviour in the ceramics. Dc conductivity of ceramics decreases with doping. The remnant polarization (P_r) of the intergrowth compound is increased due to decreased oxygen vacancy concentration with Nb doping.

4.3.4 References

[1] T. L. Zhao, C. M. Wang, C. L. Wang, Y. M. Wang, S. Dong, Mater. Sci. Eng.: B 201 (2015) 51–56.

[2] S. Hong, S. Trolier-mckinstry, G.L. Messing, *J. Am. Ceram. Soc.* 83 [1] (2000) 113–118.

[3] J.K. Kim, J. Kim, T.K. Song, S.S. Kim, *Thin Solid Films* 419 (2002) 225–229.

[4] J.S. Kim, C.W. Ahn, H.J. Lee, I.W. Kim, B.M. Jin, *Ceramics International* 30 (2004) 1459–1462.

[5] S.K. Singh, H. Ishiwara, *Thin Solid Films* 497 (2006) 90–95.

[6] J. Hou, R.V. Kumar, Y. Qu, D. Krsmanovic, *Scripta Materialia* 61 (2009) 664–667.

[7] J.D. Bobić, M.M. Vijatović Petrović, J. Banys, B.D. Stojanović, *Mater. Res. Bull.* 47 (2012) 1874–1880.

[8] H. Sun, J. Zhu, H. Fang, X.B. Chen, *J. Appl. Phys.* 100 (2006) 074102.

[9] M. Adamczyk, L. Kozielski, M. Pilch, M. Pawełczyk, A. Soszyński, *Ceramics International* 39 (2013) 4589–4595.

[10] W. Wang, J. Zhu, X.Y. Mao, X.B. Chen, *Mater. Res. Bull.* 42 (2007) 274-280.

[11] W. Wang, D. Shan, J. Sun, X. Mao, X. Chen, *J. Appl. Phys.* 103 (2008) 044102 (7 pages).

[12] G. Parida, J. Bera, *Phase Transitions* 87 (2014) 452-459.

[13] http://www.ing.unitn.it/~maud/

[14] J. Tellier, P. Boullay, D. Mercurio, *Z. Kristallogr.* 222 (2007) 234-243.

[15] R.D. Shannon, *Acta Crystallogr.* A32 (1976) 751-767.

[16] H. Hao, H. Liu, S. Ouyang, *J. Electroceramics* 22 (2009) 357–362.

[17] D.Y. Suarez, I.M. Reaney, W.E. Lee, *J. Mater. Res.* 16 (2001) 3139-3149.

[18] W. Cao, J. Xiong, J. Sun, Mater. Chem. Phys., 106 (2007). 338-342.

[19] J. Tellier, Ph. Boullay, M. Manier, D. Mercurio, *J. Solid State Chem.* 177 (2004) 1829-1837.

[20] D.B. Jennet, P. Marchet, M. El Maaoui, J.P. Mercurio, *Materials Letters* 59 (2005) 376–382.

[21] Y. Noguchi, I. Miwa, Y. Goshima, M. Miyayama, *Jpn. J.Appl. phys.* 39 (2000) L1259.

[22] T. Friessnegg, S. Aggarwal, R. Ramesh, B. Nielsen, E. H. Poindexter, D. J. Keeble, *Appl. Phys. Letters*, 77 (2000) 127-129.

4.4 Effect of La-substitution on the Structure, Dielectric and Ferroelectric Properties of Nb modified $SrBi_8Ti_7O_{27}$ Ceramics

4.4.1 Introduction

One of the major problems of these BLSFs is their high leakage current due to the presence of defects mainly in the form of Bi- and O-ion vacancies. These vacancies are generated by the volatilization of bismuth during high temperature processing of the material. Many efforts have been made to suppress the leakage current through doping of aliovalent cations like W^{6+} or Nb^{5+} at the B-site of the BLSF [1-3]. Another approach to stabilize oxygen ion in the structure is the substitution of the Bi^{3+} cation by tri-valent lanthanoid ions, which also improves the ferroelectric properties. Among the lanthanoids dopants, La^{3+} is the most popular element used in BLSFs as well as in their intergrowth compounds. For instance, Z.G. Yi *et al.*[4] reported an enhancement of remnant polarizations in $Bi_7Ti_4NbO_{21}$ intergrowth ceramics upon La-substitution. Similarly, the enhancement of $2P_r$ has been reported in BIT-SBTi4 intergrowth when Bi is substituted by La^{+3} [5-7], Nd^{+3} [8] or Eu^{3+} [9].

It has been established that both individually, donor doping of Nb^{+5} at B-site and La^{+3} substitution at A-site are effective approaches to improve the electrical properties of BIT-SBTi4 intergrowth ferroelectrics [2, 5-7]. However, the information about the effect of simultaneous A-site La^{3+} substitution and B-site Nb^{+5} doping on the properties of BIT-SBTi4 intergrowth is still not available in the literature. In the present study, the Nb-modified BIT-SBTi4 intergrowth composition $SrBi_8Ti_{6.88}Nb_{0.12}O_{27}$ have been prepared to study the effect of La-sustitution. This composition has been reported earlier [3] which showed an optimum enhancement of its electrical properties. In the present investigation La^{+3} is substituted for Bi^{3+} and it is observed that the ferroelectric properties are enhanced by the substitution.

4.4.2 Results and discussion

4.4.2.1 Phase formation behavior and structure analysis

Fig. 4.4.1 shows XRD patterns of $SrLa_xBi_{8-x}Ti_{6.88}Nb_{0.12}O_{27}$ (SLxBTN) with x= 0.0, 0.2, 0.4, 0.6, 0.8 and 1.0 ceramics. XRD peaks of all the patterns are matching with standard JCPDS file no. 31-1342 for the compound $SrBi_8Ti_7O_{27}$ and the peaks are indexed according to this standard file.

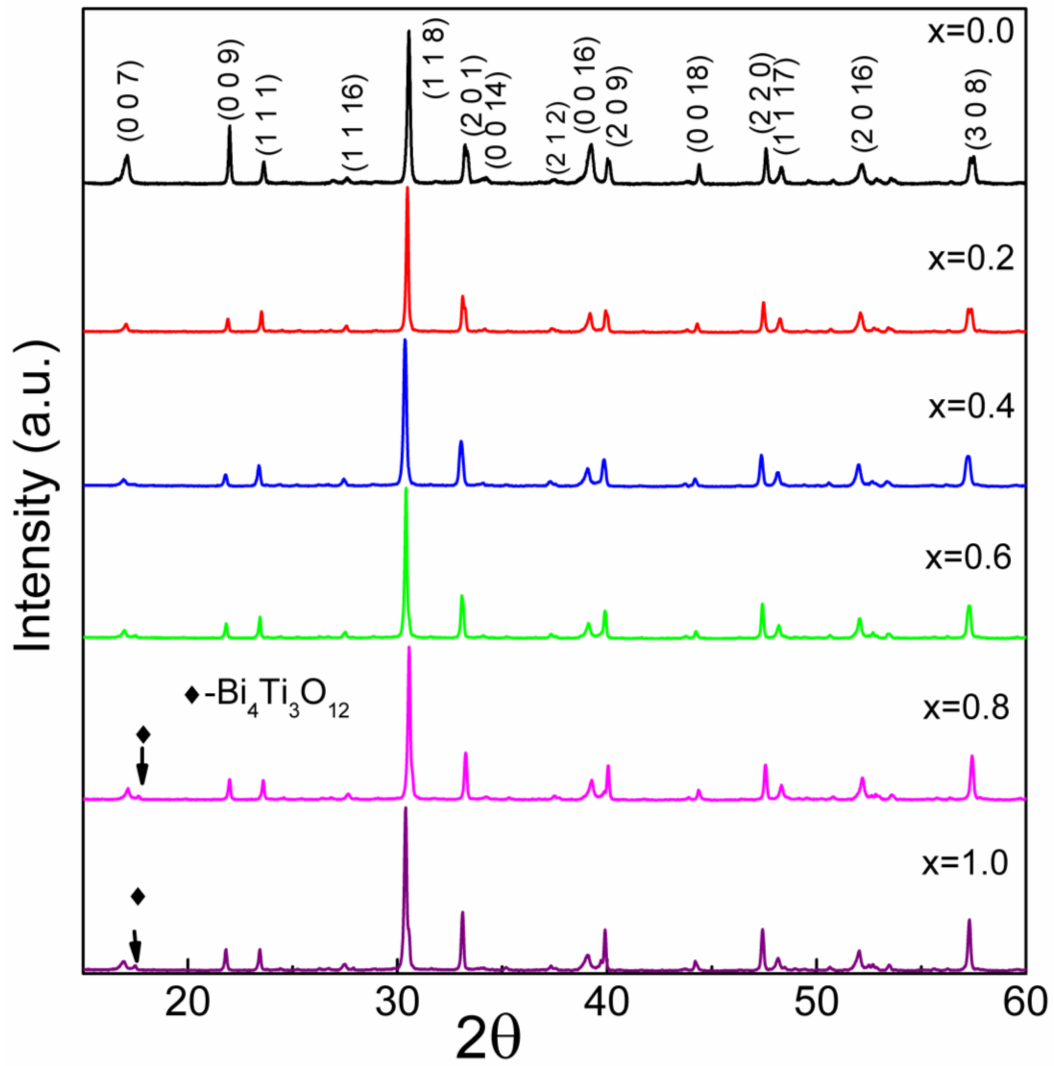

Fig. 4.4.1 Room temperature XRD patterns of SL$_x$BTN ceramics with x= 0.0, 0.2, 0.4, 0.6, 0.8 and 1.0.

There is no change in the basic structure of $SrBi_8Ti_7O_{27}$ after La-substitution. It is also expected that there will not be any major change in the structure as the valence of La^{3+} is the same as that of Bi^{3+} and their ionic radii are very close to each other (La^{3+}: 1.16 Å and Bi^{3+}: 1.17 Å). A small quantity of BIT phase is found in compositions with $x \geq 0.8$ as indicated in the Fig. 4.4.1 It has been reported that the La solid solution limit in $BaLa_xBi_{8-x}Ti_7O_{27}$ is $x \leq 0.25$ [10] and in $SrLa_xBi_{8-x}Ti_7O_{27}$ is $x \leq 0.50$ [11]. In the present study, the solid solution limit of La in $SrLa_xBi_{8-x}Ti_{6.88}Nb_{0.12}O_{27}$ has been found for $x \leq 0.60$, which is very similar to that reported for BIT-SBTi4. One important observation is that the intensities of (0 0 ℓ) peaks decreased with La substitution. This may be due to the decrease in the grain growth along preferred (0 0 ℓ) planes with La substitution, which indicates that La acts as a grain growth inhibitor.

There is small shifting of XRD peaks with the substitution. The lattice parameters are determined through Rietveld refinement of XRD patterns using the software program MAUD [12], considering the space group of the intergrowth structure as orthorhombic *I2cm* (SG No 46: *-cba*) [13]. The micro-strain of the structure is also evaluated through the refinement. Refined lattice parameters and micro-strain values are shown in the Table 4.4.1 along with volume of the unit cell and orthorhombicity. Rietveld refinement final outputs for all the compositions are shown in Fig. 4.4.2. The variations of lattice parameters with La concentration are shown in the Fig. 4.4.3. The lattice parameters and volume of the unit cell nominally decrease with La-substitution. The La^{3+} ion primarily goes to the A-site of pseudo-perovskite block in BIT-SBTi4, when La content is x≤0.50 [14]. The decrease in lattice parameters might be due to the occupancy of La in A-site.

Table 4.4.1 Lattice parameters (*a, b, c*), volume of the unit cell, orthorhombicity and micro strain of intergrowth structure for different compositions.

Composition	a (Å)	*b* (Å)	*c* (Å)	Volume of the unit cell($Å^3$)	Orthorhombicity	Microstrain ($x10^{-4}$)
SL_0BTN	5.438(2)	5.456(3)	74.18(6)	2201	0.0033	14.1
$SL_{0.2}BTN$	5.437(2)	5.453(1)	74.04(5)	2195	0.0029	8.6
$SL_{0.4}BTN$	5.438(1)	5.448(4)	74.02(4)	2193	0.0019	10.1
$SL_{0.6}BTN$	5.437(3)	5.445(3)	73.99(6)	2191	0.0014	5.2
$SL_{0.8}BTN$	5.444(3)	5.445(1)	74.05(3)	2195	0.0011	3.4
$SL_{1.0}BTN$	5.439(4)	5.439(4)	74.04(2)	2191	0.0003	0.36

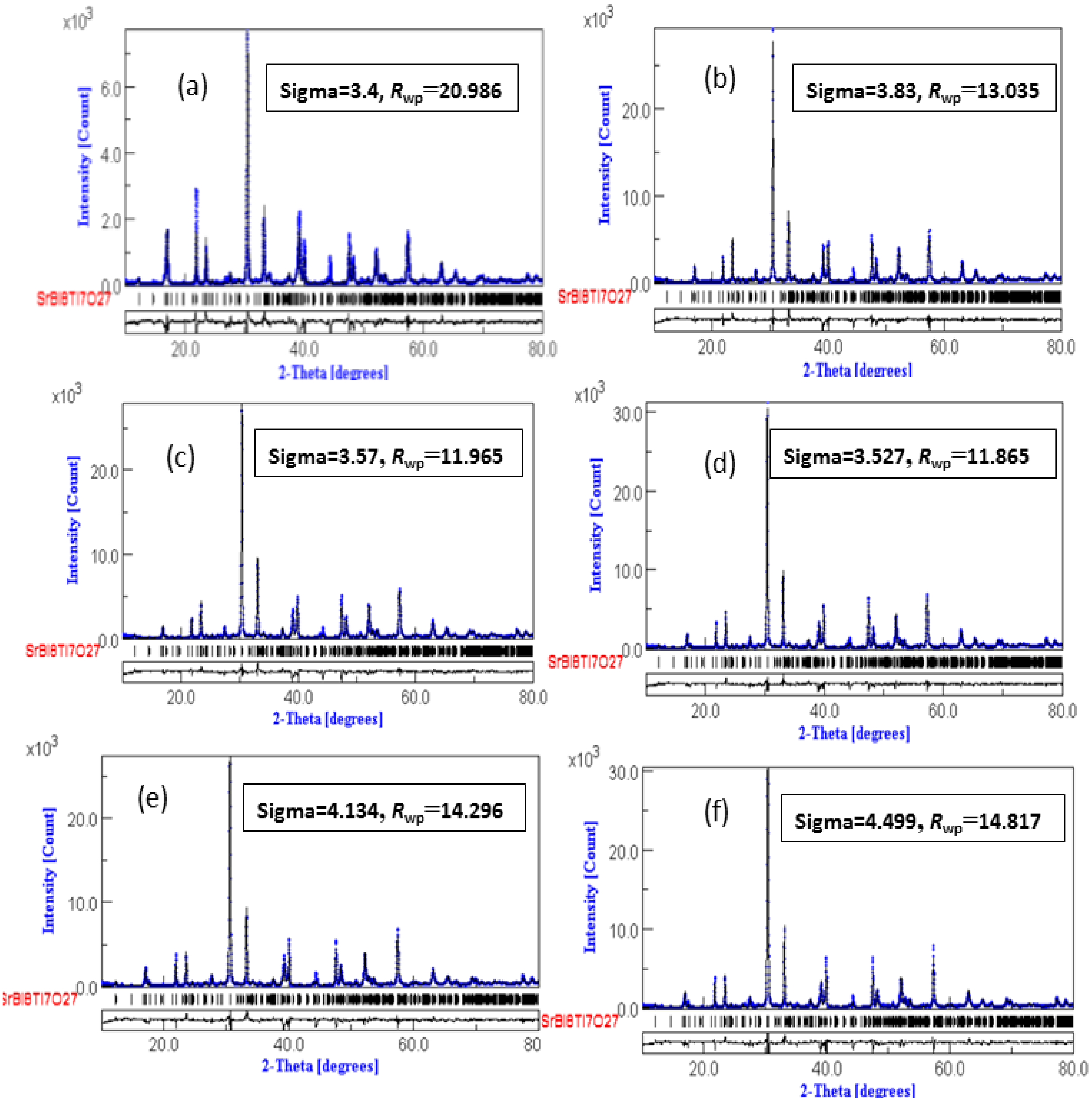

Fig. 4.4.2 Rietveld refinement output of (a) SL_0BTN, (b) $SL_{0.2}BTN$ (c) $SL_{0.4}BTN$ (d) $SL_{0.6}BTN$ (e) $SL_{0.8}BTN$ and (f) $SL_{1.0}BTN$.

It is well known that the lattice distortion is created in intergrowth BLSF structure due to the lattice mismatch between two different blocks (BIT and SBTi4) as they are sandwiched between Bi_2O_2 layer and due to their different chemical character [15, 16]. The orthorhombicity of intergrowth structure decreases with La substitution (Table 4.4.1) and the structure changes from orthorhombic to tetragonal. This is caused by the relief of lattice distortion with the substitution. Bi^{3+} ions have $6s^2$ lone pair electrons which hybridize with oxygen 2*P* orbital in the BLSF structure. However, lanthanum ions don't have lone pair electrons and there will be less hybridization with increasing La concentration. This may be one of the reasons for the decrease in the orthorhombic distortion. The micro-strain also decreased (Table 4.4.1) with La-substitution, which is primarily due to the decrease in orthorhombic distortion.

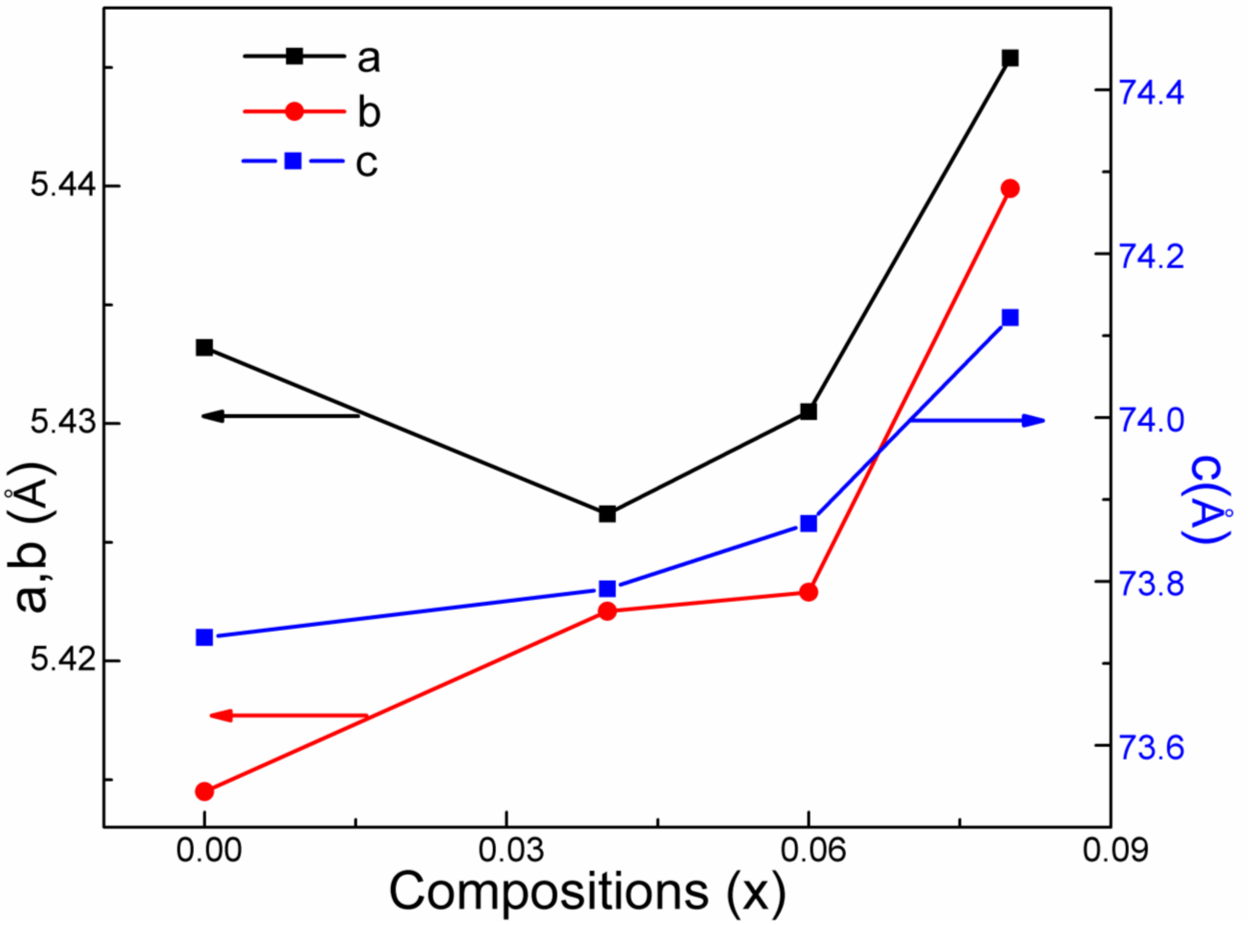

Fig. 4.4.3 Variation of lattice parameters of SL_xBTN ceramics with La substitution concentration.

4.4.2.2 Microstructural Characteristics

Fig. 4.4.4 shows the SEM microstructure of SL_xBTN (x=0.0, 0.2, 0.4, 0.6, 0.8 and 1.0) ceramics surface. It shows a typical plate like grains with random orientation and anisotropic grain growth. It is evident from the picture that the average grain size decreases with the increase of lanthanum content. This suggests that the La acts as a grain growth inhibitor [8].

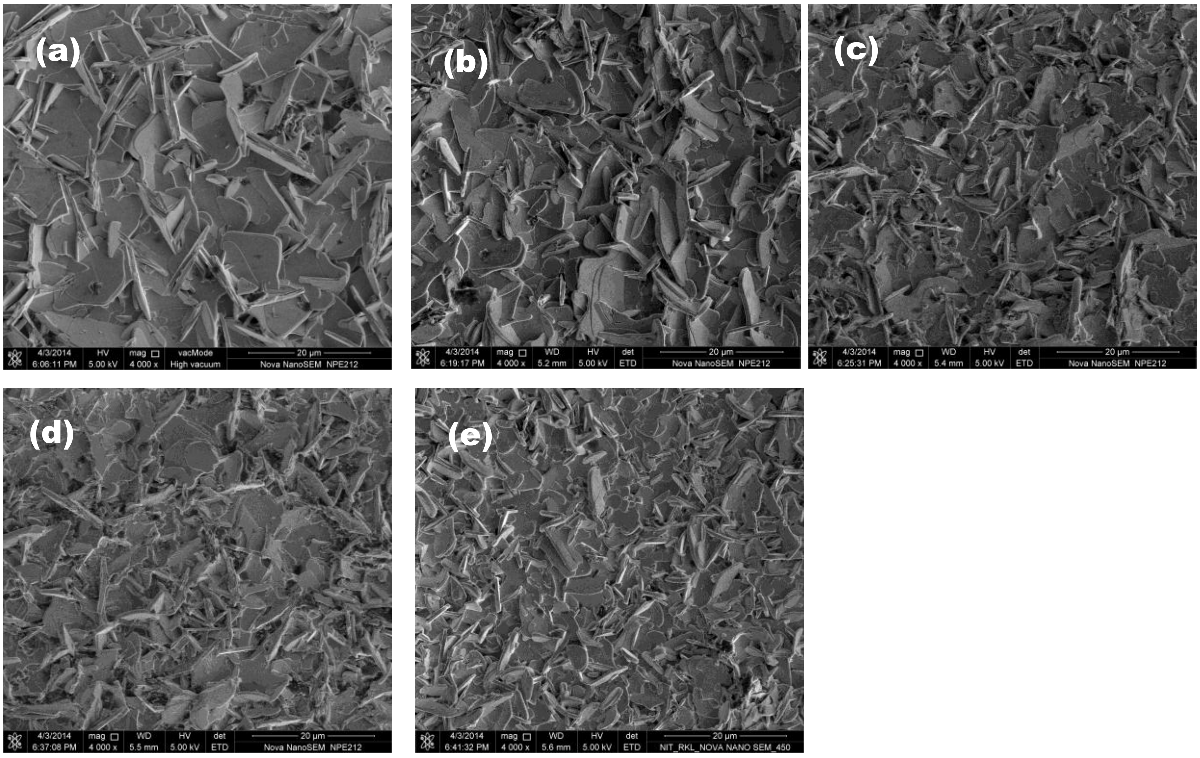

Fig. 4.4.4 FESEM micrographs of (a) $SL_{0.2}BTN$, (b) $SL_{0.4}BTN$ (c) $SL_{0.6}BTN$ (d) $SL_{0.8}BTN$ (e) $SL_{1.0}BTN$ ceramics.

4.4.2.3 Dielectric and Phase Transition Behavior

Fig. 4.4.5 shows the temperature dependence of relative dielectric permittivity (ε') and dielectric loss (tan δ) for SL_xBTN ceramics measured at a frequency of 100 kHz. Room temperature ε', tan δ and Curie temperature (T_c) values for SL_xBTN ceramics are shown in Table 4.4.2. At room temperature, the values of ε' for different compositions fall within 180 to 200 and do not apparently depend on La contents. The dielectric permittivity increases with increasing in temperature until the Curie temperature, corresponding to the maximum value of permittivity (ε'_m). With increasing La content, the T_c decreases from 590 ^oC (for L_0BTN) to 460 ^oC (for $L_{1.0}BTN$) and ε'_m value also decreases. Although the T_c decreases continuously from x=0 to 0.8, there is no change in T_c after 0.8 i.e. T_c is 460^{o}C for both of the compositions. This indicates that there is a very small quantity of lanthanum substitution in the intergrowth structures of x=0.8 and 1.0 composition, although secondary phase BIT appeared in those ceramics. At the same time, dielectric peaks become broadened with the increase in La content. Although the ionic radius of La^{3+} and Bi^{3+} is similar, the T_c decreases with La substitution. This is due to the influence that the $6s^2$ lone pair electrons of Bi^{3+} have a great effect on the Curie temperature [17]. For the broad range of bismuth layered compounds, Suarez *et al.* [17] explained that the decrease of lattice distortion generally accompanies a decrease of Curie temperature, which is also found in this study.

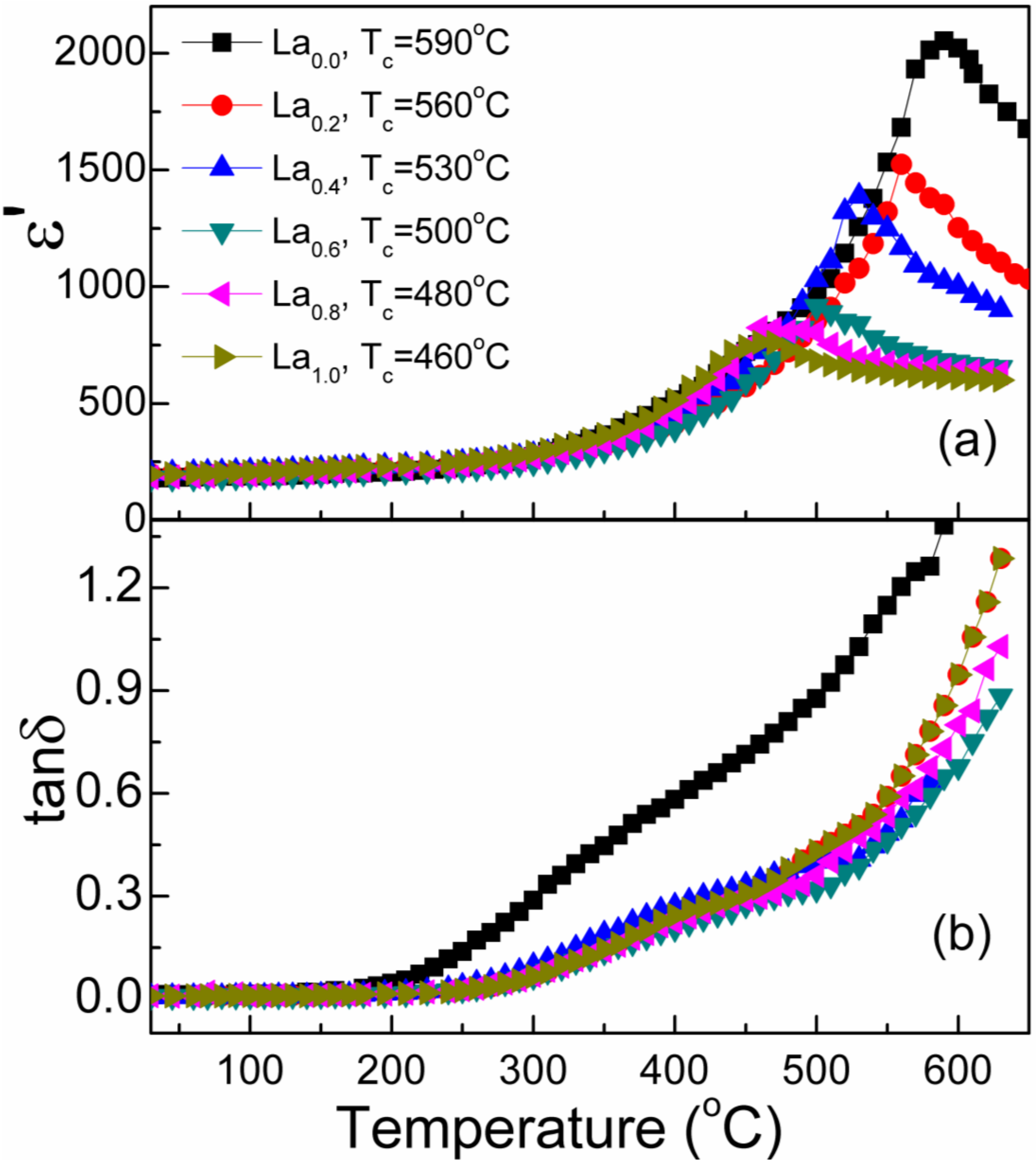

Fig. 4.4.5 The temperature dependence of (a) dielectric constant (ε') and (b) dielectric loss (tan δ) measured at a frequency of 100 kHz for SL_xBTN ceramics.

The decrease in ε'_m with increasing substitution may be related to the decrease in grain size and decrease in orthorhombicity of the structure. With increasing La substitution, ε'_m value decreases and dielectric peaks become broadened. The formation of inhomogeneous polar clusters formation plays an important role in the broadening and suppressing of dielectric permittivity peak [18]. The dielectric peak broadening with increasing La content indicates a diffusion of the phase transition. The diffusion may, particularly, be due to the inhomogeneous distribution of two different cations at the same crystallographic A-site. This distribution creates microscopic ferroelectric phase domains with slightly different T_c [8]. The diffuseness of the phase transition can be explained using a modified Curie-Weiss law, Equation 4.3.1. The degree of diffuseness values for different compositions is given in Table 4.4.2. Here γ first decreases (for x=0.2 and 0.4 compositions) and then increases with La content. The degree of diffuseness of BIT-SBTi4 has been reported to increase by Nb doping due to the formation of polar clusters induced by aliovalent Nb^{5+} cation at B-site [3]. However, that clustering effect reduces in the x=0.2 and 0.4 compositions and again increases in higher La content compositions. The initial decrease might be due to the rapid evolution in the orthorhombicity distortion of the crystal structure (decrease in *b* and *c* lattice parameters in the case of x=0.2 and 0.4 compositions).

Table 4.4.2 Dielectric constant (ε') and dielectric loss (tan δ), Curie temperature T_c and degree of diffuseness (γ) of different compositions.

Composition	ε' at 30°C	tan δ at 30°C	T_c (°C)	γ
SL_0BTN	180	0.011	590	1.23
$SL_{0.2}BTN$	199	0.009	560	0.98
$SL_{0.4}BTN$	200	0.006	530	0.99
$SL_{0.6}BTN$	179	0.007	500	1.24
$SL_{0.8}BTN$	183	0.009	460	1.30
$SL_{1.0}BTN$	198	0.009	460	1.32

4.4.2.4 Polarization Characteristics

Fig. 4.4.7 shows the polarization-electric field hysteresis loops for SL_xBTN ceramics under the electric field of 90 KV/cm. Hysteresis loops aren't saturated due to the limitation of applicable electric field of the equipment and room temperature measurement. Variation of $2P_r$ with La content is shown in the inset of Fig. 4.4.7. As the La concentration increases, $2P_r$ initially decreases upto x=0.4 composition and then increases. The Increase of $2P_r$ with substitution may be partly due to the increase in dielectric diffusion and partly due to the formation of highly ferroelectric BIT phase in cases of x=0.8, 1.0 composition. The value of $2E_C$ also increases with the La concentration. This might be explained by the initial decrease and then increase in dielectric diffusion as explained above. The results revealed that substitution of La for Bi in BIT-SBTi4 intergrowth structure significantly enhances the ferroelectric properties of the BLSF intergrowth.

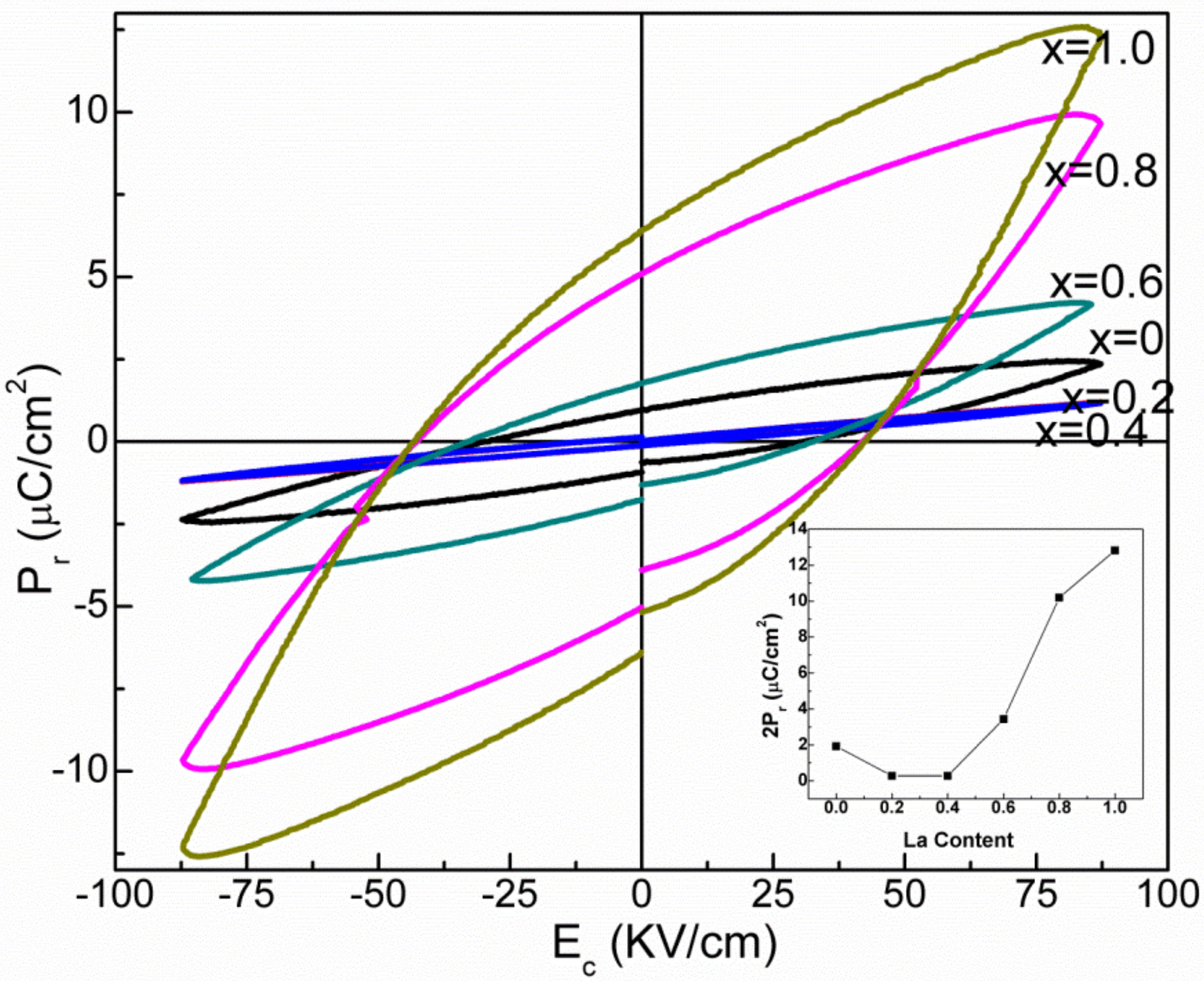

Fig. 4.4.6 P-E hysteresis loop of SL_xBTN ceramics measured at room temperature.

4.4.3 Conclusions

Lanthanum substituted $SrLa_xBi_{8-x}Ti_{6.88}Nb_{0.12}O_{27}$ ceramics are prepared by a modified chemical route. X-ray diffraction analysis confirmed the formation of single phase intergrowth BLSF up to the La concentration $x \leq 0.60$. The orthorhombic distortion and micro-strain of the structure decreased with the increase in lanthanum content. The average grain size of the ceramics reduced with the substitution. This suggests that La acts as a grain growth inhibitor. There is a shift in T_c, from 590°C (for x=0.0) to 460°C (for x=1.0), due to the decrease in orthorhombic distortion with increasing La content. The dielectric permittivity peak becomes broadened and suppressed with increasing substitution. This observation might be explained by the formation of inhomogeneous polar clusters and decrease in average grain size of the ceramics respectively. With increasing La content, the remnant polarization $2P_r$ increased significantly due to the increase in dielectric diffusion and also due to the formation of highly ferroelectric BIT phase with a preferred orientation.

4.4.4 References

[1] W. Wang, J. Zhu, X.Y. Mao, X.B. Chen, *Mater. Res. Bull.* 42 (2007) 274-280.

[2] W. Wang, D. Shan, J. Sun, X. Mao, X. Chen, *J. Appl. Phys.* 103 (2008) 044102.

[3] G. Parida, J. Bera, *Ceram. Int.* 40 (2014) 3139-3144.

[4] Z.G. Yi, Y.X. Li, Y. Wang, Q.R. Yin, *Appl. Phys. Lett.* 88 (2006) 152909.

[5] J.S. Zhu, D. Su, X.M. Lu, H.X. Qin, Y.N. Wang, D.Y. Wang, H.L. W. Chan, K.H. Wong, C.L. Choy, *J. Appl. Phys.* 92 (2002) 5420-5424.

[6] J. Zhu, R. Hui, X.Y. Mao, W.P. Lu, X. B. Chen, Z-P. Zhang, *J. Appl. Phys.* 94 (2003) 5143-5146.

[7] J. Zhu, X.B. Chen, W.P. Lu, X.Y. Mao, R. Hui, *Appl. Phys. Lett.* 83 (2003) 1818-1820.

[8] W. Wang, S.P. Gu, X.Y. Mao, X.B. Chen, *J. Appl. Phys.* 102 (2007) 024102.

[9] T. Wei, C.Z. Zhao, C.P. Li, Y.B. Lin, X. Yang, H.G. Tan, *J. Alloys Comp.* 577 (2013) 728-733.

[10] R.Z. Hou, X. M. Chen, *Mater. Res. Bull.* 38 (2003) 63-68.

[11] J. Zhu, J-H He, X-B Chen, *Integrated Ferroelectrics,* 79 (2006) 265-271.

[12] http://www.ing.unitn.it/~maud/

[13] J. Tellier, P. Boullay, D. Mercurio, *Z. Kristallogr.* 222 (2007) 234-243.

[14] J. Zhu, X-B Chen, J-H He, J-C Shen, *Solid State Chem.* 178 (2005) 2832-2837.

[15] Y. Noguchi, M. Miyayama, T. Kudo, *Appl. Phys. Lett.* 77 (2000) 3639.

[16] M. Noda, T. Nakaiso, K. Takarabe, K. Kodama, M. Okuyama, *J. cryst. Growth*, 237 (2002) 478-481.

[17] D.Y. Suarez, I.M. Reaney and W.E. Lee, *J. Mater. Res.* 16 (2001**)** 3139-3134.

[18] C. Ang, Z. Yu, J. Hemberger, P. Lunkenheimer, A. Loidl, *Physical Rev. B*, 59 (1999) 6665.

4.5 Effect of CuO addition on the structure, dielectric and ferroelectric properties of Nb modified $SrBi_8Ti_7O_{27}$ ceramics

4.5.1 Introduction

One of the important requirements for miniaturized electronic device manufacturing is the low temperature co-sintering of ceramics and internal silver electrode in the form of multi-layered structure. As it has been mentioned in the previous chapter the sintering temperature of this intergrowth BLSF ceramics is about 1150°C, a low temperature sintering of ceramics is necessary to cofire with metal electrodes. Many additives have been employed to reduce the sintering temperature of different ferroelectric materials. The most commonly employed additives are B_2O_3, CuV_2O_6, ZnBO and CuO, etc. Among these, CuO has been successfully utilised to bring the sintering temperature of KNN ferroelectrics down to as low as 950°C [1]. CuO produces a liquid phase during the sintering process and it is believed that this lowers the sintering temperature. The ionic radius Cu^{2+} is too small for the A-site occupancy and its valance is too low to occupy the B-site of the BLSFs structures. For that reason, Cu^{2+} has not been mentioned as a probable cation for substitution in BLSF structure. In the present investigation, CuO has been added in an amount; 0.02, 0.04 and 0.06 wt% to $SBTN_{0.06}$ composition and its effects on ferroelectric and dielectric properties of the ceramics has been investigated.

4.5.2 Results and discussion

4.5.2.1 Phase formation behavior

Fig. 4.5.1 (a) shows the room temperature XRD patterns of sintered pellets of $Cu_xSBTN_{0.06}$ (with x=0, 0.2, 0.4 and 0.6) ceramics. With CuO addition, there are no major changes in crystal structure of BIT-SBTi4 intergrowth. However, with a closer look, impurity phase peaks are found at ~26.7° and ~36.7° two theta. Fig. 4.5.1(b) shows the XRD patterns for impurity peak around 26.7° two theta. The intensity of the impurity phase peak increases with increasing CuO addition. A very small amount of impurity is found in $Cu_{0.2}SBTN_{0.06}$ ceramics, which contains the lowest (least) amount of CuO. For this reason, the maximum CuO content has been fixed at 0.2 wt% in all the compositions for a second series of experiments, where Nb-doping concentration is reduced to investigate the possibility of obtaining impurity free composition. It is very difficult to identify the phase associated with a single peak. However, it is logical that the un-indexed peaks are due to a Cu containing phase. The lattice parameters are refined through Rietveld refinement. The values of lattice parameters are shown in Table 4.5.1. It has been found that there was very little change in lattice parameters with CuO addition. There may be possibility of substitution of very small amount of Cu^{2+} cation in the BLSF structure. A small amount of Cu^{2+} substition in perovskite block of $Ba_{0.98}Ca_{0.02}Zr_{0.02}Ti_{0.98}O_3$ ceramics [2] and $(Na_{0.5}Bi_{0.5})_{0.94}$–$Ba_{0.06}TiO_3$ ceramics [3] has been reported. The excess CuO has been found to segregate at the grain boundaries and triple conjunctions of those ceramics [2, 3]. Since the $SBTN_{0.06}$ composition, used for this study, already has Nb cation in its structure, it has very limited capacity to uptake Cu^{2+} ions.

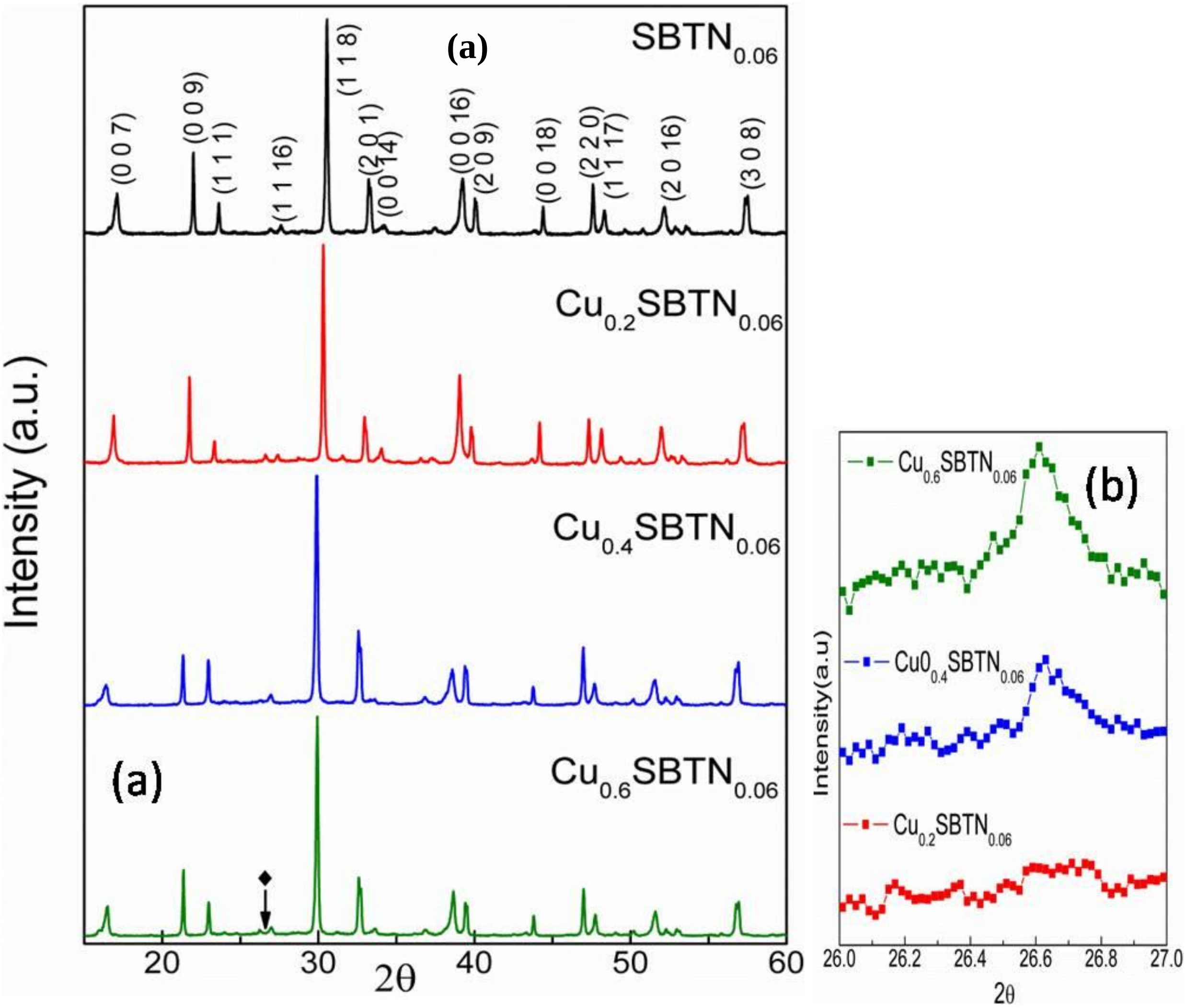

Fig. 4.5.1 (a) Room temperature XRD pattern of sintered pellets of $Cu_xSBTN_{0.06}$ (x=0.0, 0.2, 0.4 and 0. 6) intergrowth ceramics. (b) XRD peak for impurity peak near 26.7^o 2θ.

In the second experiment, CuO has been fixed at 0.2 wt% in $Cu_{0.2}SBTN_{0.06}$ composition and Nb content has been reduced from x=0.06 to 0.04 and 0.02. Fig.4.5.2 shows the room temperature XRD patterns of $Cu_{0.2}SBTN_x$ (x=0.02, 0.04 and 0.06) ceramics. In this case, the amount of impurity phase decreases with decreasing Nb content and the minimum amount of the impurity was found in the $Cu_{0.2}SBTN_{0.02}$ composition. The values of lattice parameters of all compositions are shown in Table 4.5.1.

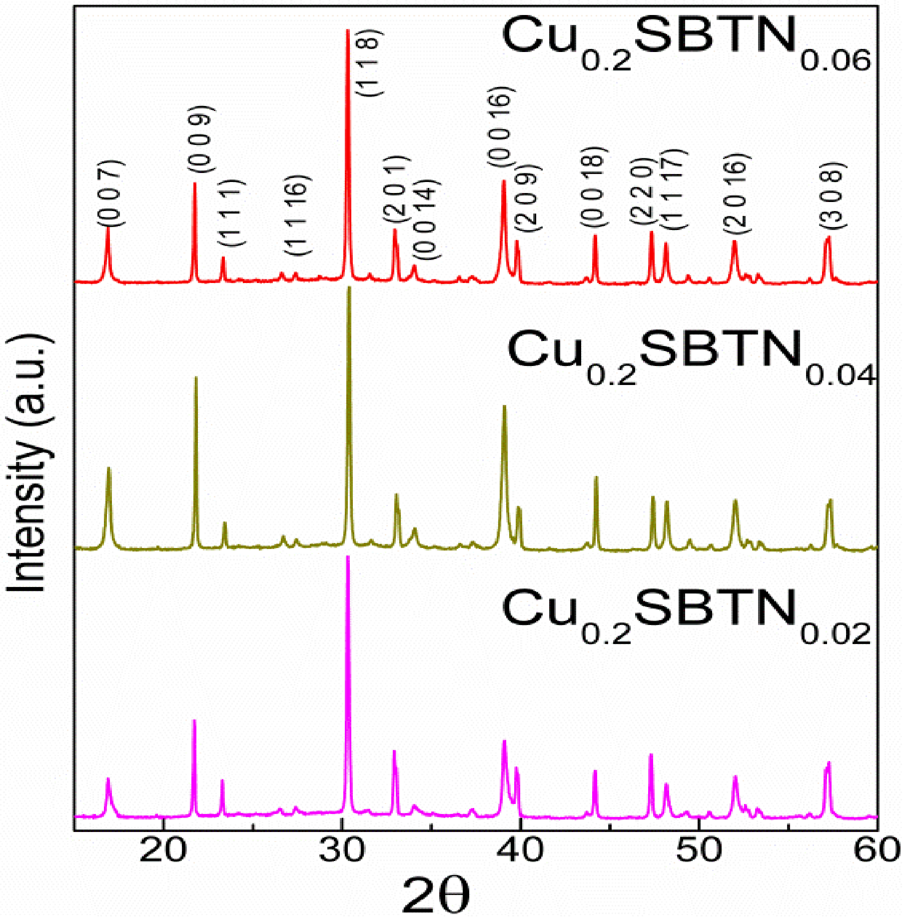

Fig.4.5.2 Room temperature XRD pattern of sintered pellets of $Cu_{0.2}SBTN_x$ (x=0.02, 0.04 and 0.06) intergrowth ceramics.

Table 4.5.1 Lattice parameter of $SBTN_{0.06}$, $Cu_{0.2}SBTN_x$ (x=0.02, 0.04 and 0.06) and $Cu_xSBTN_{0.06}$(x=0.4, 0.6) ceramics.

Compositions	a	b	c	Orthorhombicity
$SBTN_{0.06}$	5.4392	5.4571	74.1846	0.0033
$Cu_{0.2}SBTN_{0.06}$	5.4586	5.4682	74.3610	0.0017
$Cu_{0.4}SBTN_{0.06}$	5.4379	5.4501	74.1607	0.0022
$Cu_{0.6}SBTN_{0.06}$	5.4337	5.4495	74.0628	0.0029
$Cu_{0.2}SBTN_{0.04}$	5.4870	5.4910	74.6909	0.0007
$Cu_{0.2}SBTN_{0.02}$	5.4265	5.4395	73.7166	0.0024

4.5.2.2 Microstructural characteristics

Fig. 4.5.3 shows the scanning electron micrographs of $Cu_{0.2}SBTN_x$ (x=0.02, 0.04 and 0.06) intergrowth ceramics. All microstructures show plate like grains with random orientation. It has been found that the grain size in $Cu_{0.2}SBTN_{0.02}$ ceramics is highest among other $Cu_{0.2}SBTN_x$. This may be due to the fact that Nb acts as a grain growth inhibitor in BLSF ceramics as mentioned in the previous chapter (section 4.3). The aspect ratio of $Cu_{0.2}SBTN_{0.02}$ is much higher than other $Cu_{0.2}SBTN_x$ compositions.

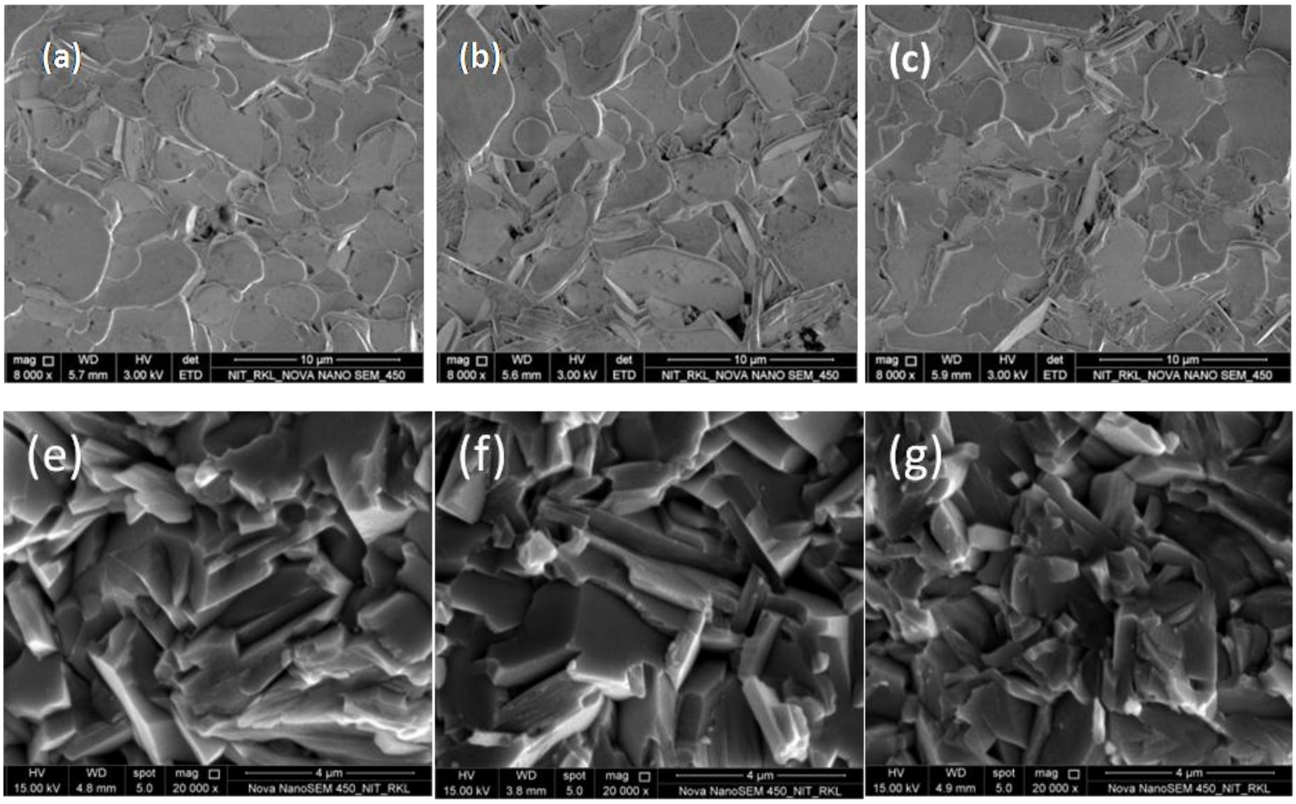

Fig. 4.5.3 (a), (b), and (c) Surface morphology and (e), (f) and (g) freshly broken bulk surface morphology of $Cu_{0.2}SBTN_x$ (x=0.02, 0.04 and 0.06) intergrowth ceramics.

Fig. 4.5.3 (e), (f), (g) show freshly broken bulk surface morphology of three composition. Bulk of the ceramics has shown very compact dense pore free microstructure. This is due to the effect of CuO addition. CuO helps in sintering by forming liquid phase.

4.5.2.3 Dielectric Behavior

The room temperature permittivity (ε_{rm}) and room temperature dielectric loss (tan δ), the maximum relative permittivity (ε_m) and loss factor at the Curie temperature of the $Cu_{0.2}SBTN_x$ (x=0.02, 0.04, 0.06) and $SBTN_{0.06}$ based ceramics at frequency 100 KHz are shown in the Table 4.5.3. Fig. 4.5.4 shows the temperature dependence of relative permittivity (ε′) and dielectric loss (tan δ) for $Cu_{0.2}SBTN_x$ (x=0.02, 0.04, 0.06) intergrowth ceramics. The room temperature permittivity (ε_{rm}) and dielectric loss (tan δ), the maximum relative permittivity (ε_m) and loss factor at the Curie temperature are shown in the table 4.5.2. With the increase in Nb content in $Cu_{0.2}SBTN_x$ (x=0, 0.02, 0.04, 0.06) intergrowth ceramics, the dielectric constant increases as shown in Fig. 4.5.5.

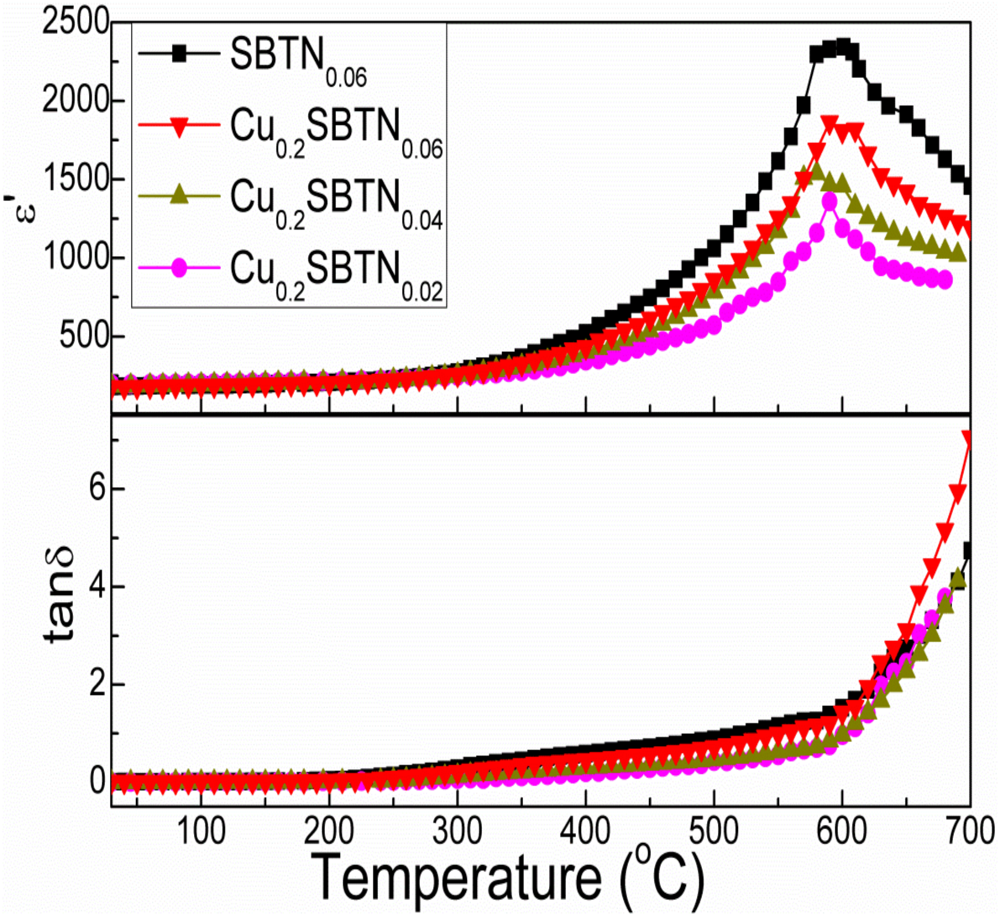

Fig. 4.5.4 Temperature dependence of dielectric permittivity (ε´) and dielectric loss (tan δ) for $Cu_{0.2}SBTN_x$ (x=0.02, 0.04, 0.06) intergrowth ceramics measured at a frequency of 100 kHz.

Table 4.5.2 Dielectric constant (ε') and loss (tan δ) of $Cu_{0.2}SBTN_x$ (x=0.02, 0.04, 0.06) and $SBTN_{0.06}$ based ceramics at room temperature and Curie temperature with frequency 100 KHz.

Sample ID	ε'_{rm} at 30°C	tanδ at 30°C	T_c	ε'_c at T_c	tanδ at T_c
$Cu_{0.2}SBTN_{0.02}$	197	0.00745	590	1360	0.6998
$Cu_{0.2}SBTN_{0.04}$	186	0.00761	580	1540	0.7347
$Cu_{0.2}SBTN_{0.06}$	178	0.00937	590	1863	1.2096
$SBTN_{0.06}$	180	0.0117	590	2344	1.3825

4.5.2.4 Impedance Spectroscopy

The AC activation energy of the sample is calculated by plotting Ln of relaxation time versus reciprocal temperature of the peak, showing an Arrhenius relationship, for $Cu_{0.2}SBTN_x$ (x=0.02, 0.04, 0.06) intergrowth ceramics at 100 kHz with temperature at 450°C shown in the Fig. 4.5.5. The activation energy of *ac* conductivity of the samples at various temperatures as determined from Eq. 4.1.10 based on the relaxation frequency.

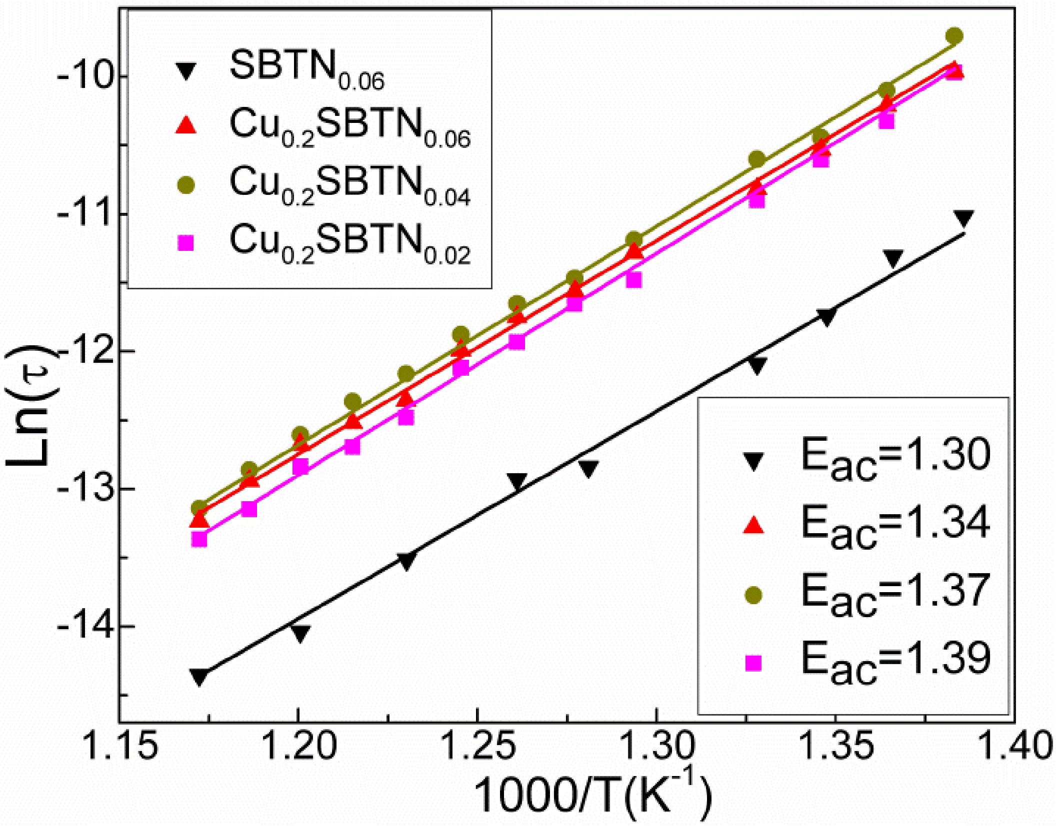

Fig. 4.5.5 Arrhenius plot of ac conductivity, for $Cu_{0.2}SBTN_x$ (x=0.02, 0.04, 0.06) intergrowth ceramics at 100 kHz. Activation energy of ac (E_{ac}), calculated from the slope are shown in inset.

Fig. 4.5.6 shows the complex impedance curve illustrating the variation of Z' and Z'' for $Cu_{0.2}SBTN_x$ (x= 0.02, 0.04, 0.06) intergrowth ceramics measured at a frequency of 100 kHz and temperature 450°C. It is very interesting to observe that that the grain resistance decreases with the increase in Nb content in $Cu_{0.2}SBTN_x$. This may be due to the increase in the amount of impurity with increasing Nb. The dc conductivity values for all sample is calculated from the Arrhenius relation, Eq. 4.1.10, and as listed in the Table 4.5.3. Unlike the other $Cu_{0.2}SBTN_x$ systems, the *dc* conductivities of those samples are in the order 10^{-6} and is lowest in $Cu_{0.2}SBTN_{0.02}$ composition possibly due to the presence of least amount of CuO additive.

From the plot of ln σ_{dc} versus T^{-1}, E_{dc} values are calculated based on Arrhenius relation Eq. 4.1.11. The dc activation energy is mainly for grain (E_{dc}) and is listed in Table 4.5.3. E_{dc} is maximum for $Cu_{0.2}SBTN_{0.02}$. The difference in the morphology of the grains and their aspect ratio may be the reason behind such behaviour. The aspect ratios of all the compositions are less compared to $Cu_{0.2}SBTN_{0.02}$. The dc conductivity of ceramics increased with increasing CuO additive due to the dis-balance of donor-acceptor level

Table 4.5.3 DC-conductivity (σ_{dc}) at 450°C, dc-Activation energy for $Cu_{0.2}SBTN_x$ (x=0.02, 0.04, 0.06) intergrowth ceramics.

Formula	$Cu_{0.2}SBTN_{0.02}$	$Cu_{0.2}SBTN_{0.04}$	$Cu_{0.2}SBTN_{0.06}$	$SBTN_{0.06}$
σ_{dc} (Ω^{-1})	2.2 x10^{-6}	2.5 x10^{-6}	3.4 x10^{-6}	7.125 x10^{-6}
E_{dc} (eV)	1.26	1.23	1.22	1.07

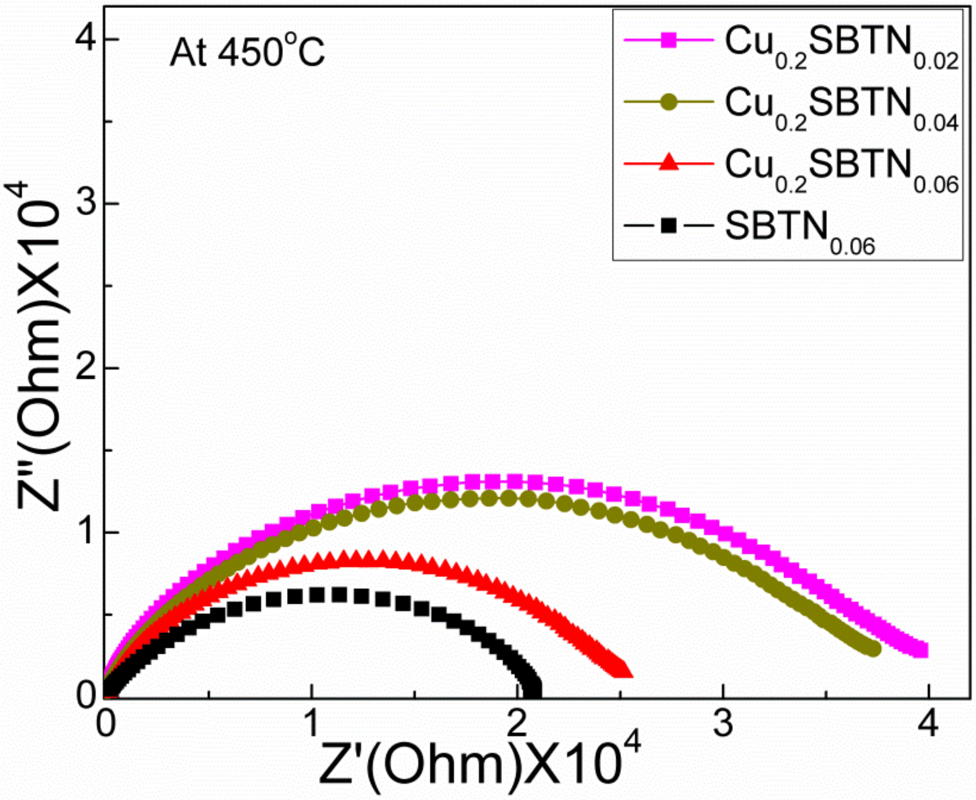

Fig 4.5.6 Complex impedance curve of Z′ and Z″ for $Cu_{0.2}SBTN_x$ (x=0.02, 0.04, 0.06) and $SBTN_{0.06}$ intergrowth ceramics at 100 kHz with temperature at 450°C.

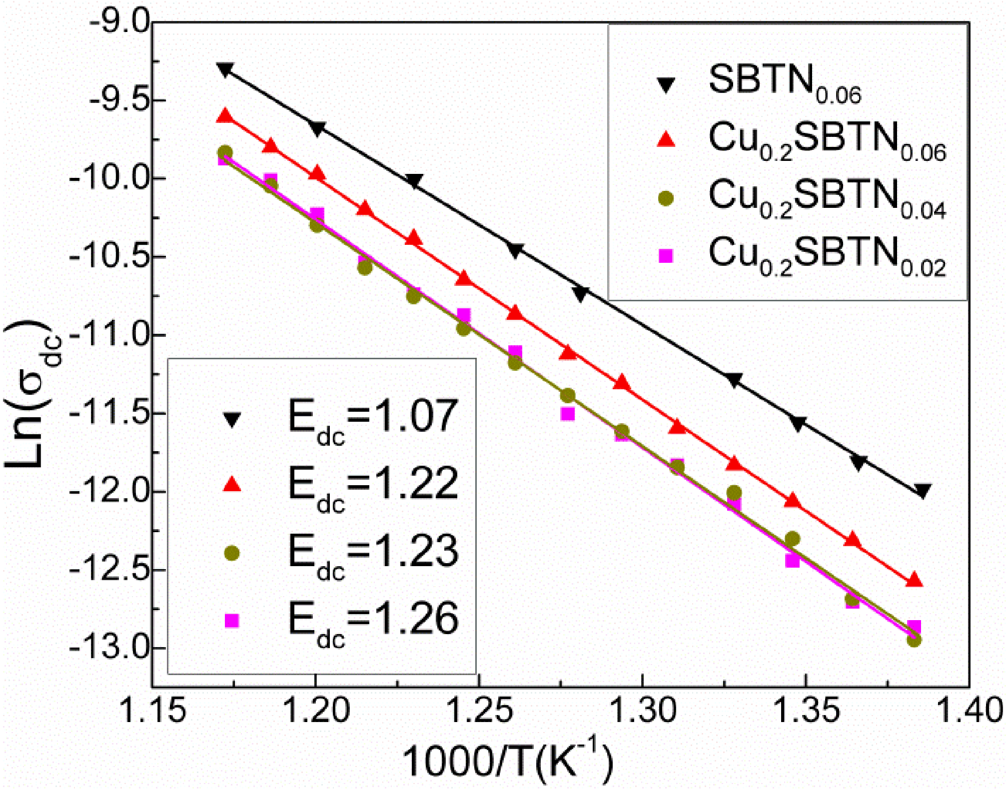

Fig 4.5.7 Arrhenius plot of dc conductivity, for $SBTN_{0.06}$ and $Cu_{0\cdot 2}SBTN_x$ (x=0.06, 0.04, 0.02) intergrowth ceramics at 100 kHz with temperature at 450°C.

4.5.2.5 Polarization Hysteresis Characteristics

Fig. 4.5.7 shows the polarization-electric field hysteresis loops for $Cu_{0.2}SBTN_x$ (x=0.02, 0.04, 0.06) intergrowth ceramics under the electric field of 80 KV/cm. Table 4.5.4 shows the ferroelectric data (P_r and E_c) of $Cu_{0\cdot 2}SBTN_x$ (x=0, 0.02, 0.04, 0.06) intergrowth ceramics. Hysteresis loops aren’t saturated due to the limitation of the applicable electric field of the equipment. The value of P_r of $Cu_{0\cdot 2}SBTN_{0.02}$ is highest in this series. This may be due to the lowest impurity phase present in the composition and highest grain size, as well as highest resistivity of the composition. The results indicate that a small amount of CuO, as well as low level Nb doping is simultaneously required for improving the ferroelectric properties of the intergrowth. The addition of CuO in small quantities significantly enhances the ferroelectric properties of BIT-SBTi4 intergrowth due to improved densification.

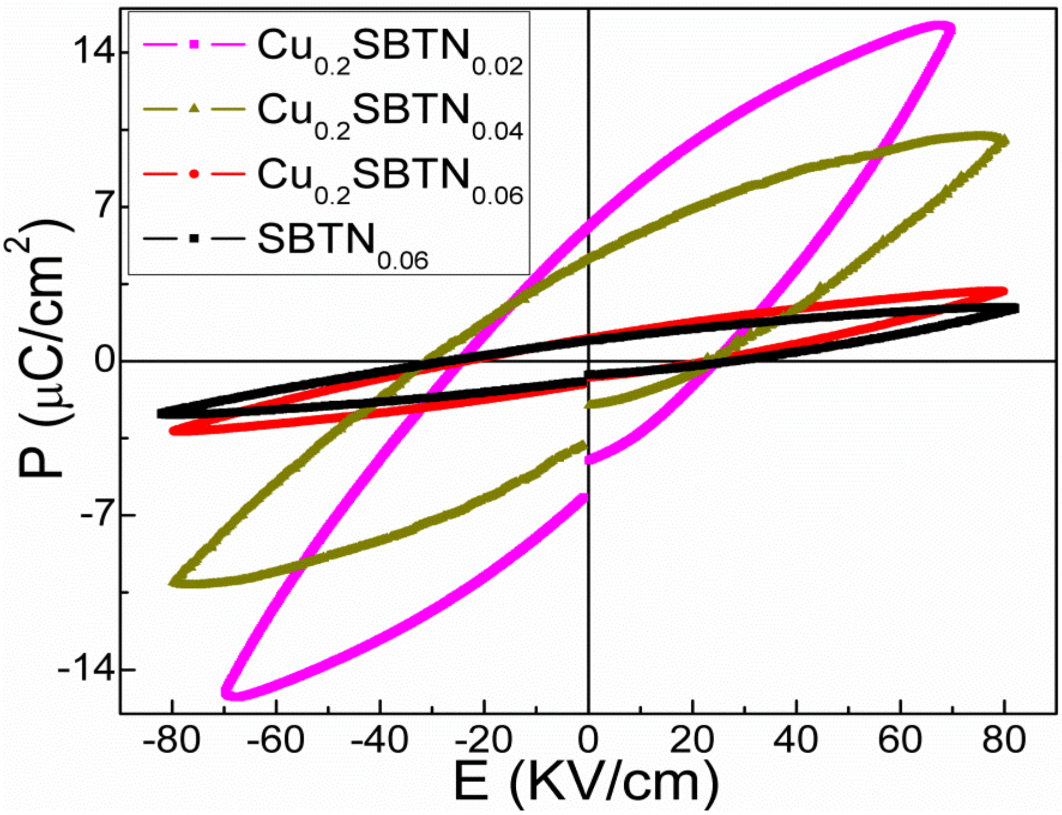

Fig 4.5.8 P-E hysteresis loops for $Cu_{0.2}SBTN_x$ (x=0, 0.02, 0.04, 0.06) intergrowth ceramics.

Table 4.5.4 P_r and E_c of $Cu_{0.2}SBTN_x$ (x=0, 0.02, 0.04, 0.06) intergrowth ceramics

Sample ID	P_r(μC/cm2)	E_c(kV/cm)
$Cu_{0.2}SBTN_{0.02}$	6.2	25.2
$Cu_{0.2}SBTN_{0.04}$	4.8	28.9
$Cu_{0.2}SBTN_{0.06}$	1.2	25.1
$SBTN_{0.06}$	1.1	27.9

4.5.3 Conclusions

Effects of CuO additive on dielectric and ferroelectric properties of Nb modified BIT-SBTi4 intergrowth ceramics has been investigated. CuO additive has been used in 0.2, 0.4 and 0.6 wt % in $SrBi_8Ti_{6.88}Nb_{0.12}O_{27}$ (abbreviated as $Cu_xSBTN_{0.06}$). The T_c of the intergrowth ferroelectrics remains unchanged. The dc conductivity of ceramics increased with increasing CuO additive due to the dis-balance of donor-acceptor level. The P_r of $Cu_{0.2}SBTN_{0.02}$ ceramics is highest among all. This may be due to the lowest impurity phase present in the composition and highest grain size as well as highest resistivity of the composition.

4.5.4 References

[1] H.Y. Park, J.Y. Choi, M. K. Choi, K. H. Cho, S. Nahm, H. G. Lee, et al., *J Am Ceram Soc* 91 (2008) 2374–2377.

[2] H. Sun, Y. Zhang, X. Liu, Y. Liu, W. Chen, *Ceramics International* 41(2015) 555–565.

[3] N. Zidi, A. Chaouchi, S. d'Astorg, M. Rguiti, C. Courtois, *J. Alloys Compd.* 590 (2014) 557–564.

Chapter V

Conclusions and Future Work

Conclusions and Future Work

Intergrowth bismuth layered structure ferroelectrics (BLSFs) in the system SrO-Bi_2O_3-TiO_2 have been investigated with an objective of improving their dielectric and ferroelectric properties. Three BLSF compounds in this system were studied namely $Bi_4Ti_3O_{12}$ (BIT), $SrBi_4Ti_4O_{15}$ (SBTi4) and $Sr_2Bi_4Ti_5O_{18}$ (SBTi5) together with one stable intergrowth BLSF compound, $Bi_4Ti_3O_{12}$-$SrBi_4Ti_4O_{15}$ (BIT-SBTi4). All these BLSFs compounds have been synthesized through a modified oxalate route. SBTi4-SBTi5 composite ceramics were also synthesized and characterized. Their phase formation behavior, during synthesis, has been investigated in details using TG/DSC and XRD analysis. The crystal structures of all the compounds were refined through Rietveld analysis to find accurate structural parameters. Densification characteristics, microstructure development, dielectric and ferroelectric properties of all the compounds were analysed and correlated with each other. The some major findings were:

i. BIT, SBTi4, SBTi5 ceramics have been successfully synthesized through a modified oxalate route. For these three compounds, pure phases were formed at 800°C, 1050°C and 1100°C for BIT, SBTi4 and SBTi5 respectively. This indicates that 4 and 5 layered compounds are difficult to synthesize due to their longer unit cell length along *c*-axis. Similarly, the sintering of SBTi5 was most difficult. The grain size and preferred orientation of the plate like grains was highest in the SBTi5 ceramics. The Curie temperature of BIT ,SBTi4 ,SBTi5 ceramics were 660°C, 530°C and 290°C, respectively. SBTi5 showed highest remnant polarization P_r among all.

ii. A phase pure BIT-SBTi4 intergrowth ferroelectric has been successfully synthesized through the same modified oxalate synthesis route at a temperature as low as 800°C. The Rietveld analysis of XRD pattern showed that there was increase of lattice parameters due to the crystal structure mismatch and stresses generated in intergrowth ceramics.

iii. Dielectric measurement revealed that the T_c of BIT-SBTi4 was 610^{o}C and the room temperature ε′, and tan δ was about 200 and 0.002 respectively. The intergrowth ferroelectric showed a larger $2P_r$ than their constituents BIT and SBTi4. All these results suggest that this modified oxalate route may be an alternative and effective processing route for commercial preparation.

iv. Only a short range intergrowth structure between SBTi4-SBTi5 could be achieved with broaden permittivity temperature characteristics. The composite exhibited two prominent dielectric anomaly peaks at 310 and 530^{o}C corresponding to SBTi5 and SBTi4, respectively and one diffuse anomaly peak at 470^{o}C. This diffuse peak may be due to the formation of short range intergrowth structure. The broader permittivity with temperature shown by the composite may be useful for elevated temperature application.

v. Nb-doping in BIT-SBTi4 intergrowth has been found to be very effective for improving the electrical properties of the ferroelectrics. The preferred orientation of plate-like grains and their sizes decreased with Nb doping. This indicates that Nb acts as a grain growth inhibitor. The T_c of the intergrowth ferroelectrics decreases due to the decrease in orthorhombicity and hence, distortion of the structure. The peak permittivity increased, due to the increase in density and decrease in preferred orientation of the grains. Doping also introduces relaxor like behaviour in the ceramics. The dc conductivity decreased and remnant polarization (P_r) increased due to decreased oxygen vacancy concentration with Nb doping.

vi. The ferroelectric properties of Nb modified BIT-SBTi4 intergrowth has been further enhanced by the substitution of La for Bi. With increasing La substitution, the average grain size of the ceramics was reduced, orthorhombic distortion and micro-strain of the structure decreased, and there was decrease in T_c due to the decrease in orthorhombic distortion, the dielectric permittivity peak becomes broadened and suppressed due to the formation of inhomogeneous polar clusters, etc. The remnant polarization $2P_r$ increased significantly due to the increase in dielectric diffusion.

vii. The ferroelectric property of the intergrowth ceramic can be improved by CuO addition without impacting T_c. A small amount of CuO (~0.2 wt%) and Nb doping (0.02 atom %) were simultaneously required to improve the ferroelectric properties. This may be due to the better densification of the ceramics due to the addition of CuO.

The scopes of the future works are:

- Application of these optimized composition in FeRAM device preparation where the materials will act as capacitor material.
- High temperature piezoelectric applications of these materials.
- Investigation of doping in SBTi4-SBTi5 composite materials.

1. $Bi_4Ti_3O_{12}$ structural model for Rietveld Refinement.

Reference for structural model: C. H. Hervoches and P. Lightfoot, *Chemistry of materials*, 11 (1999) 3359-3364.

Table-1: Refinement parameters were taken for $Bi_4Ti_3O_{12}$.

Crystal system		Orthorhombic
Space group		B2cb
Cell parameters (Å)	*a*	5.4444(1)
	b	5.4086(1)
	c	32.8425(6)
V (Å^3)		967.10(3)
Data range (d/Å)		0.66-2.48
No. of reflections		2292
No. of Variables		50
χ^2		3.9
R_{wp}		9.0

Table-2: Atomic coordinates and Isotropic temperature factors for $Bi_4Ti_3O_{12}$

atom	*x*	*y*	*z*	*U*(iso), Å^2
Bi(1)	0.0000	0.9982(7)	0.06639(8)	0.0130(7)
Bi(2)	1.001(1)	0.0139(9)	0.21127(8)	0.0180(8)
Ti(1)	0.052(2)	0	0.5	0.002(2)
Ti(2)	0.037(2)	1.004(2)	0.3717(2)	0.016(2)
O(1)	0.322(2)	0.265(1)	0.0069(2)	0.032(2)
O(2)	0.265(1)	0.263(2)	0.2485(2)	0.007(1)
O(3)	0.086(1)	1.0640(9)	0.4406(2)	0.014(1)
O(4)	1.052(1)	0.9453(9)	0.3193(1)	0.010(1)
O(5)	0.284(2)	0.253(2)	0.1109(2)	0.023(1)
O(6)	0.217(2)	0.201(2)	0.8756(2)	0.034(2)

2. $SrBi_4Ti_4O_{15}$ structural model for Rietveld Refinement.

Reference for structural model: B.J. Kennedy, Q. Zhou, Ismunandar, Y. Kubota, K. Kato, *J. Solid State Chem.*, 181 (2008) 1377–1386.

Table-3: Refinement parameters were taken for $SrBi_4Ti_4O_{15}$.

Crystal system		Orthorhombic
Space group		$A2_1am$
Cell parameters (Å)	a	5.4509(3)
	b	5.4373(3)
	c	41.005 (22)

Table-4: Atomic coordinates and Isotropic temperature factors for $SrBi_4Ti_4O_{15}$

atom	x	y	z	B_{iso}(Å^2)	N
Bi(1)/ Sr	0.25	0.2600(24)	0	0.66(9)	0.81(1)
Bi(2)	0.256(3)	0.2394(16)	0.1051(2)	1.37(7)	0.83(1)
Bi(3)/ Sr	0.248(3)	0.2582(13)	0.2189(1)	1.24(5)	0.98(1)
Ti(1)	0.270(3)	0.251(5)	0.4507(1)	0.3(1)	1
Ti(2)	0.247(3)	0.246(3)	0.3466(1)	0.1(1)	1
O(1)	0.297(4)	0.197(3)	0.5	0.5(2)	1
O(2)	0.558(4)	0.5351(24)	0.0488(3)	1.5(2)	1
O(3)	0.302(3)	0.2967(22)	0.4001 (2)	0.3(2)	1
O(4)	0.508(3)	0.4919(29)	0.1394(2)	1.3(2)	1
O(5)	0.244(4)	0.2255(25)	0.2999(2)	1.7(2)	1
O(6)	0.510(4)	0.4966(22)	0.2504(3)	1.4(1)	1
O(7)	-0.006(4)	-0.0292(27)	0.0452(3)	1.6(2)	1
O(8)	0.014(5)	0.012(4)	0.1472(3)	2.6(3)	1

3. $Sr_2Bi_4Ti_5O_{18}$ structural model for Rietveld Refinement.

Reference for the structural model: Ismunandar, T. Kamiyama, A. Hoshikawa, Q. Zhou, B.J. Kennedy, Y. Kubota, K. Kato, *J. Solid State Chem.*, 177 (2004) 4188–4196.

Table-5: Refinement parameters taken for $Sr_2Bi_4Ti_5O_{18}$.

Crystal system		Orthorhombic
Space group		B2cb
Cell parameters (Å)	*a*	5.4647(2)
	b	5.4625(2)
	c	48.8515(7)
V (Å^3)		1458. 23 (7)
T		1.00
R_p		4.67
R_{wp}		6.06
R_{Bragg}		2.17
GOF		1.43

Table-6: Final Atomic coordinates and Isotropic temperature factors were taken for $Sr_2Bi_4Ti_5O_{18}$.

atom	*x*	*y*	*z*	*B*
Bi(1)/Sr(1)	0	0.000(2)	0.0421(1)	0.9(1)
Bi(2)	0.003(2)	-0.021(2)	0.2241(1)	1.6(1)
Bi(3)/Sr(2)	0.002(4)	0.004(2)	0.1297(1)	1.6(1)
Ti(1)	0.011(5)	0	0.5	0.6
Ti(2)	0.013(4)	0.994(4)	0.4168(2)	0.6
Ti(3)	0.018(3)	0.007(5)	0.3314(2)	0.6
O(1)	0.290(3)	0.254(2)	0.0021(3)	0.6
O(2)	0.266(3)	0.246(2)	0.2491(2)	0.5(1)
O(3)	0.005(3)	0.020(4)	0.2960 (1)	1.2(2)
O(4)	0.041(4)	0.966(3)	0.3790(1)	0.6
O(5)	0. 042(3)	0. 041(3)	0.4598(2)	1.0(2)

O(6)	0. 262(3)	0.230 (2)	0. 0776(2)	0.6
O(7)	0. 316(2)	0. 295(2)	0. 9182(2)	0.6
O(8)	0. 263(3)	0. 251(2)	0. 8413(2)	0.6
O(9)	0. 282(2)	0. 257(2)	0. 1630(2)	0.7(2)

4. $Bi_4Ti_3O_{12}$-$SrBi_4Ti_4O_{15}$ intergrowth structural model for Rietveld Refinement.

Reference for structural model: J. Tellier, P. Boullay and D. Mercurio, *Z. Kristallogr.*, 222 (2007) 234-243.

Table-7: Refinement parameters taken for $SrBi_8Ti_7O_{27}$.

Crystal system		Orthorhombic
Space group		I2cm(SG n^o 46:-cba)
Cell parameters (Å)	*a*	5.4460(2)
	b	5.4242(2)
	c	74.291(3)

Table-8: Atomic coordinates and Isotropic temperature factors taken for $SrBi_8Ti_7O_{27}$

	x	*y*	*z*	U_{iso} (Å^2)
Ti1	-0.024	0	0	0.0035
Ti2	-0.024	0	0.4429	0.0035
Ti3	-0.024	0.5	0.2781	0.0035
Ti4	-0.024	0.5	0.1630	0.0035
Bi1	0	0.0008	0.25	0.0213
Bi2	0	-0.0117	0.6899	0.0213
Bi3	0	0.4842	0.0919	0.0213
Bi4	0	0.4966	0.5293	0.0213
Bi5	0	-0.0113	0.1270	0.0213
O1a	-0.040	-0.056	0.0275	0.02
O1b	-0.017	-0.030	0.5826	0.02
O1c	-0.031	0.454	0.1950	0.02
O1d	0	0.488	0.6397	0.02

O1e	-0.043	0.441	0.75	0.02
O2a	0.221	0.252	0.0036	0.02
O2b	0.226	0.246	0.1109	0.02
O2c	0.25	0.271	0.2269	0.02
O2d	0.220	0.239	0.3326	0.02
O2e	0.25	0.223	0.4490	0.02
O2f	0.200	0.276	0.5556	0.02
O2g	0.230	0.264	0.6699	0.02
O2h	0.195	0.226	0.7795	0.02
O2i	0.221	0.253	0.8902	0.02

Curriculum Vitae

GEETANJALI PARIDA
Q/No-C/311, Sector- 16
Rourkela-769003, Odisha, India
Mobile: +91-9178510270
Email: geeta.lily@gmail.com

Date of Birth: 22.10.1985

Education: M.Sc. (Physics), M.Tech (Metallurgy and Materials Engg.)

Research Interest: Ferroelectric Ceramic, Electro-Ceramic. Nano material synthesis, Thin Flim

Technical Exposure: Publications: 7, Conference: 6

Publications Related to PhD:

[1] **Geetanjali Parida**, J. Bera, "Dielectric properties of $Bi_4Ti_3O_{12}$-$SrBi_4Ti_4O_{15}$ intergrowth ceramics synthesized by a modified oxalate route", Phase Transitions 87, 452-459, (2013).

[2] **Geetanjali Parida**, J. Bera, "Electrical properties of Niobium doped $Bi_4Ti_3O_{12}$-$SrBi_4Ti_4O_{15}$ intergrowth ferroelectrics", Ceramics International 40, 3139-3144, (2014).

[3] **Geetanjali Parida**, J. Bera, "Dielectric and ferroelectric properties of $SrBi_4Ti_4O_{15}$-$Sr_2Bi_4Ti_5O_{18}$ composite ceramics", Ceramics International, 40, 14913–14917,(2014).

[4] **Geetanjali Parida**, J. Bera, "Effect of La-substitution on the Structure, Dielectric and Ferroelectric Properties of Nb modified $SrBi_8Ti_7O_{27}$ Ceramics", Material Research Bulletin, 68 (2015) 155-159.

[5] **Geetanjali Parida**, J. Bera, "Processing and electrical properties of $Bi_4Sr_{n-3}Ti_nO_{3n+3}$ (n=3,4 and 5) ceramics synthesized by a modified oxalate route"(to be communicated)

[6] **Geetanjali Parida**, J. Bera, "Effect of CuO addition on ferroelectric properties of Nb-modified $SrBi_8Ti_7O_{27}$ ceramics" (to be communicated)

Conference/Seminars Publications Related to PhD:

[1] Geetanjali Parida, J. Bera, "Characterization of $Sr_2Bi_4Ti_5O_{18}$ Ferroelectrics Synthesized by Modified Chemical Route", XVII NSFD-2012, December 17-19 (2012), ITER, **Bhubaneswar**.

[2] Geetanjali Parida, J. Bera, "Synthesis and Characterization of $SrBi_4Ti_4O_{15}$ and $Sr_2Bi_4Ti_5O_{18}$ Mixed-layered Ferroelectrics", MR13, May 8-10 (2013), IIT Bombay, **Bombay.**

[3] Geetanjali Parida, J. Bera, "Electrical properties of niobium doped $Bi_4Ti_3O_{12}$-$SrBi_4Ti_4O_{15}$ intergrowth ferroelectrics", NCPCM – 2013, December 6-7 (2013), NIT **Rourkela.**

[4] Geetanjali Parida, J. Bera, "Dielectric properties of niobium doped $Bi_4Ti_3O_{12}$-$SrBi_4Ti_4O_{15}$ intergrowth ferroelectrics Ceramics", ICAFM 2014, February 19-21, 2014, Thiruvananthapuram, **Kerala**.